Current-induced motion of magnetic domain walls in cylindrical nanowires with chemical modulations

Laura Alvaro Gomez

THESIS

To attain the degree of

DOCTOR OF UNIVERSITÉ GRENOBLE ALPES
and UNIVERSIDAD COMPLUTENSE DE MADRID

Doctoral school: Physics
Speciality: Nanophysics

Current-induced motion of magnetic domain walls in cylindrical nanowires with chemical modulations

Presented by:

Laura Álvaro Gómez

Thesis supervisors :

Olivier FRUCHART
Director of research, Laboratoire Spintronique et Technologie des Composants (SPINTEC)
Lucas PÉREZ GARCÍA
Professor, Universidad Complutense de Madrid

Thesis defended in public on 26th June 2023 before a jury composed of the following members:

Arantzazu MASCARAQUE SUSUNAGA Professor, Universidad Complutense de Madrid	President
Liliana BUDA-PREJBEANU Professor, Université Grenoble Alpes, SPINTEC, CNRS, CEA	Examiner
Aurelio HIERRO RODRIGUEZ Doctor in Science, Universidad de Oviedo	Examiner
Javier TORNOS CASTILLO Doctor in Science, Universidad Complutense de Madrid	Examiner
Christian BACK Professor, Technical University Munich	Rapporteur
Matthieu BAILLEUL Director of research, Institute Physical And Chemistry Materials De Strasbourg	Rapporteur

UNIVERSIDAD COMPLUTENSE DE MADRID

FACULTAD DE CIENCIAS FÍSICAS

TESIS DOCTORAL

Current-induced motion of magnetic domain walls in cylindrical nanowires with chemical modulations
Movimiento de paredes de dominio magnéticas inducido por corriente en nanohilos cilíndricos con modulaciones químicas

MEMORIA PARA OPTAR AL GRADO DE DOCTORA

PRESENTADA POR

Laura Álvaro Gómez

DIRECTORES

Olivier Fruchart
Lucas Pérez García

UNIVERSIDAD COMPLUTENSE MADRID

DECLARACIÓN DE AUTORÍA Y ORIGINALIDAD DE LA TESIS PRESENTADA PARA OBTENER EL TÍTULO DE DOCTOR

D./Dña. Laura Álvaro Gómez,
estudiante en el Programa de Doctorado Física - D9AD,
de la Facultad de Ciencias Físicas de la Universidad Complutense de Madrid, como autor/a de la tesis presentada para la obtención del título de Doctor y titulada:

Current-induced motion of magnetic domain walls in cylindrical nanowires with chemical modulations

Movimiento de paredes de dominio magnéticas inducido por corriente en nanohilos cilíndricos con modulaciones químicas

y dirigida por: Olivier Fruchart y Lucas Pérez García

DECLARO QUE:

La tesis es una obra original que no infringe los derechos de propiedad intelectual ni los derechos de propiedad industrial u otros, de acuerdo con el ordenamiento jurídico vigente, en particular, la Ley de Propiedad Intelectual (R.D. legislativo 1/1996, de 12 de abril, por el que se aprueba el texto refundido de la Ley de Propiedad Intelectual, modificado por la Ley 2/2019, de 1 de marzo, regularizando, aclarando y armonizando las disposiciones legales vigentes sobre la materia), en particular, las disposiciones referidas al derecho de cita.

Del mismo modo, asumo frente a la Universidad cualquier responsabilidad que pudiera derivarse de la autoría o falta de originalidad del contenido de la tesis presentada de conformidad con el ordenamiento jurídico vigente.

En Madrid, a 15 de mayo de 2023

Fdo.: Laura Álvaro Gómez

Fecha: 2023.05.15 20:09:07 +02'00'

Esta DECLARACIÓN DE AUTORÍA Y ORIGINALIDAD debe ser insertada en la primera página de la tesis presentada para la obtención del título de Doctor.

Abstract

Title : Current-induced motion of magnetic domain walls in cylindrical nanowires with chemical modulations

Cylindrical magnetic nanowires are a prototypical system for exploring the physics of three-dimensional magnetization dynamics, and are also proposed as building blocks for three-dimensional storage devices. Among other curvature-induced effects, they can host a unique type of magnetic domain wall (DW) known as Bloch-Point-Wall (BPW), whose topology allows for ultra-fast DW motion, thanks to the significant delay in the Walker instability threshold. A crucial feature of BPWs and other spin textures in nanowires, common to three-dimensional systems, is the curling of magnetization induced by dipolar energy. Another key feature is the long-overlooked strong Œrsted field that arises when an electric current flows in the wire, which plays a key role by directly coupling to curling structures. Recent pioneering work in the host group has shown experimental BPW motion under spin-transfer-torque with velocities of several hundred of m/s, but with stochastic pinning. Simulations suggest a non-trivial underlying mechanism for the switching of circulation in the case of an initially-antiparallel Œrsted field.

To achieve better control of DW motion, this thesis investigates engineered nanowires, composed of Permalloy segments separated by magnetic chemical modulations serving as controlled pinning sites. The synthesis was performed by single-bath template-assisted electrodeposition. Subsequently, individual nanowires were electrically contacted to enable the injection of electrical pulses in the nanosecond range. The average resistivity of the wires is $20\,\mu\Omega \times \mathrm{cm}$, compared to $15\,\mu\Omega \times \mathrm{cm}$ for bulk Permalloy. We used several types of magnetic microscopy to access the three-dimensional magnetization textures, all based on X-Ray Magnetic Circular Dichroism (XMCD) : Photo Emission Electron Microscopy (PEEM) in shadow mode, Transmission Electron Microscopy (TXM), Scanning Transmission Electron Microscopy (STXM) or ptychography. Magnetic contrast was obtained by imaging at the Fe L3 edge with the incident X-ray beam nearly perpendicular to the axis of the nanowire, with an offset of 10 degrees. This allows for the clear observation of transverse magnetization components in domain walls, as well as keeping track of the axial domains. Post-processing scripts were used to extract quantitative information on the magnetization components from magnetic images. Complementary experimental techniques such as electron holography were used to study and quantify the magnetic induction field within the nanowire and the stray field arising from it. Micromagnetic simulations were performed using feeLLGood, a homemade finite-element-based code, and mumax3 micromagnetic code, combined with post-processing tools.

Magnetic images revealed axial magnetization at the Permalloy segments, as expected for such long wires. However, they show curling of magnetization around the wire axis at the chemical modulations. This occurs to decrease magnetic charges at the modulations, by trying to maintain a uniform longitudinal magnetization component. In addition, the curling at the modulations can be coupled to the azimuthal magnetization of a BPW. Both can be addressed by the Œrsted field associated with an electric current. We have found that, depending on its amplitude and duration, it can cause circulation switching, DW transformations or long-distance motion. We have identified the underlying mechanism of these phenomena, which relies on the interplay between volume topological objects (Bloch points) and surface objects (vortex-antivortex pairs). In addition, we provide 50 ps time-resolved experiments of both modulation and BPW switching that allow a direct bridge to the micromagnetic simulations. Finally, ultra-fast DW motion above $1\,\mathrm{km} \cdot \mathrm{s}^{-1}$ from one modulation site to the next was achieved, driven by the combined effects of STT, Œrsted field, and Joule heating, which cannot be disentangled experimentally.

Résumé

Titre : Déplacement de parois magnétiques dans des nanofils cylindriques à modulations de matériau

Les nanofils magnétiques cylindriques constituent un cas d'école pour étudier la dynamique d'aimantation dans un système tridimensionnel, et ont également été proposés comme brique de base de dispositifs tridimensionnels de stockage d'information. Parmi les effets induits par la courbure, ils peuvent héberger un type unique de paroi de domaine magnétique appelée Bloch-Point-Wall (BPW). Sa topologie spécifique permet le déplacement ultra-rapide de la paroi, en repoussant considérablement le seuil d'instabilité dynamique dit de Walker. Une caractéristique cruciale des BPW et autres textures de spin dans les nanofils, est le curling de l'aimantation induit par l'énergie dipolaire. Une autre caractéristique clé est le champ Œrsted longtemps négligé qui apparaît lorsqu'un courant électrique circule dans le fil, et qui joue un rôle clé en se couplant directement aux structures de curling. Des travaux pionniers récents dans le groupe hôte ont montré expérimentalement le déplacement BPW sous l'effet d'un courant polarisé en spin avec des vitesses de plusieurs centaines de m/s, mais associé à un piégeage aléatoire. Les simulations suggèrent un mécanisme sous-jacent non trivial pour le basculement de la circulation en cas de champ Œrsted initialement antiparallèle.

Afin d'obtenir un meilleur contrôle du mouvement des paroi, cette thèse étudie des nanofils synthétiques, constitués de segments de Permalloy séparés par des modulations magnétiques chimiques pour induire un piégeage contrôlé. La synthèse a été réalisée par électrodéposition pulsée dans des gabarits poreux et un bain unique. Par la suite, des nanofils individuels ont été contactés électriquement pour permettre l'injection d'impulsions électriques de l'ordre de la nanoseconde. La résistivité moyenne des fils est de $20\,\mu\Omega \times \mathrm{cm}$, comparée à $15\,\mu\Omega \times \mathrm{cm}$ pour le Permalloy. Nous avons utilisé plusieurs types de microscopie magnétique pour accéder aux textures de l'aimantation tridimensionnelles, tous basés sur la Dichroïsme Circulaire Magnétique aux Rayons X (XMCD) : Microscopie Électronique par Émission de Photoélectrons (PEEM) en mode ombre, Microscopie Électronique en Transmission (TXM), Microscopie Électronique en Transmission par Balayage (STXM) ou ptychographie. Le contraste magnétique a été obtenu en imagerie au niveau du bord L3 du fer avec le faisceau de rayons X incident presque perpendiculaire à l'axe du nanofil, avec un décalage de 10 degrés. Cela permet d'observer les composantes de aimantation transversale, ainsi que de suivre les domaines axiaux. Des scripts de post-traitement ont été utilisés pour extraire des informations quantitatives à partir des images magnétiques. Des techniques expérimentales complémentaires telles que l'holographie électronique ont été utilisées pour étudier et quantifier le champ d'induction magnétique. Des simulations micromagnétiques ont été réalisées à l'aide de feeLLGood, un code basé sur les éléments finis développé en interne, et du code micromagnétique mumax3, combinés à des outils de post-traitement.

Les images magnétiques ont révélé une aimantation axiale au niveau des segments de Permalloy, comme prévu pour des fils aussi longs. Cependant, elles montrent une aimantation azimutale autour de l'axe du fil au niveau des modulations chimiques. Cela se produit afin de réduire les charges magnétiques au niveau des modulations, en essayant de maintenir une composante d'aimantation longitudinale uniforme. De plus, cette composante azimutale peut être couplé à l'aimantation azimutale d'un BPW. Ces deux phénomènes peuvent être contrôlés par le champ d'Œrsted associé au courant électrique. Nous avons ainsi constaté que, selon son amplitude et sa durée, ce courant induit le renversement de la circulation azimutale de l'aimantation, des transformations de parois ou des mouvements à longue distance. Nous avons identifié le mécanisme sous-jacent de ces phénomènes, qui reposent sur l'interaction entre les objets topologiques en volume (des points de Bloch) et les objets de surface (paires vortex-antivortex). De plus, nous présentons des expériences résolues dans le temps de 50 ps à la fois de modulation et de basculement du BPW qui permettent de faire le lien direct avec les simulations micromagnétiques. Enfin, un mouvement ultra-rapide de parois supérieur à $1\,\mathrm{km} \cdot \mathrm{s}^{-1}$ d'un site de modulation à l'autre a été réalisé, sous l'effet combiné du transfert de spin, du champ d'Œrsted et du chauffage par effet Joule, effets qui cependant ne peuvent être désintriqués expérimentalement.

Resumen

Título : Movimiento de paredes de dominio magnéticas inducido por corriente en nanohilos cilíndricos con modulaciones químicas

Los nanohilos magnéticos cilíndricos son un sistema prototípico para explorar la física de la dinámica de la imanación tridimensional, y también se proponen como unidades básicas para dispositivos de memorias magnéticas tridimensionales. Entre otros efectos inducidos por la curvatura, destaca la estabilidad de un tipo único de pared de dominio magnético conocida como Bloch-Point-Wall (BPW), cuya topología permite un movimiento ultrarrápido, gracias a que retrasa en gran medida el umbral de inestabilidad de Walker. Una característica crucial de las BPW y otras texturas de espín en nanohilos, común en sistemas tridimensionales, es la imanación azimutal inducida por la energía dipolar. Otra característica clave es el campo Œrsted fuerte y largamente pasado por alto que surge cuando circula una corriente eléctrica en el hilo, y que desempeña un papel clave al acoplarse directamente a las estructuras de rizado. Recientes trabajos pioneros del grupo anfitrión han demostrado el movimiento experimental de la BPW bajo torques por transferencia de espín con velocidades de varios cientos de m/s, pero con anclaje estocástico. Las simulaciones sugieren un mecanismo subyacente no trivial para el cambio de circulación en el caso de un campo Œrsted inicialmente antiparalelo.

Para lograr un mejor control del movimiento de la pared magnética, esta tesis investiga nanohilos modulados en composición, basados en segmentos de Permalloy separados por modulaciones químicas magnéticas como sitios de anclaje controlados. La síntesis se realizó mediante electrodeposición asistida por membrana. Posteriormente, los nanohilos individuales se contactaron eléctricamente para permitir la inyección de pulsos eléctricos en el rango de los nanosegundos. La resistividad promedio de los nanohilos es de $20\,\mu\Omega \times \mathrm{cm}$, en comparación con $15\,\mu\Omega \times \mathrm{cm}$ para el Permalloy. Utilizamos varios tipos de microscopía magnética para acceder a las texturas de imanación tridimensionales, todos basados en el Dicroísmo Circular Magnético de Rayos X (XMCD, por sus siglas en inglés) : Microscopía de Emisión de Electrones por Fotoemisión (PEEM) en modo de sombra, Microscopía Electrónica de Transmisión (TXM), Microscopía Electrónica de Transmisión por Barrido (STXM) o ptycografía. El contraste magnético se obtuvo mediante la obtención de imágenes en el borde L3 del hierro con el haz de rayos X incidente casi perpendicular al eje del nanohilo, con un desplazamiento de 10 grados. Esto permite la observación clara de las componentes de imanación transversal en las paredes de dominio, así como el seguimiento de los dominios axiales. Se utilizaron scripts de posprocesamiento para extraer información cuantitativa de las componentes de imanación a partir de las imágenes magnéticas. Se utilizaron técnicas experimentales complementarias, como la holografía electrónica, para estudiar y cuantificar el campo de inducción magnética dentro del nanohilo. Se realizaron simulaciones micromagnéticas utilizando feeLLGood, un código creado por colaboradores basado en elementos finitos, y el código micromagnético mumax3, combinados con herramientas de posprocesamiento.

Las imágenes magnéticas revelaron imanación axial en los segmentos de Permalloy, como era de esperar para nanohilos tan largos. Sin embargo, muestran imanación azimutal alrededor del eje del nanohilo en las modulaciones químicas. Esto ocurre para disminuir las cargas magnéticas en las modulaciones, tratando de mantener una componente de imanación longitudinal uniforme. Además, esta componente azimutal en las modulaciones puede acoplarse a la imanación azimutal de una BPW. Ambas pueden abordarse mediante el campo Œrsted asociado a una corriente eléctrica. Hemos encontrado que la pared, dependiendo de la amplitud y duración del pulso, puede cambiar de circulación, transformarse o moverse una larga distancia. Hemos identificado el mecanismo subyacente de estos fenómenos, que se basa en la interacción entre objetos topológicos de volumen (puntos de Bloch) y objetos de superficie (pares vórtice-antivórtice). Además, presentamos experimentos con resolución temporal de 50 ps ps tanto de modulación como de cambio de BPW que permiten un enlace directo con las simulaciones micromagnéticas. Por último, se ha logrado un movimiento ultrarrápido de la pared magnética de una modulación química a la siguiente, con velocidades superiores a $1\,\mathrm{km}\cdot\mathrm{s}^{-1}$. Este movimiento es impulsado por torques de transferencia de espín, el campo de Œrsted y el calentamiento Joule, los cuales no pueden separarse experimentalmente.

"Courage doesn’t always roar. Sometimes courage is the little voice at the end of the day that says I’ll try again tomorrow."

Mary Anne Radmacher

Acknowledgments

What a journey! That's the first thing that comes to mind when I reflect on my PhD period. It's been a turning point in my life, both professionally and personally. While it hasn't been easy, I'm grateful for the experience because it pushed me to my limits and expanded my horizons. Looking back, I can only express my gratitude to all the people I've encountered during this journey.

First and foremost, I'd like to thank my supervisors, Olivier and Lucas. This joint PhD program between Grenoble and Madrid was ideal for me because it allowed me to be in two very different cities that feel like home. Thank you for trusting me and giving me the opportunity to work in four different labs across two countries. I also appreciate your patience with the endless bureaucratic we faced. Olivier, I've learned so much from you about magnetism and professionalism. Thank you for your guidance, time, and endless discussions. Lucas, who would have thought that five years after my undergraduate thesis, we'd be here? I always admired the great lab group dynamics you had, but I never thought I'd end up in your group! Thank you for your grounded approach to science, making difficult things easy, and for always transmitting such a positive vibe.

I would like to express my gratitude to everyone who has been part of the spin-textures team during these years. A huge thank you to Aurélien, one of the people I have enjoyed working with the most. Your contagious energy and tremendous help during TEM work, beamtimes, and endless periods at the cleanroom have been invaluable. It has been a great pleasure to work with someone who possesses such vitality and a unique perspective. I also want to thank Daria for your guidance and insightful discussions on simulations. Working with you has been enjoyable, and I have learned a lot from your calm and organized approach to everything. Moving on to Christophe, I want to extend an enormous thank you for all your help with electronics. I was a complete newbie in this area, and now I feel like I have a handle on it! Without your contributions, no experiment would have been possible. Michael, thank you for sharing your thesis knowledge, which provided the foundation for mine. I appreciate your great help and motivation throughout the different challenges. Arnaud and Jerome, thank you for your contributions with micromagnetic simulations. Mahdi, thank you for your help with TEM work. And finally, Dhananjay, thank you for your help with MFM and for all the valuable discussions.

During this work, we conducted many beamtimes at synchrotron facilities, which, despite the complexity of the experiments, were enjoyable thanks to the people I worked with there. Specifically, I want to express my gratitude to Michael, Lucia, Miguel Angel, and Waqas at ALBA and Nico and Rachid at SOLEIL. Your expertise made the experiments presented in this thesis possible, and you continuously pushed the limits to optimize the measurement conditions. But above all, thank you for making the endless hours and issues pleasant, and for celebrating the achievements with me. I value you all not only professionally but also personally. I would also like to extend my thanks to the team that accompanied me on these beamtimes: Aurélien, Olivier, Lucas, Sandra, Claudia, Michael, Mia, and Dhananjay. I believe we were always a fantastic working team!

I arrived at SPINTEC for my master's internship, and I am grateful to Lucian and Liliana for giving me the opportunity to work in this excellent laboratory. I always felt there at home and enjoyed the good atmosphere. So many faces and memories come to my mind, that I wish I could thank you one by one. The first people I shared very good times with were Sabrina, Odilia, Rana, Rafael, Steven, Aurélien, Marco,

Álvaro, Dani, Michael, Arnaud, Luis, Cecilia, Nuno, Oji, Ahmed, Sambit, Mahdi, Pedro, etc. Then, it was such a pleasure to meet the people that joined later the lab: Joseba, Miina, Charles, Samuel, Aurélie, Hasan, Javi, Andrea, Arijit, Eline, Johanna, Jay, Kamal, Bruno, David, Louis, Rodri, Mateo, Salvatore, Théo, Libor, Quentin, Dhananjay, and more. So many memories of our time together from coffee breaks to Friday drinks, Wednesday picnics to climbing sessions, skiing days to beautiful hikes, board games to parties, and conferences, in short, time together. I would like to extend a special thank you to Joseba for the your friendship and the many moments we spent together in the office. Alvarito, thank you for being there since day one. Thank you Miina for all the moments we spent together, I really value them. Samuel, thank you for your unlimited energy and always being ready for everything. Aurélie, thank you for making everything easy and fun, and Charles, your charisma and positive attitude are infectious. Hasan, cannot imagine a better person. Thank you for all the time and talks, keep challenging yourself. Kamal and Andrea, thank you for the good times at the office. Dani, thank you for always making us laugh and creating such a fun atmosphere. Nuno, I will miss hearing you say "Ca va mon amie?" all the time. Javi, thank you for all the social plans you organized. Arijit, I will always remember our chat just after submitting my first article, thank you for your time!. Eline, it was a pleasure meeting you during your few months in Grenoble. I will always remember the time we ran up Bastille together for the first (and only!) time. Libor, it was so nice to meet you, thank you for all your hike advices. Mateo, thank you for the very nice moments together.

It my spanish laboratories at UCM and IMDEA Complutense, I would like to start with a huge thank you to my Permalloy partner, Claudia. Thank you for the infinite hours together trying to get good samples, but above all thanks for keeping up the good vibes despite the tiredness and stress. I enjoyed so much the time together, and the way we support each other every time. A key person for me as well was Sandra, who has been like an older sister since day one. Thank you Sandra, for all your help during these years, and also for all the fun moments, hugs and contagious laughs. To my Anas, each of them so special in their way, thank you for your lovely way of being and all the support you always give me. Clara, you literally saved me so many times! Infinite thanks for your tremendous help. Ale, you are the person with who I spent with my first day, and look at us now, time flies! Thank you for all the time together. Matilde, your arrival to the group was the best thing that could have happened. Thank you for always having such a joy and spirit, cannot enjoy more your company!. Jairo, thank you for our chats at the office, which brought me a sense of calm during the writing period. Lucia, it was a pleasure to meet you, and I hope we stay in touch in the years to come. Bea, you were the first person I met during my undergraduate studies, and I remember being impressed by your determination to keep trying with the samples. Who would have thought that I would be doing the same a few years later? Thank you for all the good moments together.

Living between two different countries can be challenging, especially when it comes to starting over. However, I am grateful to have had people who made me feel at home, even though I had just left mine. Although I cannot list everyone who made my nomadic life feel like a familiar path, I want to thank you all for your warmth and love. I would also like to extend a special thanks to Vladis, Gloria, Jorge, Marina, Inés, Andrea, Elena, Rosario, Jesús, Clau, Eva, Gareth, María, Joan, Luis, Eli, Valentin, etc. Your support and friendship have meant the world to me. To my sister, thank you for your unconditional support and for always reminding me of who I am. To my parents, thank you for your patience and love. And last but not least, to you Juan, thank you for being my trampoline and always giving me the boost I needed to keep going.

Introduction

Magnetism is present everywhere. We rely on magnets in our daily lives, as they are part of our credit cards, cellphones, cars, computers, fridges, television, hard drives etc. Magnetic materials are fundamental in satisfying basic societal demands, such as energy generation, distribution and conversion, telecommunications, medical diagnosis or data storage. The annual global market was valued at 20 billion euros in 2021, which is expected to grow 6 % per year. There is a clear big demand, especially for permanent magnets present in industrial and consumer electronics, such as in drive systems and advanced motors. With the global goal of zero carbon emissions by 2050, an even higher demand is expected for permanent magnets since they are present in renewable energy applications. In terms of information technologies, magnetic hard drives remain the primary technology to store data in computers and servers. The storage capacity worldwide will grow to 147 ZB in 2024. Research on new magnetic storage devices has managed to reduce the bit size to the nanoscale (15×35 nm^2), but due to fundamental and technological bottlenecks, the maximum density has almost already been achieved.

The field of spintronics explores the spin of the electron instead of, or as an additional degree of freedom, to its charge. The field emerged in the mid 80's with the breakthrough in the field of magnetism: the discovery of the giant magnetoresistance (GMR) effect, an effect combining electronics and magnetism, as the resistance of a stacked device may strongly depend on the arrangement of magnetization in the substacks. This gave rise to the study of spin-transport phenomena, aiming to understand basic magnetism and develop technological applications. More generally, in a ferromagnet, the current may be spin-polarized due to the imbalance of electrons with spin up and down. Depending on the spin polarization, a determined efficiency of the spin-polarized electron transport is obtained, which is a critical parameter for magnetic devices. In addition, bulk magnets often break up magnetization into magnetic domains, large regions with uniform magnetization. These domains are separated by a magnetic Domain wall (DW), whose length could range from a few nanometers to microns. These DWs can be moved by the torque exerted by the spin-polarized electrons, i.e., the spin-transfer torque (STT). STT is a reverse effect compared with GMR, i.e., an action of the spin of conducting electrons on magnetization. This effect, that has shown its potential for controlling DW motion in both two-dimensional and three-dimensional magnetic systems, is the driving force for developing a new type of memory logic-device. In the case of three-dimensional nanomagnetic systems, it can also solve the intrinsic limitations associated with 2-dimensional devices on parameters such as bit density and speed. Magnetic nanowires are the building blocks of this new memory, so-called racetrack memory. The nanowires would be vertically arranged and interconnected in three-dimensional systems with an outstanding storage density.

DW logic devices based on nanowires were first investigated in flat, two-dimensional nanostrips with in-plane magnetization. However, research has shown that steady-state DW motion is not possible above a speed of a few tens of $\mathrm{m \cdot s^{-1}}$. A much higher speed was later demonstrated using perpendicularly magnetized films combined with Dzyaloshinskii-Moriya interaction on low magnetization materials, such as nearly compensated ferrimagnets or antiferromagnets. In cylindrical three-dimensional nanowires, steady-state DW motions above $1000\,\mathrm{m \cdot s^{-1}}$ are predicted with no requirements on the material. The curvature-induced effects in this system allow the stabilization of a new type of DW known as the Bloch-point domain wall (BPW). Its magnetic texture is based on the curling of magnetization around the wire axis with a magnetic

singularity, known as the Bloch Point (BP), located at its core. These predictions make cylindrical nanowires a perfect platform to study fundamental condensed matter physics and also in the future, to realize a racetrack memory device.

The current-induced DW dynamics in cylindrical nanowires have been widely studied with micromagnetic simulations and analytical models during the last two decades. However, experimental evidence, even for the spin texture at rest, is scarce due to the complexity of characterizing the magnetization not only at the surface but also at the core of the nanowires. The first experimental evidence of a BPW was reported in 2014 by shadow X-ray magnetic circular dichroism (XMCD)-photoemission electron microscopy (PEEM) by Da Col *et al.*. In 2018, Wartelle *et al.* reported, using the same technique, the transformation of a BPW into a transverse-vortex domain wall (TVW) under a quasistatic magnetic field. The first evidence of current-driven motion was reported in 2019 by Schöbitz *et al.*, where DW velocities above $600\,\mathrm{m\cdot s^{-1}}$ were estimated. In addition, the impact of the previously overlooked Œrsted field was highlighted, since it stabilizes the BPW and deterministically sets its sense of circulation. However, DWs were pinned on grain boundaries or material defects, inducing stochastic pinning. Additionally, the direction of motion was not always along the STT direction, raising concerns about the role of the Œrsted field and Joule heating.

In search of an additional handle to control DWs, the aim of this thesis was to investigate the micromagnetics of a new type of system based on chemically-modulated nanowires. This system was chosen as a platform where the energy landscape of a DW is tuned along the nanowire axis and preferential locations for the DWs are set. Specifically, the system considered was $\approx 120\,\mathrm{nm}$ diameter Permalloy ($Fe_{20}Ni_{80}$) nanowires with chemical modulations of several tens of nanometers in length of a higher magnetization $Fe_{80}Ni_{20}$ alloy. Experiments based on X-ray magnetic imaging revealed curling of the magnetization at the chemical modulations. The curling circulation can be reversed by an Œrsted field of antiparallel circulation, as in the case of a BPW. Experiments in static and in time-resolved mode, along with simulations, have revealed the circulation switching mechanism of a BPW and a modulation, along with its characteristic time scales. In addition, the curling of the modulation can be coupled to the curling of a BPW. This leads to a new collective dynamics driven by the Œrsted field, where new topological features arise. We have also identified the impact that the electrical pulse duration has on the final micromagnetic state, which has been proven to be crucial. Lastly, long-distance DW motion from modulation to modulation and speeds above $1000\,\mathrm{m\cdot s^{-1}}$ were evidenced.

The results obtained for the micromagnetic characterization of the system are published in:

- L. Álvaro-Gómez, S. Ruiz-Gómez, C. Fernández-González, M. Schöbitz, N. Mille, J. Hurst, D. Tiwari, A. De Riz, I. M. Andersen, J. Bachmann, L. Cagnon, M. Foerster, L. Aballe, R. Belkhou, J.-C. Toussaint, C. Thirion, A. Masseboeuf, D. Gusakova, L. Pérez, and O. Fruchart. "Micromagnetics of magnetic chemical modulations in soft-magnetic cylindrical nanowires". Physical Review B **106**, 054433 (2022).

From this article, some figures and sentences are re-used throughout this manuscript. Finally, three articles are in preparation regarding the results on time-resolved dynamics of modulations and of BPW, and the interplay of modulations and DWs. An outline of this thesis is provided below.

Outline

Chapter 1: From micromagnetism to curved three-dimensional nanomagnetism

This chapter provides a background of the key concepts of micromagnetism, which form the basis of the physics described in this manuscript. Emphasis is placed on the precessional dynamics of magnetic DWs in thin-films and nanowires. Finally, the curved-induced magnetization dynamics in cylindrical nanowires is addressed, highlighting the behavior of the two types of DWs (BPW and TVW) under an external field or

current stimulus. The latter brings new physics due to the associated Œrsted field.

Chapter 2: Methods and instrumentation

This chapter details the experimental and theoretical techniques mentioned throughout the manuscript. Details are given on the chemical synthesis and in-lab magnetic characterization and imaging of the nanowires. This is followed by a description of the X-ray microscopy techniques used to characterize the three-dimensional magnetization at rest, under a quasistatic field or a nanosecond current pulse. This includes details on the setup adaption to high-frequency (HF) electric pulses, as well as the electrical contacting process of nanowires.

Chapter 3: Synthesis and material optimization and characterization

This chapter focuses on the experimental steps taken to achieve defect-free chemically-modulated nanowires. It describes the different issues that arise due to the combination of two different electrochemical growth regimes. Finally, it provides the ingredients for a successful synthesis along with structural characterization.

Chapter 4: Micromagnetics of chemical modulations in FeNi nanowires

This chapter details the micromagnetics of high-magnetization chemical modulations inserted within a Permalloy nanowire. First, the magnetic flux arising from the modulations due to the magnetization mismatch is described. Then, the curling of the magnetization at the modulation is revealed by several three-dimensional X-ray imaging techniques. The source of this curling is charge screening, which is identified by an analytical model and supported by micromagnetic simulations. Finally, the dependence of the curling on the geometry is addressed.

Chapter 5: Curling in modulations controlled by magnetic fields

This chapter studies the response of the curling of the magnetization at the chemical modulations under the stimulus of an external magnetic field. First, the decrease of the curling angle reduction under an increasing axial magnetic field is addressed. The experimental magnetic contrast images are quantified into a curling angle by applying an analysis considering experimental aspects. The inputs and constraints of this analysis are detailed. Finally, X-ray imaging experiments revealed Œrsted-field-induced circulation switching of the chemical modulations. The underlying mechanism is detailed by combining time-resolved experiments and micromagnetics simulations. Also the critical current evolution versus modulation length is detailed, identifying two different switching regimes, and showing an analogy with coherent versus nucleation-propagation magnetization processes.

Chapter 6: Interplay of curling at modulations and domain walls

This chapter studies new physics arising from the interaction of a DW with a chemical modulation. First, it describes the energy landscape that a modulation induces on a BPW, depending on their relative circulations. Then, BPW propagation through the modulation under an external magnetic field is studied, where BPW transformations are described. Finally, the impact of the Œrsted field on DW transformations is addressed in a homogeneous and in a modulated nanowire. This is done by combining experiments in static or time-resolved mode, micromagnetic simulations and post-treatment codes to follow topological surface objects (vortex-antivortex) and volume objects (BPs).

Contents

Chapter 1

From micromagnetism to curved three-dimensional nanomagnetism

1.1 Brief introduction to the history of magnetism

The history of magnetism goes back over 2000 years [1]. Since the Iron Age, the attraction of ferrous materials to permanent magnets was known. Many magnetic materials are naturally present in nature, such as loadstones made with magnetite and iron oxide Fe_3O_4, and they were studied in the ancient Greece, Egypt, China, and Mesoamerica. Around 1088, it was discovered that a steel needle get magnetized with the magnetic field of the Earth, thought to be the field of the stars at that time. This allowed the creation of the navigational compass used in marine expeditions centuries later. In 1600, William Gilbert wrote what could be considered the first scientific text, *De Magnete* [2], claiming that the Earth is one great magnet. The similarities between electricity and magnetism led to deep research during the 17th and 18th centuries. In 1785, Charles-Augustin de Coulomb established the inverse square law of attraction and repulsion between electric charges or magnetic poles. Then, Siméon Denis Poisson developed the concept of scalar magnetic potential. In 1820, Hans-Christian Oersted discovered by chance the connection between electricity and magnetism, demonstrating that a current flowing through a wire deflects a compass needle due to the circumferential magnetic field it generates. A few months later, André-Marie Ampère wrote a paper to the French Academy stating that ferromagnetism in a material was caused by internal currents perpendicular to the direction of magnetization. All of this launched the start of electromagnetism. One of the main contributors was Michael Faraday, who set the concept of magnetic field as lines of force [3]. In 1831 Faraday discovered electromagnetic induction, demonstrating that moving a permanent magnet in and out of a coil induces a current in the coil. His conviction that a magnetic field should have some effect on light led in 1845 to his discovery of the magneto-optic Faraday effect – that the plane of polarization of light rotates upon passing through a transparent medium. All of this inspired Maxwell in 1865 to unify the theory of electricity, magnetism and light in the famous Maxwell equations [4]. Heinrich Hertz demonstrated Maxwell's electromagnetic waves experimentally in 1888, and he showed that their behavior was essentially the same as that of light. A large set of discoveries was achieved throughout the 19th century, such as magnetostriction by James Joule [5], anisotropic magnetoresistance by William Thomson [6], the Hall effect by Edwin Hall, Kerr effect by John Kerr [7], magnetic hysteresis by James Alfred Ewing [8] and the Curie temperature of a material by Marie and Pierre Curie [9]. However, despite these astonishing discoveries, classical physics could not explain magnetism at a microscopic level.

A new era in the world of magnetism began with the discovery of the electron by George Johnstone Stoney in 1891. In 1907, Pierre Weiss postulated the existence of an internal molecular field, proportional to magnetization, to explain collective ordering. However, there were still some unexplained gaps, such as the continuity in the component of **B** normal to the surface of a magnet, as established in Maxwell's equations.

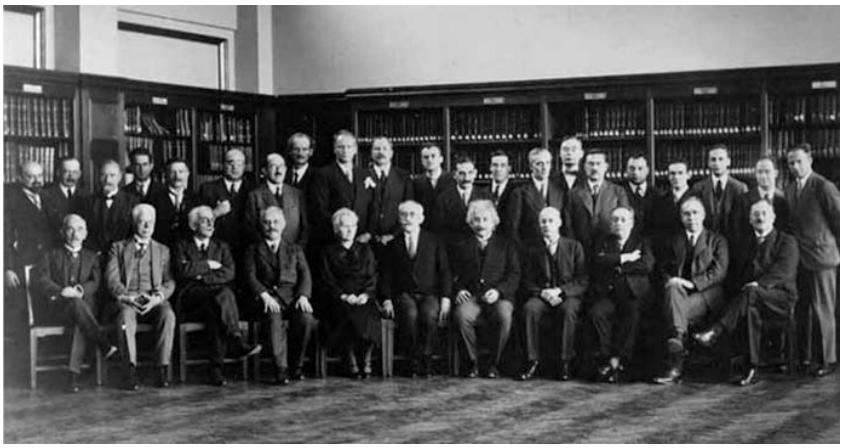

Figure 1.1: The 1930 Solvay Conference on Magnetism. Back row: Herzen, Henriot, Verschaffelt, Manneback, Cotton, Errera, Stern, Piccard, Gerlach, Darwin, Dirac, Bauer, Kapitza, Brioullin, Kramers, Debye, Pauli, Dorfman, van Vleck, Fermi, Heisenberg. Front row: de Donder, Zeeman, Weiss, Sommerfeld, Curie, Langevin, Einstein, Richardson, Cabrera, Bohr, de Haas. Figure used with permission from [16].

The explanation for this was satisfactorily explained with quantum mechanics and relativity in terms of the physics of Einstein, Bohr, Pauli, Dirac, Schrödinger, and Heisenberg. A quantum description came in 1925 by Pauli with the discovery of the intrinsic magnetic moment of an electron, the spin, which is quantized in two possible orientations [10]. The coupling between the spins of two nearby electrons was formulated by Paul Dirac and Werner Heisenberg and is known as exchange interaction. The value of the exchange integral J is positive for ferromagnetic materials (parallel spins) and negative for antiferromagnetic materials (antiparallel spins). Friedrich Hund in 1927 set the Hund rules for finding the ground state of a multi-electron atom. Briefly, the rules assume the total magnetic moment of an atom is the sum of the intrinsic spin angular moment and the quantized orbital angular momentum. First, the spin angular momentum S is maximized while respecting the Pauli principle, which states that no two electrons can be in the same quantum state. Secondly, the orbital angular momentum L is maximized, consistent with the value of S, and thirdly the spin and orbital momenta are coupled together to form the total angular momentum $J = L \pm S$, according to whether the electronic shell is more or less than half full [11]. The third rule is based on the energy splitting due to the spin-orbit interaction proposed by Llewellyn Thomas [12, 13]. The concept of spinwaves, as quantized elementary excitations, was proposed in 1930 by Felix Bloch [14]. All these discoveries in theoretical physics allowed to understand the physics driving magnetism. However, as Dirac said in 1930 at the sixth Solvay Conference devoted to magnetism [15] (Figure 1.2), "The underlying physical laws necessary for the mathematical theory of a large part of physics and the whole of chemistry are completely known, and the difficulty is only that the exact application of these laws leads to equations much too complicated to be soluble."

1.2 Micromagnetism

The computational challenge of the many-body electron problem can be addressed with micromagnetism. Micromagnetism is a continuum theory that describes magnetization processes on significant length scales, from a few nanometers to micrometers, that are: (i) large enough to use a continuous function of position (magnetization) and (ii) small enough to resolve the magnetization transition between magnetic domains. Micromagnetism was initially developed by Brown in 1959 [17]. Its main assumption is that the spin direction is continuous, i.e., it changes only a small angle between two lattice points [18]. Therefore, a ferromagnet can be described as a continuous vector field: the magnetization $\mathbf{M}(\mathbf{r},t)$, which is the magnetic moment

per unit volume. The SI unit for magnetization is A/m. Standard micromagnetics assumes a constant length of the magnetization vector, thus the unit vector is rather considered $\mathbf{m} = \mathbf{M}/M_s$, being M_s the spontaneous magnetization at room temperature. Just to note that temperature can be accounted for in the mean field by considering the values of magnetic quantities at a specific temperature, such as $M_s(T)$. In the following, we will briefly summarize the key aspects of micromagnetism. A more detailed description of magnetism [11, 19, 20] and micromagnetism and nanomagnetism can be found in the literature [21–24].

1.2.1 Magnetic energy terms

The total energy of a micromagnetic system is a sum of different contributions: exchange, dipolar, Zeeman, magnetocrystalline anisotropy and magnetoelastic anisotropy. There is a distinction between local and non-local magnetic energy terms. The local terms are based on energy densities, which depend on the local values of the magnetization direction and its gradients only. The non-local terms give rise to torques on the magnetization vector that depend at any point on the magnetization directions at every other point. Therefore, they cannot be calculated by a single integration [23]. The interplay of these terms determines the magnetic behavior at rest and its dynamical properties. For the sake of simplicity the following descriptions are restricted to ferromagnetic materials.

Exchange energy

The origin of this term is of quantum mechanical nature. It is based on the fact that the energy of two electrons depends on their relative spin orientations. The lowest energy state is achieved for parallel spins. Therefore, the spin energy between two localized spins is given by:

$$\mathcal{E}_{ij} = -J\mathbf{S}_i \cdot \mathbf{S}_j, \tag{1.1}$$

where J is the exchange integral, which is positive for ferromagnetic materials and $\mathbf{S}_i$ is the spin of the atom i. We can conclude that ferromagnetic exchange interactions lead to keeping magnetization uniform. The micromagnetic description of exchange is manifested as an energy cost for non-uniform magnetization. The exchange energy density is written as:

$$E_{\text{ex}} = A\left[(\nabla \mathbf{m})^2\right], \tag{1.2}$$

where $A \approx JS^2/2a$ is the magnetic exchange stiffness constant, in units $\mathrm{J/m}$. Common materials such as Fe [25, 26], Co [27–29] and Ni [29, 30] show A values of 2.1, 3.3 and $0.8 \times 10^{-11}\,\mathrm{J \cdot m^{-1}}$. Lastly, just to highlight that exchange is a short-range interaction since it is related to neighboring spins.

Magnetostatic energy

Magnetostatic energy, also called dipolar energy E_{d}, has its origin on the dipolar interactions within the ferromagnetic material. Therefore magnetostatic interactions are long-ranged. It is the energy of a ferromagnet in its own demagnetizing field. Just to clarify, the name dipolar field is synonym of magnetostatic field, whereas the stray and demagnetizing field refer to the part of the dipolar field outside or inside the sample, respectively. The total dipolar field is expressed as the energy of each magnetic moment $\mathbf{u}_i$ in the field $\mathbf{H}_{\text{d}}(\mathbf{x}_i)$ that derives from all the other moments

$$\mathcal{E}_{\text{d}} = -\frac{\mu_0}{2}\int_V \mathbf{M} \cdot \mathbf{H}_{\text{d}}\, \mathrm{d}V. \tag{1.3}$$

The factor 1/2 avoids counting each pair of atoms twice. Alternatively, it can be expressed in terms of a magnetic scalar potential ϕ_{d} and effective magnetic surface charges $\sigma = \mathbf{M} \cdot \mathbf{n}$ and volume charges $\rho_{\text{m}} = -\nabla \cdot \mathbf{M}$. This is done by making an analogy with Gauss's law in electrostatics and replacing H_d by ϕ_{d}:

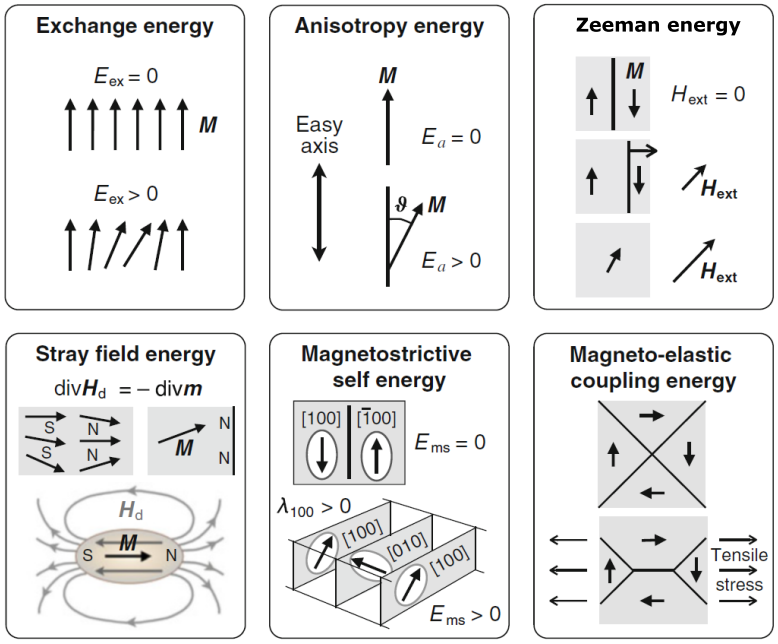

Figure 1.2: Schematic of the different magnetic energy terms. Figure used with permission from [31].

$$\mathcal{E}_\mathrm{d} = \frac{1}{2}\mu_0 \left(\int_V \rho_\mathrm{m}\phi_\mathrm{d}\,\mathrm{d}V + \oint_{\partial V} \sigma\phi_\mathrm{d}\,\mathrm{d}S \right) \tag{1.4}$$

This method was introduced by LaBonte [32] and Schabes and Aharoni [33]. With this interpretation it is evident that a reduction of magnetic charges implies a reduction of the magnetostatic energy. The surface charges are minimized when the magnetization lies along the surface, bringing here the concept of shape anisotropy, i.e., the existence of a specific preferential magnetization direction that minimizes magnetostatic energy. Another equivalent formulation is:

$$\mathcal{E}_\mathrm{d} = \frac{\mu_0}{2} \int_\mathrm{Space} H_d^2\,\mathrm{d}V, \tag{1.5}$$

where integration is performed over the entire space. From this last formula we can conclude that $\mathcal{E}_\mathrm{d}$ is always positive or zero.

The calculation of the magnetostatic energy is not trivial, so one often uses an approximation to reality instead, based on the demagnetizing factors N_i:

$$\langle \mathbf{H}_{\mathrm{d,i}} \rangle = -N_\mathrm{i}\mathbf{M} \tag{1.6}$$

where i is the mean value and N is generally defined as a tensor for non-main directions. Each coefficient N_i represents the strength of the demagnetizing field along the i main direction. They are called demagnetizing because they are positive such that the magnetostatic field is opposite to magnetization along the main directions. Therefore, the density of demagnetizing energy is:

$$E_\mathrm{d} = m_\mathrm{i}^2 N_\mathrm{i} K_\mathrm{d} \tag{1.7}$$

with $K_\mathrm{d} = 1/2\mu_0 M_s^2$. In a hand-waving way, the dipolar energy should be lower when the magnetization is along the long dimension of the system. This implies lower N_i along this direction. $N_\mathrm{x} + N_\mathrm{y} + N_\mathrm{z} = 1$, and for an infinitely long cylinder, $N_\mathrm{z} = 0$, as no magnetic charges arise. Expressions for other shapes may be

found for finite-length cylinders [34, 35], infinite cylinders with a triangular cross-section [36], tetrahedrons [37, 38], or torii [39].

Zeeman energy

When a magnetic dipole moment $\mathbf{u}$ is subjected to an externally applied field $\mathbf{H}_\mathrm{a}$, it experiences a torque that causes its precession around the external field. However, due to damping, in a condensed-matter body, it will gradually align along $\mathbf{H}_\mathrm{a}$. This alignment entails a reduction of the Zeeman or external energy density, which is expressed as:

$$E_\mathrm{Z} = -\mu_0 \mathbf{M} \cdot \mathbf{H}_\mathrm{a} \tag{1.8}$$

where $\mu_0 = 4\pi \times 10^{-7}\,\mathrm{H/m}$ is the magnetic permeability of free space.

Magnetocrystalline anisotropy energy

Another energy term is the magnetocrystalline anisotropy energy E_mc, also known as magnetic anisotropy energy. This term is related to the crystal lattice of the material and the tendency of magnetization to align along certain axes of a solid, called the easy axis, or in certain planes, then called easy planes. These directions correspond to the minimum energy, whereas the ones related to the maximum energy are known as hard axis or hard planes. This energy is at the origin of coercivity, as a magnetic field is needed to align magnetization along the hard axis in a material. The calculation of E_mc relies on multiple order terms for all possible geometries, such as all three axes in cubic crystals. They are all functions of the type

$$E_\mathrm{mc} = K f(\theta, \varphi) \tag{1.9}$$

where K is a coefficient and θ and φ are angles defining the direction of magnetization. This can be simplified by writing solely the second order term for a uniaxial anisotropy energy density:

$$E_\mathrm{mc} = K_\mathrm{u} \sin^2 \theta, \tag{1.10}$$

where θ is the angle between $\mathbf{m}$ and the easy axis and K_u is the uniaxial magnetocrystalline anisotropy coefficient in units of $\mathrm{J/m^3}$. This approximation allows gaining an idea of the impact of E_mc in a material. In addition, materials with low magnetocrystalline anisotropy are referred to as magnetically soft. This is the case for Fe and Ni (with K of 48 and $-5.4\,\mathrm{kJ/m^3}$, respectively), however, not for Co for which $K_\mathrm{u} = 530\,\mathrm{kJ/m^3}$, and is therefore considered a harder material. Finally, since magnetocrystalline anisotropy arises from interactions with the atomic lattice, values for K_u vary with temperature and depend on the crystal structure. Certain materials thus exhibit changes in anisotropy coefficients at phase transitions.

Inverse magnetostriction

This term relates to the coupling effect between magnetic energy and mechanical energy. Magnetostriction refers to the change in dimensions with the magnetization direction. This occurs in magnetostrictive materials where the crystal lattice is spontaneously elongated or contracted along the magnetization direction, if λ, the magnetostriction constant is positive or negative, respectively [31]. Inverse magnetostriction is conversely the (anisotropy) energy that arises from strain (deformation) of a body. The source of this strain can be either external or from atomic dislocations or structural or compositional inhomogeneities. Also called magnetoelastic energy, it reads:

$$E_\mathrm{me} = -\frac{3}{2} \lambda_\mathrm{s} \sigma \sin^2 \vartheta \tag{1.11}$$

where σ is the uniaxial mechanical stress, λ_s is the isotropic magnetostriction coefficient, and ϑ is the angle between the magnetization vector and the strain axis.

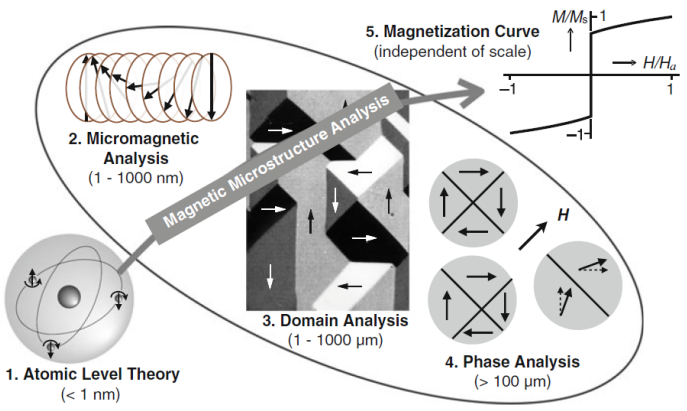

Figure 1.3: Five scale-dependent hierarchic levels of magnetically ordered materials. The link of magnetic microstructure between atomic foundations and technical applications of magnetic materials. Sample dimensions are indicated. Figure used with permission from [31].

1.2.2 Characteristic length scales

When several energy terms are involved, a balance between them is sought. This gives rise to characteristic length scales that set the threshold for qualitative changes in behavior. In a system with strong magnetocrystalline anisotropy, the anisotropy exchange length Δ_u or Bloch wall parameter [40] is written as

$$\Delta_u = \sqrt{\frac{A}{K_u}} \tag{1.12}$$

It denotes the relative importance of the exchange energy versus crystalline anisotropy energy. Dominated by these two types of energy, in a Bloch wall (Figure 1.8a), the magnetization rotates in a way so that no magnetic volume charges are created. The mutual competition between exchange and anisotropy determines the domain wall width: minimizing the exchange energy favors wide transition regions, whereas minimizing the crystal anisotropy energy favors narrow transition regions [11]. In a system with low magnetocrystalline anisotropy, dipolar fields play a more significant role, leading to the characteristic dipolar exchange length Δ_d [23], given as

$$\Delta_d = \sqrt{\frac{A}{K_d}} = \sqrt{\frac{2A}{\mu_0 M_s^2}} \tag{1.13}$$

It describes the relative importance of the exchange energy with respect to the magnetostatic energy. Δ_u is of the order of 1 nm in materials exhibiting high magnetocrystalline anisotropy, such as permanent magnets, and Δ_d takes values of the order of 10 nm. One added value of the characteristic length scales is that they allow direct comparison between different systems.

1.2.3 Magnetic domain walls

Uniform magnetization over a large distance implies a high cost of dipolar energy. When we increase the size of a ferromagnet, the magnetization can split up into domains such that dipolar energy is reduced at the smaller cost of exchange energy. The regions separating two adjacent domains are known as Domain wall (DW)s.

The existence of magnetic domains was suggested by Pierre Weiss in his mean field theory of magnetism in 1907. Within them, a fast change of magnetization occurs, entailing a high cost in exchange energy and possibly magnetocrystalline energy as well. This inspired Bloch in 1932 [41] to analyze theoretically the

transition between domains, finding that the walls must have a width of several hundreds of lattice constants due to Heisenberg's exchange interaction, that opposes an abrupt transition. In 1935, Landau and Lifshitz proved that a flux-closure type domain minimizes the stray field energy by keeping the magnetization parallel to the sample edges [42]. The Bloch model is a simplified view of a DW. It is a one-dimensional model that considers a chain of spins, where the magnetization remains in the plane of the DW. This implies zero volume charges (-div**M**), and thus zero associated dipolar energy. Therefore, the total density of magnetic energy reads:

$$E(x) = K_{\mathrm{u}} \sin^2 \theta + A \left(\frac{\mathrm{d}\theta}{\mathrm{d}x} \right)^2 \tag{1.14}$$

where the first term corresponds to the uniaxial magnetic anisotropy term and the second term to the exchange energy. After some algebra, one finds the exact solution of the energy minimization:

$$\theta_{\mathrm{ex}} = 2 \arctan \left[\exp \left(x \right) / \Delta_{\mathrm{u}} \right)] \tag{1.15}$$

$$\varepsilon_{\mathrm{ex}} = 4 \sqrt{A K_{\mathrm{u}}} \tag{1.16}$$

where Δ_{u} is the width of the DW, highlighting that exchange favors the enlargement of the DW, whereas anisotropy promotes the decrease of its width. The prefactor depends on the wall angle and anisotropy type. The above solution describes the magnetic configuration that minimizes the total energy in a one-dimensional chain of spins.

Even though the origin of magnetic domains is atomistic, nowadays, there is a direct connection to its macroscopic detection. Figure 1.3 shows the interlink between the five descriptive levels of magnetically ordered materials. Starting from the atomic level theory in level (1), that deals with the origin of the magnetic moments and their arrangement, it is followed by the *magnetic microstructure analysis*, levels (2) to (4). The continuum micromagnetic theory (2) deals on a sub-micron scale with domains, DWs and their inner structure. Then, *domains analysis* (3) is in the core of magnetic microstructure analysis. This is followed by *phase analysis*, which is focused on the volume distribution of a specific magnetic phase, i.e. domains magnetized along a specific direction. These phases are rearranged under a magnetic field, which gives rise to magnetization curves (5), which is a macroscopic descriptive level.

Magnetic domain wall in thin films

The above-mentioned textbook case of a DW is considered of translational invariance. However, this cannot be applied to the case of thin films where magnetic surface charges appear at both surfaces in the case of a Bloch domain wall (Figure 1.8a). This was addressed by Louis Néel [43], who considered the finite-size effect of the size along the normal of the film. For a thin film of thickness t and DW width $w \approx \Delta_{\mathrm{u}}$, the magnetostatic energy of a Bloch wall is proportional to $\approx K_{\mathrm{d}} w/(w+t)$. Therefore, if the thickness decreases, it will be more favorable to turn the magnetization in the plane of the film, i.e., perpendicular to the DW. In this configuration, the DW is now called a Néel wall (Figure 1.8b), and its density of magnetostatic energy is $\approx K_{\mathrm{d}} t/(w+t)$. Figure 1.4 shows the Bloch and Néel wall path in an infinite uniaxial material. The top vector view corresponds to a Bloch wall, where the magnetization domains are parallel to the wall. In this case, in the volume, which is representative of the entire system, the magnetic charges are of opposite sign at the top and bottom surfaces, responsible for a non-zero energy. The bottom vector image shows a Néel wall, which has always dipolar field energy if M_{s} is large. However, in thin films of soft magnetic material, where the magnetostatic impact is high, micromagnetic simulations have shown that the Néel wall is stable for thickness below $\approx 7\Delta_{\mathrm{d}}$, over the Bloch wall [44].

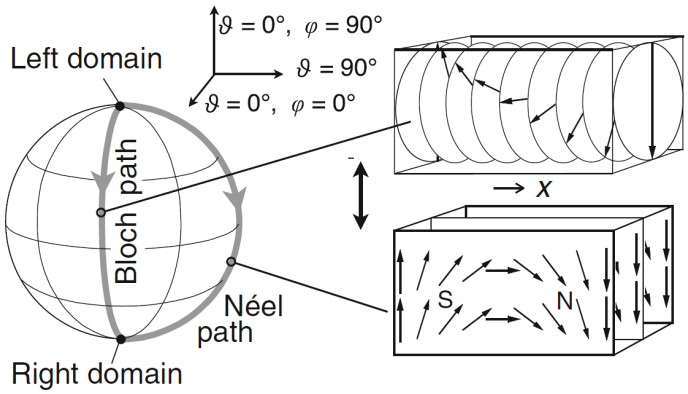

Figure 1.4: Bloch and Néel paths in an infinite uniaxial material. Top and bottom vector plots show Bloch and Neel wall magnetization vectors. Figure used with permission from [31].

1.2.4 Vortices and antivortices

The energy of a domain wall depends on its angle θ. In thin films, Néel walls show an energy varying like θ^4, much faster than that of a Bloch wall in thicker films, varying like θ^2. Therefore, in some situations, new DW types, such as cross-tie or zig-zag, may be favorable [45, 46]. The region of perpendicular magnetization separating two Néel walls is known as Bloch lines. Bloch lines also manifest within a Bloch wall, acting as a one-dimensional wall. The polarity of a Bloch line is set by the direction of the perpendicular magnetizations $p = \pm 1$. These are sometimes named topological defects and are characterized by a winding number n that reads as:

$$n = \frac{1}{2\pi} \oint \Delta\theta \cdot \mathrm{d}l \tag{1.17}$$

where θ is the angle between the in-plane component of magnetization and a reference in-plane component. The integration is performed along the path encircling the Bloch line. The winding number is the total number that the magnetization rotates along a circular contour. A Bloch line with $n = 1$ is also called a vortex and a Bloch line with $n = -1$ an antivortex [47]. Figure 1.5 illustrates the magnetization vectors of a vortex and antivortex as a function of the polarity p, winding number n and circulation c. The circulation number is define like:

$$c = \frac{1}{2\pi} \oint (\nabla \times \mathbf{m}) \cdot \hat{\mathbf{z}} \mathrm{d}l \tag{1.18}$$

where $\hat{\mathbf{z}}$ is the (arbitrary) normal to the plane defining the chirality. The circulation c gives the orientation of the in-plane magnetization for a vortex curling either clockwise ($c = -1$) or anticlockwise ($c = 1$) around the core. The product pc is defined as chirality. An antivortex is non-chiral since it has zero circulation. A general tendency in ferromagnets is the appearance of vortex structures to minimize the magnetostatic energy due to its cumulative long-range nature [48]. However, constraints imposed by topology and boundary conditions can lead to complex magnetic structures, specially in the three-dimensional case. This is the case of a Bloch Point (BP) [49], which will be the scope later in this manuscript, but for now, just to remark that cylindrical nanowires are a perfect platform to study the dynamics of Bloch Points [50].

For the case of chiral magnetic bubbles, the so-called skyrmion winding number or topological charge reads:

$$w = \frac{1}{4\pi} \iint \mathbf{m} \cdot \left(\frac{\partial \mathbf{m}}{\partial \mathrm{x}} \times \frac{\partial \mathbf{m}}{\partial \mathrm{y}} \right) \mathrm{d}x\mathrm{d}y \tag{1.19}$$

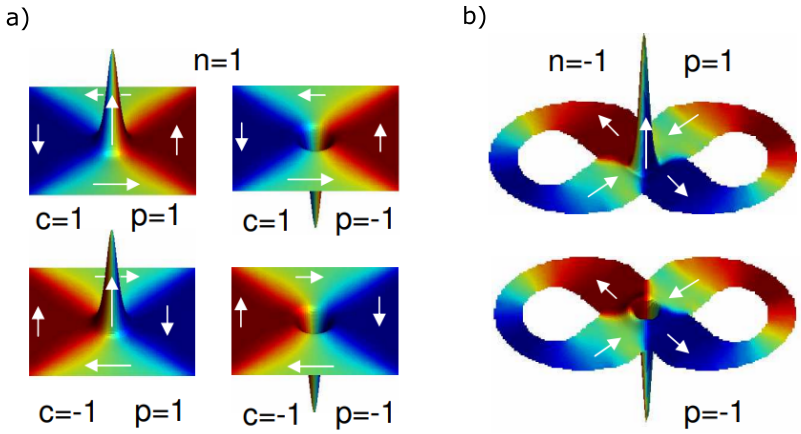

Figure 1.5: **a)** Vortex ground states and **b)** antivortex ground states in an infinity-shaped sample. Vortices and antivortices are characterized by the winding number n, the polarity p and the circulation c. Figure used with permission from [51].

In this case, integration is performed over an area. The absolute value w represents how many times magnetization maps all possible 4π directions in space. The skyrmion number is more suitable for magnetization textures over a surface, as we will see in the case of cylindrical nanowires in Chap. 6 of this manuscript.

1.2.5 Field-driven precessional magnetization dynamics

The magnetization dynamics under the stimulus of an external magnetic field or spin-polarized current have a precessional nature. In the above description of the Zeeman energy, it was detailed that a magnetic moment will precess around the external field until, due to damping, it is aligned along it. The precession mechanism can be described by modeling an angular magnetic moment as a circular loop of current $\mu = \mathbf{S}I$. Here, $\mathbf{S}$ corresponds to the area normal to the loop of current. We can reduce the dipole moment to an angular momentum:

$$\boldsymbol{\mu} = \frac{ge}{2m_e}\boldsymbol{\ell} = \gamma\boldsymbol{\ell} \tag{1.20}$$

where e is the electron charge, m_e is its mass, and $\boldsymbol{\ell} = \mathbf{r} \times \mathbf{p}$ is its angular momentum. $\gamma = ge/(2m_e)$ is the gyromagnetic ratio in units of $\text{rad} \cdot \text{s}^{-1} \cdot \text{T}^{-1}$ and takes a negative value for electrons. g is the Landé factor, equal to 1 for orbital magnetic moments and ≈ 2 for spin magnetic moments. Classical mechanics states that the time derivative of the angular momentum is equal to the mechanical torque, which in this case is of magnetic origin:

$$\dot{\boldsymbol{\mu}} = \gamma\dot{\boldsymbol{\ell}} = \mu_0\gamma\boldsymbol{\mu} \times \mathbf{H}_a \tag{1.21}$$

Therefore, this term represents the precession of a magnetic moment around the external field $\mathbf{H}_a$. The angular frequency of the precession, typically in the tens of GHz/T [19], does not depend on the angle between the magnetization and the external field. Also, the precession trajectory is energy conservative in the absence of damping, as its projection along the applied field remains constant.

In practice, the field exerted on the magnetization is not only the external field but also all the internal fields derived from the internal energy . Therefore, $\mathbf{H}_a$ must be replaced by an effective field $\mathbf{H}_{\text{eff}}$. This leads to Eq.(1.21) normalized per unit volume:

$$\dot{\mathbf{m}} = -\gamma_0\mathbf{m} \times \mathbf{H}_{\text{eff}} \tag{1.22}$$

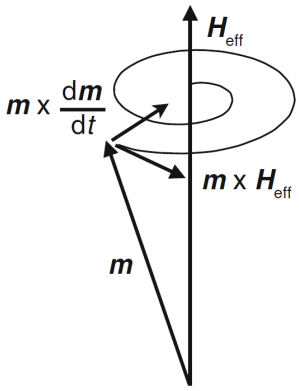

Figure 1.6: Schematic of the precessional ($\mathbf{m} \times \mathbf{H}_{\text{eff}}$) and damping ($\mathbf{m} \times \dot{\mathbf{m}}$) terms of the LLG equation. Figure used with permission from [31].

with $\gamma_0 = \mu_0 |\gamma|$ [52]. However, since magnetization is coupled to the system through the lattice (phonons), an exchange of angular momentum and energy leads to a damping term. This Gilbert damping term, $\alpha \mathbf{m} \times \dot{\mathbf{m}}$, leads to the progressive alignment of the magnetization along the external field [53, 54]. The direction of the damping torque is towards the external field and perpendicular to it. The damping coefficient, α, sets the rate of this alignment, and typical values are of the order of 1×10^{-3} to 1×10^{-1}. It is usually determined experimentally by ferromagnetic resonance linewidth [55, 56]. The sum of the precessional and damping terms leads to theLandau-Lifshitz-Gilbert (LLG) equation:

$$\dot{\mathbf{m}} = -\gamma_0 \mathbf{m} \times \mathbf{H}_{\text{eff}} + \alpha \mathbf{m} \times \dot{\mathbf{m}} \tag{1.23}$$

In Figure 1.6, a schematic of the precessional torque and damping torque vector directions is illustrated. A dipole moment $\mathbf{m}$ precesses around the effective field $\mathbf{H}_{\text{eff}}$ driven by a precessional term $\mathbf{m} \times \mathbf{H}_{\text{eff}}$ and a damping term $\mathbf{m} \times \dot{\mathbf{m}}$. This equation represents the time evolution of the magnetization under a magnetic field. The condition of low damping $\alpha << 1$ is relevant for most of the experimental cases, and to first order, it consists of a relative decrease of the angle between $\mathbf{M}$ and $\mathbf{H}$ of $2\pi\alpha$ per turn.

Since the 90's, precession of magnetization has been combined with nanosecond magnetic pulses to reverse the magnetization of thin films. In conventional and quasi-static reversal, the magnetic field direction is antiparallel to magnetization. However, shorter reversal durations down to the picosecond regime can be achieved if the field is applied perpendicular to magnetization, for which the torque is maximum. For the case of an in-plane magnetized thin film, a perpendicular magnetic field pulse provokes the tilt of $\mathbf{M}$ out of the plane. This induces a demagnetizing field normal to the surface, that leads an azimuthal dynamics, even when the external field is turned off. Therefore, the demagnetizing field completes the reversal process [57].

Field-driven precessional motion of domain walls

If we consider the one-dimensional model of a 180° Bloch wall with uniaxial anisotropy perpendicular to the plane of the film, we can easily describe precessional motion of DWs. If a slowly increasing magnetic field $\mathbf{H}_{\text{ext}}$ along the domains direction is applied, the dominant term in the LLG equation would be the damping term. This leads to a direct torque on the DW as sketched in Figure 1.7a. When the depinning field is reached, the DW will move favoring the enlargement of the domains along the external field. On the other hand, if a fixed magnetic field with a relatively high amplitude is applied, the precession term will lead the dynamics as illustrated in Figure 1.7b. In this case, first, there will be precession of the magnetization around the external field $\mathbf{m} \times \mathbf{H}_{\text{ext}}$, that will tilt $\mathbf{m}$ out of the plane of the wall. This will generate a transversal demagnetizing

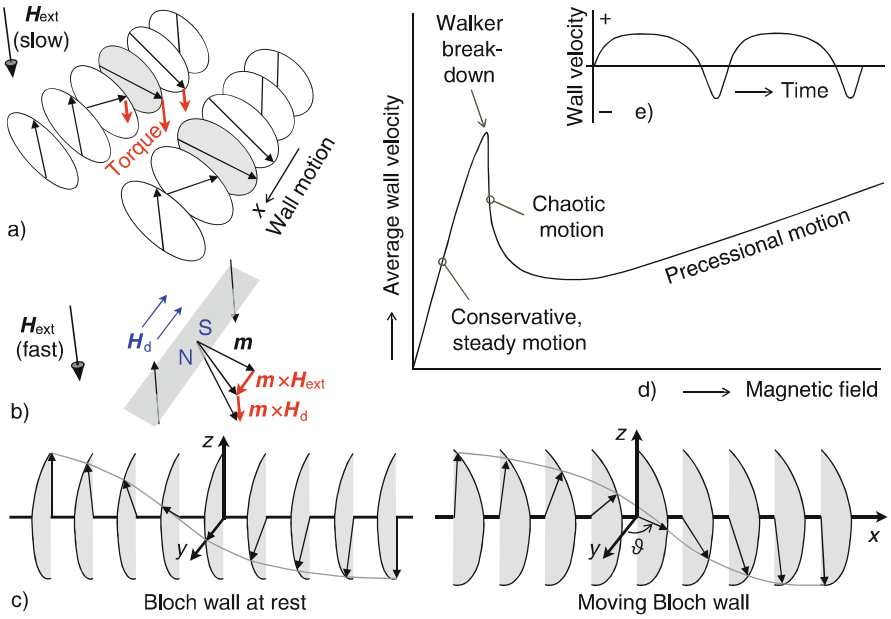

Figure 1.7: Precessional 180° Bloch wall motion. a) Slowly increasing magnetic field. **b)** Rapidly changing magnetic field. **c)** Moving Bloch wall. **d)** Wall velocity versus magnetic field shows three regimes: steady, chaotic and precessional motion. Figure used with permission from [31].

field $\mathbf{H}_\mathrm{d}$. Therefore, a subsequent precession of $\mathbf{m}$ around this field $\mathbf{m} \times \mathbf{H}_\mathrm{d}$ leads to DW motion. For the case of dynamical equilibrium, the torque due to the external field is offset by the demagnetizing field torque and damping, so that the DW moves at a constant velocity and with a fixed spin structure as visualized in Figure 1.7c [31]. This corresponds to the steady-state regime of wall motion, and as shown in the graph in Figure 1.7d, the velocity increases linearly with the external field. The velocity reads as:

$$v = (\gamma_0/\alpha)\Delta H_\mathrm{ext} \tag{1.24}$$

During motion, the wall width $\pi\Delta$ is not constant, since it tends to decrease to lower the associated demagnetizing energy. Above a certain external field, known as the *Walker field* [58], the equilibrium between the damping-demagnetizing torque and the external field torque is broken. Therefore, the leading term is the Zeeman torque. This leads to chaotic motion, where the velocity decreases with the external field, and the wall oscillates through Bloch and Néel configurations. This phenomenon is known as the *Walker breakdown* [58], and determines the maximum stable speeds of DWs $v_\mathrm{W} = \gamma_0 M_\mathrm{s}\Delta/2$. Above this threshold, the torque is too large to be compensated by damping, leading to a precession regime as sketched in Figure 1.7d.

1.2.6 Current-driven magnetization dynamics

The physics described above is based on the LLG equation, which treats external fields as part of the total effective field. However, for the case of spin-polarized currents, this cannot be applied [59, 60]. spin-transfer torque (STT) is the torque that non-equilibrium conduction electrons exert on a ferromagnet to rotate its magnetization towards the electron flow direction [61]. The mechanism behind relies on the conservation of angular momentum, thus, the spins of the conduction electrons exert an equal torque but in the opposite direction on the local spins, causing the latter to change their direction. In the adiabatic regime, i.e., when the spin conduction electrons are nearly aligned along the local d electrons spin, the STT is expressed as [62]:

$$\dot{\mathbf{m}} = -\frac{jg\mu_B P}{2eM_s}\frac{\partial \mathbf{m}}{\partial z} = -(\mathbf{u}\cdot\nabla)\mathbf{m} \tag{1.25}$$

where $\mathbf{u} = \mathbf{j}g\mu_B P/(2eM_s)$, Landé factor g and Bohr magneton μ_B. Therefore, adiabatic STT can be represented by an equivalent velocity $\mathbf{u}$, that is proportional to the current density $\mathbf{j}$ and its polarization P, and inversely proportional to magnetization M_s. For Permalloy, the factor $g\mu_B/(2eM_s)$ is $\approx 7\times10^{-11}\,\mathrm{m^3/C}$ [63]. However, experimental reports have found values below those predicted by the adiabatic term [64, 65]. The reason lies in a certain degree of deviation from perfect adiabaticity, which gives rise to the non-adiabatic STT term $\mathbf{m}\times[(\mathbf{u}\cdot\nabla)\mathbf{m}]$ [60, 63]. This term has the same effect as the field-like term in the original LLG equation. With this, the resulting modified LLG equation reads [63, 66]:

$$\dot{\mathbf{m}} = -\gamma_0\mathbf{m}\times\mathbf{H}_{\mathrm{eff}} + \alpha\mathbf{m}\times\dot{\mathbf{m}} - (\mathbf{u}\cdot\nabla)\mathbf{m} + \beta\mathbf{m}\times[(\mathbf{u}\cdot\nabla)\mathbf{m}] \tag{1.26}$$

where $\beta << 1$ is the deviation to adiabaticity, comparable to α. Eq.(1.26) describes magnetization dynamics under a current stimulus. In some situations other terms may be added such as spin-orbit torques [67, 68] or Dzyaloshinskii–Moriya interactions [69, 70]. Since the end of the 20th century, current-driven magnetization dynamics was broadly studied [61, 71].

Current-driven domain wall dynamics in nanostrips

In flat nanowires of rectangular cross-section, i.e. nanostrips, there may occur two types of DWs for in-plane magnetization. The first type is a transverse domain wall (TW), which shows an in-plane magnetic moment oriented transverse to the nanostrip axis (Figure 1.8c). The DW region has a triangular shape due to the non-uniform demagnetizing fields [62, 72]. The second type is the vortex domain wall (VW), which is stabilized at thicker strips, such that a flux-closure structure is allowed (Figure 1.8d). Here, there is no singularity at the vortex core, but there is an out-of-plane magnetization component. Therefore, four VW configurations may occur as there are two possible out-of-plane orientations and two curling circulations. The phase diagrams of the TW and VW were first investigated in [73], with a limit at $t \approx 75\Delta_d^2$. However, a refined calculation showed that an asymmetric transverse domain wall (ATW) can be also stabilized at larger thicknesses, which is obtained from a second-order transition [63]. These three DWs can be metastable depending on the geometry sizes. A transformation of a VW to a TW involves the expulsion of the vortex at one of the strip edges. A transformation from aTW to a VW involves the creation of a vortex core with perpendicular magnetization.

Regarding current-induced DW motion in nanostrips in the perfect adiabatic case [62], we may start with the case of a TW. For currents below a threshold, the TW displaces a little until it stops. The reasoning for this is the following: first, the wall structure at rest and under current is not the same, since the transverse components change. Second, the STT is compensated by the demagnetizing field, stopping the motion [74]. For large currents, the DW moves in a non-steady fashion involving the rotation of the magnetic moments. DW motion occurs only when the antivortex is present [75–77]. Regarding the VW, its structure is conserved at very low currents, but as in the case of the TW, it finally stops, adopting a deformed structure under current. However, the displacement is much faster than for a TW, even though the VW maximum velocity is $\approx 60\,\mathrm{m\cdot s^{-1}}$. For higher currents, the vortex core is expelled, and the VW transforms to a TW.

However, experimental reports showed larger velocities that those predicted in the perfect adiabatic case [78, 79]. Here comes the relevance of adding a non-adiabatic term to the LLG equation. With it, a TW velocities increase linearly with field since now there is not a cancellation of the STT with the demagnetizing field torque. The velocity reads

$$v = \frac{\beta}{\alpha}u \tag{1.27}$$

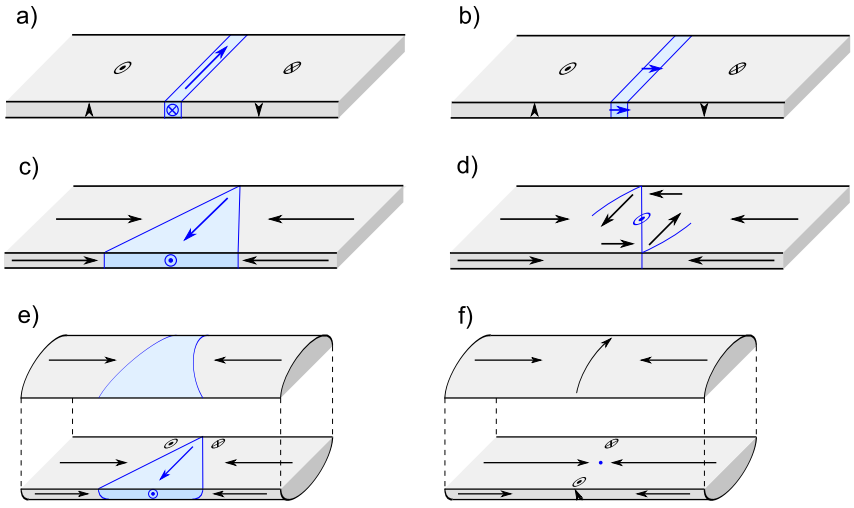

Figure 1.8: Schematic of domain walls in 2D nanostrips and 3D cylindrical nanowires. For an out-of-plane magnetized nanostrip **a)** Bloch or **b)** Néel wall. For an in-plane magnetized nanostrip **c)** TW or **d)** VW wall. For an in-plane magnetized cylindrical nanowire **e)** TVW or **f)** BPW wall. Courtesy of OLIVIER FRUCHART.

which holds as soon as there is a steady DW motion. However, in this stationary regime the DWs suffer from structural changes. Above the Walker regime, the motion is no longer stationary and a precession of magnetization occurs. A notable difference with the field case is that, depending on the value of β the velocity can increase (if $\beta < \alpha$) or decrease (if $\beta > \alpha$) compared to the linear regime [62]. Finally, for the case of a VW, the velocities are equal as for a TW in the linear regime, implying also a structural transformation. At the end of the linear regime a vortex expulsion, and thus transformation to TW occurs [80]. To sum up, no steady-state current-induced DW motion occurs in nanostrips due to DW deformations and low Walker field. In the next section we will explore a new type of DW that is stable under motion and does not suffer the Walker breakdown.

1.3 Curved three-dimensional nanomagnetism: cylindrical nanowires

Traditionally, the field of magnetism has focused on planar structures, with maturity now reached in this field [81]. The curvature-induced effects in magnetism attracted attention in the 1990s [82, 83]. This gave rise to a curvilinear magnetism field, where fascinating geometry-induced effects in the magnetic properties appear [84]. The impact of curvature on the magnetic properties of ferromagnets has been widely discussed in [85–90], and with a focus on domain walls in nanostrips, nanotubes and nanowires in [91]. The new degree of freedom allows to pattern new geometries and with that new spin textures as shown in Figure 1.9. For magnetoelectric nanodevices, DWs are used as bits of information that can be displaced in a controlled way [92]. In the case of three-dimensional nanostructures, the concept of a racetrack logic device was proposed in 2004 by Stuart S. Parkin [93, 94]. In this case, STT allows magnetic bit propagation without needing mechanical motion in the device. However, significant challenges remain before such applications may become a reality. For the moment, research has shown that using nanostrips as building blocks is not favorable due to the periodic DW transformations and reduced speed [95]. Therefore, a solution to this is to use as building blocks cylindrical nanowires, where ultra-fast DW velocities are predicted.

Research on magnetic nanowires started in the 1990s with the emergence of template-based chemical synthesis of nanostructures [96–99]. One of the earliest reviews was published in 1999 [100], where track-etched polymer membranes were used to electroplate magnetic nanowires. Years later, it was reported more on synthesis, modeling, and magnetometry measurements [101]. A specific review of magnetization reversal

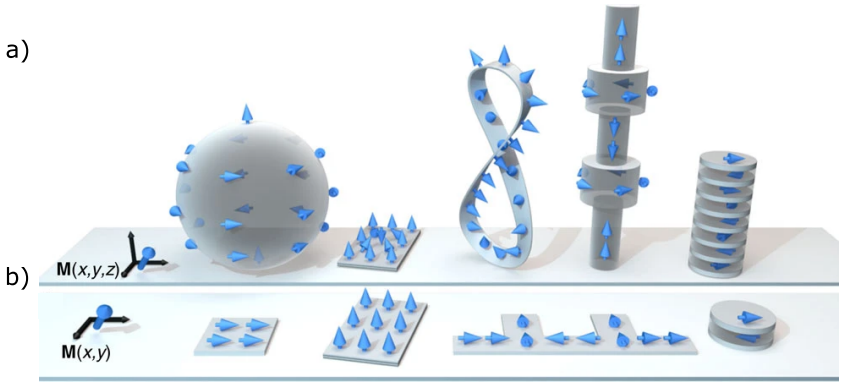

Figure 1.9: Schematic view of different geometries and magnetic configurations for **a)** 3D and **b)** 2D nanostructures. Figure used with permission from [89].

in nanowires was published in [102]. Also, a book dedicated to magnetic nanowires was written by several authors in [103]. A review on magnetic nanowires and nanotubes was published in 2018 [104]. The latest books on magnetic nanowires or curvilinear magnetism can be found in [105] and [90], respectively.

1.3.1 Fabrication

The synthesis of magnetic cylindrical nanowires can be done by means of top-down or bottom-up approaches, being the later the most common method. One of the most common top-down technique used is focused electron beam induced deposition (FEBID) [106, 107], which allows the direct writing of nanostructures with the electron beam of a scanning electron microscope equipped with a gas injection system that doses a gaseous precursor. Regarding bottom-up techniques the most common technique is template-based electrodeposition. The most used templates are porous anodised aluminium oxide (AAO) templates [108–110], which are based on the anodic oxidation of a high purity Al disk in an acid electrolyte. Under certain parameters (acid, voltage, temperature..), self-organized cylindrical pores are obtained. Afterward, a chemical etching can be use to enlarge the pore diameter. Or on the other hand, atomic layer deposition (ALD) can narrow it. Another type of porous templates are polycarbonate membranes prepared by irradiation of foils of the material with high energy ions [111]. However, they show a non-ordered pore distribution.

Regarding deposition techniques, electroplating takes the lead [112]. It is based on the reduction of metallic ions of an aqueous electrolyte. It is usually performed with DC current in galvanostatic (constant current) or potentiostatic (constant potential) mode. The common setup is a three-electrode cell, where the material is deposited at the cathode, complementary redox reactions occur at the anode, and the potential is controlled by a reference electrode. One of its key features is that it allows to deposit multilayers of materials. The most common materials deposit are Fe [113], Co [114, 115], Ni [116, 117], NiCo [118], NiFe [119], CoFe [120, 121], CoNiFe [122], CoPt [123, 124].

During the last few years, a branch of research in this field has focused on tuning the energy landscape along the nanowire's axis such that effective pinning sites for the DW are created. The first tries were focused on diameter modulations, which were induced by changing the potential during the fabrication of the porous alumina templates [117, 125–130, 130–136]. A similar result can be obtained by inducing chemical modulations during the electrodeposition process, achieving alternating material segments. This can be done either by changing the electrolyte [137, 138] or by changing the potential during growth [139–142]. The later, known as single-bath electrodeposition has been use widely in system such as Ni/Cu [143, 144], Fe/Cu [145], FeCoCu/Cu [146], FeGa/Cu [147], Co/Au [148], Co/Cu [149, 150], NiCo/Cu [139], CoCu/Cu [151], Ag/Co [152, 153], Au/FeAu [154], Au/Ni [155], Co/Pt [156], CoPt/Pt [157], etc.

In the following we will detail the theoretical research on DW dynamics in cylindrical nanowires, along

with the scare experimental reports on it.

1.3.2 Domain wall dynamics in cylindrical nanowires

Cylindrical nanowires can host two types of DWs: a TVW or a BPW. The behavior of these walls under an external stimulus is drastically different due to their different topology. Therefore, in the following sections, we will detail first the characteristics of the walls followed by their dynamics under a magnetic field or current pulse stimulus. Then, we will detail the most relevant experimental reports on their dynamics, along with the most recent theoretical investigations. This will be the starting point of the work reported in this manuscript.

Transverse vortex wall

In soft magnetic nanowires, the magnetization lies along the nanowire's axis. Therefore, there are two possible orientations of the magnetic domains that are separated by a 180° DW. The three-dimensional picture of a TW of a nanostrip is a TVW [158–160]. At the wall center, the magnetization is transverse to the wire axis, and again a triangular shape is adopted due to the non-uniform demagnetizing field to avoid the occurrence of volume charges (Figure 1.8e). It is called vortex since the magnetization rotates around the transverse component and around the wire axis [161]. This allows to decrease the associated magnetostatic energy of the wall. With respect to topology, the transverse feature means that there are two areas at the wire outer surface, such as $\mathbf{m}\cdot\mathbf{n}=\pm 1$. Therefore, the associated curling appears as a continuous transformation of this transverse feature, such that topology is unchanged. This topological feature is also shared with the TW and VW in nanostrips. For the former, the transverse component lies in-plane, whereas for the latter, it lies out-of-plane in the core of the vortex.

Regarding TVW field-driven motion, most of the driving force leads to the precession of the transverse component around the wire axis, and the forward motion has very slow velocities proportional to $\alpha\Delta\gamma_0 H_{\text{ext}}/(1+\alpha^2)$. Therefore, only the weak damping term contributes to wall motion. This behavior found in several studies with micromagnetic simulations, and it was named as corkscrew motion [158, 160, 162–165]. As an example, for $\mu_0 H_{\text{ext}} = 10\,\text{mT}$, $\Delta = 50\,\text{nm}$, and $\alpha = 0.01$, $v \approx 1\,\text{m}\cdot\text{s}^{-1}$. Formally, the Walker field is zero.

The current-induced TVW motion in cylindrical nanowires shows similar dynamics as in the field-driven case [166–168]. The adiabatic term of the Eq.(1.26) contributes to forward motion, while the non-adiabatic term contributes to purely azimuthal rotation. Therefore the TVW moves with a velocity that read as

$$v = \frac{1+\beta\alpha}{(1+\alpha^2)}u \tag{1.28}$$

and a precessional speed of

$$v = \frac{\alpha-\beta}{(1+\alpha^2)}u \tag{1.29}$$

being the sense of rotation determined by the sign of $\alpha-\beta$ [168]. To give an example, for $P=0.7$, $j = 1\times 10^{12}\,\text{A}\cdot\text{m}^{-2}$ and M_s, $u \approx 50\,\text{m}\cdot\text{s}^{-1}$. The first experimental TVW observation was reported in 2013 in by electron holography [169], followed by its observation in 2014 using shadow X-ray magnetic circular dichroism (XMCD)-photoemission electron microscopy (PEEM) [170] (see bottom image in Figure 1.12b). For diameters lower than $7\Delta_d$, the TVW is of lower energy than the BPW [72, 161].

Bloch Point Wall

One of the curvature-induced effects that arises in a nanowire with a cylindrical cross-section is the stabilization of a new type of DW, known as BPW [160, 162]. A BPW is characterized by an azimuthal magnetization

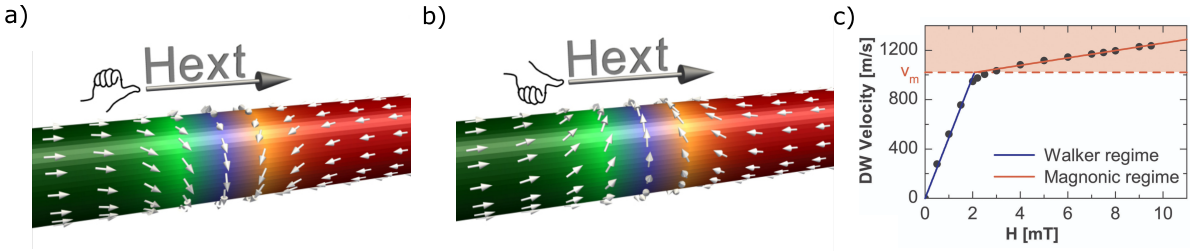

Figure 1.10: Chirality definition of magnetic field-driven head-to-head BPW in a nanotube. The same notation applies to cylindrical nanowires. **a)** "good" or right-handed chirality. **b)** "bad" or left-handed chirality. **c)** DW velocity as a function of the applied field. Black dots correspond to micromagnetic simulations. The blue and orange lines are linear fits to the data at two different regions. Figure used with permission from [171, 172].

around the wire axis and a Bloch point located at its core (Figure 1.8f). The associated cost in exchange energy is balanced by the gain in magnetostatic energy. A key feature of the BPW is that there is no point at the wire surface with $\mathbf{m}\cdot\mathbf{n} = \pm 1$, so that it is clear that its topology is distinct from the one of the TVW. In addition, it has a sizeable radial component to reduce magnetostatic effects.

The precessional torque may not be sufficient to change the sign of the radial component imposed by magnetostatics [171]. This results in a DW that can reach ultra-fast speeds above $1000\,\mathrm{m}\cdot\mathrm{s}^{-1}$, much delaying the Walker breakdown. However, this depends whether the precessional torque and the magnetostatic field act in opposite or in the same directions. The former, also known as "good" chirality with respect to the external field comes with DW propagation at high speeds [72]. The latter, known as "bad" chirality, has lower DW mobility and can be converted into the "good" chirality upon the increase and switching of the radial component [172]. Dynamics lifts the degeneracy between the two possible circulations of the BPW, which were equivalent at rest. The definition of "good" chirality is sketched in Figure 1.10a, where it is shown the outer micromagnetic view of a head-to-head BPW right handed, i.e., with positive circulation sense with respect to the direction of motion. On the other hand, Figure 1.10b shows a left-handed or negative circulation head-to-head BPW. The reverse notation on "good" and "bad" chirality is applied to a tail-to-tail BPW, since its associated magnetic charge, and thus radial component, is opposite. Therefore, we can conclude that depending on the field sign an easier precession can be induced.

Figure 1.10c shows the DW velocity as a function of the applied magnetic field [172]. The black dots corresponds to the data from micromagnetic simulations, and the blue and orange lines to the linear fits of the data in two different regions. It is evidenced that at low fields the velocity increases linearly with the field, as shown also for the case of thin films in Figure 1.7d. However, above a critical velocity of $\approx 1000\,\mathrm{m}\cdot\mathrm{s}^{-1}$, there is a sudden decrease of the DW mobility. In this regime, there is still steady DW motion (no Walker precessional motion), which is accompanied by the excitation of spin waves. This is known as the magnonic regime of DW propagation which was predicted analytically in extended films [173]. However, in thin films there is a lack of reports on this since the Walker limit is usually below the magnonic velocity. This magnetic version of the Cherenkov effect was predicted in 2011 in nanotubes [172], and later on cylindrical nanowires [49, 174]. Above this velocity, the BP mobility is lower than the DW one, leading to a cone-like DW distortion, which will be discussed within the next section.

Bloch point field dynamics

A peculiar characteristic of magnetic cylindrical nanowires, with respect to nanotubes, is that the BPW contains a magnetic singularity at its core [50, 170, 174, 175]. In the micromagnetic theory, these structures are known as BP [163, 176, 177], and its generic version can be imagined as a point where the magnetic moments are pointing radially away from it. There are different BP structures but all of them share the

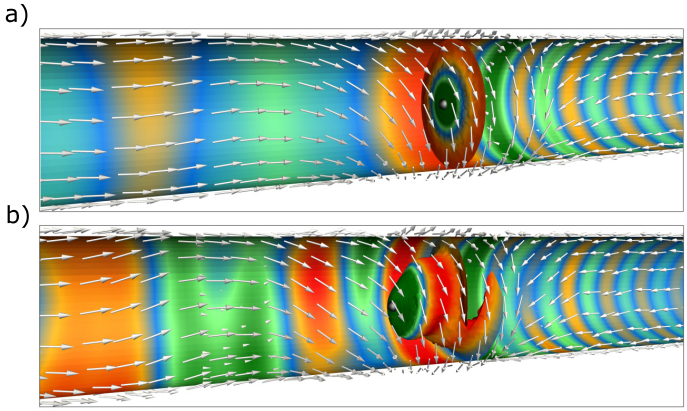

Figure 1.11: Field-driven BPW dynamics in a 80 nm diameter cylindrical nanowire. White arrows represent the direction of magnetization, and the color code represents m_ρ. The BP is represented by the small white dot. **a)** BPW moves at $1200\,\mathrm{m}\cdot\mathrm{s}^{-1}$ at 10 mT. Spin waves are visible. **b)** BPW moves at 30 mT to the right. Now, the BP lags behind the wall and moves on a spiraling orbit. Figure used with permission from [171].

following properties: (i) at the BP core the net magnetization is asymptotically zero, which is in disagreement with the assumption of continuity in micromagnetism. (ii) a BP carries a magnetostatic monopolar charge and (iii) it can be considered as a three-dimensional analog of a magnetic vortex, where magnetic moments rotate by 4π on a spherical shell around the BP. (iv) the exchange term is strong near the BP, which leads its dynamics. (v) a BP is magnetostatically favorable even though the cost in the short-range exchange. Therefore, it should be studied with its three-dimensional ferromagnetic surrounding. In micromagnetic simulations, the BP position can be tracked by the intersection of three isosurfaces of the magnetization field: $m_\mathrm{x} = 0$, $m_\mathrm{y} = 0$ and $m_\mathrm{z} = 0$ [174]. Its dynamics have been studied by micromagnetic simulations, as in vortex configurations in Permalloy thin films, where it was shown that the reversal of the core involves nucleation and propagation of the BP along the surface [164].

Regarding BP dynamics under a magnetic field, the following has been reported in the literature [171]: at moderate fields, the BP remains in the center of the BPW, whose structure remains unchanged even in the presence of spin waves and velocities up to about $1200\,\mathrm{m}\cdot\mathrm{s}^{-1}$. This is sketched in Figure 1.11a, where a BPW moves to the right at $1200\,\mathrm{m}\cdot\mathrm{s}^{-1}$ at 10 mT. The BP, displayed as the white dot, remains in the core of the DW. In front and behind the wall spin waves are developed. However, at higher wall velocities, the BP lags behind the DW and moves in a complex spiraling orbit around the central axis, as shown in Figure 1.11b for a 30 mT field. A distorted conical wall shape is displayed. This can be understood by the fact that the BP is moved by exchange forces rather than by external torque because its net magnetization is zero [171]. This is because as displayed in Eq.(1.24) $v \approx \Delta \approx |1/\nabla \mathbf{m}|$. And at the wire surface there is a very strong external torque, leading to a higher mobility in this region. The frequency of the spiraling motion matches that of the excited spin waves [178]. Finally, if the external field keeps increasing, a Bloch point-anti-Bloch point pair will be generated, resulting in a droplet formation.

When it comes to current-driven motion, a straight DW motion occurs, whose velocity reads:

$$v = \frac{\beta}{\alpha} u \tag{1.30}$$

Above certain speeds above $1000\,\mathrm{m}\cdot\mathrm{s}^{-1}$ there is saturation of the velocity due to the emission of spin waves, as shown in Figure 1.10c for the field-driven case. The energy injected in the spin waves does not contribute to accelerating the wall, whose speed therefore reaches a near plateau. This process was confirmed theoretically for BPWs [174].

The first experimental evidence of a BPW was given by shadow XMCD-PEEM in cylindrical Permalloy

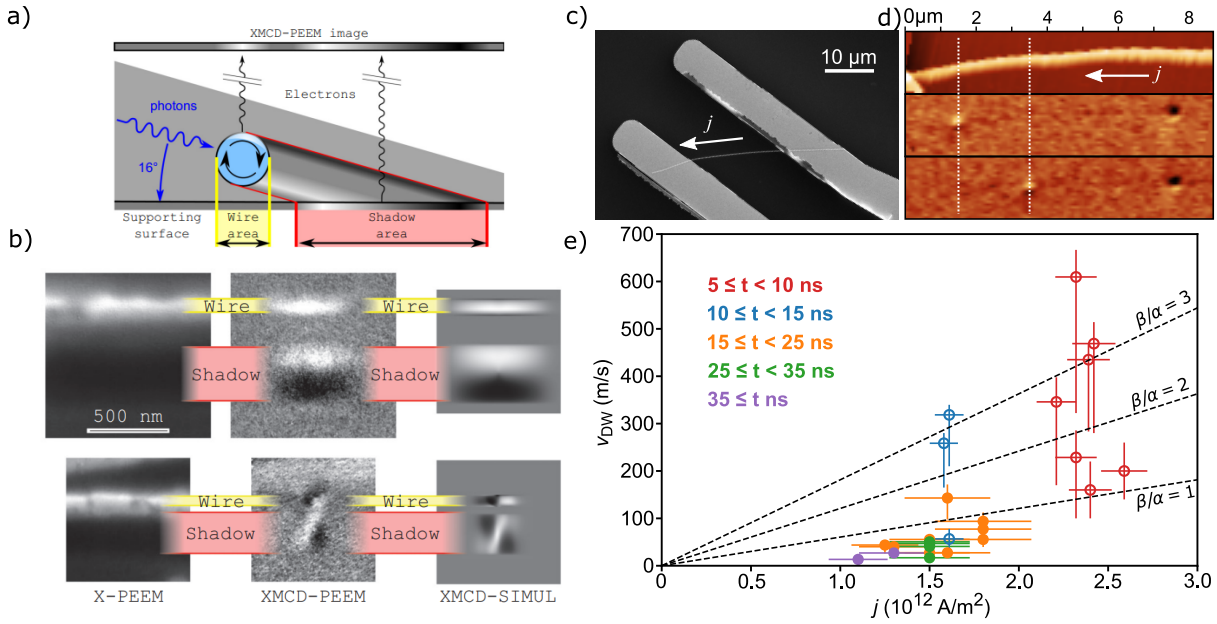

Figure 1.12: BPW experimental evidence. **a)** Schematic of the working principle of shadow XMCD-PEEM technique used to characterize three-dimensional nanostructures. **b)** First experimental evidence of a BPW (top) and a TVW (bottom) in a Permalloy cylindrical nanowires. The last column shows its corresponding XMCD-PEEM simulation. **c)** SEM image of an electrically contacted nanowire. **d)** MFM imaging of current-induced BPW motion. **e)** Experimental reported DW velocity as a function of the applied current density. Figures adapted and used with permission from [170, 181].

nanowires in 2014 [170]. The shadow XMCD-PEEM X-ray microscopy technique is described in detail in Chap. 2, but in brief, it is based on the observation of the magnetic contrast arising from the shadow created by the transmitted photons (Figure 1.12a). Since a BPW has azimuthal magnetization components, when the X-ray beam is along this direction (perpendicular to the wire axis), a dark and bright magnetic contrast is observed at the BPW location, as illustrated in the XMCD image at the top in Figure 1.12b. The last column corresponds to the micromagnetic simulations of the XMCD-PEEM contrast. BPW transformation to TVW was first reported due to an axial decrease in diameter [133, 179]. In addition, recent experimental and theoretical evidence has shown TVW transformations to BPW under nanosecond field pulses [180]. This process involves the annihilation of the vortex-antivortex pair and injection of a BP into the volume, conserving topology. Regarding current induced DW motion, the first experimental evidence was reported in 2019 with BPW velocities in excess of $600\,\mathrm{m}\cdot\mathrm{s}^{-1}$ [181]. An example of an electrically contacted nanowire is shown in Figure 1.12c, where two Au pads intersect with the nanowire. Figure 1.12d shows magnetic force microscopy (MFM) imaging of current-induced DW motion. Even though with this technique it is not possible to know the DW type, a quantification of DW speeds can be made. A summary of the DW velocity as a function of the applied field is shown in Figure 1.12e, where the shortest electric pulses get the highest velocities.

1.3.3 Œrsted field-driven dynamics

Any flow of current is associated with an orthoradial magnetic field, known as the Œrsted field. In cylindrical nanowires, their circular cross-section gives rise to an Œrsted field that reads:

$$H_{Œ} = \frac{jr}{2} \tag{1.31}$$

at a distance r from the nanowire axis. As an example, for a radius of 50 nm and a current density of $1 \times 10^{12}\,\mathrm{A \cdot m^{-2}}$ the resulting Œrsted field is 31 mT, which is rather high compared to common applied fields for DW motion [182]. However, for many years, theory has developed without including this term into the LLG equation, and also scarce reports have mentioned its impact, claiming that the magnetization was partially unaffected by the presence of the Œrsted field for the case of square cross-section nanowires [183]. Since 2019, reports on the high Œrsted field impact are emerging. The first experimental report of BPW motion reported that the direction of motion did not always follow the electron flow direction dictated by STT, and that the BPW circulation matches in sign with the Œrsted field applied. This highlights that the driving force may not be STT but also Œrsted field and heating effects. The system studied was $Co_{30}Ni_{70}$ cylindrical nanowires of 90 nm diameter. The current densities required for motion were $\approx 2.50 \times 10^{12}\,\mathrm{A \cdot m^{-2}}$, which correspond to an associated Œrsted field of 70 mT at the periphery [181]. This Œrsted field amplitude cannot be neglected. On the other hand, when both circulations are antiparallel, it was show experimentally that the Œrsted field drives the circulation switching of the BPW.

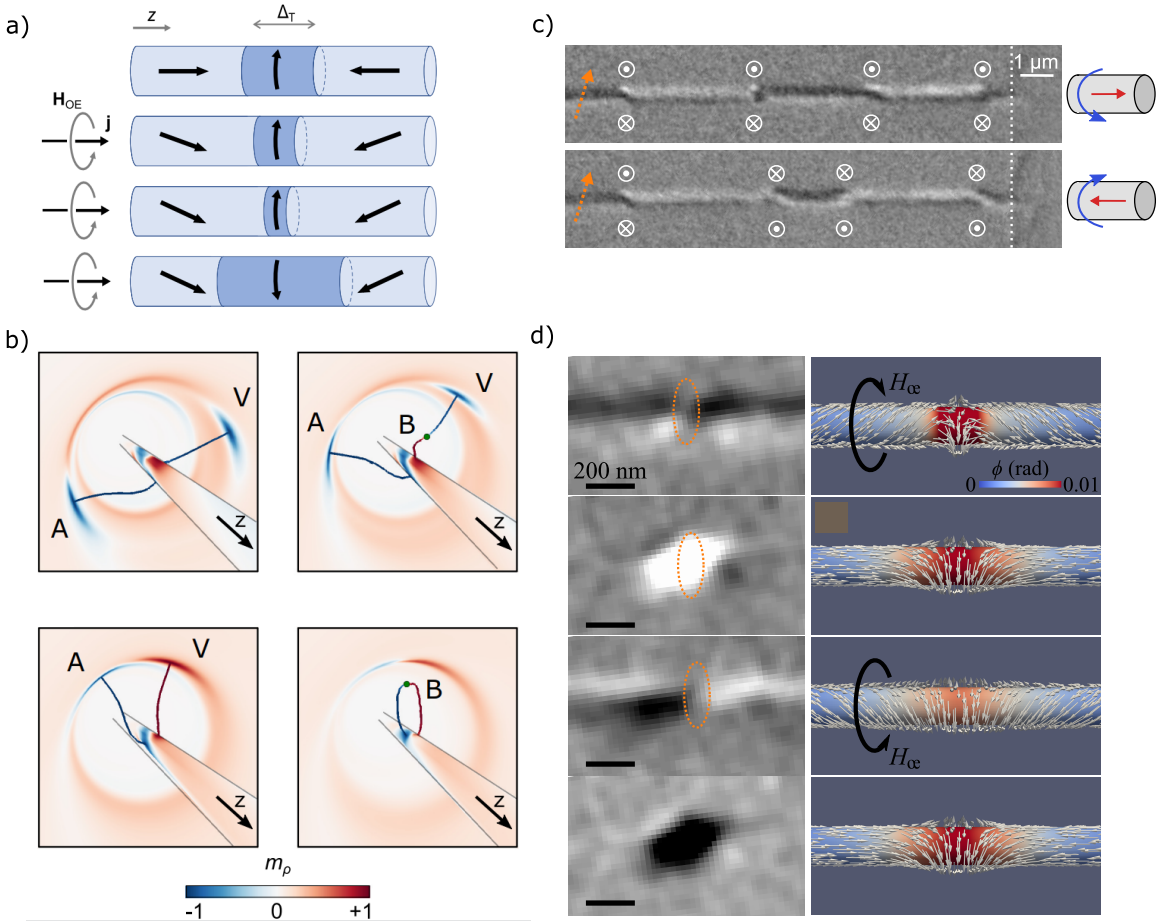

Figure 1.13: Œrsted field driven BPW switching on cylindrical nanowires. **a)** Schematics of BPW switching shows shirking and expansion of the wall when the Œrsted field is antiparallel and parallel, respectively. **b)** Micromagnetic simulated inner view of the BPW switching mechanism. Color-code corresponds to m_ρ. **c)** Shadow XMCD-PEEM images show BPW circulation reversal after the application of an antiparallel Œrsted field. **d)** Time resolved STXM imaging of the differential magnetic contrast frames acquired during the application of a 3 ns pulse of amplitude $0.75 \times 10^{12}\,\mathrm{A \cdot m^{-2}}$. They BPW breathing (shrinking and expansion under Œrsted field). Figures adapted and used with permission from [181, 184, 185].

The circulation reversal of the BPW was studied in detail by micromagnetic simulations in [185]. When an Œrsted field is applied with antiparallel circulation, the domains tilt along the Œrsted field circulation and the BPW shrinks. Once the wall has switched its circulation, the BPW width expands since its circulation is parallel to the Œrsted field. These steps are sketched in Figure 1.13a. The underlying mechanism is based on the interplay of volume singularity (the BP) and surface singularities (vortex-antivortex pairs). Note that strictly speaking the vortex-antivortex are not a singularity, so we want to clarify that throughout this manuscript it is used as such since if one considers a 2D vector field (XY), such perpendicular magnetization is not allowed. Therefore, is not possible to describe the core of the vortex-antivortex with the XY field, and these appear as singularities. In Figure 1.13b the inner view of the nanowire is displayed, and the color-code represents radial magnetization m_ρ. Before the BPW switches, one pair of vortex-antivortex is created at the same surface location. This pair moves azimuthally away from each other until they are diametrically opposed. The isoline that links them ($|m_\rho = 1|$) contains the BP. Afterward, the the vortex-antivortex move azimuthally towards each other while the BP travels to the surface. At the moment the BP reaches the surface vortex, it is annihilated and the vortex changes its polarity to positive. Afterward, the vortex-antivortex pairs annihilate and a BP re-enters in the volume with opposite polarity.

Regarding the first experimental evidence of BPW circulation switching [181], Figure 1.13c shows the XMCD-PEEM images of the process. The top image shows the initial state, and the bottom image shows the state when an antiparallel Œrsted field is applied. White symbols indicate the circulation senses. The most recent experimental report involving the Œrsted field impact was based on time resolved STXM imaging [184]. It was proven that the so-called breathing of the BPW occurs when an Œrsted field is applied parallel (expansion) or antiparallel (contraction). This is shown in Figure 1.13d, where the left panel corresponds to the STXM differential magnetic contrast frames acquired during the application of a of a 3 ns pulse of amplitude $0.75 \times 10^{12}\,\mathrm{A \cdot m^{-2}}$. The right panel corresponds to the micromagnetic simulations. In this case the current densities required for BPW switching in a 90 nm nanowire were $\approx 1.4 \times 10^{12}\,\mathrm{A \cdot m^{-2}}$. This made it impossible to do pump-probe experiments on the switching mechanism since the BPW would drift during the course of the measurement, averaging over billions of pulses.

To sum up, research on current-induced DW dynamics in cylindrical nanowires is at the early stage of development but is progressing rapidly. The main initial complexity was to characterize the three-dimensional magnetic texture, which needs to be done by means of X-ray microscopies. This was achieved in 2014 by shadow XMCD-PEEM technique, followed by STXM and transmission X-ray microscopy (TXM) imaging. The second challenge was to image under the application of nanosecond current pulses, skipping the risk of electrical discharges. This has also been successfully achieved. In addition, time-resolved experiments are at hand, which will provide access to the time-scale of the different dynamical processes. Therefore, the starting point of this work is an optimum platform to explore the physics of modulated nanowires and their interaction with DW under a current pulse stimulus.

Chapter 2

Methods and instrumentation

Throughout this thesis, a wide range of different experimental techniques have been used in combination with micromagnetic simulations and post-processing codes for data analysis. This combination has made it possible to obtain a complete picture of the object under study. Experimentally, the first step consisted of synthesizing chemically modulated nanowires by single-bath electrodeposition into anodised aluminium oxide (AAO) templates. This was followed by their morphological and compositional characterization by scanning electron microscopy (SEM) and transmission electron microscopy (TEM). Furthermore, their magnetic characterization in the laboratory was done by magnetic force microscopy (MFM) or TEM, which indirectly proves their magnetic properties. To characterize the three-dimensional magnetic behavior, X-ray magnetic imaging was performed using X-ray magnetic circular dichroism (XMCD) technique coupled with photoemission electron microscopy (PEEM), transmission X-ray microscopy (TXM), scanning transmission X-ray microscopy (STXM) or X-ray ptychography. A process based on laser lithography was carried out for the electrical contacting of the nanowires to allow high-frequency (HF) pulses injection. This allows the study of current-induced Domain wall (DW) dynamics. The experimental data are combined with micromagnetic simulations to identify the physics driving the different phenomena.

In the following, the different experimental techniques that have been used in this thesis are detailed. In addition, details of the experimental procedures carried out are given, so that they can serve as a guide for future research on this topic. Regarding the micromagnetic simulations, it will be briefly described the two micromagnetic codes used. To clarify the contribution of my work, I have performed all the techniques unless otherwise indicated.

2.1 Synthesis of ferromagnetic nanowires

This section describes the experimental techniques used in this work to synthesize chemically modulated cylindrical nanowires by template-assisted electrodeposition. The synthesis was carried out at UNIVERSITY COMPLUTENSE OF MADRID and IMDEA NANOSCIENCE.

2.1.1 Porous anodized aluminum oxide templates

Self-ordered porous AAO templates were reported for the first time in 1995 by Masuda and coworkers [108, 186]. After electrochemical oxidation of aluminum, a porous oxide film is created, containing parallel cylindrical nanopores that extend from the aluminum film to the film surface. Under certain electrochemical conditions, the pores organize into hexagonal cells, forming a honeycomb-like structure. The possible pore diameters range from 5 nm to 900 nm, and pore densities from 10×10^8 pores/cm^2 to 10×10^{10} pores/cm^2.

When aluminum is positively polarized in an acidic solution, a passivation layer is formed due to the transfer of electrons from Al to O. This leads to a drop in the intensity due to the high resistivity of the layer. The minimum values of intensity are reached when pores start to form at the surface defects or weak areas of

the Al sheet. Since the electric field at this location is stronger, local heating is induced, which leads to the chemical dissolution of the alumina (Al_2O_3) and the formation of pores. At this point, a rise in the intensity is detected until a constant value is obtained. This corresponds to the equilibrium conditions where the porous AAO membrane grows at a constant rate. The chemical reactions behind this process are as follows: first, the water molecules split and oxygen is released at the electrolyte/oxide interface:

$$H_2O \rightarrow 2H^+ + O^{2-} \tag{2.1}$$

Then the oxidation of Al occurs at the Al/alumina (anode) interface and Al^{3+} ions are released:

$$Al \rightarrow Al^{3+} + 3e^- \tag{2.2}$$

Al^{3+} ions react with O^{2-} ions, that travel through the oxide layer driven by the electric field, to form alumina [187]:

$$2Al^{3+} + 3O^{2-} \rightarrow Al_2O_3 \tag{2.3}$$

In parallel, hydrogen evolution takes place at the cathode:

$$H^+ + e^- \rightarrow \frac{1}{2}H_2 \tag{2.4}$$

Depending on the anodization conditions, such as applied voltage, temperature, acidity, concentration, and pH of the electrolyte, the structure of the porous AAO template, including pore diameter, interpore distance, barrier thickness, density of pores and porosity, can be tuned [109, 189]. The pore diameter increases with temperature and voltage, and decreases with the pH of the electrolyte [190]. The most common electrolytes used are sulfuric acid for a pore diameter in the range of 20 nm, oxalic acid for a pore diameter in the range of 50 nm, and phosphoric acid for a pore diameter in the range of 200 nm. The pore size can also be enlarged afterward by chemical etching [191, 192], where H_3PO_4 (5 % vol.) is usually used. Pore distributions with square or triangular shapes can also be formed if nanoindentation is performed beforehand [193].

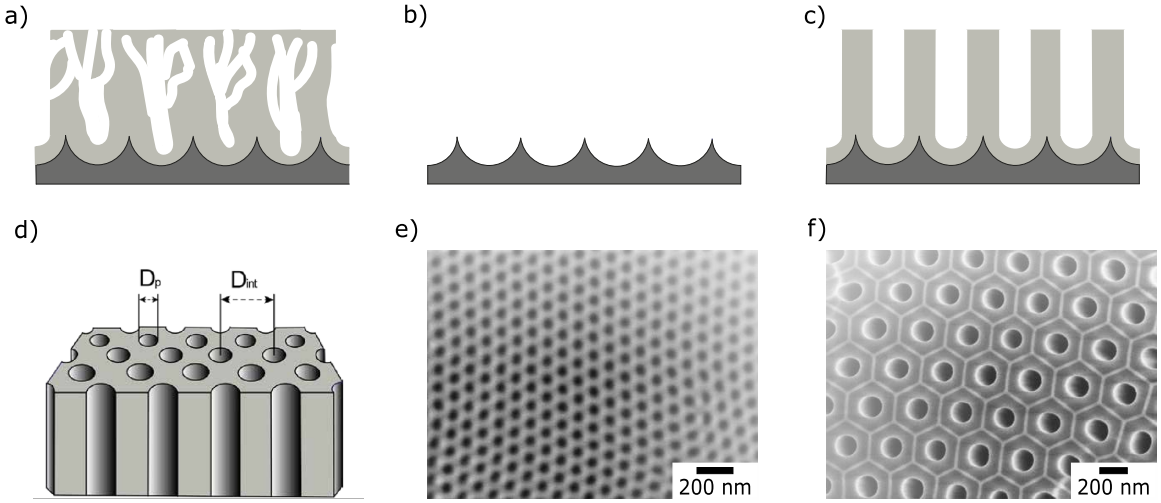

Figure 2.1: Porous AAO membranes. **a)** Transverse view scheme of pore morphology after the first mild anodization. **b)** Scheme after the removal of the alumina. **c)** Transverse view scheme of pore morphology after the second mild anodization shows ordered pores. **d)** AAO scheme indicates pore diameter D_p and interpore distance D_{int}. **e)** Top view SEM image of an AAO membrane obtained by mild anodization. **f)** Top view SEM image of an AAO membrane obtained by hard anodization. Adapted from [188].

There are typically two voltage regimes for fabricating AAO templates: mild (or two step) and hard (or one step) anodization. In the mild anodization regime, a first and long anodization (typically around 24 h) is performed usually by applying 40 V at 3 °C in a 0.3 M oxalic bath. The aim of the first anodization is to pattern a hexagonal template for the pores, which become less orderly as they move away from the barrier layer. This is shown in Figure 2.1a, where the ordered template in the barrier layer is shown in dark grey, the alumina pores in light grey and the pores ramifications in white. Afterwards, the entire alumina porous layer is removed by chemical etching to later perform a second anodization with the anodization conditions. In this thesis, we performed chemical etching with 0.18 M CrO_3 and 0.72 M H_3PO_4 at 60 °C for 1 h. The current densities obtained during the process are $\approx 1.8\,\mathrm{mA\cdot cm^{-2}}$. After the second anodization, the pores are highly ordered as displayed in Figure 2.1c. The duration of the second anodization determines the length of the pores, being of $\approx 60\,\mu$m for 20 h. A top view SEM image of a porous AAO template obtained from mild anodization is shown in Figure 2.1e, where the pore diameter is of ≈ 50 nm.

If longer diameters, above 100 nm, are desired, a hard or one-step anodization process is indicated [194]. In this case, the applied potential is larger (≈ 140 V) and the oxalic bath is usually combined with additives such as ethanol [194, 195] to dissipate heat and to reduce the anodization temperature. Specifically, we have performed hard anodization at 140 V in a 0.3 M oxalic acid and 0.9 M ethanol bath at 0 °C to 1 °C for 2.5 h. The current densities obtained during the process are $\approx 23\,\mathrm{mA\cdot cm^{-2}}$. A pore length of $\approx 80\,\mu$m is obtained. The initial pore diameter is 100 nm, which can be widened up to 250 nm by chemical etching with H_3PO_4 (5 % vol.) at 45 °C.

After the anodization process, to allow nanowire growth, the remaining Al below the AAO template must be removed by chemical etching so that alumina pores form the top and bottom of the template. We have used 3.25 M HCl and 0.74 M $CuCl_2$ for this process.

2.1.2 Atomic layer deposition

In some cases, it is interesting to coat the pores of the AAO templates with a specific and controlled thickness of a different material. In this sense, the most optimal technique to do this is atomic layer deposition (ALD) due to its precise thickness control at the monolayer level, self-limiting reactions and conformal deposition. In fact, ALD has shown to be a powerful tool for fabricating nanomaterials, including three-dimensional nanostructures. For the case of nanowires and nanotubes, the coating of the porous AAO templates allows for the creation of core-shell and multilayered materials [196]. In addition, it can reduce the pore diameter of the templates or protect the nanowires from oxidation once they have been released from the template.

The protocol for ALD is based on cycles of four steps: (i) precursor dosing, (ii) purge and/or pump, (iii) co-reactant dosing and (iv) purge and/or pump [197]. This cycle is repeated as many times as necessary to obtain the desired thickness [198]. The purge or pump steps remove parallel gas reactions from the chamber. The most common materials deposited are metal oxides, but noble metals, metals, tertiary and quaternary compounds or alloys are also possible. In this thesis, we have performed 5 nm HfO_2 ALD coating of the alumina pores in some cases. This step was performed at INSTITUT NÉEL by LAURENT CAGNON and at IMDEA NANOSCIENCE by MANUEL RODRIGUEZ.

2.1.3 Electrodeposition

Electrodeposition is a synthesis technique in which metal ions of an aqueous electrolyte are reduced by the application of a cathodic potential on a conductive substrate (working electrode) to form metal atoms [199, 200]:

$$\mathrm{M}^{n+}_{(\mathrm{aq})} + n\mathrm{e}^- \rightarrow \mathrm{M}_{(\mathrm{s})} \tag{2.5}$$

The most common setup is a three-electrode electrochemical cell, where a cathodic potential is applied between the working electrode or substrate and a reference electrode. The anode or counter electrode is

usually made of a Pt, C or W mesh. More information about electrochemical cells can be found in the literature [201, 202]. The electrical circuit is closed by means of an external power supply that generates the electron flow. Specifically, for a three-electrode cell, the device usually used is a potentiostat, which controls the electric potential between the cathode and the reference electrode while the current flows between the cathode and the anode [203]. The electrolytes are normally water-based solutions with electroactive ions, as well as supportive chemicals and additives in solution. It is important to note that the concentration of ions in the electrolyte does not correlate with their concentration in the deposited material. The reason relies first on the different reduction potentials of the different metals and second on the so-called anomalous codeposition detailed in Sec. 3.2.1. Although two or more separate baths can be used to deposit multilayer materials [204–207], this configuration has some drawbacks, and usually single bath electrodeposition is recommended for the preparation of multilayered materials [208]. In this case, the reduction potentials of the different ions should be far enough apart to avoid the growth of an alloy instead of a multilayer system.

Electrodeposition, in combination with porous AAO templates, can be used for the synthesis of nanowires [97]. For that, a metal, usually Au, is sputtered onto the bottom of the template to act as the working electrode or cathode. Specifically, in this thesis, 10 nm of Ti was sputtered at $0.03\,\mathrm{nm}\cdot\mathrm{s}^{-1}$, followed by 150 nm of Au at $0.25\,\mathrm{nm}\cdot\mathrm{s}^{-1}$. The electrodeposition setup is based on a three-electrode cell, as sketched in Figure 2.2a. The metal layer on the alumina template is electrically connected to the stainless-steel electrochemical cell by a small drop of silver paint. A Pt mesh is used as the anode or counter-electrode and a BASi Ag/AgCl (3M NaCl) electrode serves as a reference electrode. The electrochemical cell is connected to a potentiostat PGSTAT (Metrohm-Autolab), which monitors the electrodeposition process. Potentiostatic deposition, i.e., electrodeposition at a constant voltage, was chosen for the synthesis of the nanowires because it allows control of the electrodeposition process independent of the template conductive area.

An example of the current evolution during the electrochemical growth of magnetic nanowires is shown in Figure 2.2b. The different growth regimes identified are: (i) Nucleation regime that sets the nucleation and plating of material on the working electrode. The drop in the current is due to the charging of the interface metal/electrolyte (Helmholtz double layer [209]). (ii) Steady regime due to the constant growth rate while the channels are being filled since the active surface area is constant. The growth is linear with

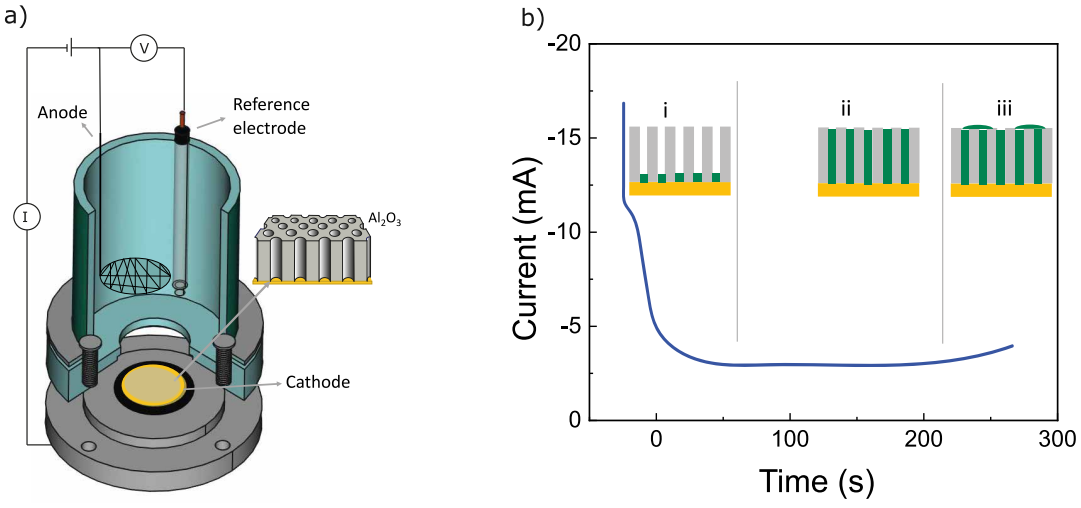

Figure 2.2: **a)** Schematic of a three-electrodes electrochemical cell. The Au layer sputtered on the AAO template acts as the cathode, a Pt mesh as the anode, and a BASi Ag/AgCl (3M NaCl) electrode as the reference electrode. **b)** Evolution of the cathodic current during the electrodeposition process of nanowires inside an AAO template. Adapted from [188, 203].

time and therefore the growth rate can be calibrated. The last regime (iii) is reached when the pores are filled and the material deposits on the top surface of the AAO template. The increase in the deposited surface is accompanied by an increase in the current.

Permalloy ($Fe_{20}Ni_{80}$) nanowires with $Fe_{80}Ni_{20}$ chemical modulations were synthesized by single-bath electrodeposition. The electrolyte used is composed of $NiSO_4$ (0.8 M), $NiCl_2$ (0.02 M), $FeSO_4$ (0.16 M) and H_3BO_3 (0.4 M). The pH was adjusted to 2.3 by dropping H_2SO_4 (10% vol.). The synthesis was performed at room temperature. Details on the growth potential and additional details on the synthesis of chemically-modulated nanowires can be found in Chap. 3.

Finally, it is worth mentioning that the electrochemical parameters set the properties of the deposited material, which determine its magnetic behavior. In short, the applied voltage not only drives the rate of deposition but also the grain size, crystallinity and mechanical properties [210–214]. The pH directly affects the hydrogen evolution during the electrodeposition, which is directly related to the grain size [215]. Temperature has shown to affect the composition of the grown material [216, 217]. Finally, the role of additives is crucial to achieving a stable growth. The most common ones are boric acid, which prevents local pH changes, or saccharine, which reduces grain size [218, 219].

2.1.4 Single nanowire manipulation

To manipulate individual nanowires, they should be released from the AAO template. To do so, first, the underlying Ti and Au layer is removed at room temperature with 0.1 M I_2 and 0.6 M KI for $\approx$ 10 min. Afterwards, a $\approx 1\,mm^2$ piece of alumina membrane is dissolved in an Eppendorf in $\approx 150\,\mu L$ 0.4 M H_3PO_4 and 0.2 M H_2CrO_4 for 12 h at 40 °C. It should be noted that the chromic acid in this solution creates a chromium oxide layer of $\approx 2\,nm$, that acts as a protective layer on the nanowire surface, preventing it from etching and oxidation. Several rinses of the nanowires were done in deionized water. The use of an ultrasonic bath is not recommended as it has been shown to break the nanowires. The last rinsing step was done with pure ethanol. The nanowires are preserved in ethanol before use. For dispersion, a drop of the solution is placed on a Si substrate. The ethanol evaporates leaving individual nanowires stuck on the substrate.

2.2 Electron microscopy imaging and characterization

2.2.1 Scanning electron microscopy

In conventional optical microscopy, the maximum magnification is about 1000x, which is limited by the wavelength of the light ($\lambda = 380\,nm$ to $760\,nm$). Therefore, for better resolution, the sample can be probed with a focused electron beam, whose wavelength is $\lambda = 0.012\,nm$ when accelerated at 10 keV. This can be achieved with SEM imaging with a spatial resolution down to 1 nm. The setup consists of an electron gun at the top, that generates the electron beam. The beam travels through the electron column and it is focused by electromagnetic lenses. The coils in the column probe the beam over the surface. Then, secondary and back-scattered electrons are detected. In addition, the emission of characteristic X-rays can be probed with energy dispersive X-ray analysis (EDX) to determine the chemical composition.

SEM was used to characterize the morphology and quality of the nanowires. The criteria used to validate a batch of samples were that the nanowires should be of sufficient length for future electrical contact, have the desired diameter and have a clean surface without traces of AAO or impurities. Therefore, a magnification range of 15.000x to 150.000x was used. Several microscopes were used in this work: a SEM JEOL JSM 6335F (at National Center of Electron Microscopy - UCM), a ZEISS EVO HD15 SEM microscope (at IMDEA NANOCIENCIA) and a Zeiss Ultra+ microscope with Bruker QuanTax EDX system (at the PTA clean room at SPINTEC). Electron beam energies of 2 keV to 15 keV were used. Special care was taken when imaging samples prepared for PEEM or atomic force microscopy (AFM) experiments, since the effect of charges from SEM imaging can be later on seen later on PEEM or AFM images.

2.2.2 Transmission electron microscopy

An in-depth characterization of the composition, morphology and crystallinity can be obtained by performing TEM. In this case, the electrons are accelerated from 60 keV to 300 keV and focused on the sample with electromagnetic lenses. The beam travels through the sample, and the scattered electrons reach the back focal plane of the objective lens to form a diffraction pattern. The transmitted electrons strike a fluorescent screen in an image plane at the bottom of the microscope. A magnification up to 2.000.000x can be achieved with a resolution in the sub-nanometer regime. Various characterization techniques, such as diffraction, imaging, spectroscopy and holography, can be combined to characterize nanostructures of relatively low thickness ($>$ 100 nm). The electron beam is generated either by thermo-ionic emission by heating a tungsten filament or a LaB6 tip, or by field emission by applying a high voltage at the tungsten tip. A combination of both methods is also possible.

In the case of scanning transmission electron microscopy (STEM), the electron beam scans the sample and undergoes diffraction and scattering events at different angles. The possible imaging modes are annular dark field (ADF) and bright field (BF). The ADF detector collects high-angle scattered electrons. Since the scattering angle depends quadratically on the atomic number Z (Rutherford equation), a Z-contrast image provides information about the composition. The high angle annular dark field (HAADF) detector collects an angular range of 100 mrad to 200 mrad. BF or annular bright field (ABF) detectors provide coherent images similar to high-resolution electron microscopy, where atomic columns appear as dark spots. The ABF detector produces a contrast similar to BF but is still sensitive to light atoms. Quantitative compositional characterization can be performed with electron energy loss spectroscopy (EELS). The transmitted beam reaches the EELs spectrometer after undergoing an inelastic scattering process. The scattering angle depends on the energy lost and transferred to the sample. One can also collect X-rays emitted by de-excitation of atoms in the sample, giving similar chemical sensitivity as EELS but with lower resolution.

Lorentz microscopy can be performed in TEM to perform magnetic characterization. This technique is based on the Lorentz force experienced by propagating electrons when they undergo the magnetic field of the sample, where $\mathbf{F} \sim q\mathbf{v} \times \mathbf{B}$, where $\mathbf{v}$ is the electron velocity and $\mathbf{B}$ is the magnetic induction. Note that, the deflection of the electron trajectory depends only on the components of the magnetic induction perpendicular to the optical axis. The magnetic properties can be studied by defocusing the image (Fresnel mode) or by selecting one of the deflected beams in the back focal plane of the Lorentz lens using an aperture (Foucault mode) [220, 221]. It is worth noting that the magnetic field produced by the objective lens is in the range of 2 to 3 Tesla. For magnetic imaging, this lens must be turned off and another lens must be used. This degrades the resolution power of the TEM in such mode, but still allows slightly exciting the objective lens to apply a magnetic field to the sample (along the optical axis). In this work, we have used the Fresnel mode to observe magnetic DWs. This is possible due to the convergence or divergence of the deflected electron beams in opposite directions on either side of the DW, leading to bright or dark contrast lines in the image plane. Since the sample holder can be tilted, a strong transverse field can also be applied to move DWs. Furthermore, TEM can be adapted to HF current pulses to study DW current-induced dynamics.

In this work, images of STEM were obtained with a JEOL JEM-ARM200CF by ALEJANDRA GUEDEJA-MARRÓN GIL and MARÍA VARELA at the National Center of Electron Microscopy at UCM. AURÉLIEN MASSEBOEUF performed TEM, STEM and electron holography at PFNC using a FEI TITAN Ultimate and at CEMES using a Hitachi HF3300 (I^{2}TEM) under HF pulses.

2.2.3 Electron holography

Electron holography is based on the change of the electron amplitude and phase when it interacts with a material. In TEM, the square of the intensity of the electron wave reaches the detector and the phase is lost. Electron holography allows for retrieving the electron phase shift [222, 223]. In this work, off-axis electron holography was performed. Its mechanism relies on the interference of two biprism deflected coherent electron waves [224]. The first one passes through the sample, interacting with its electromagnetic fields. The

second one passes through a vacuum or a region without electromagnetic fields. Their interference creates hologram interference fringes with electrostatic and magnetic information. After numerical reconstruction (Fourier transform), the electrostatic potential and the in-plane induction field can be studied separately [225, 226]. Usually, the electric field contribution is subtracted by measuring two holograms, for both longitudinal magnetization directions. The induction field obtained corresponds to the components that are perpendicular to the electron beam.

2.3 Magnetic imaging and characterization

2.3.1 Atomic and magnetic force microscopy

AFM operates very differently from other microscopes. In this case, light, electrons or X-rays are not used to probe the sample, but a probe physically interacts with the sample surface [227]. In conventional microscopy, a two-dimensional image is obtained, with no information on the height if the sample is not rotated. However, AFM provides a map of the topography of the sample obtained by scanning a probe over it. The spatial resolution obtained can be down to a few nanometers. Usually, it is combined with an optical microscope so that a larger field of view allows for speeding up the search for the spot to measure. In addition, a vibration isolation platform is required to minimize external noise. The working mechanism is based on the following steps: (i) A tip is moved over the sample by a piezoelectric transducer. (ii) The force between the tip and the sample is measured by the force transducer, which is usually a cantilever with an integrated tip and an optical lever. The interaction type is the short-range van der Waals force. Finally, (iii) a constant force between the tip and the sample is kept by the feedback control. This maintains the tip-sample distance fixed. Usually, the common mode is the "tapping mode", where the cantilever vibrates near its resonant frequency, causing the tip to oscillate up and down. A laser is shone onto the cantilever and, depending on its height, is reflected into a specific position of a photodiode.

If the tip is coated with a magnetic material, MFM measurements can be made to probe the long-range magnetic interaction [228, 229]. The stray field arising from the sample generates a force on the magnetic tip. Depending on the sign of the force, the magnetic contrast will be dark or bright. Usually, the working mode is a first AFM scan in tapping mode to determine the topography. A second scan is then performed with a longer tip-sample distance to avoid the non-magnetic signal.

MFM allows the magnetic characterization of three-dimensional objects such as cylindrical nanowires [230]. However, imaging is not that straightforward due to the object curvature, and therefore some considerations must be taken into account. Firstly, different scanning orientations of the tip lead to different magnetic contrasts. Since the cantilever is slightly tilted from the vertical direction, if the nanowire axis and the cantilever axis are perpendicular, the tip will be closer to the surface on one side of the wire than on the other side. Therefore, the stray field arising from the bottom of the nanowire, which has the opposite sign to the one arising from the top, is only detected on one side of the wire. This results in a strong contrast coming from the top of the wire and a weak opposite contrast on one side [231]. Therefore, the optimal configuration to obtain symmetrical contrast is to have the nanowire axis parallel to the cantilever axis. Concerning the nanowire's magnetization, if the domains are longitudinally magnetized, no magnetic contrast is expected apart from at the wire ends [232]. At these locations, the magnetic surface charges are proportional to magnetization. In the case of a magnetic DW, there are only volume charges at its center, which are proportional to twice the value of the magnetization. This implies that the MFM contrast is twice as high at the location of a DW than at the wire ends [233].

AFM and MFM imaging were performed at INSTITUT NÉEL using a NT-MDT NETGRA AFM. The magnetic tips were obtained by coating a commercial Si tip with 20 nm or 30 nm of CoCr. The tip had a stiffness of $2\,\mathrm{N\cdot m^{-1}}$ and a resonant frequency of 70 kHz. Then, 4 nm of SiO_2 was grown as a protective layer. I performed measurements at rest and under the application of HF current pulses. For the latter, a home-made sample holder was fabricated by CHRISTOPHE THIRION, by designing two coplanar waveguides

Figure 2.3: Sample holder and setup for MFM imaging under HF current pulses. **a)** Sample holder dedicated to HF pulses used for MFM imaging. SMP connectors' transmission line is connected to Co-planar waveguides. Microbonds electrically connect the waveguide with the Au contacts of the nanowire. **b)** Schematics of a nanowire connected to an electronic circuit. SMA cables are connected to zero-Ω shorts to isolate samples. One BNC cable coming from the pulse generator is plugged on the other end of the T-junction. Lastly, another BNC cable from the oscilloscope is connected to measure the transmitted pulse. Figure used with permission from [234].

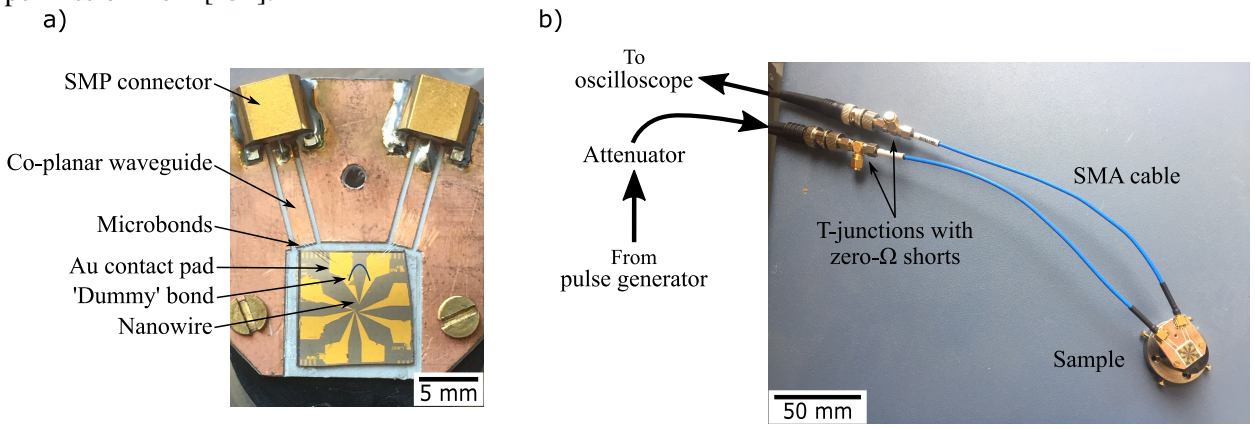

on a strongly vibration-absorbing substrate. The sample holder is displayed in Figure 2.3a. The transmission line or "live" of the sub-miniature push-on (SMP) connectors is connected to the "live" of the coplanar waveguides. A Si substrate with electrically contacted nanowires is glued to the PCB with silver paint.

The procedure for electrically connecting a nanowire to the electronics was as follows: first, a security microbond from the Au to the Au pad was made so that the sample is short-circuited. Then, another short is made by microbonding both transmission lines of the printed circuit board (PCB) to each other, and finally microbonds from the co-planar waveguides to the Au pads were made. This is followed by plugging the SMP connectors into a sub-miniature version A (SMA) cable that has a T-junction at its end with a zero-Ω short in one termination (see Figure 2.3b). By doing this, when the security bonds are removed, the sample is shorted/protected by these loads. It is also possible to connect a shorting bar between the two SMA cables. Afterwards, the oscilloscope (ground) is connected to a Bayonet Neill–Concelman (BNC) or a SMA cable, which is later connected to the other termination of the T-junction. Lastly, the pulse generator is connected to an attenuator, then to a BNC or a SMA cable which connects to the other T-junction termination. The different steps and safety precautions needed to connect a nanowire to an electronic circuit are detailed in Sec. 2.6.

2.4 X-ray magnetic imaging and characterization

The main experimental work of this thesis has focused on the three-dimensional magnetic characterization of chemically-modulated nanowires. In this sense, the most powerful techniques are X-ray microscopies with the possibility of performing XMCD. These X-ray-based microscopes are normally placed in synchrotron radiation laboratories [235]. Shortly, the X-ray radiation emitted by a synchrotron comes from accelerated particles that follow a curved trajectory due to the application of bending magnets and/or undulators. A wide range of energies can be produced from *hard* to *soft* X-rays. In the following, we will first describe the XMCD technique, followed by the description of the different microscopes used. We will also detail the experimental specifications and developments to perform experiments under field and under HF current pulses.

2.4.1 X-ray magnetic circular dichroism

X-ray magnetic imaging makes use of the XMCD technique to probe, in a non-destructive manner, the magnetization of a material [236, 237]. The interaction of light with matter, i.e., magneto-optics, is well known since the 19th century, with the pioneering work of Faraday [3] and Kerr [7]. Both effects manifest the dependence of reflection or absorption on the angle between light polarization and magnetization. However, these optics are limited by the wavelength of the light (400 nm to 700 nm). Therefore, probing magnetic materials with X-rays allows reaching a spatial resolution of a few nanometers in the case of *soft* X-rays (100 eV - 2 keV), or down to the Å for *hard* X-rays (3 keV to 100 keV). The word dichroism means different light absorption by a medium depending on the polarization of light. In the case of XMCD, it means that the absorption of circularly polarized X-rays depends on the relative orientation of the photon helicity and the magnetization direction, being maximized for parallel or anti-parallel orientations.

The materials of interest in this work are ferromagnetic $3d$ transition materials (Fe, Co, Ni), whose L-edges are covered in the *soft* X-ray regime [238]. The spin-orbit coupling leads to a splitting of the $2p$ band into $2p_{1/2}$ ($L-S$) and $2p_{3/2}$ ($L+S$) bands, corresponding to the L_2 and L_3 absorption edges. When the photon energy is set at one of the edges, an electron is excited from the $2p$ band to the $3d$ band. Since the density of states in the $3d$ band is asymmetric, above the Fermi level there are more holes of one type of spin (up or down), inducing the presence of magnetization. In addition, the electrons' orbital momentum in the $2p_{1/2}$ ($2p_{3/2}$) band is antiparallel (parallel) to the spin. Therefore, when an incoming photon with a fixed angular momentum $\pm\hbar$ reaches the $2p$ band, the probability to excite a particular spin direction is governed by the conservation of the angular momentum. Different transition probabilities lead to an asymmetric absorption spectrum for a left or right circular photon helicity. Therefore, the XMCD signal can be calculated as:

$$C_{\mathrm{XMCD}} = \frac{I_- - I_+}{I_- + I_+} \tag{2.6}$$

where I_- is the absorbed intensity for a circularly left polarized photon and I_+ is the absorbed intensity for a circularly right polarized photon.

As an example, we will consider a Fe $3d$ ferromagnet, which has a majority of spin down states below the Fermi level and a majority of spin up empty holes above the Fermi level [240]. We will consider the case of a parallel orientation between the magnetization and the X-ray beam $\mathbf{k}$. When circularly left-polarized X-rays $+\hbar$ (up) at the L_3 edge interact with the $2p_{3/2}$ band, mostly spin up polarized electrons are excited. A schematic of this is shown in Figure 2.4a, where the electronic transitions from the $2p_{3/2}$ to the $3d$ band above the Fermi level are shown. In blue and yellow are displayed the spin up and down states, respectively. Considering that this material has a majority of spin up empty states above the Fermi level, circularly-left polarized photons (purple arrow) with angular momentum $+\hbar$ (up) and energy corresponding to the Fe L_3 absorption edge interact with the $2p_{3/2}$ band, leading to a larger population of spins up excited to the $3d$ band. This is indicated by the thicker red arrow. This is because the photon's angular momentum is parallel to the spin up. On the other hand, circularly right polarized photons $-\hbar$ (down) will excite more spin down electrons, but since the total spin down empty holes are much smaller, less X-ray absorption will occur. The difference in the absorption for left or right-polarized photons determines the XMCD signal.

Figure 2.4b shows an example of a XAS spectrum of a Fe thin film at the Fe L_3 and Fe L_2 edges for parallel (red) and antiparallel (blue) orientations between the sample's magnetization and the photons' angular momentum. It can be observed that for parallel orientations the Fe L_3 edge shows the highest absorption for spins up, whereas for antiparallel orientations there is less absorption. The opposite occurs at the Fe L_2, showing maximum absorption for antiparallel orientations. The difference between the two XAS profiles, i.e., the XMCD signal, is shown in black. Here, it is pronounced the sign reversal between the L_3 and L_2 edges [239]. Note that the same profiles would be obtained if instead of changing the X-rays' helicity, we change to antiparallel magnetization configurations. Therefore, experimentally we can measure XMCD either by reversing the polarity of the light or by reversing the magnetization of the sample. Finally, it should

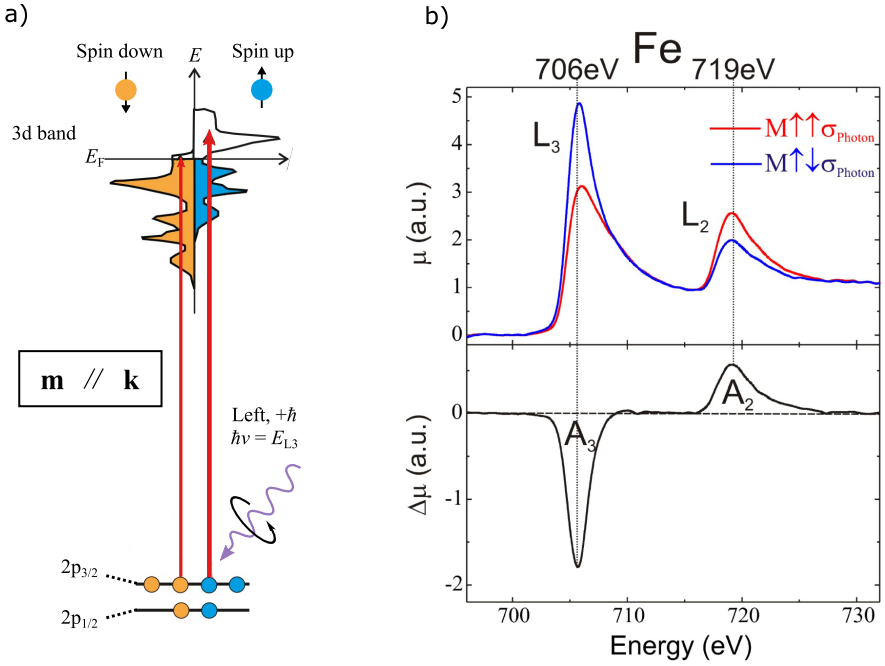

Figure 2.4: **a)** Schematic of an electron transition from the $2p_{3/2}$ band to the $3d$ band after absorbing X-rays at the Fe L_3 edge. The sample is a Fe film with magnetization parallel to the X-rays direction **k**, which are circularly left polarized with an angular momentum $+\hbar$. The thicker red arrow shows a majority of spins up (blue) excited to the empty $3d$ bands above the Fermi level. Adapted from [234, 236]. **b)** Example of an experimental XAS spectrum at the Fe L_3 and Fe L_2 edges for parallel (red) and antiparallel (blue) orientations between the sample's magnetization and the X-ray. In black, the difference of the two profiles corresponds to XMCD spectra. Figure used with permission from [239].

be mentioned that the XMCD amplitude depends on the material. For example, in the case of Ni at the Fe L_3 edge, the difference in absorption for right and left circularly polarized light (distance between peaks) is much smaller than in Figure 2.4b, resulting in a weaker magnetic contrast. This is the reason why, in the experiments performed in this work, the photon energy is always set at the Fe L_3 edge, so that the magnetic contrast is maximized.

In the following, we will detail the different ways to detect X-ray absorption: either by collecting the electrons emitted from the sample (PEEM) or by measuring the transmitted intensity through the sample (TXM, STXM or X-ray ptychography).

2.4.2 Photoemission electron microscopy

The first X-ray magnetic images were measured with PEEM by Stoehr *et al.* in 1993 [241]. The mechanism behind this imaging technique is based on the emission of a cascade of secondary electrons induced by the absorption of X-rays from a shallow layer at the sample surface . Figure 2.5a shows the schematic of a PEEM microscope setup. In purple, it is sketched a circularly polarized X-ray beam, which has an incident angle of 16° with respect to the substrate. The vertical emission of secondary electrons is shown in red. To accelerate the electrons towards the detector, a voltage (typically of 20 kV across a 2 mm gap) is applied between the sample and the imaging column [242]. If necessary, the potential can be reduced to 15 kV or 10 kV to avoid electrical discharges in the sample with the disadvantage of losing spatial resolution. Inside the electron column, an aperture rejects the higher energy electrons that are not properly focused [236]. Another aperture that is adjusted manually, known as the contrast aperture, prevents the electrons with a high emission angle

from reaching the detector, thereby reducing image aberrations. When the electrons reach the multichannel plate (MCP), an image is formed. The base pressure is below 1×10^{-10} mbar, and is limited by the arcing due to the high voltages. Due to the low escape depth of the electrons, the secondary emitted electrons come from a surface depth of a few nanometers, making PEEM a surface sensitive technique. A minimum electron kinetic energy to leave the sample is set by the start voltage. Usually ≈ 2 eV is applied to the substrate, which should be conductive[243]. A metal cap with a small hole is placed on top of the sample holder to reduce the risk of discharges. Therefore, the maximum image field of view is limited by the size of the hole which has a diameter of ≈ 1.5 mm. Lastly, since the X-ray energy can be tuned by the user, the emitted secondary electrons are element-sensitive. Therefore, the areas appearing bright in the image correspond to the strong absorption regions. This allows the creation of chemical contrast images by subtracting images acquired at two different photon energies. The spatial resolution is typically ≈ 30 nm.

Regarding image acquisition, since the X-ray beam spot size is larger than the image field of view (FoV), a full-field image is obtained without the need to scan the sample. In order to improve the signal-to-noise ratio, the exposure time can be increased. However, this may also lead to image drift. Instead, a better option is to capture several frames (typically 64 or 128) and then align and average them using dedicated software. The rotation of the manipulator around the sample normal allows imaging at any relative orientation between the sample and the X-ray beam. Acquisition times can be reduced to 50 ps [244], which allows for studying time-resolved micromagnetic dynamics. In addition, magnetic field or electrical pulses can be applied to the sample. Quasistatic magnetic field pulses are applied through a coil fitted in the sample cartridge below the sample. These coils or electromagnets are powered by the standard filament current supply through a switching unit that allows spike-free current direction reversal, achieved by connecting a bypass between the

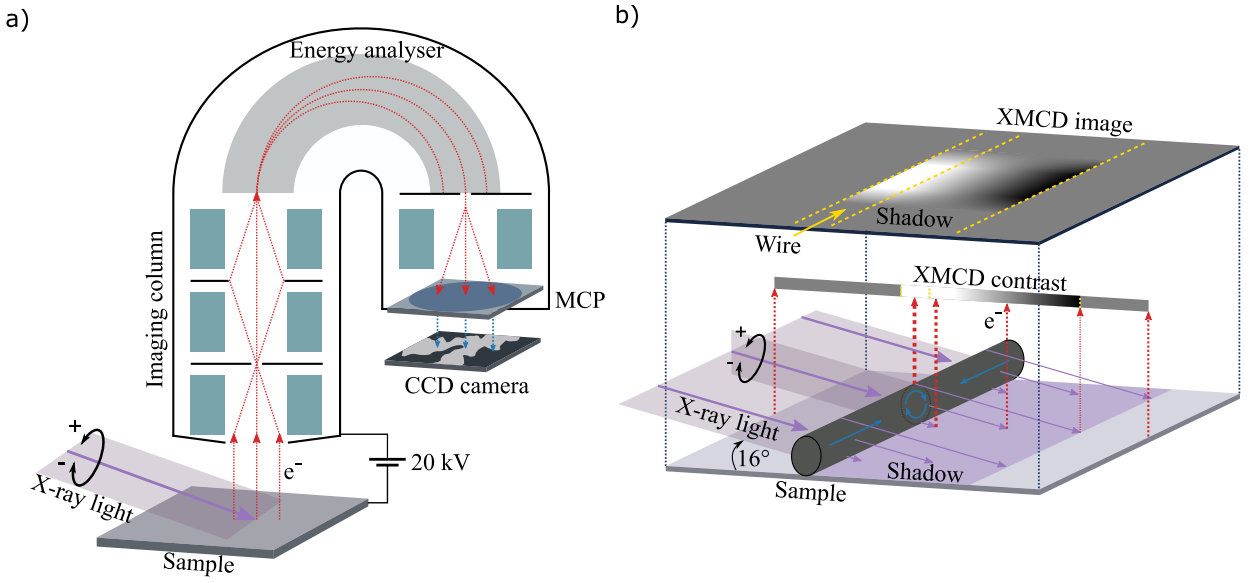

Figure 2.5: Schematic of PEEM setup. **a)** Circularly polarized X-ray light (purple) hits the sample with an incident angle of 16°, inducing the photo-emission of electrons (red arrows). A 20 kV potential difference drives the electrons through the imaging column , the energy analyzer until they reach the multichannel plate (MCP) detector and form an image. **b)** Schematic of shadow XMCD-PEEM of a nanowire. Magnetization direction is shown in blue, showing a DW with azimuthal magnetization in the center. The photo-emitted electrons give surface magnetic contrast of the object (white at the DW position). In addition, the photoemitted electrons coming from the shadow of the object (transmitted photons) give opposite volume magnetic contrast. At the top the resulting XMCD image is shown, where the location of the wire surface and shadow are indicated. Adapted from [234].

power supply outlets (with a small resistance) while the polarity is switched [245]. It enables magnetic field pulses of ms duration or longer. The maximum applicable field is limited on the one hand by the current source (12 V compliance) and the heating of the wire (max 0.4 A can be applied for longer times, while up to 1 A could be applied for short pulses), but also by image distortions due to electron deflection by the field [246]. The application of electrical pulses implies a more complex setup. It should be noted that, in the case of PEEM, all the electronics instrumentation (pulse generator, oscilloscope, glass fiber link, etc.) should be at high voltage. We will describe later the setup used for HF pulses.

When imaging three-dimensional nanostructures, such as nanowires or nanotubes, a surface-sensitive technique is not sufficient because the volume magnetization must be probed. For this purpose, shadow XMCD PEEM, a technique pioneered by Kimling *et al.* in 2011 [247], can be used. In contrast to the short depth of the emitted secondary electrons, the X-ray photons have a penetration depth of ≈ 250 nm. Due to the 16° X-ray incident angle, the photons that travel through the sample's cross section, can reach the opposite side of the substrate, creating the nanowire's shadow. Then, the vertically emitted electrons from the shadow reach the detector, carrying the information of the absorption process of the volume crossed by the X-rays. In addition, the shadow width is ≈ 3.6 times larger than the sample's width, enhancing the spatial resolution. In this case, the strongly absorbing areas in the sample, that appear bright in the image, will appear dark in the shadow since they correspond to the weakly transmitted areas (fewer photons reach the substrate). Conversely, weakly absorbing regions will appear dark in the object and bright in the shadow (more photons reach the substrate). A schematic of this is shown in Figure 2.5b, in a nanowire with axial domains and a Bloch-point domain wall (BPW) at its center. Since the X-ray beam is perpendicular to the nanowire axis, no magnetic contrast from the domains is obtained (grey). However, the curling magnetization of the DW gives a bright contrast at the wire's location. If we look into the shadow, the furthest region corresponds to the top of the wire, and therefore a dark (opposite) contrast. At the center of the wire, the azimuthal magnetization contributions are offset, resulting in a grey contrast. Then, the contrast in the shadow coming from the bottom part of the wire should be white. However, it is hidden underneath and can only be observed if the wire is slightly elevated.

We have performed PEEM experiments at the CIRCE beamline [242, 246] at ALBA synchrotron with the beamline and instrument managers MICHAEL FOERSTER, LUCIA ABALLE, SANDRA RUIZ GÓMEZ, WAQAS KHALIQ and MIGUEL ANGEL NIÑO. The nanowires were dispersed on a $10\times10\,\mathrm{mm}^2$ squared N-Ph-doped Si chip with a resistivity of $500\,\Omega\cdot\mathrm{cm}$ to $1000\,\Omega\cdot\mathrm{cm}$. High-resistivity wafers were required to ensure that no electrical short circuit occurred through the substrate, but at the same time, the substrate had to be slightly conductive for PEEM imaging to allow surface charges to dissipate and avoid electrical discharges. Alignment marks of 20 nm Au were created by conventional photolithography using a pre-designed mask. Due to the rather large chip size, this step was crucial not only to identify nanowires for electrical contact, but also to locate a specific wire once it is inside the PEEM chamber. The design used was created by MICHAEL SCHÖBITZ and based on 500 µm long squared grids, where each corner is identified with a letter and a number. The same letter is kept throughout each row, and the same number is kept throughout each column. Inside each grid, different geometrical forms were used to facilitate the identification of the nanowires (see Figure 2.6a). Due to the metallic cap used at the top of the sample, only nanowires dispersed at the center of the wafer could be imaged. This corresponds to nanowires along the *I*09 alignment mark. Therefore, during the electrical contacting process described in Sec. 2.5, four nanowires close to the *I*09 mark and at least 100 nm separated from each other were located by SEM. Then, the SEM images were adjusted to the alignment marks design using *K-layout* software. Afterward, the electric contacts are designed. An example of this procedure is shown in Figure 2.6a, where the *K-layout* design of a $10\times10\,\mathrm{mm}^2$ chip is shown. The alignment marks are displayed in purple. At the center of the image, the gray squares correspond to the SEM images. The electric pads designed are shown in red, green, blue and yellow. Each color corresponds to one nanowire, thus in total up to four nanowires can be contacted per chip. A higher magnification view is shown in Figure 2.6b. Now, the alignment marks can be properly observed, being *I*09 at the center of the image. Note that the pads are as much as possible separated from each other to avoid capacitance effects.

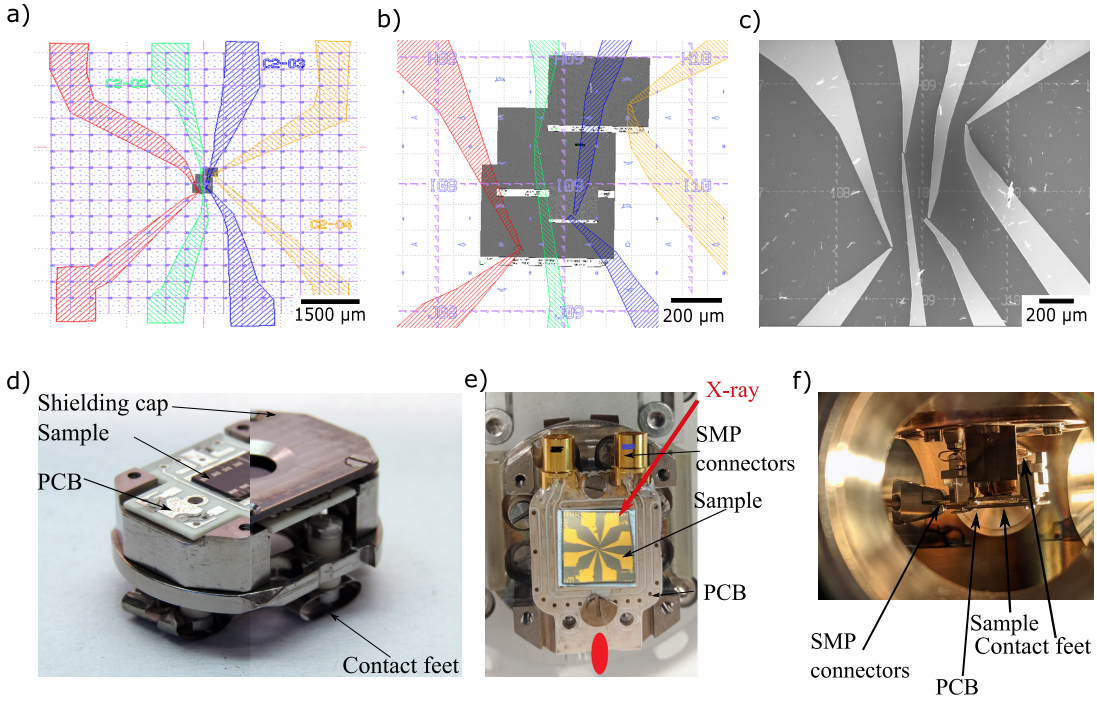

Figure 2.6: **a)** and **b)** Alignment marks and electrical pads designed by *K-layout* to contact four nanowires for PEEM imaging. **c)** SEM image of four electrically-contacted nanowires on a high resistivity Si wafer. **d)** Standard sample cartridge used for PEEM imaging [246]. The life of the PCB is connected to the contact feet by a Cu cable. **e)** Recently developed HF setup allows a PCB with SMP connectors. **f)** The inside view of the PEEM chamber shows SMA cables directly connected to the PCB.

Their profiles are rather smooth, avoiding corners or squared angles, such that HF pulse transmission is as optimum as possible. Figure 2.6c shows a SEM image of four contacted electrically magnetic nanowires prepared for PEEM imaging.

Sample mounting was performed first by gluing the wafer with silver paint onto a dedicated PCB and performing microbonding following the steps detailed in Sec. 2.6. Afterward, it is mounted on the sample cartridge, which may include coils for applying a magnetic field. A Cu cable is used to connect the transmission line of the PCB with the feet of the cartridge. An example of a PEEM sample cartridge is shown in Figure 2.6d, where half of the image shows the shielding metallic cap at the top. This cap is placed a few millimeters above the wafer such that the microbonds do not touch it. An important step is to calibrate the sample tilt using a laser. This can be done by loosening or tightening the screws at the four edges of the cartridge. Also, note that the contact feet should remain parallel to each other. Through them, it is made the electric contact between the electronic devices and the sample. This is the reason why pulse durations are above 10 ns due to the impedance mismatch between vacuum feed-troughs and the sample cartridge. A new HF setup was recently developed by MICHAEL FOERSTER and his team. It is based on a direct SMP connection to the PCB as shown in Figure 2.6e. In this case, sample rotation is not allowed and the X-ray beam has an incident angle of 45° with respect to the SMP connectors (red arrow). Therefore, the nanowire orientation needs to be selected a priori, being ideally transverse to the beam direction such that azimuthal domains are detected. Figure 2.6f shows a view inside the PEEM chamber of the direct connection between the SMA cables and the PCB for this new HF setup. This allows unprecedented transmitted pulse frequency allowing squared pulses of duration below 1 ns. We collaborated with the beamline team in the testing of this new setup on contacted nanowires. However, unfortunately at that early stage of development, we could not image under stable conditions and without electric discharges.

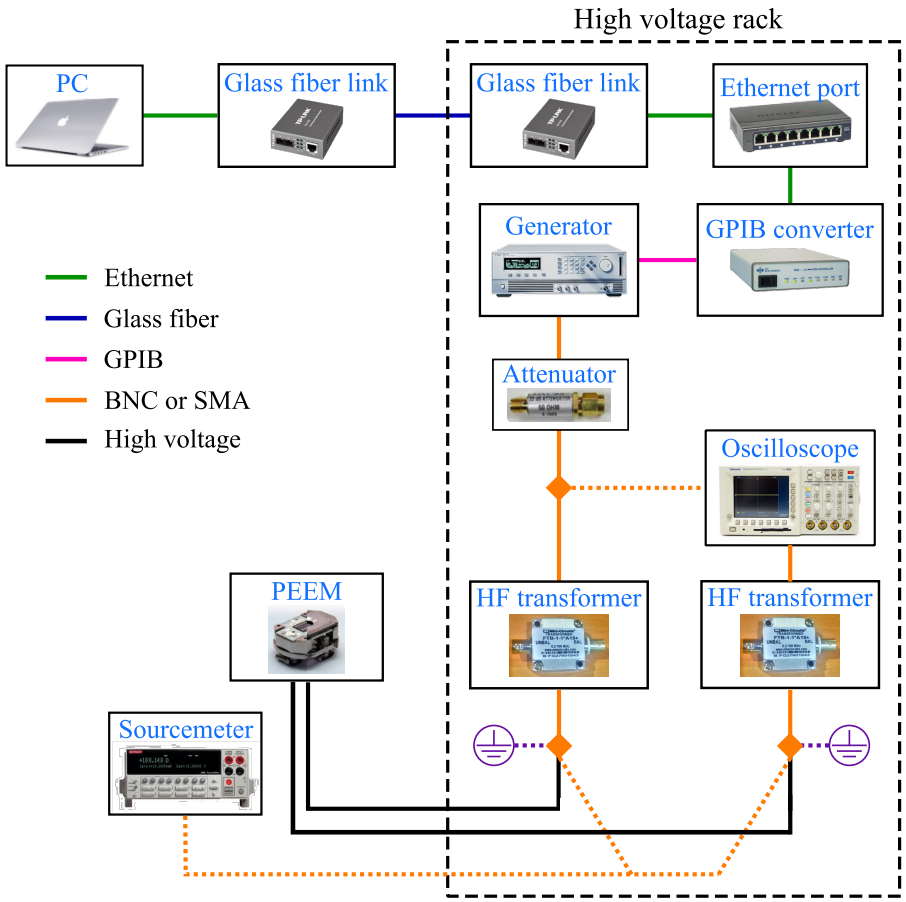

Figure 2.7: Schematic of the PEEM setup for current pulse injection. The electronics are kept inside a high-voltage rack, at the same voltage as the imaging column (10 kV to 20 kV). Outside of it, a computer sends a trigger signal, that is transmitted to the trigger box (GPIB converter) inside the high voltage rack through an optical fiber. The GPIB sends a 5 V signal to trigger the pulse generator. The output pulse goes through an attenuator connected to a T-junction: one end connected to the oscilloscope, coupled to 1 MΩ to measure input and reflected pulses, the other end transmits the pulse through a transformer towards the Au pad in the sample. The transmitted pulse travels from the sample to another channel of the oscilloscope coupled to 50 Ω. When the high voltage is turned off, a connection to a sourcemeter allows measuring the sample resistance. Courtesy of ONDŘEJ NOVOTÝ.

High frequency pulses in PEEM

The HF electronics in PEEM requires a dedicated setup, different from that the one used in conventional imaging techniques where the electronics are at ground potential. In the case of PEEM, imaging is performed under ultra-high vacuum and high voltage conditions, which hampers the application of electric pulses. A strong electrical insulation is provided by keeping all the electronic devices inside a high voltage rack. Therefore, we need to find a way to connect the external world to the high-voltage electronics inside the rack. The schematic of Figure 2.7 shows the setup we used to send clean pulses in a manner such that the electronics and ourselves are protected. The mechanism is the following: a computer sends a trigger signal through an Ethernet cable that is connected to a glass fiber link. The signal output travels through an optical fiber that enters in the high voltage rack, where it reaches another glass fiber link. Then, a signal transformer (GPIB) converts the trigger to an electric signal that triggers the pulse generator. We always use an attenuator at the pulse generator output, which not only attenuates the signal but also protects the device from signal

reflections. After the attenuator, a T-junction is placed, where a SMA cable is connected to one channel of the oscilloscope coupled to 1 MΩ. This channel measures the input and the reflected pulse. The other termination of the T-junction is connected to a HF transformer (MINICIRCUITS FTB-1-1B*A15+), which only transmits frequencies in the range $0.2-500$ MHz and thus blocks high voltage discharges. Then, a T-junction is added to the circuit, one end connected to the sample, the other allowing for the addition of a zero-Ω short-circuit. This is done to protect the sample when mounting the electronics. The pulse reaches the nanowire, and the transmitted pulse travels to the other HF transformer towards another channel in the oscilloscope coupled to 50 MΩ, such that the transmitted pulse can be quantified. The application of current pulses requires setting to zero the high voltage followed by setting also the start voltage to zero. These are safe steps to avoid electric discharges. Afterward, the desired pulse is set, and the voltages are re-set to imaging values, taking special care to increase progressively the voltage values.

2.4.3 Transmission X-ray microscopy

Full-field TXM is also a microscope that allows three-dimensional magnetic imaging. In this case, the optics are very similar to those of a conventional optical microscope. A monochromatic X-ray beam is focused on the sample by a condenser zone plate (CZP). Then, the transmitted photons are collected by an objective Micro zone plate or Fresnel zone plate and a magnified image is delivered to a charge-coupled device (CCD) camera (Figure 2.9a). The field of view (FoV) is determined by the focal spot size. The spatial resolution is ≈ 25 nm. A bending magnet can select circularly left or right polarized light to allow magnetic dichroic measurements. An undulator or bending magnet X-ray source is used, providing the former much higher intensity and better spectral purity [248]. Similar to PEEM, the photon efficiency of TXM is reduced at higher magnifications. Hence, TXM is best suited for investigations requiring a larger field of view at moderate magnifications, like imaging of the evolution of domain patterns at the mesoscale [249].

In this work we performed TXM imaging at the MISTRAL beamline at ALBA synchrotron [250] with the beamline manager LUCIA ABALLE. Prior to the experiment, collaborative work was done to design a setup that would allow current pulse injection, making us the first users to do so. Specifically, tremendous work was done by CHRISTOPHE THIRION to develop a PCB that fits into the reduced TXM chamber and allows HF pulses injection. This is shown in Figure 2.8a, where two SMP connectors are shown at the top . Their core is connected to the transmission line of the co-planar waveguides. A 2 mm diameter hole with a conical shape is placed at the bottom, to place a transparent substrate. A plastic adapter (in grey) is glued, which is later pinned on the sample holder within the chamber . An inside view of the TXM chamber with the electric setup is displayed in Figure 2.8b. The SMA cables come from the top and a T-junction is placed at their termination. One terminal is connected to a zero-Ω short, and the other i connected to the SMP connector of the PCB. This is done to protect the sample from electrical discharges when placing the PCB inside the chamber. Once this is done, the zero-Ω shorts are removed, starting with the one connected to the cable connected to the oscilloscope (ground).

Regarding sample preparation, home-made chips were prepared by AURÉLIEN MASSEBOEUF at NANOFAB cleanroom at INSTITUT NÉEL as detailed in Sec. 2.5.1. These chips are based on a 5×5 mm^2 Si substrate with 100×100 µm^2 Si_3N_4 membranes fabricated at the center. The thickness of these membranes is of 20 nm to allow correlative TEM imaging. Therefore, special care must be taken during their manipulation, especially during spin-coating or pumping events. Figure 2.8c shows a *K-layout* design of a chip with five Si_3N_4 membranes placed at the center. This is done to enhance the chances of having a dispersed nanowire on a membrane and also to be able to contact more than one nanowire per chip. In this case, it is shown in orange the design of two pairs of Au pads. The ones at the top are adapted to the PCB design shown in Figure 2.8a for TXM imaging, whereas the Au pads below are adapted not only for TXM imaging but also for TEM imaging under current pulses. Below, it is shown the corresponding optical image after contacting the two nanowires. It may be noted as well the number of dispersed nanowires throughout the Si substrate.

Image acquisition was performed at the Fe L_3 edge unless otherwise stated, using right or left circularly

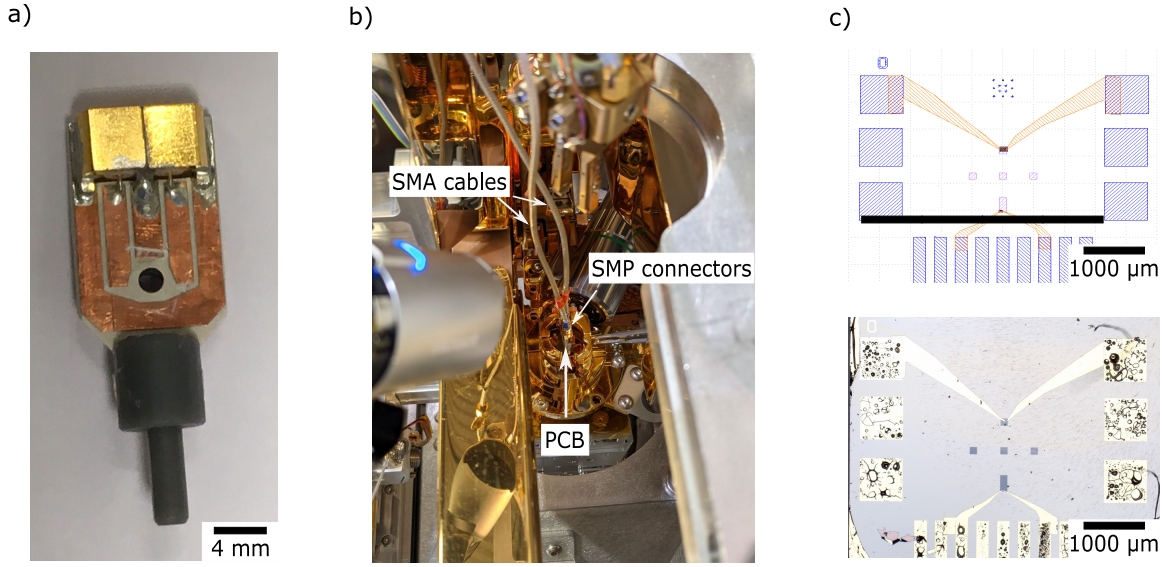

Figure 2.8: **a)** PCB with SMP connectors to fit within the TXM chamber. Developed by CHRISTOPHE THIRION. **b)** Setup used at MISTRAL beamline at ALBA synchrotron for current pulses injection. **c)** Top: Design of electric Au pads for nanowire electrical contacting within a 100 µm long Si_3N_4 membranes of 20 nm thickness. Bottom: optical image of two contacted electrically nanowires.

polarized X-rays, such that the XMCD signal can be calculated. Sample rotation was not possible with the dedicated PCB for pulse injection. It should be noted that the stress produced by the SMA cables tilted the sample $\approx 10°$, resulting in an optimal position to visualize three-dimensional magnetization components. The large field-of-view of ≈ 7 µm allows imaging of a 15 µm long nanowire with two images. Usually, 200 images of 1 s were acquired and averaged, being image acquisition very fast. One importante advantage of this microscopy is that there are no risks of electrical discharges as in PEEM microscopy. This highly facilitated the implementation of HF electronics. In addition, the cabling length is rather short and based on SMA cables, leading to square pulse shapes of > 1 GHz.

2.4.4 Scanning transmission X-ray microscopy

The working principle of STXM is very similar to TXM. The schematics of its optics setup is shown in Figure 2.9b. In this case, a monochromatic X-ray beam is focused on an illumination spot size of several nanometers by a Fresnel zone plate (FZP) [251]. Typically, FZP with 25 or 50 nm outer zone width are used, which focus the beam with a spot size of 31 or 62 nm, respectively, and this determines the spatial resolution. Between the sample and the FZP there is an order separating aperture (OSA) (not shown in the image), which is a pinhole that blocks non-diffracted light transmitted through the FZP, commonly referred to as zero-order light, and higher diffraction orders starting from the second one. For example, a typical distance at 700 eV from OSA to the FZP is ≈ 3 mm and from OSA to the sample is $\approx$700 µm. By using a piezo-controlled nanopositioners, the sample is scanned pixel-by-pixel, and the transmitted photons are recorded by a single point integrating (0-D) detector. One of the most common detectors is a Photomultiplier Tube (PMT), which has a minimum exposure time of ≈ 2 ms.

In this work, we performed STXM imaging at HERMES beamline at SOLEIL synchrotron [252] with RACHID BELKHOU. Home-made chips were fabricated by AURÉLIEN MASSEBOEUF as detailed in Sec. 2.5.1. They consisted of a 5×5 mm^2 Si substrate with a 100 nm thick Si_3N_4 membrane at its center. A customized PCB that allows HF current pulses injection was developed by CHRISTOPHE THIRION, and it is displayed in the top image of Figure 2.11a. In this setup, the SMA cables from the pulse generator

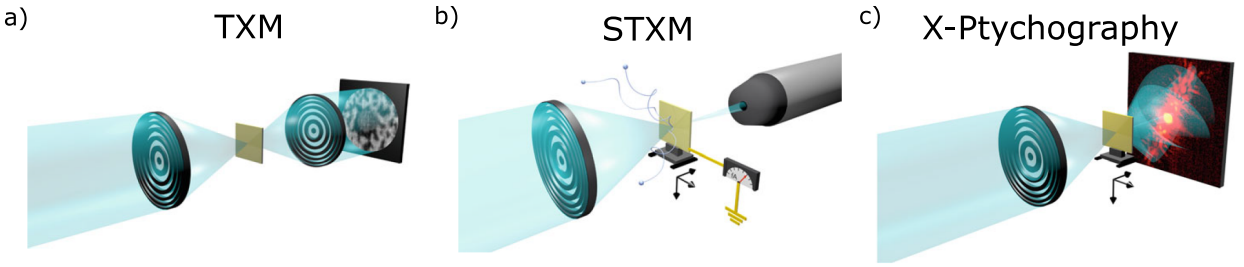

Figure 2.9: Schematic of the optics setup of different X-ray transmission microscopes. **a)** In a TXM, the sample (brown square) is illuminated with a condenser lens, and the transmitted beam is focused on the CCD camera by an objective lens (Fresnel zone plate). **b)** In a STXM, an illumination spot is focused on the sample by the Fresnel zone plate. Between the sample and the Fresnel zone plate an OSA (not shown) is used to eliminate higher diffraction orders of the FZP. The sample is scanned, and the transmitted X-rays are recorded by a point (0-D) detector. **c)** Combination of STXM with CDI gives rise to X-ray ptychography. The X-ray beam is focused on an illumination spot by a FZP. The sample is scanned, and the diffraction patterns are recorded for the different overlapping illumination spots. The complex transmission function is reconstructed by an algorithm. Figure adapted and used with permission from [249].

and oscilloscope come from one side, thus the design of the co-planar waveguides is adapted to this (see Figure 2.11b). Note also that one of the tracks has a very short length, which makes a bit tedious the microbonding. The sample chip corresponds to the black square, where a hole is placed to allow transmission. Furthermore, the designed Au pads at the chip must follow the design of the PCB, which is shown in the inset. For better visualization, the inset is displayed in the image below, which shows a SEM image of a chip with a contacted electrically nanowire. The STXM setup of HERMES beamline is shown in Figure 2.11b, being the top and bottom images the lateral and top view, respectively. The X-ray beam provided by an undulator comes from the left part and an illumination spot is focused on the sample by the FZP. In between, the OSA is placed less than 2 mm away from the sample. Note that the height of the SMP connectors of the PCB are above the OSA. Therefore, a delicate sample mounting should be done so that the OSA is not touched. In addition, note that the PCB is tilted $\approx 10°$ to enable the visualization of the axial domains. In order to maximize this rotation, the nanowire should be lying horizontally, i.e., along the SMP connector axis. The transmitted beam is collected by a phosphor-PMT integrating detector. The chamber pressure was kept at 4×10^{-6} mbar throughout the experiment. The injection of current pulses was performed through the SMA cables connected to the PCB. Special care was taken to avoid vibrations coming from the cables, since this does not allow proper imaging. The images acquisition was done at the Fe L_3 edge. The typical parameters used were a scan area of $2 \times 2\,\mu m^2$ image, an accelerated distance of 0.50 ms, a dwell time of 5 ms, a line delay of 75 ms and 100 points in steps of 20 nm. The acquisition time was ≈ 5 min. Note that the adjusting of the focus is done by a focus scan, i.e., moving the FZP. However, once the focal distance is found the FZP comes back to its original position and it is the sample stage which moves the focal distance.

Time resolved imaging with STXM

Conventional X-ray imaging is done in a static mode, i.e., before and after an external stimulus is applied. However, this does not provide insight into the real time magnetization dynamics, which can be probed only by acquiring images in between. In pump-probe measurements, time resolved imaging is achieved under the excitation of a current pulse, magnetic field or laser pulse [253–258]. The intrinsically pulsed structure of the X-rays generated by the synchrotron [259] allows for pump-probe X-ray imaging. One of the most common microscopies to do so is STXM since it allows the use of a point detector that can temporally resolve the incoming photons. Therefore, if the external signal is phase locked with the frequency of the photon bunches,

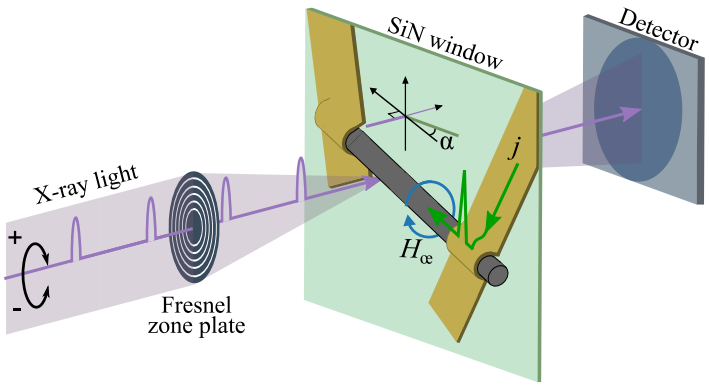

Figure 2.10: Schematic of the STXM setup for time-resolved imaging of a nanowire contacted electrically. In purple, they are sketched the incoming circularly polarized X-ray photon bunches, with an incident angle α to the normal of the SiN window. In green, it is shown the frequency of the applied current pulses, which is phase-locked with the photon bunch frequency. The associated Œrsted field on the nanowire (grey) is displayed in blue. Figure adapted and used with permission from [260].

images of the sample response during the stimulus can be acquired.

In the early days, these measurements required to work in a single-bunch of few-bunches mode, with the period of rotation of electrons in the ring setting the period of the excitation of the sample. A specific acquisition scheme has been developed and implemented at the SLS and BESSY synchrotrons, allowing one to make use of all bunches in normal operation, providing a much higher average flux. In its simplest implementation, it consists of using a period of excitation whose ratio with the period between two bunches is an irreducible ratio of two integers. This way, the phase shift between the excitation and the probe is changed every electron bunch. A low-level electronics allocates the photon count of the photodiode for a given bunch to a registry, selected keeping track of the associated phase shift. In practice, while the STXM remains at a given pixel, the registries progressively build up statistics over the entire time frame of the excitation period. The time step and number of points depends on the irreducible fraction of the two periods, ring versus excitation. The typical acquisition time per pixel to get a decent TR-series is about 100 ms. This acquisition scheme implies that magnetization dynamics have to be reproducible many millions of times. With this, the initial and final states must be the same in each series, which limits the type of processes that can be imaged with time-resolved techniques. Spin waves are textbook examples suitable for this scheme, as they can be periodic, and related to a periodic excitation. To the contrary, many processes such as domain-wall or skyrmion motion cannot be investigated due to stochasticity, making them different for each excitation period.

The sequence of images is obtained for a chosen polarization of light (i.e., left or right), thus, the time-resolved series of images is not a direct XMCD image series. Instead, it is a differential XAS contrast with sensitivity to magnetization related to the magnetization-dependence of the X-ray absorption. To evidence the magnetic contribution, the series of XAS images is divided by the average of all the XAS frames in the series. A schematic of the setup is displayed in Figure 2.10, where the circularly polarized X-ray beam and its frequency are shown in purple. The SiN window (green) is usually perpendicular to the X-ray beam, but can be rotated at an angle α to visualize also the axial components. Current pulses of a certain frequency are sent through the nanowire (green), which generate an associated Œrsted field (blue).

In this work, time-resolved experiments were performed at MAXYMUS beamline [261] at BESSY II synchrotron with the beamline and instrument managers SEBASTIAN WINTZ and MARKUS WEIGAND. The RF-pump-probe setup allows imaging with time resolutions $<$100 ps and spatial resolutions $<$30 nm. The sample preparation was the same as the one described above for STXM imaging. My contribution was the synthesis of the samples and their electrical contacting, but I was unable to attend the beamtime as it

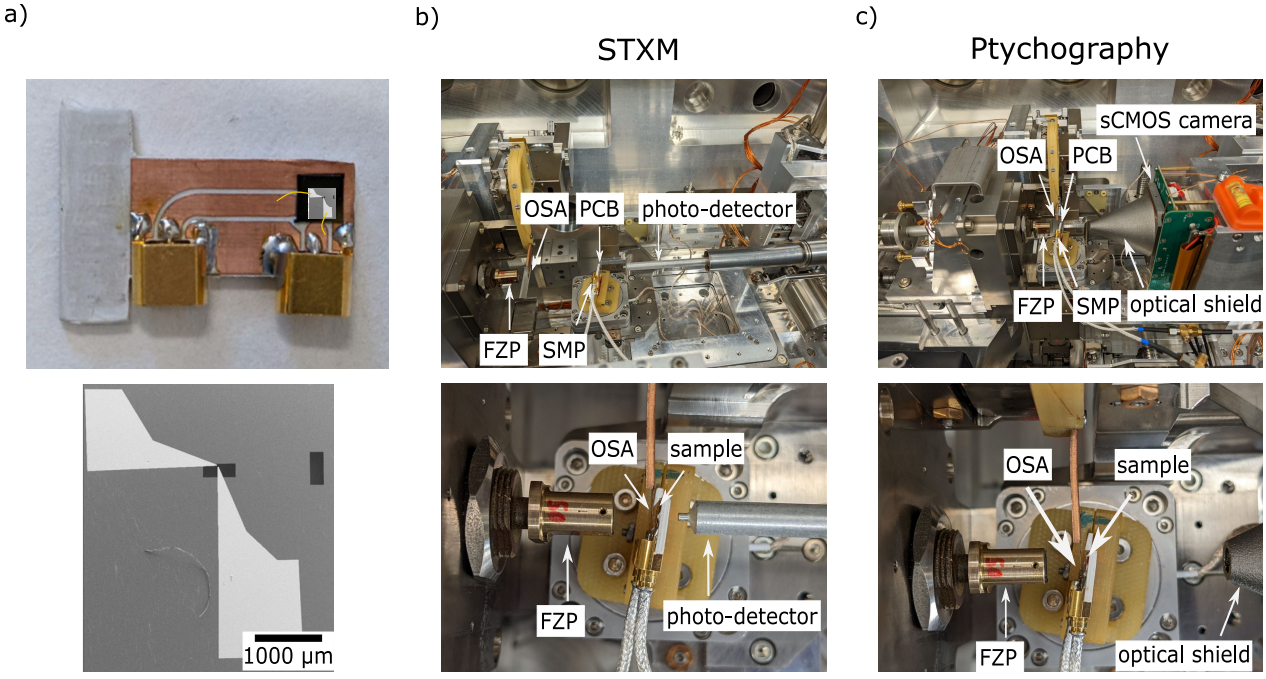

Figure 2.11: Setup used at HERMES beamline at SOLEIL synchrotron for current pulse injection. **a)** Top: Customized PCB with a co-planar waveguide design and SMP connectors. Microbonds are sketched in yellow. The inset image at the sample's position, is shown at the bottom for better visualization. Bottom: SEM image of the customized Au pads adjusted to the co-planar waveguide of the PCB. **b)** Top and bottom images show lateral and top view of the experimental setup for STXM imaging. **c)** Top and bottom images show lateral and top view of the experimental setup for X-ray ptychography imaging.

took place during the last stage of the writing period of this manuscript. Therefore, the measurements were performed by OLIVIER FRUCHART and AURÉLIEN MASSEBOEUF. Image series were taken, each spaced by 200 ps, 100 ps or 50 ps. A single point time-resolved acquisition took $\approx$ 100 ms, which results in $\approx$ 30 min per series.

2.4.5 X-ray ptychography

The just discussed microscopies for three-dimensional X-ray magnetic imaging (PEEM, TXM and STXM) have been used extensively during the last decades. A common feature among all of them is that their spatial resolution is $\approx$ 25 nm to 50 nm, being limited by the optics. Therefore, to overcome this limitation, a lensless imaging technique should be used. The most well-known lensless technique is electron holography, which solves the phase problem by a single and non-iterative Fourier transform of the hologram. However, in the case of X-ray holography, some difficulties arise from the fact that a stable reference wave is needed. This can be achieved either by patterning a hole in a thick Au mask [262] or by using a small gold sphere as a reference wave source [263]. However, in this case, the spatial resolution is limited by the size of the scattering source. Therefore, an alternative route is to use CDI, that not only evaluates the transmitted photon intensity but also the scattered photons [264]. The scanning form of CDI is known as X-ray ptychography, which can be described as the non-holographic solution to the phase problem [265]. This concept was proposed in the 70s by Hoppe and first demonstrated in transmission microscopy [266]. It is well-coupled with the brilliance and coherence of synchrotron sources, whose application to the X-ray regime [267] is reviewed in [268].

For the case of standard CDI in crystals, there is just one illumination spot and, therefore, a unique

diffraction pattern. The diffraction peaks that contain phase information are convolved with the Fourier transform of the illumination function. However, the non-zero intensity between the peaks makes very challenging the retrieval of the phase due to the ill-posed nature of the problem. Here is where the key ingredient of ptychography comes in: the overlapping illumination spots. The combination of oversampling in the detector space and overlapping illumination on the object makes the reconstruction algorithms very robust [269, 270]. Ptychogram sampling in real space can be done with step sizes much larger than the resolution, as long as the illuminated regions have sufficient overlap [271]. The spatial resolution is not limited by the size of the illumination spot, but instead, by the highest scattering angle measured.

As the intensity of the scattered light is decreasing with the angle, the resolution is mostly affected by the signal-to-noise ratio of the 2D detector used, as well as the sample scattering power. Therefore, the morphology of the sample affects the resolution. A well-crystallized sample will scatter more than an amorphous one. A too-thick sample will absorb its own scattered light, and a too-thin one will not interact enough with the light to scatter, both resulting in a loss of resolution. We found that a curved three-dimensional object, such as the nanowires explored in this work, shows a largely increased resolution compared to a 2D film. The phase-retrieval procedure also decouples the contributions of the object and the probe, thereby enabling each to be separately reconstructed. Another quality of ptychography is that the sample does not need to be at the focus of the FZP since the focal distance is an input in the reconstruction code. This allows an increase in the spot size to reduce the radiation dose to the sample and carbon contamination and to reduce the number of diffraction images. Another quality is the contrast enhancement compared to STXM. It comes from the fact that more light is acquired thanks to the 2D detector as well as the reconstruction procedure itself, which makes use of oversampling and removes noise in the final images. Figure 2.9c shows the schematics of the setup used for ptychographic imaging, where overlapping diffraction patterns are displayed on the camera.

We performed X-ray ptychography imaging at HERMES beamline at SOLEIL synchrotron [252] with the beamline and instrument managers RACHID BELKHOU and NICOLAS MILLE. The experimental setup used was the above described for STXM but using an imaging scientific complementary metal oxide semiconductor (sCMOS) camera instead of a photo-detector. The lateral and top views of the ptychographic setup are shown in Figure 2.11c. Note also that a conical optical shield in Titanium is used to let only the light emitted from the sample to reach the detector and block light coming from other parts of the chamber. This shield is normally as close as possible to the sample, the picture here is taken before the last approach. A combination of both imaging techniques is possible due to the short pumping periods (below 10 min) and fast changes of the detectors. Therefore, it is highly recommended to start imaging in STXM mode due to its larger acquisition rate. Once the sample is found, preliminary XMCD images can be acquired by STXM, even under current pulse stimulus, just to test the behavior of the sample, thus saving a considerable amount of time. After this, one can move to X-ray ptychography mode to obtain high-resolution images. In addition, while being in ptychographic mode, before reconstructing an image we can obtain its STXM-like image by numerically integrating the camera data at each scanning position. The first beamtime on magnetic X-ray ptychography at HERMES was done in December 2020, being us the first users to use this technique in this beamline.

The sCMOS camera used was a Tucsen Dhyana 95, whose characteristics are described elsewhere [272–274]. It has a pixel size of 11 µm and a minimum exposure time of 40 ms, which is 20 times longer than the photo-detector used for STXM. A water cooling system for the camera is installed so that the camera is at -20 °C. The chamber pressure was kept at 1×10^{-4} mbar throughout the experiment, also to ensure no condensation in the camera. Ptychographic reconstruction was carried out using the open-source PyNX software [275] developed at the European Synchrotron Radiation Facility. The acquisition time of a $2 \times 2\,\mu m^2$ image took ≈ 15 min and its reconstruction ≈ 20 min. However, the PyNX code is under constant development to reduce reconstruction times, such as by implementing distribution over multiple graphical processing units. The size of one XMCD ptychographic dataset is ≈ 10 GB. The reconstruction gives as a final output four images, the illumination amplitude and phase and the transmitted light amplitude and phase, the whole weighting ≈ 1 MB. A final XMCD image is the subtraction of two transmitted amplitudes and weights $\approx$

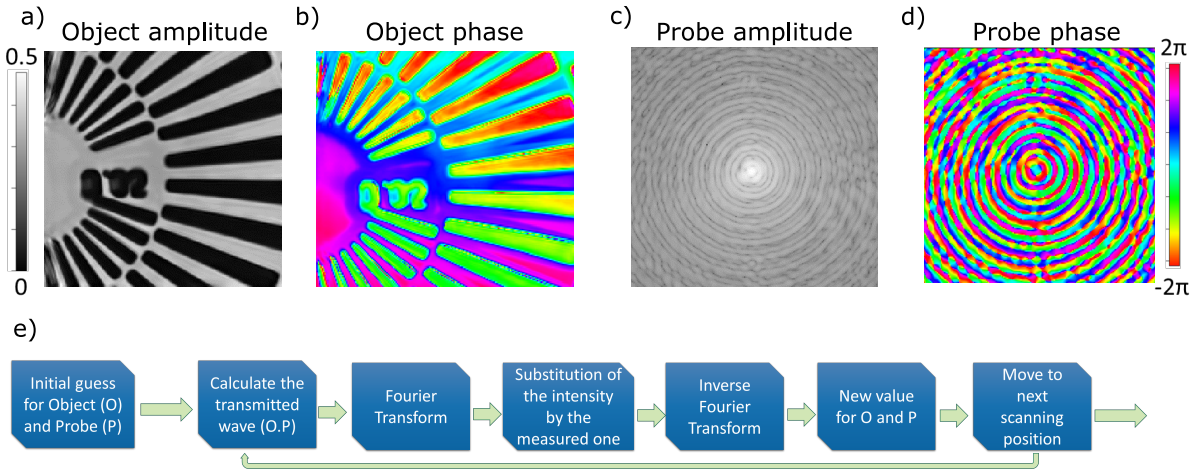

Figure 2.12: Example of a ptychographic reconstructed dataset at 700 eV of a lithographed gold pattern. The size of the images are $2\times2\,\mu m^2$. **a)** and **b)** display reconstructed object amplitude and phase. **c)** and **d)** display reconstructed probe amplitude and phase. **e)** Summary of the steps involved in the algorithm reconstruction code. Courtesy of NICOLAS MILLE.

250 KB.

The full complex transmission function is retrieved using an algorithmic reconstruction code. Its working principle can be summarized as follows: (i) a transmitted ($O(\mathbf{r})$) and an illumination ($P(\mathbf{r})$) function are initialized at a scanning position $\mathbf{r}$, based on a 2D complex matrix named Object ($O(\mathbf{r})$) and Probe ($P(\mathbf{r})$), respectively. Most of the time random numbers are sufficient. (ii) Calculation of the transmitted wave ($W(\mathbf{r}) = O(\mathbf{r})P(\mathbf{r})$), for a Probe at a defined scanning position. (iii) The recorded diffraction pattern is proportional to the absolute value of the Fourier transform of the transmitted wave $FT(W(\mathbf{r}))$, i.e., the wavefield coming from the sample to the detector. This gives a complex 2D matrix with an amplitude and a phase. The camera intensity measurement is indeed $FT(W(\mathbf{r}))FT(W(\mathbf{r}))^*$, where * is the complex conjugate. This signal measured by the detector contains only intensity information. (iv) Substitution of the $FT(W(\mathbf{r}))$ amplitude by the square root of the intensity measured by the camera at this scanning position. (v) Inverse Fourier Transform, which gives an updated complex transmitted wave W'. (vi) Calculation of new values for the complex Object, based on the equation in (ii) $W(\mathbf{r}) = O(\mathbf{r})P(\mathbf{r}) \rightarrow O(\mathbf{r}) = P(\mathbf{r})^* W(\mathbf{r})$. So we use $O_{j+1}(\mathbf{r}) = O_j(\mathbf{r}) + k(P_j^*(\mathbf{r})W_j'(\mathbf{r}) - P_j^*(\mathbf{r})W_j(\mathbf{r}))$ with k being a parameter defining the amount of correction taken into account for each iteration, and j is a number of diffraction pattern. The complex Probe can be calculated the same way, as P and O are interchangeable in the formula in (ii). (vii) Return to (ii) for the next scanning position and repeat steps (ii) to (vi). The output is now an Object and a Probe function updated for each illumination position, this is one iteration. (viii) Redo from (ii) to (vi), a fix iteration number, calculation of the error and check of convergence. Different algorithms are most of the time differentiated by the way they fulfill step (viii). More information on this can be found in [275]. An example is given in Figure 2.12. It shows the output of the reconstruction of a ptychographic dataset acquired at 700 eV on a Siemens Star, a lithographed gold pattern. The size of the images is $2\times2\,\mu m^2$. The separation between two branches of the smallest part of the star is less than 10 nm and can be distinguished despite the illumination spot size being 61 nm. Figure 2.12a and Figure 2.12b, display the reconstructed object amplitude and phase. Figure 2.12c and Figure 2.12d, display reconstructed probe amplitude and phase. Please, see [268, 276] for more details on this. A summary of the reconstruction code is sketched in Figure 2.12e.

2.5 Electrical contacting of nanowires

Since most of the experiments in this thesis were based on injecting electrical current into nanowires, the electrical contacting of nanowires has been a crucial step. The process is based on a multi-step photolithography routine that was initially developed by SYLVAIN MARTIN and optimized by MICHAEL SCHÖBITZ. In the following, the different steps involved in the process will be detailed, as well as the new steps that were optimized during this work. The starting point is always an ethanol solution with thousands of nanowires, and the final point is an individual nanowire contacted electrically. I carried out all the involved steps at the Nanofab cleamroom at INSTITUT NÈEL.

2.5.1 Nanowires dispersion on a customized substrate

One key aspect of a successful contacting process is to adjust it to the imaging setup that will be used for the current-induced experiments. The reason is that each experiment has specific requirements or limitations that cannot be overcome at the moment of imaging. Therefore, thinking ahead of the future experimental needs avoids future limitations. In the sections above, within the description of each microscopy, we have detailed the experimental setup, sample holders, PCB, substrate, alignment marks and electric pads design customized for each of the techniques. To sum it up briefly, regarding PEEM imaging, the substrate must be slightly conductive to overcome the risk of electric discharges. Due to the space allowed on the PCB with a co-planar waveguide design, we used a $10\times10\,\mathrm{mm}^2$ squared N-Ph-doped Si chips with a resistivity from $500\,\Omega\cdot\mathrm{cm}$ to $1000\,\Omega\cdot\mathrm{cm}$. In Figure 2.6, we showed the customized contacting of four nanowires within a square of $1\times1\,\mathrm{mm}^2$ at the center of the substrate, due to the metallic cap limitation. The substrate used for transmission experiments is based on a Si chip of $5\times5\,\mathrm{mm}^2$ at maximum with at least one 20 nm thick Si_3N_4 membrane at its center, with a window size of $100\times100\,\mu\mathrm{m}^2$. The fabrication steps of these chips are detailed below. To facilitate the manipulation of these chips, a wafer containing several of them was used and then cleaved after the contacting. Therefore, the dispersion of nanowires was usually done onto a large wafer of $2\times2\,\mathrm{cm}^2$. More details of the PCB and substrate design are shown in Figure 2.8 for TXM and in Figure 2.11 for STXM and X-ray ptychography.

An important parameter to consider is the size of the chip where the wires are going to be dispersed. This is because the concentration of nanowires suspended within an Eppendorf filled with $\approx 100\,\mu\mathrm{L}$ of pure ethanol should be adjusted to the size of the chip. Therefore, to fix the proper concentration, it is recommended to do several tries on a dummy chip of the same size. To do so, a magnet is placed below the chip such that the nanowires will be aligned along a specific direction. Then, the nanowire concentration is mixed up with the help of a pipette, such that a homogeneous light grey color is obtained. This is followed by dropping $10\,\mu\mathrm{L}$ on the center of the substrate that spreads to the corners. Special care should be taken during the evaporation of the ethanol. Most of the time, it takes place in a homogeneous manner. However, if a few small drops remain, they will attract the nanowires towards them, creating regions with too high density of nanowires. This is solved by drying with a nitrogen gun from the center to the substrate edges. For the case of chips with a transparent Si_3N_4 membrane, this drying step should be avoided to not destroy the window. These types of chips are the hardest for dispersion, since the nanowires should lay within the $100\times100\,\mu\mathrm{m}^2$ window. Therefore, the concentration of nanowires should be higher, and dispersion may be repeated several times until one nanowire is within the window. For the case of PEEM, several wires should lay within $1\times1\,\mathrm{mm}^2$ at the center of the substrate. To achieve a complete drying of the substrate, a drying time of at least 5 min was set. Then, the substrates were immersed in a baker with pure ethanol to clean them from residual pieces coming from the dispersion. This step is also very important since it optimizes the subsequent spin coating.

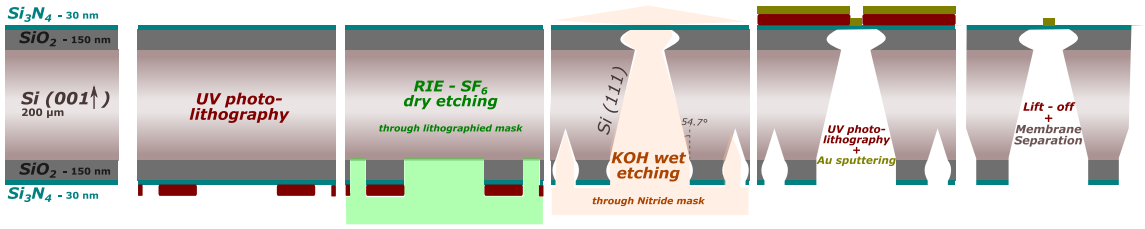

Figure 2.13: Schematic of the steps involved in the nanofabrication of transparent Si_3N_4 membranes. Courtesy of AURÉLIEN MASSEBOEUF.

Membrane fabrication

The transparent Si_3N_4 membranes used in this work were nano-fabricated at NANOFAB cleanroom by AURÉLIEN MASSEBOEUF. The different steps involved in the process are sketched in Figure 2.13. Starting from a double-side polished thin Silicon wafer (001) with thermal SiO_2 (150 nm) and low pressure chemical vapor deposition (LPCVP) nitride (30 nm), openings are designed in the nitride (conventional lithography with reactive-ion etching (RIE)) on the backside that serves as a mask for the wet etching (KOH at 80 °C). These openings are designed according to the wafer thickness (200 µm) and the (111) plane orientation that is too dense for the etching, giving rise to such a pyramidal shape. The resulting membranes (typical size $100\times100\,\mu m^2$) are thus both X-ray and electron transparent and enable further processing according to the flat surface. For STXM experiments a membrane thickness of 100 nm was used, whereas for TEM, TXM and X-ray ptychography a 20 nm thickness was used.

2.5.2 Photolitography

Once the dispersion is done, the next step is to acquire low and high magnification images of the nanowires to design the electric pads with *K-layout* software. If time is short or we are confident that all the nanowires are defect-free, we can image them by optical microscopy. However, it is better recommended to check them with SEM since the sample quality is crucial for future X-ray imaging. By SEM we can check the diameter and length, the surface smoothness, the lack of branches or diameter modulations as well as the surface cleanliness. All of this is important to have reproducible physics between all the samples. The SEM images of the chosen nanowires were uploaded in *K-Layout* and aligned with the alignment marks of the substrate or the transparent membrane corners. A correct scaling and alignment were done by using two landmarks. The design of the contacts was adjusted to the X-ray imaging setup as described in the previous sections. Some considerations must be taken to allow HF pulses. First, the pads should be as symmetric as possible, avoiding having parallel pads for possible capacitance effects. The size of the pad should increase linearly as we move further from the nanowire. Usually, a pad width of 10 µm was set at the nanowires location, and the final width was of 1000 µm to allow enough space for microbonding (see bottom image in Figure 2.11a). Curved contacts or 90° angles should be avoided, to limit impedance mismatches. Then, if several wires are contacted within the same chip, the contacts should be as far as possible from each other. Usually, a nanowire length of $\approx 20\,\mu m$ was contacted, which is a good compromise between X-ray imaging acquisition times and sufficient length to study DW dynamics.

Just before the lithography, a UV-light photoresist layer of LOR-3A was spin coated on a chip at 6000 rpm, with an acceleration of 4000 rpm/s for 30 s and then cured at 200 °C for 60 s. This was followed by a second spin coated UV-light photoresist layer of S1818 at 6000 rpm, with an acceleration of 4000 rpm/s for 30 s and then cured at 115 °C for 60 s (Figure 2.14c). Special care must be taken to not place the Si_3N_4 membrane on the pump hole. Afterwards, the photolithography was carried out using a HEIDELBERG

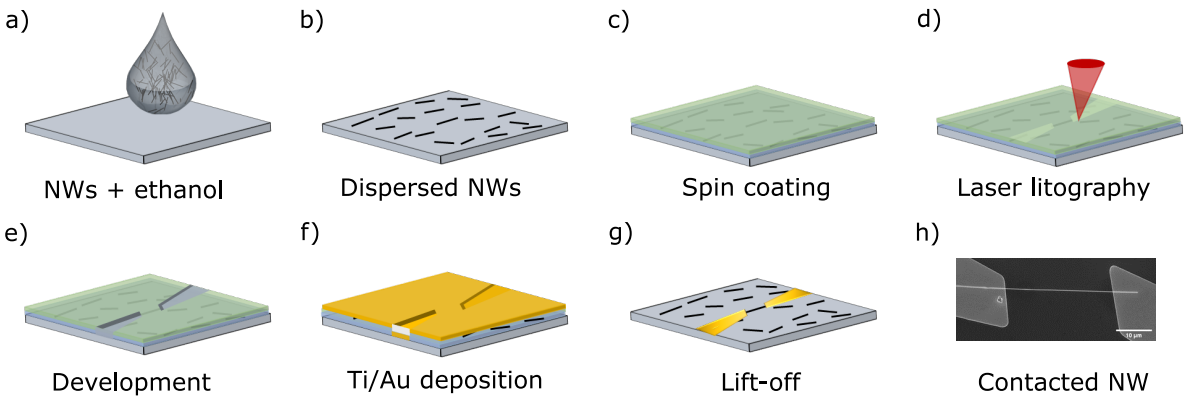

Figure 2.14: Schematics of the steps for the electrical contacting of nanowires. **a)** and **b)** Dispersion of nanowires onto a customized substrate. **c)** Spin coating of LOR-34 and S1818 resists. **d** Laser litography of electric pads on a chosen nanowire. **e)** Resist development in MF26-A. **f)** Ti/Au deposition. **g)** Lift-off in Remover PG. **h)** SEM image of an electrically-contacted cylindrical nanowire of 120 nm diameter.

DWL66FS which has an integrated camera to perform sample alignments before exposure and has a maximum resolution of 500 nm. To optimize the calibration, the origin of the lithography was set at a position close to the nanowire and thus one lithography was performed per nanowire. This makes the process quite long but with the advantage of a good calibration (Figure 2.14d). Afterward, the lithography was checked in the optical microscope using the orange light filter. If it was successful, the resist was developed in MF26-A for 35 s, to remove the lithographed resist (Figure 2.14e).

The deposition of metal was carried out in a PLASSYS MEB 550 metal evaporator, which uses an electron gun to heat a metal target. Before the metal evaporation, it is crucial to etch the native-oxide layer on the sample surface. If this is not done, an ohmic metallic contact will not be achieved. Therefore, Ar etching at 400 V for 60 s was performed. Then, without extracting the sample from the vacuum chamber, 10 nm of Ti was sputtered at a rate of 0.25 nm/s, and 150 nm of Au was sputtered at a rate of 0.50 nm/s (Figure 2.14f). The lift off was done in Remover PG at 80 °C for at least 2 h (Figure 2.14g). Ideally, the lift-off is left during more than 12 h to enhance the removal of the Au. If the Au is not removed, we activate it by creating bubbles with a pipette. However, this should be done carefully, specially with Si_3N_4 membranes, since this step comes with a high risk of membrane destruction or nanowire explosion. Figure 2.14h shows a SEM image of an electrically-contacted nanowire of 120 nm of diameter.

2.5.3 Heating management

The last step performed consisted of a 20 nm ALD alumina coating of the chip with contacted nanowires. This step enhances the thermal path to dissipate heat during the electric stimulus, reducing Joule heating in the sample. In addition, the samples are protected from degradation and oxidation. However, note that this step does not allow high-resolution electron holography. For PEEM imaging, this process must be accompanied with ion beam etching (IBE) etching of the alumina on the top of the wire, leaving only the alumina below the wire in contact with the Si substrate. Another important step for heat management in the Si_3N_4 membranes is to deposit 100 nm of Al on the backside of the membrane.

2.6 High frequency electronics

Once a nanowire is contacted electrically, the first check to do is to measure its resistance to validate the electrical contact and disregard possible shorts or high resistances. Then, we need to create an electric circuit in which all the instrumentation is coupled to 50 Ω (coaxial cables, oscilloscope, pulse generator, attenuators) to reduce signal reflections. However, even though the experimental setup is adapted at its best for a 50 Ω impedance, the design of the co-planar waveguides on the PCB is constrained by the microscope limitations. In addition, the Au electric pads are designed also for HF electronics, but experimental limitations bring also sources of reflection. Lastly and most importantly, the sample resistance is far from a 50 Ω coupling. In our case, we obtained resistances in the range of 150 Ω to 500 Ω, corresponding the smaller values to shorter contacted lengths. These values are very optimal for HF electronics since previous reports showed resistances above 1000 Ω. A change in resistance in the circuit will imply a change in the current since the voltage at the pulse generator remains constant. This is because the pulse generator, which has an internal resistance of 50 Ω is set to be coupled to something that is also 50 Ω, thus as an output, it will supply double the asked voltage.

The following section, details the different considerations to take into account when injecting electric current through a nanowire. This includes sample resistivity measurements, microbonding, protection from discharges, connection to a HF electronic circuit and measurement of the transmitted pulse.

2.6.1 Nanowire resistivity

The calculation of the nanowire resistivity is first done by measuring its resistance. The fastest way to do this, if the sample is not microbonded, is by using a point-probe setup connected to a sourcemeter. In this work, a KEITHLEY 2400 sourcemeter was used. The first step is to adjust the source-meter parameters. In our case, we set a compliance voltage of 40 mV, and pre-select measure "voltage" and source "current". Then, it is important to set the device "ON" before connecting it to the sample. Two BNC cables connect the "live" and ground of the sourcemeter to a tungsten needle of the point-probe. A grounding bracelet connected to the setup must be worn. To avoid electric discharges, the first contact of the needle with the sample is done on the Si substrate and not on the Au pad. Then, first, the needle that is connected to the ground of the sourcemeter is placed carefully on an Au pad, followed by the second needle. Next, the current in the source-meter is set to 10 µA and the resulting voltage is noted, and the current is then re-set to zero. Then, the needle connected to the live is removed followed by the one connected to the ground. The resulting voltage should be in the mV range to get a resistance of hundreds of Ω. Low resistance values indicate the presence of a short circuit, whereas very high resistance $> 20\,\mathrm{k}\Omega$ indicate that current is flowing through the Si substrate underneath the Au pad. The resistivity was calculated following $\rho = RA/L$, where R, A and L are the sample resistance, cross-sectional area and length, respectively. We obtained homogeneity in the resistivity values of $20\,\mu\Omega\cdot\mathrm{cm}$, in comparison with $15\,\mu\Omega\cdot\mathrm{cm}$ for bulk Permalloy.

2.6.2 Microbonding

The electrical connection between the transmission line of the co-planar waveguide of the PCB and the Au pads is done by doing a microbond between them. However, special attention should be taken to do so. Firstly, a security bond is done between the Au pads of the contacted nanowire- This is to short the circuit and protect the sample from discharges. Then, another security microbond is done between the live tracks of the co-planar waveguides. Lastly, at least two microbonds are done from the live of the tracks to the Au pads. These microbonds should be as short as possible and of the same length. A grounding bracelet connected to the microbonding machine should be worn.

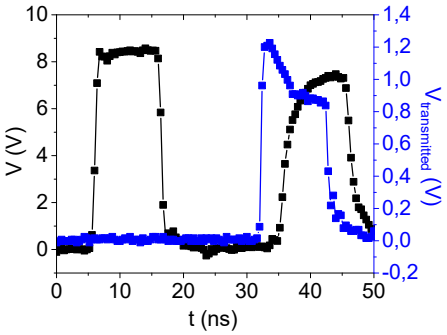

Figure 2.15: Characterization of a 10 ns current pulse through a nanowire of $d = 135\,\text{nm}$, $length = 17\,\text{um}$, resistance $R = 282\,\Omega$ and resistivity $\rho = 23\,\mu\Omega\cdot\text{cm}$. The black curve shows an output voltage of $V_{\text{output}} = 8.5\,\text{V}$ and reflected voltage $V_{\text{reflected}} = 6.25\,\text{V}$. The blue curve shows a transmitted voltage of $V_{\text{transmitted}} = 1.25\,\text{V}$. Adapted from [142].

2.6.3 Connecting a nanowire to an electric circuit

Once microbonding has been done on the PCB, we are ready to close the circuit by connecting the sample to the electronics. This procedure should be done carefully to avoid electric discharges, either induced by the electronics or from the static electrostatic discharges from our hands. Therefore, a grounding bracelet needs to be worn during the whole process. In addition, when manipulating the chip with tweezers, we should avoid touching the Au pads. Since the discharges follow the path of least resistance, the security microbonds should protect the wire. First of all, we prepare two SMA cables with a T-junction, which has a zero-Ω short in one termination. This was shown in Figure 2.3b for the case of MFM imaging. The next step is to connect the SMA cables to the SMP connectors of the PCB. Then, we proceed to turn on the electronics (pulse generator and oscilloscope). One SMA cable from the PCB is connected to a channel of the oscilloscope coupled to 50 Ω, to measure transmitted pulse. Then, after the pulse generator an attenuator is placed, for device protection from reflections, and to it a T-junction. A SMA cable is connected from one terminal of the T-junction, that ends in one channel of the oscilloscope. This is done to measure the input current so the channel is coupled to 1 MΩ. However, if the sample resistance is of several kΩ, signal reflections may be a problem. Therefore, in this case, using a power splitter to measure the input pulse may be a better solution. The other termination of the T-junction is connected to the SMA cable, that has been already connected to the PCB. Once everything is connected, we may remove the security bonds with the tweezers. Lastly, the zero-Ω short of the SMA cable connected to the oscilloscope is removed, followed by the zero-Ω short in the SMA connected to the pulse generator. Now we have a closed electric circuit.

2.6.4 Measurement of transmitted current

In order to calculate the transmitted current that flowed through the nanowire, it is important to consider several aspects. First, when applying HF pulses to a setup that is not fully coupled to 50 Ω, signal reflections play an important role. In addition, the signal is attenuated throughout its path. Therefore, the transmission, t, and attenuation, β, coefficients need to be calculated from the output voltage from the pulse generator V_{output}, the reflected voltage from the sample $V_{\text{reflected}}$ and the transmitted voltage through the sample $V_{\text{transmitted}}$. These coefficients are described as:

$$t = \frac{V_{\text{transmitted}}}{V_{\text{transmitted}} + V_{\text{reflected}}} \tag{2.7}$$

$$\beta = \frac{V_{\text{transmitted}} + V_{\text{reflected}}}{V_{\text{output}}} \tag{2.8}$$

As an example, Figure 2.15 shows the voltage evolution over time for a 10 ns pulse with $V_{\text{output}} = 8.5\,\text{V}$, $V_{\text{reflected}} = 6.25\,\text{V}$ and $V_{\text{transmitted}} = 1.25\,\text{V}$, which results in $t = 0.17$ and $\beta = 0.88$. The decrease and increase over time in the transmitted and reflected signal is due to the increase of temperature due to Joule heating that changes the electrical resistance of the wire. We consider that the dynamics of our events happens within the first nanoseconds and we always consider the maximum transmitted signal accordingly. This nanowire had the following properties $d = 135\,\text{nm}$, $length = 17\,\text{um}$, resistance $R = 282\,\Omega$ and resistivity $\rho = 23\,\mu\Omega\cdot\text{cm}$. The associated current density is $j = V_{\text{transmitted}}/(\sqrt{\beta}\times A\times R_{\text{osciloscope}}) = 1.25\,\text{V}/(0.94\times 14314\,\text{nm}^2\times 50\,\Omega) = 1.86\times 10^{12}\,\text{A}/\text{m}^2$. It is important to take into account that the value of β strongly depends on the setup used for each experiment ($\beta = 0.30$ for the PEEM setup used in this work) and its is crucial to consider the appropriate value for the calculation of the real current density.

2.7 Micromagnetic simulations

In this work, micromagnetic simulations were performed to study the equilibrium states of the magnetic textures as well as their dynamics under an external field or an Œrsted field. To do so, two micromagnetic codes were used: the *mumax3* and the *FeeLLGood* code. Both of them are based on the integration of the Landau-Lifshitz-Gilbert (LLG) equation on a discrete space and time. Their difference lies in the way they discretize the space. Two of the most used methods of space discretization are the finite differences and the finite elements methods. The finite differences method is based on a direct approximation of the differential operators using Taylor series expansions. It usually uses prismatic meshes, which makes it easy to implement and it has a very fast computing power. This is the case of the open free *mumax3* micromagnetic code [277]. However, when the system of study is a curvilinear system, the prismatic mesh introduces an artificial symmetry and surface roughness in the system. This can be partially solved by using a cell size below 2 nm, and/or performing extrapolation to zero cell size from a series of simulations. Another option is to use finite elements methods, which discretize the system usually into polyhedrons, which allow to better discretize curved geometries. The home-made software *FeeLLGood* [278] (Finite element Landau-Lifshitz-Gilbert object oriented development), which uses tetra-hedrons to discretize the system, was also used during this work to simulate cylindrical nanowires.

The reason for using two different micromagnetic codes was to exploit the resources at hand. Whereas *mumax3* code allows to model nanowires of several microns long, *FeeLLGood* is more suitable to model in detail systems of reduced length. Also, in the recent years dedicated post-scripts were developed by former members in the group that only work with *FeeLLGood* outputs. These codes are very powerful and allow to go one step beyond conventional simulations. These include: extraction of the magnetization components over the cylinder surface, extraction of the maximum or minimum magnetization components to calculate current thresholds, unrolled surfaces visualization, detection of magnetic singularities [Bloch Point (BP), vortex, antivortex...] etc. Therefore, we found the most convenient to combine the benefits that both micromagnetic codes provide.

Chapter 3

Synthesis and material optimization and characterization

Cylindrical magnetic nanowires are an excellent system to explore different magnetization phenomena. The degree of freedom gained by their three-dimensional nature allows for specific topologies of magnetization textures, closely linked to flux-closure driving force, and curvature-induced effects. Among others, this results in a unique type of magnetic domain wall (DW) known as the Bloch-point domain wall (BPW), that is able to reach ultra fast velocities above $1\,\mathrm{km}\cdot\mathrm{s}^{-1}$. The synthesis of these nanostructures is a critical step to achieve the desired magnetic properties. The reason relies on the impact that the quality and properties of the material have on its functionality. Thus, there are many parameters to consider to achieve a defect-free and desired material, such as grain size, strain, composition, oxidation, crystallinity, or curvature.

Modulated nanowires have been widely explored in the last decades in order to control the magnetization processes, and to set systems with specific DW pinning sites. The most common ones are based on tuning the energy landscape along the axial direction by local and periodic changes in the diameter or composition. With regards to diameter-modulated nanowires, the pore diameter is mainly tuned by modifying the potential during the anodization process [194]. There are several experimental studies describing these systems with materials such as Ni [117, 125, 132], Ni/Permalloy [126], FeCoCu [130] etc. However, for spintronics, modulations of composition are preferable to modulations of diameter since they avoid local changes in the current density [131]. With respect to multilayered nanowires, different systems have been studied. On the one hand, dual-bath electrodeposition has been used to grow nanowires combining two or more magnetic materials such as Co/Ni [138], CoNi/Ni [279], NiFe/Ni [126] or $Co_{54}Ni_{46}/Co_{85}Ni_{15}$ among others. However, single-bath electrodeposition is preferable in terms of control of interlayers as well as to prepare multilayered nanowires with a large number of layers. In this sense, many examples are found in the literature of the growth of nanostructured nanowires alternating ferromagnetic and non-ferromagnetic materials such as Ni/Cu [143, 144], Fe/Cu [145], FeCoCu/Cu [146], FeGa/Cu [147], Co/Au [148], Co/Cu [149, 150], NiCo/Cu [139], CoCu/Cu [151], Ag/Co [152, 153], Au/FeAu [154], Au/Ni [155], Co/Pt [156], CoPt/Pt [157], etc.

Our case of interest is $Fe_{20}Ni_{80}/Fe_{80}Ni_{20}$ modulated nanowires grown by single-bath electrodeposition. The reason to use Ni-Fe alloys relies on the fact that they are magnetically soft materials, which come with rather low magnetization, they show high permeability, near zero magnetostriction, low thermal expansion, etc. In addition, this system provides a building block material for the concept of a domain-wall-based racetrack memory [93, 94]. The only experimental reports found on this system relate to nanowires with diameters of $\approx 200\,\mathrm{nm}$ grown on commercial nanoporous alumina templates (Anodisc from Whatman). On the one hand, nanowires were galvanostatically electrodeposited at 40 °C by applying current pulses of $5\,\mathrm{mA/cm^2}$ ($Fe_{80}Ni_{20}$) and $20\,\mathrm{mA/cm^2}$ ($Fe_{80}Ni_{20}$) [280] . On the other hand, in a previous work performed in our group by SANDRA RUIZ GÓMEZ, nanowires were potentiostatically electrodeposited at room temperature by applying voltage pulses of $-1\,\mathrm{V}$ ($Fe_{80}Ni_{20}$) and $-1.5\,\mathrm{V}$ ($Fe_{20}Ni_{80}$) [141, 281].

For this thesis, a wire diameter of $\approx 100\,\text{nm}$ was required not only to allow for transmission experiments such as transmission X-ray microscopy (TXM), scanning transmission X-ray microscopy (STXM), X-ray ptychography and transmission electron microscopy (TEM) but mainly to avoid azimuthal magnetic domains [141, 281], that occur in Permalloy nanowires for diameters above $\approx 150\,\text{nm}$. We aimed to simplify the system by removing the extra degree of complexity that azimuthal domains add such as the high impact of the Oersted field. In addition, working with a smaller diameter simplifies the task of electrical contacting. Furthermore, we aimed to obtain nanowire lengths above $40\,\mu\text{m}$ to achieve very long contacted samples. During the growth of the desired nanowires, where the pore diameter was reduced from 200 nm to 100 nm, we encountered several issues that were not present in thicker nanowires.

The following sections describe the complexities, problems, and solutions encountered in the search for a high quality sample. For ease of reading, I will simultaneously detail the problems and solutions found for each specific topic. We hope these details can help the scientific community if similarities are found. In concrete terms, I have carried out mostly all the work that is presented in this chapter, unless otherwise stated. Also CLAUDIA FERNÁNDEZ GONZÁLEZ and CLARA GUILLÉN helped with the discussions and in the experimental steps. SANDRA RUIZ GÓMEZ, LUCAS PÉREZ and OLIVIER FRUCHART participated in the discussions of synthesis optimization. The TEM characterization was performed by ALEJANDRA GUEDEJA-MARRÓN GIL, MARÍA VARELA and AURÉLIEN MASSEBOEUF.

3.1 Porous Anodic Aluminum Oxide templates with pore diameter $\approx 100\,\text{nm}$

In this section we detail the different approaches followed to obtain home-made homogeneous nanoporous anodised aluminium oxide (AAO) templates with a pore diameter of approximately 100 nm. We could not make use of commercial alumina templates since their pore sizes available of this kind of templates are above 200 nm or below 50 nm, and the maximum nanowire length is normally below $20\,\mu\text{m}$.

3.1.1 Two steps anodization

An anodization procedure is defined by the electrochemical conditions, including the composition of the electrolyte, concentration, voltage, time, and temperature. The combination of these parameters determines the pore size and interpore distance, as well as the quality of the pores, such as their geometry and homogeneity in diameter. One of the most standard conditions to prepare AAO templates is the two-step anodization process. In particular, in this work, a two-step process was performed using 0.3 M oxalic acid at 40 V and 2 °C. The duration of the first and second anodization was $t_1 = 24\,\text{h}$ and $t_2 = 20\,\text{h}$, respectively. The resulting

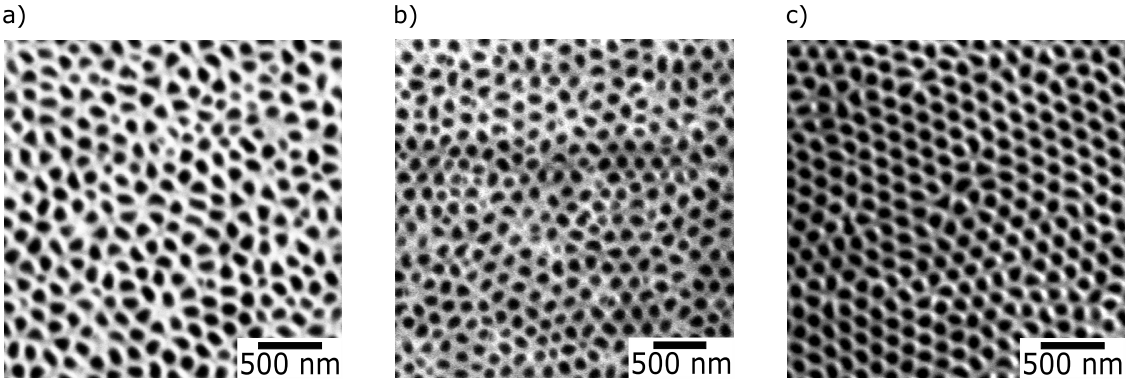

Figure 3.1: Top view of AAO templates with $\approx 90\,\text{nm}$ pore diameter obtained by a two-step anodization process in oxalic acid at 60 V and at 20 °C. **a)** 0.3 M oxalic acid, $t_1 = 4\,\text{h}$ and $t_2 = 3\,\text{h}$. **b)** 0.3 M oxalic acid, $t_1 = 15\,\text{h}$ and $t_2 = 3\,\text{h}$. **c)** 0.9 M oxalic acid, $t_1 = 15\,\text{h}$ and $t_2 = 1.5\,\text{h}$.

AAO template had 50 nm of pore diameter and 70 µm of pore length. Therefore, since we were interested in obtaining a pore diameter ≈ 100 nm, we had to set new anodization conditions.

The pore diameter has been reported to be directly proportional to the anodizing potential, the temperature and the electrolyte concentration [282]. Therefore, we decided to set new anodization conditions: an electrolyte based on 0.3 M oxalic acid, a voltage of 60 V and a constant temperature of 20 °C. Since higher voltage and temperature imply faster anodization, we set the anodization times to $t_1 = 4$ h and $t_2 = 3$ h. Afterward, the remaining Al was etched with an aqueous solution of $CuCl_2$ (0.74 M) and HCl (3.25 M). Once the oxide barrier was removed, the pores were opened to the final diameter with H_3PO_4 (5 % vol.) at 45 °C for 40 min. The top-view of the resulting AAO template with pores diameter ≈ 90 nm is shown in Figure 3.1a. It can be noticed that there is a lack of order in the pores' location, diameter and shape. This is a direct consequence of the additional stress added to the process due to the increase of voltage and temperature.

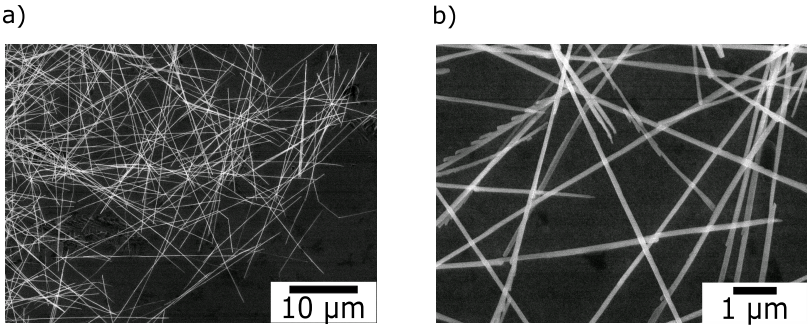

Figure 3.2: **a)** Dispersed $Fe_{80}Ni_{20}$ chemically modulated Permalloy nanowires with a 90 nm diameter image by SEM. **b)** High magnification image of **a)** evidences ramifications with diameter variations.

In order to increase the quality of the templates, the duration of the first anodization was increased to $t_1 = 15$ h, which should have a direct impact on better pore order. This can be evidenced in Figure 3.1b, where slightly better organized pores are shown. However, the arrangement is still not adequate since the range of pore diameters varies from 75 nm to 100 nm. This is not a big issue since, in the end, we will study an isolated wire but it makes more complex the further manipulation. A second approach we took was to increase the molarity of the oxalic acid to 0.9 M with $t_1 = 15$ h and $t_2 = 1.5$ h. With this, a better-ordered template was obtained with a pore diameter of 90 nm and length 80 µm (Figure 3.1c). As a technical note, just to mention that this electrolyte cannot be used more than once, and it evaporates very rapidly compared to 0.3 M oxalic acid.

The final validation consists of imaging by SEMof electrodeposited nanowires released from the last described porous AAO template. Figure 3.2a shows dispersed nanowires on a Si substrate. The length of the nanowires is above 40 µm, which was desired. However, if we take a closer look, variations in the diameter can be appreciated, with ramifications or branches (Figure 3.2b). This undesirable result cannot be accepted, as it drastically modifies the micromagnetic of the system. To solve this, we decided to move to a hard anodization process.

3.1.2 Hard anodization

In order to obtain high-quality porous AAO templates with pore diameter ≈ 100 nm we performed hard anodization using an electrolyte of 0.3 M oxalic acid and 0.9 M ethanol at 140 V at a controlled temperature of 0-1 °C during 2.5 h. It was used an auto-regulated anodization system, named *XEO*. This equipment includes control of the applied voltage, current and temperature. The aluminum disc is located inside the cell (Figure 3.3a) and the electrolyte is continuously stirred by the white helix shown in Figure 3.3b. The aperture of the pores was done with H_3PO_4 (5 % vol.) at 32.5 °C during 1.75 h and at 45 °C during 50 min. An example of the resulting highly-ordered nanoporous template with 120 nm pore diameter is shown in

Figure 3.3c. The honeycomb-like arrangement, the high interpore distance, the homogeneity in diameter and the circularity of the pores, in comparison with the templates in Figure 3.1, establish this procedure as the procedure of choice for synthesizing high-quality AAO templates.

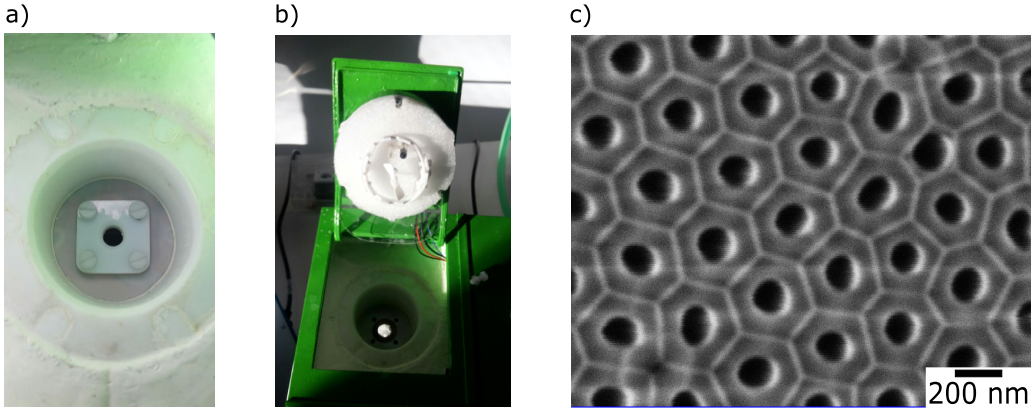

Figure 3.3: **a)**, **b)** Images of the *XEO* anodization device used to perform hard anodization processes. **c)** Top view of a porous AAO template with $\approx$ 120 nm pore diamter. It was obtained from a hard anodization process at 140 V in 0.3 M oxalic acid and 0.9 M ethanol at a controlled temperature of 0-1 °C during 2.5 h.

3.2 Electrodeposition of chemically-modulated Permalloy nanowires

In the following, we will delve into the complexities faced during the optimization of the electrochemical parameters to grow high-quality chemically-modulated permalloy nanowires. The starting point was the aforementioned porous AAO templates with $\approx$ 100 nm pore diameter, and with 150 nm of Au thermally evaporated on one side acting as a working electrode or cathode. The electrolyte used was composed of $NiSO_4$ (0.8 M), $NiCl_2$ (0.02 M), $FeSO_4$ (0.16 M), H_3BO_3 (0.4 M). The pH was adjusted with H_2SO_4 (10% vol.) to 2.3. A platinum mesh was used as a counter-electrode and a BASi Ag/AgCl (3M NaCl) electrode as a reference electrode. The synthesis was carried out at room temperature.

3.2.1 Anomalous codeposition

When plating an alloy of two metals belonging to the iron group, the less noble metal deposits preferentially over the more noble one [283]. This effect is known as anomalous codeposition, and it is enhanced in the case of electrodeposition of nanomaterials [284]. In the case of FeNi alloys, this results in a higher fraction of Fe being deposited than the ratio $[Fe^{2+}]/([Fe^{2+}]+[Ni^{2+}])$ in the electrolyte. The origin of this phenomenon is a pH dependent competitive adsorption of monohydroxide species, MOH^+, which may react in parallel to the hydrated metal ions, M^{2+} [285–288].

The impact of voltage on the anomalous codeposition of Fe-Ni alloys can be observed in Figure 3.4a. This study, reported in [284], shows that the relative Fe concentration in the samples is much higher than the concentration of Fe^{2+} ions in the electrolyte (red horizontal line) for low growth overpotential values due to the anomalous codeposition. The evolution of Fe concentration with the growth potential shows the same qualitative and non-monotonous behavior for 100 nm diameter nanowires (green), 30 nm diameter nanowires (black) and thin film (blue). For potentials from -1.3 V to -1.5 V, the reduction of Fe^{2+} and Ni^{2+} is diffusion controlled, and the concentration of ions corresponds to that of the electrolyte.

Figure 3.4b shows the Fe concentration as a function of the length of the nanowires for different potentials and diameters. A decrease in Fe concentration with nanowire length occurs for -1.1 V. This is explained as follows: at first, the growth is kinetically controlled, but then the diffusion process is controlled by the

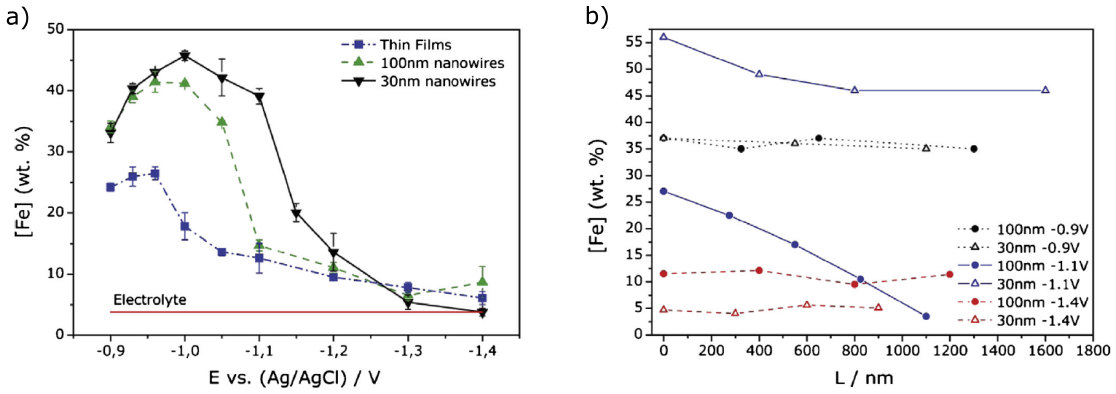

Figure 3.4: **a)** Fe concentration as a function of the plating potential for 100 nm diameter nanowires (green), 30 nm diameter nanowires (black) and thin film (blue). Red horizontal line shows the corresponding Fe^{2+} concentration in the electrolyte. **b)** Fe concentration vs. length for nanowires electrodeposited at different potentials. Figure adapted from [284].

mass transport of Fe^{2+} ions, leading to a decrease in Fe concentration. For the other potentials (-0.9 V and -1.4 V), a nearly constant Fe concentration remains since both ions are controlled by diffusion. In addition, if the rate of electrodeposition is higher than that of the transport through the pores, the metal ion concentration decreases at the bottom of the pores. Consequently, hydrogen evolution becomes the dominant process, inhibiting the homogeneous deposition and decreasing the pore filling factor and the current efficiency [289].

3.2.2 Overlayer of Permalloy

We describe in this section one of the most common phenomena observed in most of the samples grown. We have evidenced a greyish layer at the top of the AAO membrane when depositing Permalloy at rather high potentials (≈ -1.5 V). Usually, this should occur when most of the pores have been filled up to the top. However, we still evidence a thin electrodeposited layer of Ni-Fe even with the pores are almost empty. This layer grows from the edges of the membrane towards the center. At the edges, the AAO membrane is in contact with the Kapton used to isolate it (see Figure 3.5b). We believe this effect may occur during the charging of the double layer and the nucleation of the material due to the large overpotential which would have a large hydrogen evolution associated with it. The generation of large hydrogen bubbles may detach the Kapton and produce micro-cracks, allowing the growth of a continuous thin layer on top of the template.

Since we are interested in an isolated wire, it is not an issue to obtain a certain membrane overgrowth. However, the overlayer sometimes can directly affect the partial current values, and thus the rate of the deposition. This is shown in the cathodic current evolution in Figure 3.5a. For a potential of -1 V the growth of a Fe-rich material is stable, showing a constant current of ≈ -1.5 mA (red curve). After the growth, the template is black as expected (Figure 3.5b). However, for a potential of -1.5 V the growth of a Ni-rich material is not homogeneous, since there is an increase in the current from -20 mA to -40 mA, which indicates the growth of an overlayer at the top, that covers the pores and limits the growth. In this case, the membrane is gray, with a more intense color at the edges (see Figure 3.5c). To confirm that the pores are not filled and that this effect is independent of the length of the electrodeposited material, in Figure 3.5d we show a SEM image of the transverse view of the AAO template after the growth. The bright horizontal segment at the bottom corresponds to a 400 nm thick Au layer evaporated and thus the bottom of the AAO template. Adjacent to it, 2 µm long $Fe_{20}Ni_{80}$ nanowires are electrodeposited, being the rest of the porous AAO template empty. At the top, an overlayer of NiFe is evidenced. With this, we confirm that material growth at the top may be achieved at rather high voltages (≈ -1.5 V) even though the pores are almost empty.

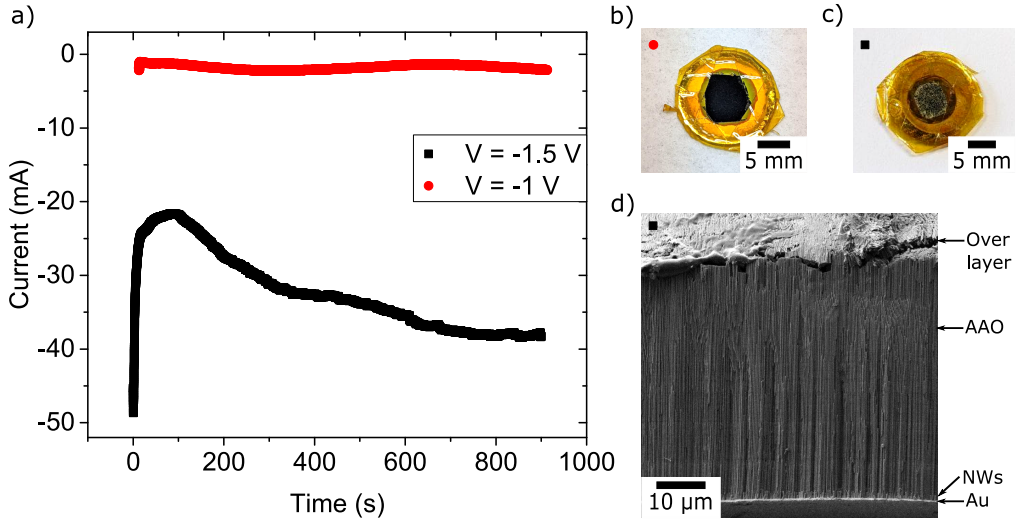

Figure 3.5: Dependance on potential of the over layer. **a)** Evolution of the cathodic current during a electrodeposition process of NiFe alloys inside a porous AAO template with 120 nm pore diameter. For a voltage of -1 V (red) the current remains constant and the aspect of the AAO template is black (**b)**). For a voltage of -1.5 V (black) the current increases and the aspect of the AAO template is greyish due to the overlayer deposited (**c**)). **d)** Transverse view of AAO template after the electrochemical deposition growth at -1.5 V (black curve in **a**)). The region at the bottom shows the Au contact followed by 2 µm long $Fe_{80}Ni_{20}$ nanowires. Top part corresponds to the Permalloy overlayer.

To reduce this effect, we first start with a voltage pulse of rather low amplitude, such as -1 V to promote nucleation at the bottom of the pores and reduce the overpotential, to cotinue then with a higher voltage pulse. In addition, we have observed that reducing the electrolyte pH to 1.7 has been shown to decrease the overlayer.

3.2.3 Optimization of the Au back contact

One of the main problems faced was the detachment of the Au electric back-contact during electrodeposition at rather high potentials (≈ -1.5 V). At this voltage value, the AAO template undergoes high stresses causing the separation of the alumina and Au. To improve the adhesion of the Au contact we have sputtered a Ti layer between the AAO template and the Au layer. First, 10 nm of Ti was sputtered at a very low rate (0.03 nm/s). Afterward, 150 nm of Au were sputtered at 0.25 nm/s. In order to enlarge the thickness of the Au layer, increasing its conductivity, we electrodeposited Au by pulse plating electrodeposition using commercial OROSENE solution. The protocol followed was based on two trains of voltage pulses. One train of 1600 pulses with a growth voltage pulse of -1.5 V during 0.001 s and a resting pulse during 0.01 s and a second train of 7500 pulses with a growth voltage pulse of -1.5 V during 0.01 s and a resting pulse during 0.1 s. The use of resting pulses reduces the tensile internal stresses and increases the stability of the Au layer.

Figure 3.6 shows SEM images of the transverse view of nanowires plated at -1.5 V inside AAO templates with different Au contact layers underneath. In all cases, there is a sputtered Ti (10 nm) / Au (150 nm) layer in contact with the AAO. In Figure 3.6a, the Au layer was enlarged by electrodepositing 150 nm of Au. After the growth of $Fe_{20}Ni_{80}$ nanowires at -1.5 V, it can be appreciated that the Au layer is physically detached from the template and thus less than 1 µm long wires are obtained. For the case of a 2 µm thick electrodeposited Au (Figure 3.6b), the electrochemical growth seems more stable as wires above 15 µm are obtained. However, when looking closer at the interface we realize that there is also a break of the metal-

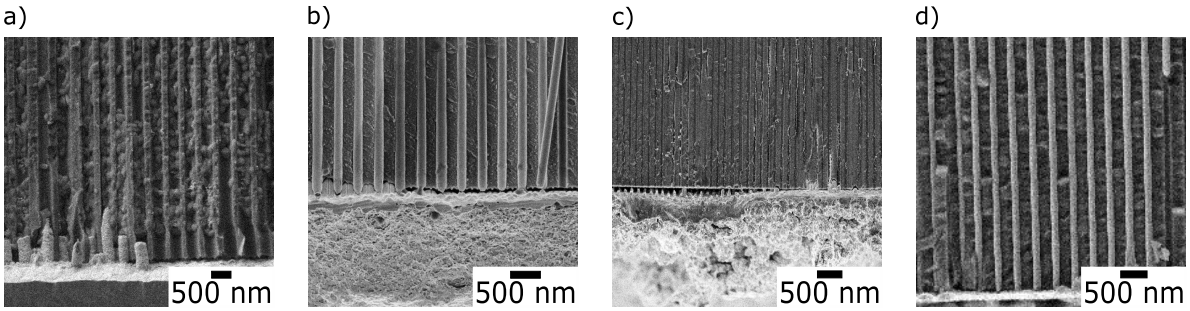

Figure 3.6: SEM images of the transverse view of AAO templates after plating Permalloy nanowires with different Au bottom layers. In all cases, there is a sputtered Ti (10 nm) / Au (150 nm) layer in contact with the AAO. The Au layer was enlarged by plating 150 nm of Au in **a)**, plating 2 µm of Au in **b)** and evaporating 1 µm of Au in **c)**. Detachment of the Au layer is observed when plating Permalloy at −1.5 V. **d)** The Au layer was not enlarge but an initial pulse of −1 V was applied for 200 s to stabilize the Au layer.

lic layer, most likely produced at a far stage of the electrochemical growth, allowing the growth of longer nanowires. To check whether the effect is just related to the thickness of the Au layer, we thermally evaporated 1 µm Au onto the already sputtered Au. The result is shown in Figure 3.6c, where not only a visible detachment of the Au layer is observed but also the lack of nanowires deposited. Therefore, although the stability of the Au layer may depend strongly on its thickness, it is important to use electrodeposition to thicken the contact. Finally, providing that the stress introduced in the growth strongly depends on the growth potential, we decided to start the growth of the nanowires with a voltage pulse of −1 V during 200 s, finding that this procedure helps to stabilize the stress at the interfaces, preventing the detachment of the Au layer (Figure 3.6d). It is important to notice that this last procedure allows the growth of the nanowires without the need to thicken the Au back-contact.

3.2.4 Reduction of diameter at the chemical modulation

One of the most unexpected and difficult issues we have faced is a reduction in diameter or etching of the nanowire at the location of the chemical modulations. Up to now, most of the studies made on chemically modulated nanowires were carried out in nanowires with diameter above 200 nm and short chemical modulations (100 nm) [141, 281]. Figure 3.7a shows a 250 nm diameter Permalloy nanowire with a 40 nm-long $Fe_{80}Ni_{20}$ chemical modulation at its center. It can be seen that, in this case, a 6 nm crack is evidenced at the center of the modulation. When moving to smaller diameters (≈ 100 nm), the effect is enlarged. Figure 3.7b shows a sharp and non-homogeneous reduction of the diameter at the location of the chemical modulations for a 60 nm long $Fe_{80}Ni_{20}$ chemical modulation in a nanowire of 130 nm diameter. However, this effect is not the same in all nanowires coming from the same AAO template. This is shown in Figure 3.7c where a full breaking of some nanowires occurs at the location of the chemical modulations, whereas other wires do not show inhomogeneities in the diameter or defects. First, the wide range of diameter reduction at the chemical modulations led us to suspect that chemical etching was occurring during the etching of the AAO template. This step is performed to release the nanowires from the template by using H_3PO_4 (0.4 M) and H_2CrO_4 (0.2 M). We tried to optimize the removal of the alumina template by testing it at different temperatures and etching times and, in all cases we obtained similar etching of the nanowires. We also tried to dissolve the AAO in NaOH without any improvement. Thus, we concluded that the reduction in the diameter is not related to chemical etching but most likely happened during the electrodeposition process. This is also supported in Figure 3.7d, where periodic diameter reductions are evidenced in the transversal AAO view, i.e. prior to membrane dissolution.

To discuss the possible origin of the observed phenomenon, it is important to remember that we use

two different voltage values during the deposition of the chemically-modulated nanowires: we use voltage pulses of -1.5 V to plate $Fe_{20}Ni_{80}$, with a growth rate of $\approx 100\,nm/s$, and pulses of -1 V to plate $Fe_{80}Ni_{20}$, with a growth rate of $\approx 4\,nm/s$. The differences in the growth rate are closely related to the growth regime. For high overpotentials, electrodeposition is controlled by mass transport, whereas for low overpotentials, the growth is in a kinetic regime. Therefore, a complex procedure occurs when trying to combine the two regimes of electrochemical growth.

Let us take a closer look at the transport of ions through the pore channel. When plating $Fe_{20}Ni_{80}$ at -1.5 V, mass transport controls the electrodeposition process, and the concentration of electroactive ions close to the cathode is negligible. When the potential is swept to -1 V, the electrodeposition moves towards a region controlled by electron transfer, in which the concentration of the electroactive ions close to the cathode is similar to the one of the electrolyte. However, it takes some time to reach this regime and, in the meantime, the composition of the electrolyte is not at equilibrium. In addition, the Helmholtz double layer changes its configuration. During this process, the electrochemical reaction may shift towards oxidation conditions, producing a partial etching of the previously grown material. Providing that this effect should be smaller when reducing the difference between the two growth potentials — less time to reach the steady state — we tried using -1.35 V instead of -1.5 V, finding a clear reduction of the etching. Although this procedure led us to obtain defect-free wires, when observed in some cases periodic reductions of the diameter just after the chemical modulation (see Figure 3.7d for a 130 nm). Therefore, to ensure we reach a steady state more rapidly after switching the overpotentials, we decided to introduce a resting potential to reset the system to the initial state before each pulse. Following this procedure, we obtained homogeneous and defect-free nanowires.

3.2.5 HfO_2 ALD coating of AAO membranes

Taking into account the importance of having nanowires with a homogeneous diameter and also to prevent oxidation, we considered coating the nanowires with HfO_2 using atomic layer deposition (ALD). In particular, we performed a 5 nm HfO_2 ALD coating of the pores of the AAO template before electrodeposition. Although, in principle, this approximation seems to be good to improve the quality of the electrodeposited nanowires, in the following we show that this approximation presented some drawbacks that prevented us from using ALD coating in the studied nanowires.

One of the main drawbacks was the poor adhesion of the metallic Au back-contact of the ALD-coated

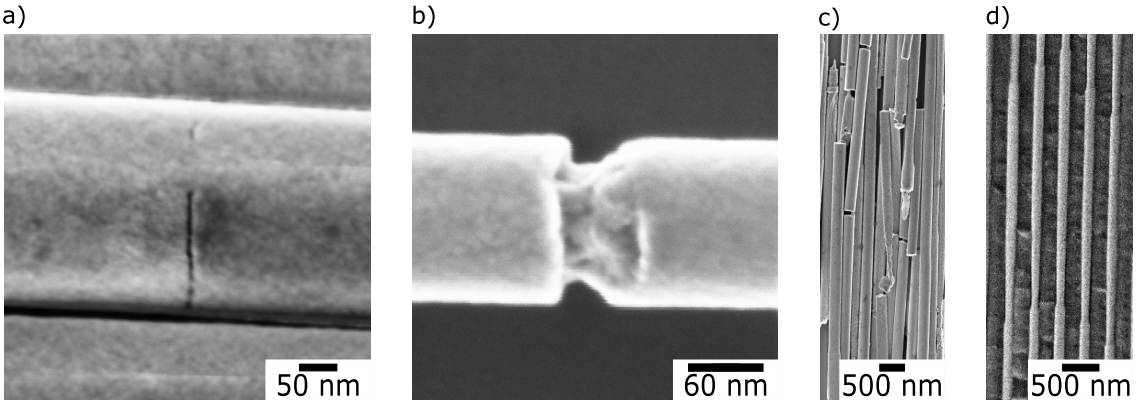

Figure 3.7: SEM images of inhomogeneities at the $Fe_{80}Ni_{20}$ chemical modulations in Permalloy nanowires. **a)** 250 nm diameter wire with a 6 nm crack at the center of a 40 nm modulation. **b)** Large reduction in diameter at the 60 nm long modulation in a 130 nm diameter nanowire. **c)** Breaking of the Permalloy nanowires at the location of the chemical modulation. **d)** Nanowires within AAO template show periodic reduction of diameter after the chemical modulation.

AAO templates, which is reflected in a reduction of the typical current for Permalloy electrodeposition, decreasing from ≈ -35 mA to ≈ -1.7 mA. The time evolution of the current is shown in Figure 3.8a, where the long pulses correspond to $Fe_{20}Ni_{80}$ and the short pulses to $Fe_{80}Ni_{20}$. Longer pulses than usual were applied due to the slow rate of growth, which resulted in a thick overlayer obstructing the pores. This is also evidenced by the drop in the current values. The final length of the nanowires was of $\approx 18\,\mu$m, as shown in the transversal AAO view in Figure 3.8b, where not all the pores are filled due to the partial detachment of the Au layer.

Figure 3.8b shows a high resolution transmission microscopy (HRTEM) image of a 120 nm diameter Permalloy nanowire with a 60 nm-long $Fe_{80}Ni_{20}$ chemical modulation. The interfaces of the modulation are indicated by the orange dashed lines and the growth direction by the yellow arrow. The coating layer made of 5 nm HfO_2 is evidenced. The diameter is homogeneous along the axial direction and thus no etching at the chemical modulation is observed. In terms of crystallinity, there is a sharp change in crystal structure at the first boundary of the modulation in the direction of growth. Unexpectedly, the Permalloy segment seems to be single crystalline until reaching the modulation where a polycrystalline texture is evidenced along ≈ 400 nm to the left. This was unexpected since nanowires with larger diameters grown under the same conditions are clearly polycrystalline.

In addition, in this particular HfO_2 coated sample we detected by X-ray ptychography at the Fe L_3 edge

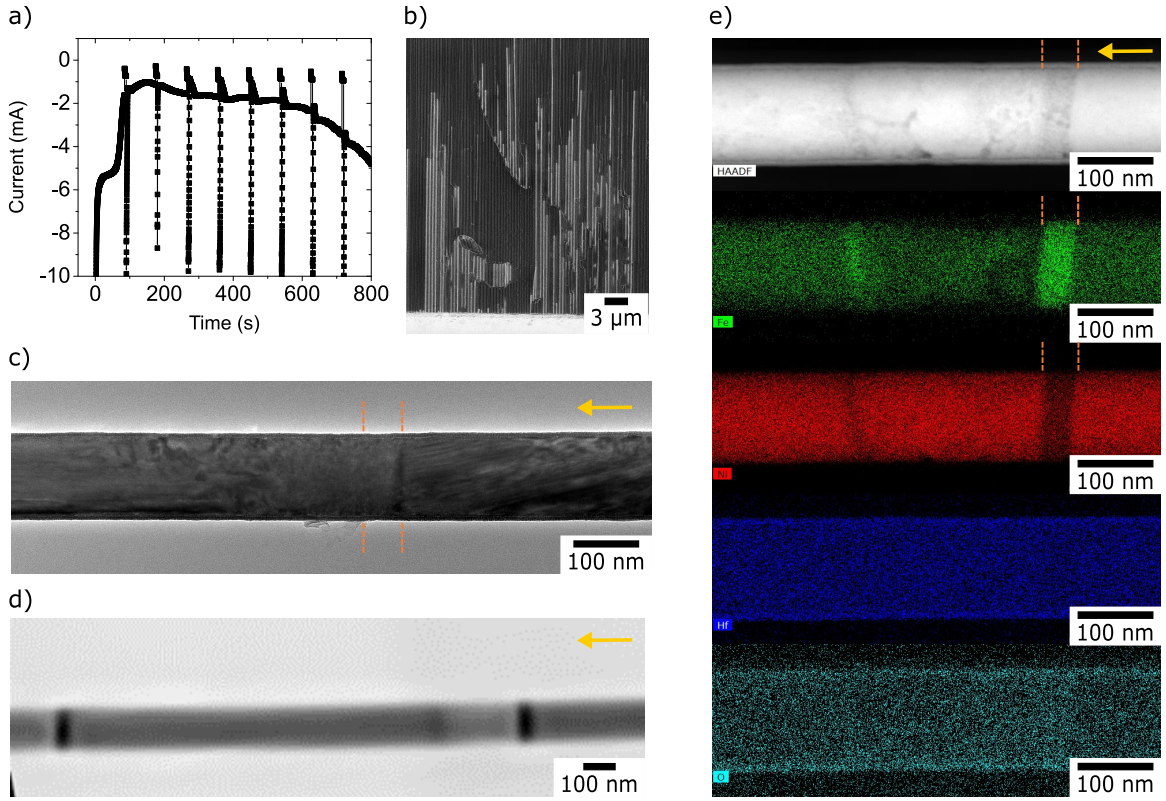

Figure 3.8: 5 nm HfO_2 ALD coated chemically modulated Permalloy nanowires. **a)** Time evolution of the current during the electrochemical growth. **b)** Transverse view of the AAO template after the nanowires growth. **c)** HRTEM image of a 120 nm diameter Permalloy nanowire with a 60 nm-long chemical modulation. Orange dashed lines indicate the interfaces of the modulation. Yellow arrow indicates the growth direction. **d)** Reconstructed XAS X-ray ptychography image at the Fe L_3 edge shows material inhomogeneities. **e)** Top shows HAADF image where the modulation is identified by the difference in the Z contrast. Bottom images show compositional maps performed by EELS.

a lack of Fe content at the left of the modulation followed by a Fe-rich second modulation. This is shown in Figure 3.8d for the same wire shown in Figure 3.8c. Here we may highlight one of the main advantages provided by the ≈ 13 nm spatial resolution obtained with X-ray ptychography, which is its excellent material sensitivity. Once this issue was identified, we performed maps of the compositions by EELS technique. The result is shown in Figure 3.8e. The top image corresponds to a HAADF image of the same wire shown in Figure 3.8c. The difference in Z contrast allows us to identify the Fe-rich chemical modulation, since it shows darker contrast. Also the material inhomogeneities at the left of the modulation predicted by X-ray ptychography are spotted. To understand it better, we may look into the corresponding Fe map (green), where it is detected a decrease of Fe content along the radial direction at the left of the modulation, followed by a short Fe-rich segment. This phenomenon also reflects the problems related to the different growth regimes explained above and the importance of using resting potentials.

The HfO_2 coating prevents the oxidation of the nanowires because only oxygen is found in this layer and not in the Fe or Ni compositional maps. However, we have checked that the CrO present in the solution used to dissolve the alumina template also deposits on the surface of the nanowires, preventing the oxidation of the sample. Therefore, coating the pores using ALD is an unnecessary step because it reduces the quality of the contact between the metallic layer and the AAO template, increases the deposition time, without adding additional functionalities.

3.2.6 Optimized electrochemical growth conditions

With all the knowledge gained throughout the synthesis optimization process, we will now detail the recipe for a successful electrochemical growth. Firstly, the electrolyte must be prepared just before the growth to avoid the oxidation of Fe^{2+} ions into Fe^{3+}, which would degrade the electrolyte. Then a Ti(10 nm) / Au(150 nm) layer is sputtered on one side of an AAO template to act as a metallic contact. Before starting the growth of the chemically modulated nanowires, a short segment is grown at -1 V for 200 s to stabilize the electric contact between the AAO template and the Au layer. Afterward, Permalloy is plated at -1.35 V for 50 s to obtain Permalloy segments of 3.5 µm. Then, $Fe_{80}Ni_{20}$ is plated at -1 V for 4 s, 12 s or 20 s to obtain modulation lengths of 20 nm, 60 nm or 100 nm, respectively. This may be repeated up to 14 times to obtain modulated nanowires with lengths of ≈ 50 µm.

An example of the expected time evolution of the current during the electrochemical growth is shown in Figure 3.9a. The current obtained for Permalloy is ≈ -11 mA for an area of 0.64 cm^2, which results in a current density of $-17\,mA \cdot cm^{-2}$. For the case of $Fe_{80}Ni_{20}$, it was obtained a current value of ≈ -2 mA, which corresponds to a current density of $-3.1\,mA \cdot cm^{-2}$. The nearly constant current values are an indication of homogeneous growth. The quality of the sample can be evidenced in Figure 3.9b, where it is shown a HAADF image of a 130 nm diameter Permalloy nanowire with 100 nm-long $Fe_{80}Ni_{20}$ chemical modulations separated by 3.5 µm. No material or shape inhomogeneities are detected, confirming that an excellent sample has been synthesized. This is also confirmed by the HRTEM higher magnification image in Figure 3.9d. Figure 3.9c shows the EELS spectra at the Permalloy segment (black) and at the chemical modulation (blue). The corresponding compositional maps performed by scanning transmission electron microscopy (STEM)-EELS are shown in Figure 3.9e for Ni (red) and Fe (green). The uniformity of the material can be observed throughout the sample. In this case, since a modulation length of 100 nm was set, the voltage pulse at -1 V to plate $Fe_{80}Ni_{20}$ had a duration of 20 s. This relatively long duration allows for the stabilization of the electrochemical growth. Composition profiles of Ni (red) and Fe (green) along the axial direction are shown in Figure 3.9f. In the Permalloy segments, the composition obtained for this case is $Fe_{30}Ni_{70}$, thus nearly the expected $Fe_{20}Ni_{80}$. The composition at the chemical modulation is $Fe_{80}Ni_{20}$.

When a shorter modulation is required, it is important to reduce the growth overpotential, allowing for longer pulses. In this case, it is also necessary to include resting potentials to allow for the recovery of the electrolyte. An example of a defect-free sample with a very short chemical modulation is shown in Figure 3.10a. The top HAADF image shows a 120 nm diameter Permalloy nanowire with a 30 nm-long

chemical modulation at its center. The orange dashed lines indicate the interfaces of the modulation. The yellow arrow indicates the direction of growth. We observe again a drastic change in the crystal structure just at the modulation. Specifically, the Permalloy segment at the right of the modulation shows a single-crystalline structure, whereas at the modulation and to its left, a polycrystalline structure is detected. We will go deeper into this in the next section. The bottom images show STEM-EELS Ni (red) and Fe (green) compositional maps, where the homogeneity in composition throughout the sample and the inverted contrast at the chemical modulation is noticeable. The atomic percentage profiles of Ni (red) and Fe (green) along the axial direction in Figure 3.10b evidence the inversion of the chemical composition at the modulation. In this sample, a $Fe_{16}Ni_{84}$ composition was detected at the Permalloy segment, whereas a $Fe_{65}Ni_{35}$ composition at the center of the chemical modulation was detected. The decrease in the Fe content at the chemical modulation may be related to the decrease of the plating potential from -1 V to -0.95 V. In addition, the 30 nm short modulation length does not allow for a constant composition throughout the modulation. This

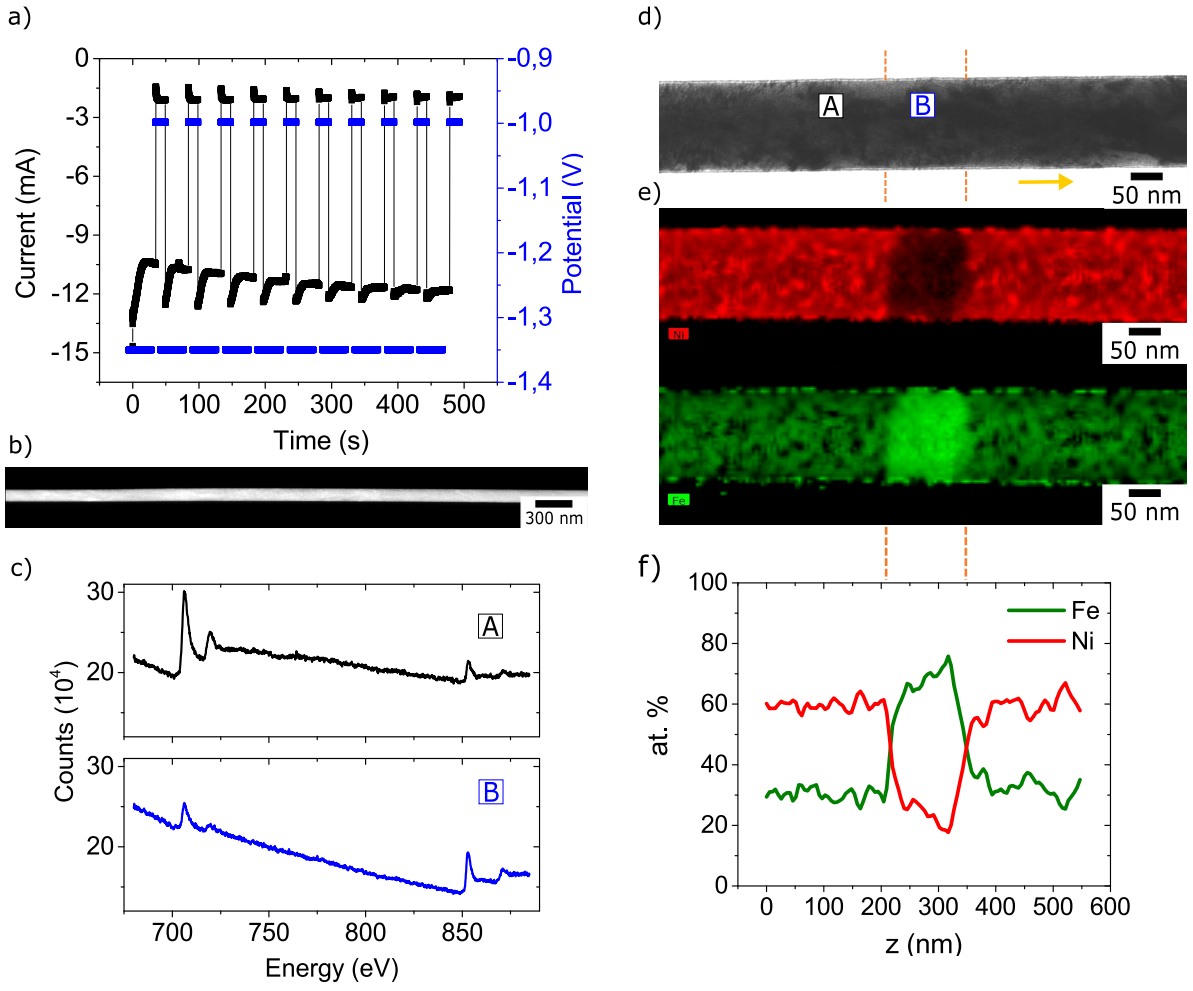

Figure 3.9: Defect-free Permalloy nanowire with 100 nm-long chemical modulations. **a)** Time evolution of the current and voltage during electrochemical growth. Pulses at -1.35 V and -1 V correspond to plating $Fe_{20}Ni_{80}$ and $Fe_{20}Ni_{80}$, respectively. **b)** HAADF image of a 130 nm diameter Permalloy nanowire with 60 nm-long chemical modulations separated by 3.5 µm. **c)** EELS spectra obtained at the Permalloy segment (black) and at the chemical modulation (blue). **d)** HRTEM image of the wire in **b)**. **e)** EELS compositional maps of Ni (red) and Fe (green). **f)** Profile of Ni (red) and Fe (green) atomic percentage composition along the axial direction.

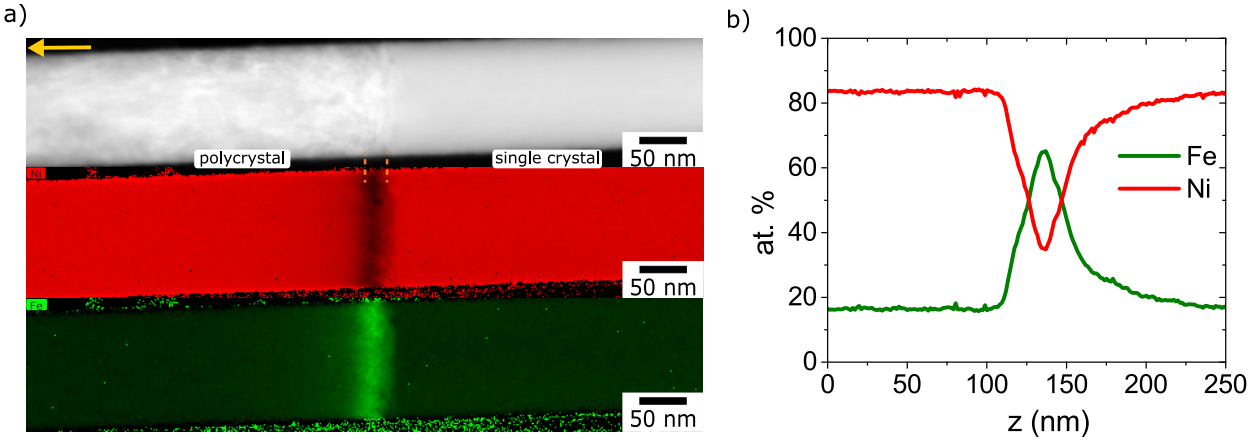

Figure 3.10: Defect-free Permalloy nanowire with a 30 nm long chemical modulations. **a)** Top: HAADF image of a 120 nm diameter Permalloy nanowire with a 30 nm long chemical modulation at its center. Yellow arrow indicates the direction of growth. Orange dashed lines indicate the interfaces of the modulation. Bottom: STEM-EELS compositional maps of Ni (red) and Fe (green) of the top image. **b)** Atomic percentage profiles of Ni (red) and Fe (green) along the axial direction.

can be noted in the characteristic length needed to reach the maximum Fe content.

3.2.7 Correlating crystallinity with growth

To conclude this chapter, we would like to point out the correlation between the optimized growth parameters and sample crystallinity. As previously mentioned, there is a sharp change in the crystal structure when sweeping the potential from -1.35 V to -1 V, i.e., at the start of the chemical modulation. Figure 3.11a shows a STEM image of a 120 nm Permalloy nanowire with a 30 nm-long Fe-rich chemical modulation. The orange dashed lines indicate the interfaces of the modulations, and the yellow arrow indicates the direction of growth. At the right side of the chemical modulation, a single-crystal texture is evidenced, whereas a polycrystalline texture is detected at the modulation up to 300 nm to its left, coming back to a single-crystal state afterward. This drastic change in the crystal texture was unexpected and undesired since it adds up more complexities to the micromagnetic system. However, we could not avoid this phenomenon since it arises from the strains associated with the change of potential. The lattice mismatch at the interfaces plus the difference in grain size make the boundary between the two regions with different composition a crystal boundary.

Regarding the single-crystal behavior at the Permalloy segments, it was also an unexpected result since polycrystalline nanowires are usually obtained for larger diameters. Therefore, we may conclude that the reduction of diameter, and thus the change in the dynamics of the electrochemical growth, has a high impact on the crystallinity of the sample. We performed a more in-depth study on the crystal texture at the Permalloy region by using atomic resolution TEM. Figure 3.11c shows a HAADF image of a 90 nm diameter Permalloy nanowire and Figure 3.11d its respective annular bright field (ABF) image. Stripes along the axial direction are observed in more detail in the higher magnification ABF image in Figure 3.11e. Atomic resolution images, as in Figure 3.11f, confirm the presence of stacking faults at these locations. In addition, atomic columns are imaged, confirming the highly crystalline texture along the [110] direction.

The presence of stacking faults could host segregation of Ni and oxygen at their location. To confirm this, we performed compositional maps using STEM-EELS, as shown in Figure 3.11b. This study confirmed that there is no major segregation of oxygen and Ni at the stacking faults. In addition, there is no gradient of composition along the radial direction, and no segregation of Ni at the wire surface. Therefore, Ni and Fe are homogeneously distributed. Finally, we confirm that the CrO present in the solution used to dissolve the

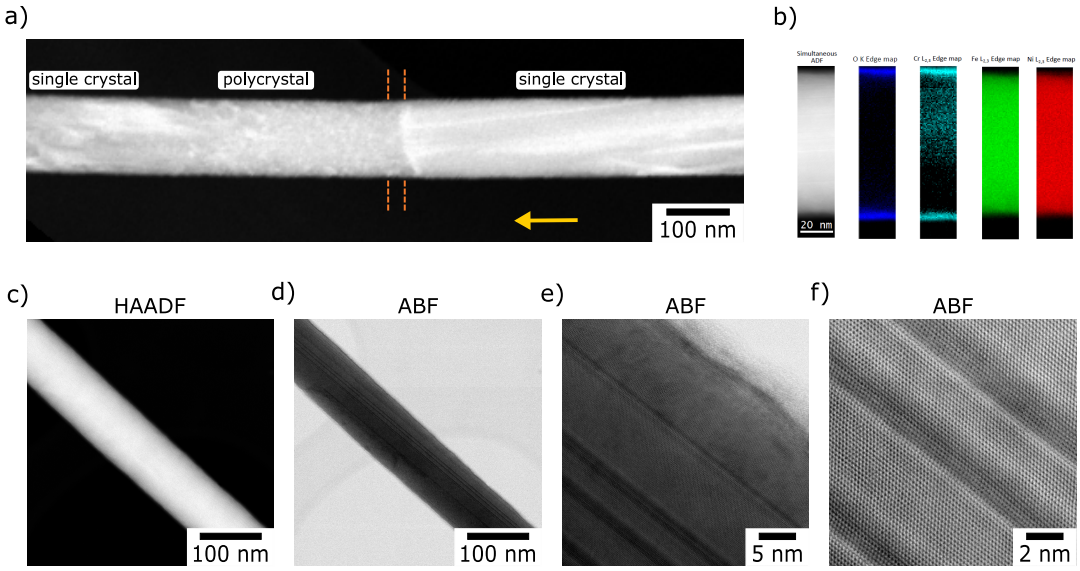

Figure 3.11: Crystallinity characterization by HRTEM. **a)** STEM image of a 120 nm diameter Permalloy nanowire with a 30 nm long chemical modulation at its center. The orange dashed lines indicate the modulation interfaces and the yellow arrow indicates the growth direction. **b)** Compositional EELS maps at the Permalloy segment. **c)** HAADF image of a 90 nm diameter Permalloy nanowire, with its respective ABF image shown in **d)**. **e)** and **f)** ABF images show atomic columns.

AAO template inhibits the oxidation of the sample. Thus, a 3 nm CrO layer coats the nanowires and prevents their oxidation.

3.3 Conclusions

In this chapter, we have reviewed the experimental steps performed in this work to achieve a defect-free chemically modulated nanowire. First, described the search for high quality home-made AAO templates with $\approx$ 100 nm pore diameter. This was accomplished by performing one-step hard anodization in 0.3 M oxalic acid, at 140 V and 1 °C. Then, pulse plating electrodeposition was performed to grow Permalloy nanowires with local changes of composition ($Fe_{80}Ni_{20}$ chemical modulations), at growth potentials of -1.50 V and -1 V, respectively (vs. Ag/AgCl). We encountered that plating Permalloy at such a high potential induces mechanical stress in the system, leading to the detachment of the Au underneath layer. This has a direct impact on the nanowire's growth, reducing its length drastically. To solve this problem, we apply an initial pulse of 200 s at a rather low potential, and then plate at -1.50 V.

The most unexpected result of the electrochemical synthesis was a reduction of the diameter at the location of the chemical modulation. We believe that this is linked to the combination of two different growth regimes (mass transport vs kinetic regime), one of them associated with each growth potential. Reducing the difference between both (plating Permalloy at -1.35 V) and introducing a resting potential between the pulses to allow the recovery of the electrolyte allowed us to obtain defect-free samples.

In order to protect the sample from external oxidation or damage, we coated the pores of the AAO template before the electrodeposition with 5 nm HfO_2 by ALD. However, we encountered more drawbacks than advantages due to the following reasons: first, poor adhesion of the metallic underneath layer was obtained, which drastically reduced the growth current. This led to a non-homogeneous ion transport, causing a depletion in the Fe content after the modulation followed by a second Fe-rich chemical modulation. Therefore, we concluded that the ALD coating step is unnecessary. This is also supported by the fact that the CrO present

in the solution used to release the wires from the template protects the nanowires from oxidation since a few nanometers of it are naturally deposited on the surface of the nanowires.

Finally, we have observed a drastic change in the crystal structure at the start of the chemical modulation. The Permalloy segments show a single-crystal behavior, whereas the chemical modulations are polycrystalline, a structure that extends for $\approx 200\,\text{nm}$ into the adjacent Permalloy segment. We could not avoid this sharp change in crystallinity at the location of the modulation, which may impact the local magnetic anisotropy.

Chapter 4

Micromagnetics of chemical modulations in FeNi nanowires

Long cylindrical nanowires made of a soft magnetic material such as Permalloy are expected to exhibit uniform axial magnetization in the ground state due to their zero magnetocrystalline anisotropy and strong shape anisotropy. However, the chemical insertion of another soft magnetic material with higher magnetization is expected to modify the micromagnetics of the system. This new micromagnetic state has been a major object of study during this PhD, since it is a necessary step to later understand its interaction with Domain wall (DW)s. There have already been several theoretical and experimental investigations of nanowires modulated in composition, addressing the physics of magnetization reversal [140, 290–295], domain-wall pinning [138, 141, 290] and field-driven domain wall motion [141, 279, 281, 291]. However, up to now, the physics of these modulations has not been broadly examined, to provide a comprehensive view of their physics.

This chapter discusses in depth the magnetic behavior of $Fe_{80}Ni_{20}$ chemical modulations periodically inserted in Permalloy ($Ni_{80}Fe_{20}$) cylindrical nanowires. The conclusions are exposed in terms of reduced magnetic quantities when applicable, for the sake of generality. Therefore, the results can be extrapolated to any nanowire composed of a soft-magnetic material with chemical modulations of higher magnetization content, and also magnetically soft. We use magnetic imaging, analytical modeling and micromagnetic simulations. Specifically, I have performed the nanowire synthesis, MFM imaging, participated in and analyzed all the X-ray magnetic imaging measurements at synchrotron facilities, and performed and post-treated the micromagnetic simulations with the advice of DARIA GUSAKOVA. Analytical modeling was done by OLIVIER FRUCHART and transmission electron microscopy (TEM) and holography measurements were taken by AURÉLIEN MASSEBOEUF and MAHDI JABER. The main results that are presented are published in [142].

4.1 Experimental characterization of the magnetic flux

Magnetization is closely connected to the magnetic field **H**, of magnetostatic origin, and thus to the total magnetic induction field **B**, which we investigate in the following.

4.1.1 Study of the stray field by magnetic force microscopy

An initial magnetic characterization of an individual chemically-modulated nanowire can be performed in the laboratory by using magnetic force microscopy (MFM). As described in Sec. 2.3.1, depending on the sign of the vertical stray field arising from the sample, the magnetic tip feels an attractive or repulsive force, which will result a dark or bright magnetic contrast. Given that the nanowire is lying on a substrate, only components of the stray field transverse to the axis of the nanowire can be detected.

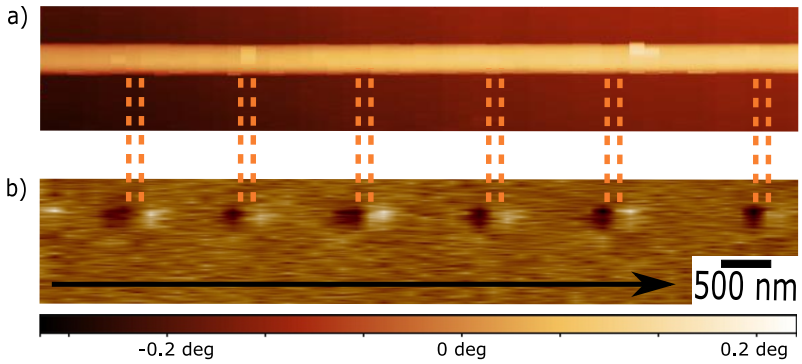

Figure 4.1: **a)** AFM image of a 130 nm diameter Permalloy nanowire with periodic 60 nm-long chemical modulations. **b)** MFM image of **a)**. Each modulation is highlighted by a dark/light bipolar contrast. Orange dashed lines indicate the location of the chemical modulations. Black arrow indicates the axial magnetization direction. Adapted from [142].

Figure 4.1a and Figure 4.1b show an atomic force microscopy (AFM) and MFM image of a 130 nm diameter Permalloy nanowire with periodic 60 nm-long chemical modulations. The interfaces of the chemical modulations are indicated by the orange dashed lines. A bipolar dark and bright magnetic contrast appears at each modulation because the mismatch of magnetization at each interface results in surface magnetic charges of opposite sign $[\sigma = \pm(M_2 - M_1))]$, for longitudinal magnetization. With this, we confirm that the insertions of chemical modulations of higher magnetization modify the micromagnetics to a new system rich in new physics. However, volume magnetic charges may also play an important role, a role that cannot be proven using MFM as it cannot distinguish between magnetic fields arising from the surface versus volume charges. This motivates the use of a complementary microscopy technique.

4.1.2 Study of the magnetic induction field with electron holography

An in-lab magnetic imaging technique complementary to MFM is electron holography. In this case, we are sensitive to the two components of the magnetic induction field **B** perpendicular to the electron beam, integrated along the entire path of the beam through the sample. We will call this the in-plane induction field in the following. It is important to note that the wave phase shift is not only due to the internal induction field $\mathbf{B} = \mu_0(\mathbf{H} + \mathbf{M}_s)$ of the nanowire but also due to the possible stray field arising from it. Since in our case there is stray field arising from the chemical modulations, as observed in Figure 4.1b, the quantification of **B** at this location would not be only the **B** contribution within the nanowire but also the stray field above and below the sample. Moreover, there is another contribution to the phase shift that has an electrostatic origin, due to the electron cloud of the material that needs to be subtracted using various routines [296].

Electron holography was performed on the same nanowire as in Figure 4.1a. The location of the chemical modulations was found by performing HAADF-STEM imaging since the materials $Fe_{80}Ni_{20}$ and Permalloy ($Fe_{20}Ni_{80}$) have different Z contrast (Figure 4.2a). The location of the $Fe_{80}Ni_{20}$ chemical modulation is indicated by the yellow dashed line. It is important to note that in this specific sample, the pores of the anodised aluminium oxide (AAO) template were coated by atomic layer deposition (ALD) with 5 nm of HfO_2, prior to electroplating, to prevent sample oxidation and external corrosion (see Sec. 3.2.5 for more details on this). This outer layer and its homogeneity can also be noticed due to its different Z contrast. Also, this image reveals material inhomogeneities on the right side of the chemical modulation, followed by a thin Fe-rich segment which is indicated by the blue dashed line. We will see below how this synthesis issue in this particular sample will slightly affect our study.

Figure 4.2b displays the magnetic phase image at the same place of Figure 4.2a where the color gradient is used to reveal the isophase lines that, by definition, follow the magnetic flux (Aharonov-Bohm effect

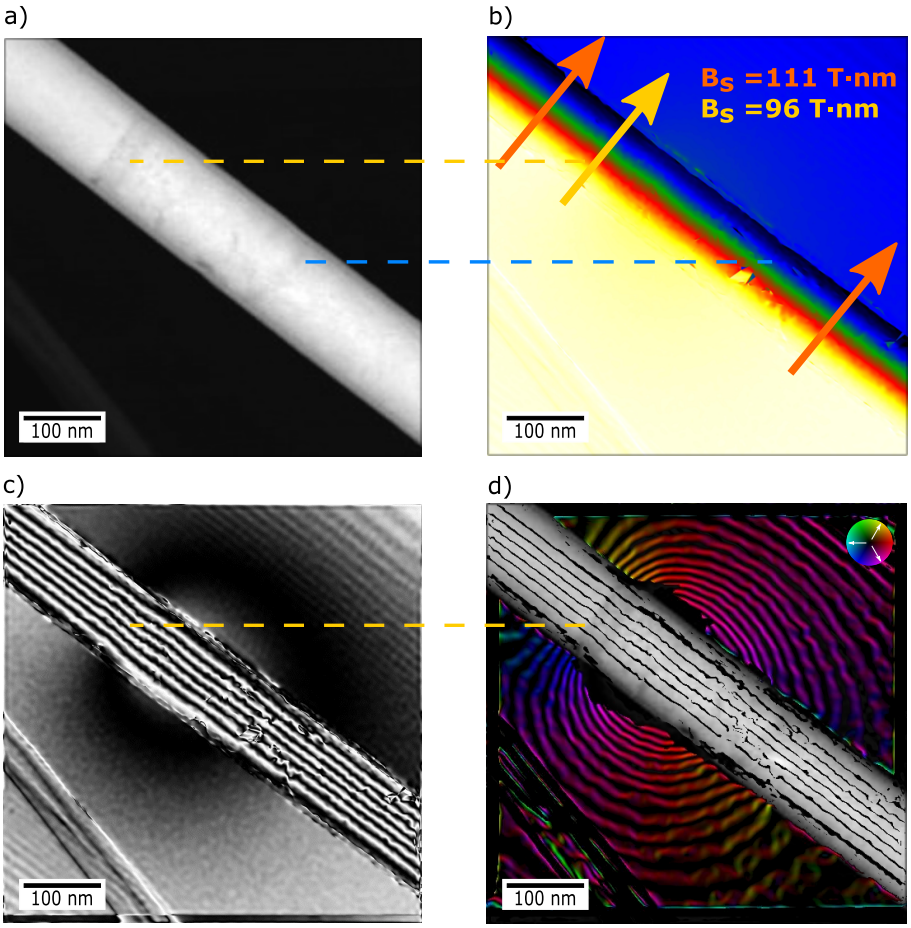

Figure 4.2: **a)** HAADF-STEM image of the nanowire in Figure 4.1a. The modulation is noticed by the slightly darker segment due to the difference in Z contrast (yellow dashed line). Slight material inhomogeneities at the right side of the modulation are revealed followed by a Fe-rich second modulation (blue dashed line). **b)** Reconstructed magnetic phase image from electron holography whose corresponding amplified magnetic flux is displayed as $\cos(3\Phi)$ in **c)**. **d)** Combination of STEM image **a)** with an amplified magnetic phase image displayed as $\cos(20\Phi)$. Black lines inside the wire show continuous induction field. Stray field lines arise from the modulation (directions sketched in the inset). The yellow dashed line indicates the location of the chemical modulation. We moreover enhanced the contrast by adding a color map of the magnetic induction in vacuum determined through phase gradients and detailed by the scale in the inset. Adapted from [142].

[297]). They indicate that here the induction field is largely aligned along the axis direction inside the wire. The value of the in-plane induction field was extracted by performing a line profile along the cross-section (arrow direction) and deriving its slope in $\mathrm{rad}\cdot\mathrm{nm}^{-1}$. The value obtained for the in-plane induction field in the Permalloy segments (orange arrows) is $B = 111\,\mathrm{T}\cdot\mathrm{nm}$ and in the Fe-rich chemical modulation (yellow arrow) $B = 96\,\mathrm{T}\cdot\mathrm{nm}$. The nanowire has a diameter of 130 nm, but the magnetic contribution is 120 nm taking into account the HfO_2 outer layer. This results in $B = 0.93\,\mathrm{T}$ ($\approx 7.40\times10^5\,\mathrm{A}\cdot\mathrm{m}^{-1}$) at the Permalloy segments and $B = 0.80\,\mathrm{T}$ ($\approx 6.36\times10^5\,\mathrm{A}\cdot\mathrm{m}^{-1}$) at the chemical modulations. The value at the Permalloy segments is very close to the expected value for a fully axial magnetization state, where $B = 1\,\mathrm{T}$ ($\approx 8\times10^5\,\mathrm{A}\cdot\mathrm{m}^{-1}$). However, the value obtained at the chemical modulation is 53 % lower than the value expected for an axially magnetized system where $B = 1.76\,\mathrm{T}$ ($\approx 14\times10^5\,\mathrm{A}\cdot\mathrm{m}^{-1}$). The reason may be that most of the induction field is not along the axial direction, and thus it cannot be detected. This would

occur if the magnetization is tilted away from the axial direction or rotating around the nanowire axis, i.e., having a component parallel to the beam that won't affect the phase shift. For the latter case, also known as curling, a full rotation of the magnetization around the nanowire would result in the cancellation of the induction field lines of opposite sign, and thus no magnetic signal can be detected by electron holography. However, since at the core the magnetization should be axial, a small in-plane **B** signal remains. In addition, since the magnetic phase signal obtained is an integration through the electron beam path, contributions of the stray field above and after the sample, from the electron's point of view, are added, which modifies the **B** signal. In conclusion, we confirm that at the chemical modulations the magnetization is not axial, thus we cannot directly measure the value of the in-plane induction field coming only from the sample.

Figure 4.2c shows the in-plane magnetic flux lines, displayed by applying a cosine function to the amplified magnetic phase shift image. Note the continuity of the in-plane induction lines inside the nanowire, as expected from Maxwell´s equations. At the location of the chemical modulation, indicated by the yellow dashed line, stray field is detected, as also observed by MFM in Figure 4.1b. To map the stray field lines arising from the chemical modulations, the magnetic flux lines were displayed as $\cos(20\Phi)$. The result is shown in Figure 4.2d, combined with a STEM image to locate the Fe-rich segment. The stray field lines are slightly shifted to the left, with respect to the nanowire's axis direction, due to the material inhomogeneities mentioned above in this nanowire. What is more remarkable is that the flux closes at the right of the modulation. For a defect-free modulation, we would expect that the stray field lines to be centered at the modulation.

4.2 3D X-ray magnetic imaging

The above-mentioned techniques provide partial evidence of the micromagnetic state, but they do not reveal directly the magnetization distribution. In addition, the three-dimensional geometry of the system makes the situation more complex, as the volume and surface magnetization may be different. In order to achieve this, X-ray magnetic imaging, is required, as it probes the magnetization components along the X-ray beam throughout the nanowire's cross section, providing a complementary view to electron holography. We performed different X-ray microscopies, all based on X-ray magnetic circular dichroism (XMCD), to better reveal the three-dimensional spin texture of the system. Since iron generally shows a higher magnetic dichroism signal than nickel, the X-ray energy was always tuned to the Fe L_3 edge (708 eV), unless otherwise stated. Also, since sample oxidation may shift the energy peak, we always performed an energy scan to set the photon energy at the maximum absorption value. The X-ray beam direction was set nearly perpendicular to the nanowire axis to maximize the magnetic contrast of the transverse components of the magnetization and to avoid confusion with the longitudinal component.

4.2.1 X-ray chemical imaging

The three-dimensional magnetic and chemical configuration in photoemission electron microscopy (PEEM) microscopy is obtained at the shadow of the object. This is because the technique itself is surface-sensitive, as only photo-emitted electrons from the top of the sample reach the detector (see Sec. 2.4.2). However, if we study an object whose width is short enough to allow the transmission of photons through the whole cross section until the outer substrate, there will be photons shooting the shadow of the object and thus emission of electrons carrying volume information. Usually, the shadow lies directly next to the object, so the information that it carries from the bottom of the object is hidden. However, if the wire is elevated by, for example, two other wires, the shadow will be fully accessible. This is the case shown in Figure 4.3a, where it is displayed a shadow-PEEM X-ray absorption spectroscopy (XAS) image at the Fe L_3 edge of a 120 nm diameter Permalloy nanowire with 40 nm-long chemical modulations. This specific wire is incidentally lying on top of other two wires, making its shadow fully visible. Note the increase in spatial resolution at the shadow, which is 3.5 times larger than the width of the sample along the X-ray beam direction. The reason

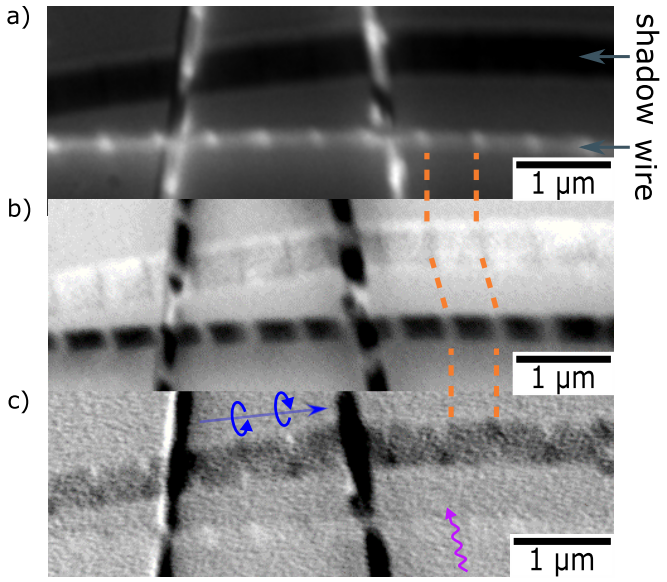

Figure 4.3: Shadow-PEEM imaging of a 120 nm diameter Permalloy nanowire with 40 nm-long $Fe_{20}Ni_{80}$ chemical modulations. **a)** XAS at the Fe L_3 edge shows the wire and its shadow. The microscope focus was set at the shadow, and the X-ray direction was almost perpendicular to the wire axis (purple arrow). The orange dashed lines guide the location of two chemical modulations. Chemical modulations appear brighter at the wire. **b)** The chemical contrast image was obtained by subtracting two XAS images taken at the Fe and Ni L_3 edges. Chemical modulations appear brighter at the wire and darker at the shadow. **c)** XMCD image reveals axial magnetization in the Permalloy segments and curling magnetization at the chemical modulations. Blue arrows indicate the magnetization direction. Adapted from [142].

is the X-ray incidence angle of 16° with respect to the plane of the substrate. This increase in width directly implies a considerable increase in spatial resolution, making it reasonable to set the focus of the image on the shadow. The X-ray beam direction is nearly perpendicular to the wire axis as indicated by the purple arrow.

An additional and outstanding feature of X-ray imaging is its chemical sensitivity, which implies that different compositions can be probed just by tuning the X-ray energy to its absorption peak. In PEEM microscopy, bright contrast at the surface reflects high absorption (more photo-emitted electrons), so we would expect that the Fe-rich chemical modulations to appear bright at the Fe L_3 edge due to their higher absorption. Consequently, the Permalloy segments should appear darker. This is evidenced in the XAS image in Figure 4.3a. However, at the shadow no chemical information is revealed since the length of the chemical modulations is at the limit of the spatial resolution. Therefore, to enhance the chemical susceptibility we performed a chemical contrast image by subtracting two XAS images, one taken at the Fe L_3 edge (708 eV) and the other at the Ni L_3 edge (854 eV). With this we can highlight the changes in the chemical composition as shown in Figure 4.3b. Here, we notice again that the Fe-rich chemical modulations show brighter contrast at the wire and darker contrast at the shadow. The contrast at the shadow is reversed since more electrons emitted from the wire implies more photons absorbed in the wire and thus less photons transmitted. On the other hand, the Ni-rich Permalloy segments show the opposite contrast to the Fe-rich modulations, as expected.

4.2.2 Curling magnetization at the chemical modulations

The three-dimensional magnetic configuration is displayed in the XMCD image in Figure 4.3c. The magnetic contrast at the shadow reveals a lack of magnetic contrast within the Permalloy segments. Since the X-ray direction is nearly perpendicular to the wire axis (purple arrow), this implies that the magnetization is

longitudinal along the wire axis in these regions, consistent with the holographic measurements in Figure 4.2. On the other hand, a bipolar magnetic contrast is detected at the top and bottom of the chemical modulations, whereas at their center no magnetic contrast is detected. The top, center, or bottom region of the shadow reflects the magnetic distribution of the top, center, or bottom region of the nanowire. So based on the magnetic contrast detected, at the top of the chemical modulation, the magnetization direction is perpendicular to the wire axis, and at the bottom as well, but in the opposite sense. The rotation of the magnetization around the nanowire axis implies that the top and bottom of the nanowire have directions of magnetization parallel or anti-parallel to the X-ray beam, leading to bright and dark contrast. However, in the central region, the sum of the transversal magnetization components canceled out along the path of the X-ray beam through the sample, thus no magnetic contrast is detected. This corresponds to a curling configuration [298] of the magnetization at the chemical modulations.

Curling for different geometries

Curling magnetization occurs spontaneously at the chemical modulations, and its circulation is random at rest, as shown and sketched by the blue arrows in Figure 4.3c. We investigated this phenomenon for different diameters, D, and chemical modulation lengths, ℓ. For the smallest studied diameter and lengths ($D = 70\,\text{nm}$ and $\ell = 20\,\text{nm}$), no curling configuration was detected at the chemical modulations (orange dashed lines in Figure 4.4a) by XMCD-PEEM. However, since $\ell = 20\,\text{nm}$ is slightly below the spatial resolution, we cannot fully confirm the absence of curling. Apart from this, we evidenced curling magnetization in the chemical modulations and axial magnetization in the Permalloy segments for the rest of the diameters and chemical modulation lengths considered. In particular, curling has been proven for $D = 90\,\text{nm}$ and $\ell = 40\,\text{nm}$ and $\ell = 60\,\text{nm}$ by XMCD-scanning transmission X-ray microscopy (STXM) (Figure 4.4b and Figure 4.4c, respectively), for $D = 110\,\text{nm}$, $D = 130\,\text{nm}$ and $D = 160\,\text{nm}$ and $\ell = 20\,\text{nm}$, $\ell = 60\,\text{nm}$ and $\ell = 150\,\text{nm}$ by XMCD-X-ray ptychography (Figure 4.4d, Figure 4.4f and Figure 4.4h, respectively), and lastly, for $D = 130\,\text{nm}$ and $\ell = 100\,\text{nm}$ by XMCD-transmission X-ray microscopy (TXM) (Figure 4.4g). In Sec. 5.2.1, we detail a method to go one step beyond conventional XMCD images by translating the magnetic contrast into a curling angle. Since this code requires special care with the input parameters, which vary in each type of microscopy, we could not dedicate time enough to quantify the XMCD contrast for the different systems shown in Figure 4.4, however, this study is on-going.

4.3 Physics driving curling magnetization

In the previous section, we reported the existence of curling at the chemical modulations. Here, we identify and analyze quantitatively the mechanism that drives this behavior. To start, let us examine a common and well-understood situation: a longitudinally magnetized homogeneous nanowire (with no chemical modulation). In this case, the mismatch of magnetization at the wire ends generates surface magnetic charges, σ_{ch}, of areal density M_{s}. This implies an associated dipolar field, thus an increase in the total energy of the system. To ease this, a rotation of the magnetization around the wire axis occurs at the wire ends to minimize the magnetostatic energy, yet with a cost in exchange energy. This curling at the wire ends is a well-known phenomenon [104, 115, 299]. Initially, it was introduced in the 50s to explain Brown paradox, and highlight a possible pathway for magnetization reversal before reaching the anisotropy fields. Finally, note also that curling at the wire ends does not remove magnetic charges from the system but instead spreads them as volume charges inside the body. By topology, the total charge is conserved.

4.3.1 Curling magnetization driving force

In the case of a chemically modulated nanowire, the observation of a bipolar MFM contrast at the chemical modulations (Figure 4.1) reveals the occurrence of positive charges at one interface and negative at the other

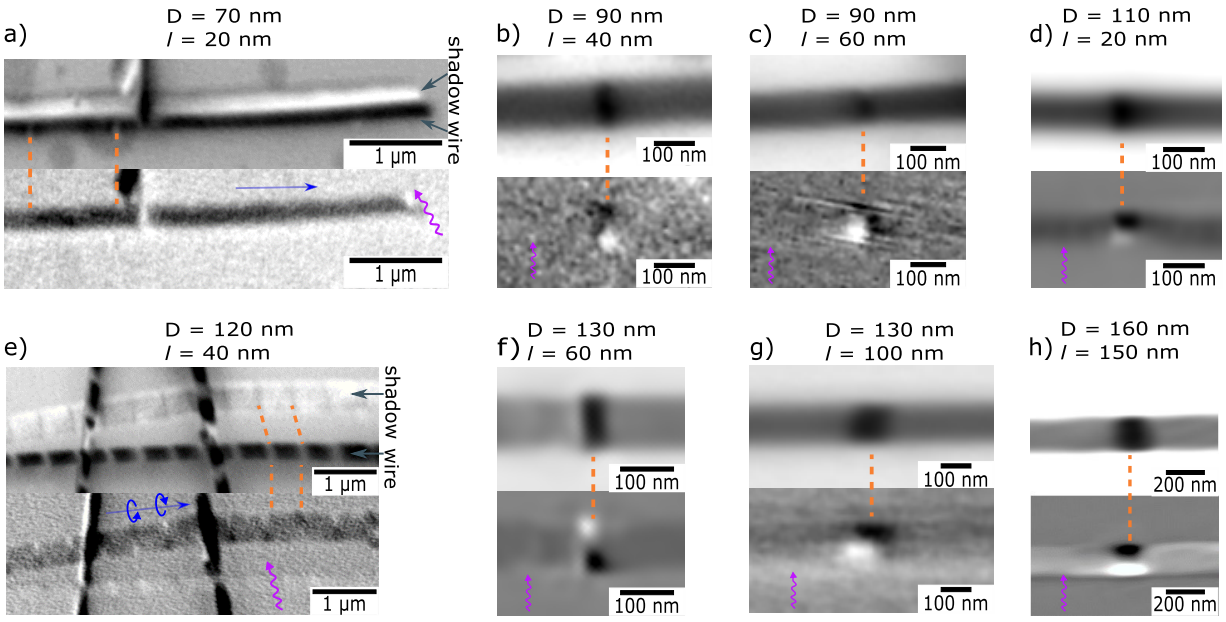

Figure 4.4: Curling magnetization in chemically-modulated nanowires evidenced by different microscopy techniques coupled to XMCD. The top and bottom of each subfigure correspond to a XAS and a XMCD image, respectively. **a)** Corresponds to PEEM imaging for $D = 70\,\text{nm}$ and $l = 20\,\text{nm}$ and **e)** for $D = 70\,\text{nm}$ and $l = 20\,\text{nm}$. **b)** corresponds to STXM imaging for $D = 90\,\text{nm}$ and $l = 40\,\text{nm}$ and **c)** for $D = 90\,\text{nm}$ and $l = 60\,\text{nm}$. **d)** corresponds to X-ray ptychography imaging for $D = 110\,\text{nm}$ and $l = 20\,\text{nm}$, **f)** for $D = 130\,\text{nm}$ and $l = 60\,\text{nm}$ and **h)** for $D = 160\,\text{nm}$ and $l = 150\,\text{nm}$. Finally, **g)** corresponds to TXM imaging for $D = 130\,\text{nm}$ and $l = 100\,\text{nm}$. Orange dashed lines indicate the location of the chemical modulations. The purple arrows indicate the direction of the X-ray beam.

interface. This distribution is indeed expected for uniform axial magnetization as it is shown in the schematics in Figure 4.5a. The red and grey arrows show the direction of magnetization and of the dipolar field respectively, and the negative and positive blue symbols correspond to the surface magnetic charges. This schematics reflects that the strength of the dipolar field $H_{\text{dip.}}$ depends on the quantity of surface charges, i.e., on the magnitude of the mismatch of magnetization. In our case, magnetization mismatch at the modulation interfacefo an axially magnetized state is non-negligible $\mu_0\sigma_{\text{ch}} = \pm\mu_0(M_2 - M_1) = 1.4\,\text{T} - 1\,\text{T} = 0.4\,\text{T}$. The magnitude of σ_{ch}, and thus of the dipolar energy E_{d}, can be decreased by creating volume charges of opposite sign, $\rho_{\text{ch}} = -\text{div}\mathbf{M}$, as sketched with the yellow arrows in Figure 4.5b. This is the purpose of curling magnetization at the chemical modulations. However, it is important to note that ρ_{ch} are non-local thus a perfect screening is not possible. Note also that the total magnetic charge is conserved an equal to zero, due the antisymmetric distribution of charges.

The comparison of the total magnetic energy between a system with axial magnetization and a relaxed system with curling magnetization was studied with micromagnetic simulations. The system size simulated is based on two Permalloy segments of 150 nm at each side of the chemical modulation. The result is shown in Figure 4.5c for a diameter $D = 130\,\text{nm}$ and chemical modulation lengths ranging from $\ell = 10\,\text{nm}$ to 120 nm. The energy associated with an axial state (black dots) raises exponentially as ℓ increases reaching its maximum at $14 \times 10^{-17}\,\text{J}$ for $\ell = 120\,\text{nm}$. This is not only because the size of the higher magnetization region is larger, but also because the extent of the dipolar field increases. On the other hand, for curling magnetization there is a slow and linear increase of the total energy reaching its maximum at $3 \times 10^{-17}\,\text{J}$ for $\ell = 120\,\text{nm}$. This drop is a direct consequence of the decrease of the dipolar energy E_{d} associated with curling at the cost of exchange energy E_{ex}.

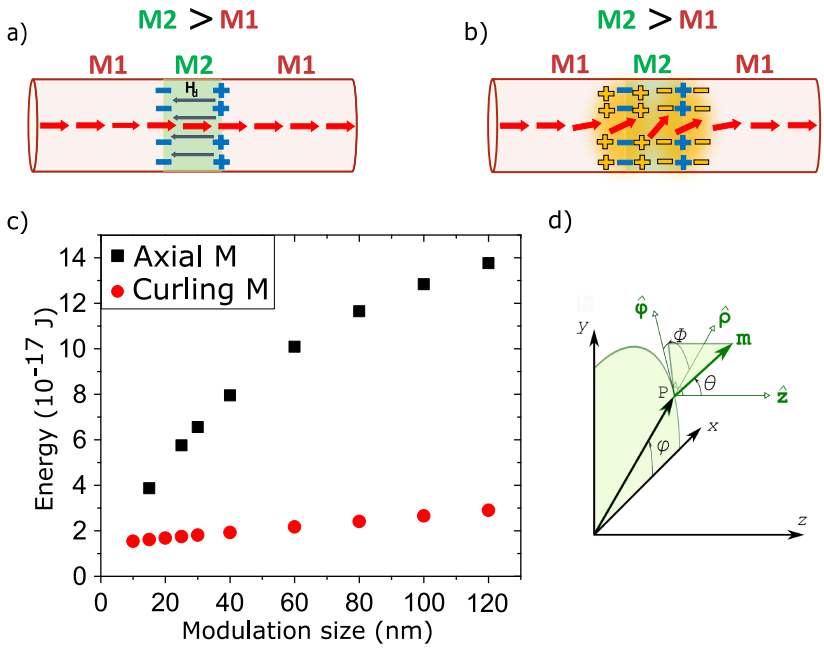

Figure 4.5: Scheme of the magnetic charge distribution at a chemical modulation for **a)** axial and **b)** curling magnetization states, for $M_2 > M_1$. The volume charges are shown in yellow, while the surface ones are shown in blue. **c)** shows the total magnetic energy of the axial and curling magnetization states, versus the modulation length for a diameter of 130 nm. Adapted from [142].

4.3.2 Analytical model of charge screening

In order to gain a more precise understanding of the physics of charge screening and to predict general features, we have developed a simplified analytical model. First, we considered only one interface, thus mimicking the case of a very long chemical modulation. The geometry consists of two semi-infinite cylinders with different spontaneous magnetization (Figure 4.6a). With this setup, charge screening of an isolated interface can be studied. Then, the radial and azimuthal contributions to exchange were neglected, thus large diameters ($D \gg \Delta_d$) are best described. The last main assumption was to assume perfect screening of σ_{ch} and ρ_{ch}. This assumption was made with the physics in mind, to maximize the gain provided by the screening of surface charges, or in other words, to obtain the largest screening for a given amount of σ_{ch}. However, perfect screening is not possible since, as mentioned above, ρ_{ch} distributes non-locally, so it cannot perfectly screen the interface charges.

The model aims to determine the maximum curling angle and the characteristic length scale of the problem. The curling angle θ is defined as the angle of magnetization away from the axial direction and towards the azimuthal direction $\hat{\varphi}$ (see schematics in Figure 4.5d). As the magnetization must remain longitudinal on the axis by symmetry, the curling angle must depend on the distance from the axis. We use an ansatz to describe the variation of the curling angle θ along r:

$$\theta(r,z) = \theta(R,z)\sin\left(\frac{\pi}{2}\frac{r}{R}\right). \tag{4.1}$$

where R is the wire radius, r is the distance to the axis, and z is the coordinate along the wire axis. This ansatz was proven to accurately describe the spatial variation of θ along r [184, 185], minimizing the (residual) exchange energy. The magnetization state of the system is then fully determined by the function $\theta(R,z)$, with $\theta(R,-\infty) = 0$ in the axial magnetized domain, being the domain material for $z < 0$, and modulation material for $z > 0$. In this simplified example, $\theta(R,+\infty)$ stands for the final curling angle at the surface of the modulation at a distance z sufficiently far from the interface.

Throughout the derivation of the analytical model, we make use of the following integrations:

$$\int r\sin^2\left(\frac{\pi}{2}\frac{r}{R}\right)\mathrm{d}r = \frac{r^2}{4} - \frac{Rr}{2\pi}\sin\left(\frac{\pi r}{R}\right) - \frac{R^2}{2\pi^2}\cos\left(\frac{\pi r}{R}\right). \tag{4.2}$$

$$\begin{aligned}\int r\cos\theta(r,z)\mathrm{d}r = &\frac{r^2}{2} - \frac{\theta^2(R,z)}{2}\times \\ &\left[\frac{r^2}{4} - \frac{Rr}{2\pi}\sin\left(\frac{\pi r}{R}\right) - \frac{R^2}{2\pi^2}\cos\left(\frac{\pi r}{R}\right)\right].\end{aligned} \tag{4.3}$$

$$\left\langle m_z(r,z)\right\rangle_r \approx 1 - \theta^2(R,z)\left(\frac{1}{4}+\frac{1}{\pi^2}\right) \tag{4.4}$$

$$\left\langle m_z^2(r,z)\right\rangle_r \approx 1 - \frac{\theta^2(R,z)}{2}\left(1+\frac{4}{\pi^2}\right) \tag{4.5}$$

The latter two equations relate to the radial areal average, and make use of the expansion of $\cos\theta$ to second order, *i.e.*, up to θ^2.

The local density of surface charge is defined as:

$$\sigma_{\mathrm{ch}}(r) = (M_2 - M_1)\cos\theta(r,0). \tag{4.6}$$

The total surface charge is obtained integrating throughout the full disk cross section. Also the cosine can be expanded to second order:

$$\begin{aligned}\Sigma_{\mathrm{ch}} &= -\int_0^R 2\pi\rho(M_2-M_1)\cos\theta(\rho,0)\mathrm{d}\rho \\ &= -2\pi(M_2-M_1)\int_0^R \rho\left[1-\frac{\theta^2(\rho,0)}{2}\right]\mathrm{d}\rho \\ &= -2\pi(M_2-M_1)\int_0^R \rho\left[1-\frac{1}{2}\theta^2(0)sin^2\frac{\pi\rho}{2R}\right]\mathrm{d}\rho \\ &= -2\pi(M_2-M_1)\left[\frac{R^2}{2}-\frac{1}{2}\theta^2(0)\left(\frac{R^2}{4}+\frac{2R^2}{2\pi^2}\right)\right] \\ &= -\pi R^2(M_2-M_1)\left[1-\theta^2(R,0)\left(\frac{1}{4}+\frac{1}{\pi^2}\right)\right].\end{aligned} \tag{4.7}$$

Some sanitary checks can be done for the case of of axial magnetization $\theta(R,0)=0$ and full curling $\theta(R,0)=\pi/2$ at the interface:

$$\theta(R,0)=0 \Rightarrow \Sigma_{\mathrm{ch}} = -\pi R^2(M_2-M_1) \tag{4.8}$$

$$\theta(R,0)=\pi/2 \Rightarrow \Sigma_{\mathrm{ch}} = -\pi R^2(M_2-M_1)\left[1-\frac{\pi^2}{4}\times\left(\frac{1}{4}+\frac{1}{\pi^2}\right)\right] < 0 \tag{4.9}$$

a negative angle is obtained due to the remaining charges because of the axial magnetization at the axis. Due to the assumed absence of radial magnetization, the local density of volume charge is only resulting from longitudinal variations:

$$\rho_{\mathrm{ch}} = -\frac{\partial M_z(z)}{\partial z} = -M_{1,2}\frac{\partial\left[\cos\theta(r,z)\right]}{\partial z} \tag{4.10}$$

Upon integration along both the radius r and the longitudinal coordinate z, we derive the total volume charge:

$$
\begin{aligned}
P_{\mathrm{ch}} &= \int_0^R 2\pi\rho\mathrm{d}\rho \int_{-\infty}^{+\infty} \rho_{\mathrm{ch}}(z)\mathrm{d}z \\
&= -2\pi \int_0^R \rho\mathrm{d}\rho \left[\int_{-\infty}^0 M_1 \frac{\partial \cos\theta(\rho,z)}{\partial z}\mathrm{d}z + \int_0^{+\infty} M_2 \frac{\partial \cos\theta(\rho,z)}{\partial z}\mathrm{d}z \right] \\
&= -2\pi \int_0^R \rho\mathrm{d}\rho \left\{ M_1(\cos\theta(\rho,0)-1) + M_2\left[\cos\theta(\rho,\infty)-\cos\theta(\rho,0)\right] \right\} \\
&= -2\pi \left[-M_1 \int_0^R \rho\mathrm{d}\rho + (M_1-M_2)\int_0^R \rho\cos\theta(\rho,0)\mathrm{d}\rho + M_2 \int_0^R \rho\cos\theta(\rho,\infty)\mathrm{d}\rho \right] \\
&= \pi R^2 \left(\frac{1}{4}+\frac{1}{\pi^2}\right)\left\{ M_1\theta^2(R,0) + M_2\left[\theta^2(R,+\infty)-\theta^2(R,0)\right] \right\}
\end{aligned}
\tag{4.11}
$$

where the first term in the brackets corresponds to charges in the Permalloy segment ($z<0$) and the second term to charges in the chemical modulation ($z>0$). Eq.(4.11) depends on the curling angle at the interface $[\theta(R,0)]$ and also applies at a sufficient distance far from the interface $[\theta(R,\infty)]$. To simplify this, we assume equal distribution of P_{ch} at both sides of the interface to achieve a quadrupolar distribution and minimize the energy of the system. This sets the condition:

$$
\theta^2(R,0) = \frac{M_2}{M_1+M_2}\,\theta^2(R,+\infty), \tag{4.12}
$$

this allows to simplify the expression for the total volume charges:

$$
\begin{aligned}
P_{\mathrm{ch}} &= \pi R^2 \left(\frac{1}{4}+\frac{1}{\pi^2}\right) \times \frac{2M_1M_2}{M_1+M_2}\,\theta^2(R,+\infty) \\
&= \pi R^2 \left(\frac{1}{4}+\frac{1}{\pi^2}\right) \times 2M_1\theta^2(R,0).
\end{aligned}
\tag{4.13}
$$

We now equal the total surface and volume charges in absolute value [Eq.(4.7) and Eq.(4.13)], assuming full screening. This leads to the following expressions:
$\Sigma_{\mathrm{ch}} + P_{\mathrm{ch}} = 0 \Rightarrow$

$$
\theta(R,+\infty) = \sqrt{\frac{M_2-M_1}{M_2}\,\frac{1}{\frac{1}{4}+\frac{1}{\pi^2}}} \approx \sqrt{2.85\frac{M_2-M_1}{M_2}} \tag{4.14}
$$

$$
\theta(R,0) = \sqrt{\frac{M_2-M_1}{M_2+M_1}\,\frac{1}{\frac{1}{4}+\frac{1}{\pi^2}}} \approx \sqrt{2.85\frac{M_2-M_1}{M_2+M_1}} \tag{4.15}
$$

Some sanitary checks can be done:

$$
M_2 = M_1 \Rightarrow \theta(R,+\infty) = \theta(R,0) = 0, \tag{4.16}
$$

since no change of material would imply axial magnetization, as expected for a magnetically soft nanowire.

$$
M_1 = 0, M_2 \neq 0 \Rightarrow \theta(R,+\infty) = \theta(R,0) = \frac{1}{\frac{1}{4}+\frac{1}{\pi^2}} \tag{4.17}
$$

this would be the case of the end of a non-modulated nanowire where all the possible surface charges, σ_{ch}, are converted into volume charges, ρ_{ch}. Eq.(4.17) gives a value ≈ 1.69 which is slightly more than the expected angle to cancel all surface charges $\pi/2 \approx 1.57$. This comes from the hypothesis of the global compensation

of charges: as no volume charge is created close to the axis for which magnetization remains longitudinal, more charges need to be created away from the axis.

Based on the expansion $m_z(r=R,z)=\cos\theta(R,z)\approx 1-\theta^2(R,z)/2$, we can rewrite these two equations for the longitudinal magnetization:

$$m_z(R,0) \approx 1-1.42\frac{M_2-M_1}{M_2+M_1} \tag{4.18}$$

$$m_z(R,+\infty) \approx 1-1.42\frac{M_2-M_1}{M_2}. \tag{4.19}$$

Note that the model does not predict the evolution of $\theta(r,z)$ along z, but it predicts the curling angle at a distance sufficiently far from the interface [Eq.(4.14)] and at the interface [Eq.(4.15)]. Since exchange is disregarded, these expressions only depend on M_s so they slightly overestimate the curling angle. In our specific case of Permalloy ($Fe_{20}Ni_{80}$) segments with modulations of inverted composition ($Fe_{80}Ni_{20}$), we get: $\theta(R,0)\approx 51°$ [$m_z(R,0)\approx 0.63$] and $\theta(R,+\infty)\approx 61°$ [$m_z(R,+\infty)\approx 0.45$].

4.3.3 Model vs micromagnetic simulations: two semi-infinite cylinders

The previous section shows the details of the analytical model that aims to reproduce the charge screening mechanism responsible for the curling at the modulations. It predicts general features based on the approaches taken such as disregarding exchange, perfect screening ($\Sigma_{ch}=P_{ch}$), infinite length modulation, and the same amount of volume charges on both sides of the interface ($P_{ch,1}=P_{ch,2}$). In this section, we will assess its validity by comparing it with micromagnetic simulations performed with *FeeLLGood* code. Moreover, we will get not only the accurate value of $\theta(R,0)$ and $\theta(R,+\infty)$ but also its evolution along z. Realistic finite-size modulations will be considered in the next section.

The model mimics the case of an infinitely long modulation to reproduce the physics behind charge screening at one interface, disregarding the impact of interactions between interfaces. To reproduce this situation with micromagnetic simulations, we have chosen as model system a nanowire with two semi-infinite segments: a Permalloy segment for $z<0$ and a $Fe_{80}Ni_{20}$ segment for $z>0$. The outer view of the relaxed configuration is shown in Figure 4.6a. The white arrows indicate the direction of magnetization and the color code the value of axial magnetization at the surface, $m_z(R,z)$. Starting from axial magnetization in the Permalloy segment magnetization curls in the $Fe_{80}Ni_{20}$ modulation, as expected due to the mismatch of magnetization at the interface (orange dashed line).

The longitudinal profile of magnetization at the surface is shown in Figure 4.6b. The evolution along the axial direction z of the curling angle [$\theta(R,z)$] and longitudinal magnetization [$m_z(R,z)$] at the surface of the nanowire is shown for systems with diameters of 90 nm, 100 nm, 110 nm, 120 nm, 130 nm and 140 nm. The part of the Permalloy segment far from the interface shows axial magnetization [$m_z(R,-\infty)=-1$ and $\theta(R,-\infty)=0$], as defined in the analytical model. However, as we approach the interface along z, curling increases, starting with the systems with larger diameter since they have a larger volume to screen and also less cost in radial exchange energy, followed by the systems with a lower diameter. Nevertheless, the slope $\partial m/\partial z$ is the same for all the diameters, indicating that the distribution of volume charges P_{ch} is equal and maximized for all. This highlights a characteristic length of screening of 22 nm, a value that will be explained in the following section. After the interface, for $z>0$, the curling angle decreases more rapidly for the smallest diameters since the total cost of radial exchange scales linearly with D. Once the curling angle has reached a plateau, there is no more screening benefit. For the largest diameters, the curling angle is constant over a large distance and its value is near to the one predicted with the analytical model $\theta_{model}(R,+\infty)=61°$, indicated by the purple dashed line. We can therefore confirm the validity of our model. However, the value predicted at the interface $\theta_{model}(R,0)=51°$, indicated by the purple cross, is 10° higher than the one obtained with micromagnetic simulations $\theta(R,0)=41°$. This is because the model assumes an equal share of magnetic charges at both sides of the interface, whereas in a real system, there are more

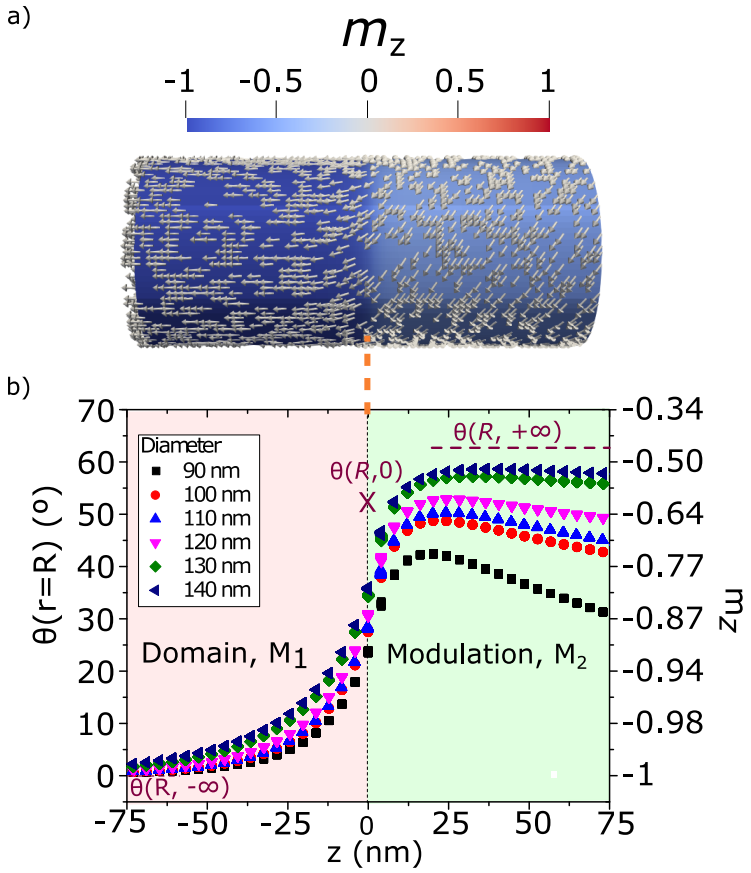

Figure 4.6: Micromagnetic simulations at rest of bi-segmented nanowires. **a)** Outer view of the magnetization distribution (white arrows) at the surface for a diameter of 150 nm. The left ($z<0$) and right ($z>0$) regions correspond to the Permalloy and $Fe_{80}Ni_{20}$ segments, respectively. The color code indicates the value of axial magnetization, $m_z(R,z)$, and the orange dashed line indicates the location of the interface. **b)** The curling angle $\theta(R,z)$ and longitudinal magnetization $m_z(R,z)$ at the surface along the axial direction $\hat{\mathbf{z}}$ for diameters ranging from 90 nm up to 140 nm. The predictions of the curling angle obtained by the analytical model at the interface $\theta(R,0)$ and sufficiently far from it $\theta(R,+\infty)$ are highlighted by a cross and a horizontal dashed line, respectively. Adapted from [142].

charges within the modulation since $d\theta/dz$ is higher for a given cost in exchange. In addition, the model assumes local screening at the interface while, in the real system, the distribution of volume charges ρ_{ch} is non-local, thus less amount ρ_{ch} at the interface implies a lower value of $\theta(R,0)$. In addition, magnetization cannot curl in the axis thus no ρ_{ch} can occur in this location. For $z\to+\infty$ the magnetization would turn back to axial, but the model does not reflect this because it disregards exchange.

4.4 Micromagnetic simulations: finite-length chemical modulation

In this section we will study the practical case of interest: a chemical modulation with finite length. Firstly, we will delve into the study and comparison with experiments of the in-plane induction field **B**, dipolar field **H** and unnormalized axial magnetization $\mathbf{m}_z$ across the chemical modulation. Then, we will explore the profile of axial magnetization $\mathbf{m}_z$ and curling angle θ for different system geometries. With this, we aim to conclude the study on the micromagnetic behavior of chemically-modulated nanowires.

4.4.1 Analysis of the magnetic induction field study for axial vs curling magnetization

In section 4.1.2, we experimentally studied with electron holography the in-plane induction field **B** in a Permalloy nanowire with 130 nm of diameter and 60 nm-long $Fe_{80}Ni_{20}$ chemical modulations. The quantification of **B** in the Permalloy segments provided a value of $B = 0.93\,\mathrm{T}\,(\approx 7.40\times10^5\,\mathrm{A\cdot m^{-1}})$, which is very close to the expected value for a longitudinally magnetized wire, where $H = 0$ and thus $B = \mu_0 \times \mathrm{M} = 1\,\mathrm{T}\,(\approx 8\times10^5\,\mathrm{A\cdot m^{-1}})$. However, inside the chemical modulation, we obtained $B = 0.80\,\mathrm{T}\ (\approx 6.36\times10^5\,\mathrm{A\cdot m^{-1}})$ which is $\approx$ 53 % lower than expected for a longitudinally magnetized modulation, if we consider that $M = 1.76\,\mathrm{T}\ (\approx 14\times10^5\,\mathrm{A\cdot m^{-1}})$, $H \approx 0$ and thus $B \approx \mu_0 M$. However, this value is overestimated since the dipolar field **H** is non-negligible at the chemical modulations. Here comes the relevance of micromagnetic simulations since they allow us to disentangle **M**, **H** and **B**. In any case, these results indicate that magnetization is not axial at the chemical modulation. We have got a more complete picture of the situation, which let us know that curling magnetization occurs at the chemical modulations and that the driving force behind this is charge screening close to the interfaces. We can now study the magnetic induction field in-depth to obtain a more comprehensive view of the micromagnetics of the system.

To do so, we have performed micromagnetic simulations with *mumax3* code in a system made of a Permalloy nanowire with 120 nm of diameter and a 40 nm-long $Fe_{80}Ni_{20}$ chemical modulation. We started by setting the configuration to axial magnetization within the whole system, i.e., non-relaxed configuration, in order to explore the isolated effect of the surface charges responsible for the dipolar field **H**. This situation is analogous to a linear combination of an axially magnetized Permalloy wire of magnetization M_1 ($H = 0$) and a disk of magnetization M_2, and thus the dipolar field of the system is the dipolar field of the disk. The distribution of dipolar field **H** is shown in Figure 4.7a, where the color code represents the component of the dipolar field along the axial direction $\hat{\mathbf{z}}$, H_z, and the arrows the direction of **H**. We obtain a value of $H_z = 0$ at the ends of the Permalloy segments since we are considering an infinitely long wire (i.e., no impact from surface charges at the edges). As we get closer to the chemical modulation, the dipolar field **H** (the arrows) starts to tilt away from the axial direction, due to the stray field loop arising from the chemical modulation interfaces. The extent of the dipolar field originated by the surface charges at the interfaces can be appreciated by the blue cloud close to the interfaces. The strong red color within the chemical modulation reflects the high cost in dipolar energy E_d that this axial configuration entails ($H_z \approx 0.60\,\mathrm{T}$). The change in the intensity of this red color gradient along the transversal direction reflects that H_z decreases with the distance from the axis r, as expected since at the axis, all the contributions from the rest of the wire are added up. The schematics below show the distribution and sign of the surface charges (blue symbols) σ_{ch} at the interface for an axial magnetization along $\hat{\mathbf{z}}$ (red arrows) and the dipolar field (blue arrows). The orange arrows represents the location of the line profiles shown in Figure 4.7b and Figure 4.7c, and the orange dashed line shows the location of the modulation interfaces.

Figure 4.7b and Figure 4.7c show the z component of the non-normalized **M**, **H** and $\mathbf{B}/\mu_0$ along the $\hat{\mathbf{z}}$, at the surface ($r = R$) and at the axis ($r = 0$), respectively. Since the magnetization is axial within the whole system, the evolution of M_z (red line) is a step function with the M values set in the simulation ($M = 1\,\mathrm{T} = 8\times10^5\,\mathrm{A\cdot m^{-1}}$ for Permalloy and $M = 1.75\,\mathrm{T} = 14\times10^5\,\mathrm{A\cdot m^{-1}}$ for the $Fe_{80}Ni_{20}$ modulation). The dipolar field (blue curve) is non-zero, even for large z values, reflecting once more the cost in dipolar energy that axial magnetization brings to the system. $H_{z,axis} = -0.5\,\mathrm{T}\,(\approx -4\times10^5\,\mathrm{A\cdot m^{-1}})$ at the center of the chemical modulation ($z = 0$), which is twice the value at the surface $H_{z,surface} = -0.25\,\mathrm{T}\,(\approx -2\times10^5\,\mathrm{A\cdot m^{-1}})$, as expected. The shape of $H_{z,surface}$ within the modulation is due to the reduction of $\cos(\theta)$ created by the projection on the axis. At the axis $\theta = 0$ thus the value of $H_{z,axis}$ is maximized. Another relevant check to do is that the subtraction of $H_{z,axis}$ peaks at both sides of the interface gives $\Delta M = M_{,Permalloy} - M_{,Fe_{80}Ni_{20}} = 6\times10^5\,\mathrm{A\cdot m^{-1}}$. The evolution of the in-plane induction field (black curve) is the sum $M_z + H_z$. Far form the modulation, $B \approx \mu_0 M$ since the dipolar field $H \approx 0$. However, inside the modulation $B << \mu_0 M$ due to the non-negligible dipolar field arising from the interfaces. This explains why the holographic results described in Sec. 4.1.2 cannot extract the value of M in a system where the contribution of the dipolar field is non-zero.

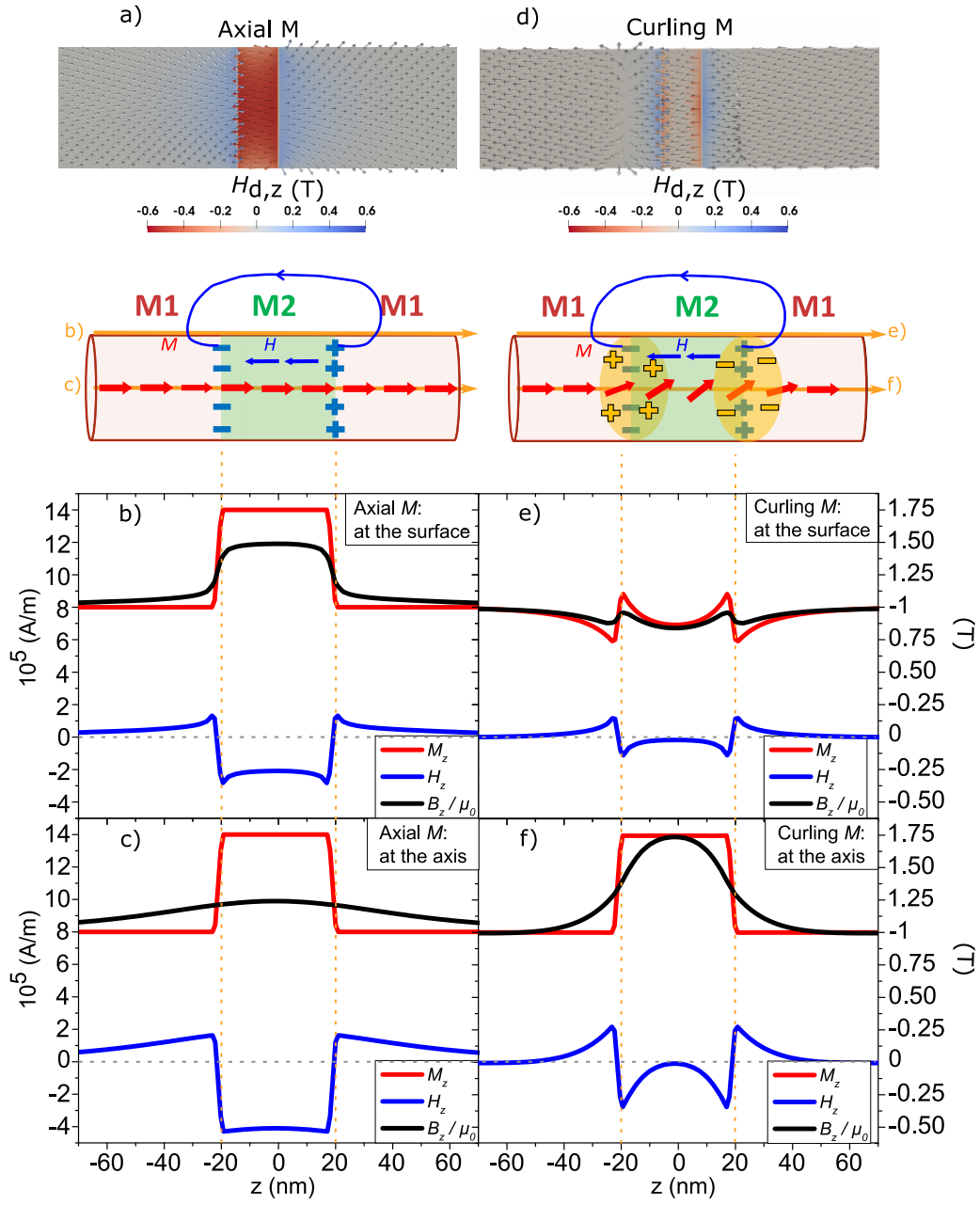

Figure 4.7: Study by micromagnetic simulations with mumax3 code of the unnormalized M, H and B/μ_0 for a system with $D = 120\,\text{nm}$ and $\ell = 40\,\text{nm}$. **a)** and **b)** show the distribution of dipolar field **H** for a system with axial and curling magnetization at the modulation, respectively. The color-code indicates the amplitude of the component of the dipolar field along the z-axis, H_z. The schematics below indicates the distribution of surface (blue symbols) and volume (yellow cloud) magnetic charges, the direction of magnetization (red arrows) and dipolar field (blue arrows). The orange arrows indicate line profiles that are represented in the graphs below. **c)**, **d)**, **e)** and **f)** show the evolution of the z-component unnormalized M, H and B/μ_0 along the $\hat{\mathbf{z}}$ direction for a non-relaxed axial magnetization state at the surface (**b)**) and at the axis (**c)**) and a curling magnetization configuration at the surface (**e)**) and at the axis (**f)**). The orange dashed line indicates the location of the interfaces and the grey dashed line the location where $H = 0$.

Finally, let's note that B_z/μ_0 is continuous at the interfaces, as expected from the electromagnetic continuity equations.

For the real case, where curling magnetization at the chemical modulations occurs, the situation is quite different. Figure 4.7d shows a significant reduction in the amplitude of H_z in comparison with the axial magnetization case (Figure 4.7a). First, in the Permalloy domains, the flux closure of the dipolar field arising from the modulation occurs at distances z very close to the modulation thus the extent and amplitude of the dipolar field are largely reduced. Finally, $H_z \approx 0$ inside the modulation, which implies that a full screening of magnetic charges has been achieved. The schematic below shows the distribution and sign of the surface charges (blue symbols) σ_{ch} and volume charges (yellow cloud) ρ_{ch} around the interfaces for a curling magnetization state, and the direction of magnetization (red arrows) and dipolar field (blue arrows). The orange arrows represent the location of the line profiles shown in Figure 4.7e and Figure 4.7f and the orange dashed line the location of the interfaces. Figure 4.7e and Figure 4.7f show the evolution of the z-component of the unnormalized M, H and B/μ_0 along the $\hat{\mathbf{z}}$ at the surface ($r = R$) and at the axis ($r = 0$), respectively. We may highlight the impact of the appearance of volume charges to screen surface charges: first, the long-range stray field is suppressed since H_z is reached very rapidly; second, the value of $M_{z,surface}$ at the center of the modulation is equal to the one in the Permalloy domains or in other words the continuity in the longitudinal magnetization, m_z reflects full screening of magnetic charges. In addition, the value obtained of the in-plane induction field at the center of the modulation is $B = 0.84\,\mathrm{T} = 6.70 \times 10^5\,\mathrm{A \cdot m^{-1}}$, in good agreement with the values obtained experimentally ($B_{exp} = 0.80\,\mathrm{T} = 6.36 \times 10^5\,\mathrm{A \cdot m^{-1}}$). Although experimentally we cannot avoid the effect of the integrated stray field outside of the sample, the experimental value obtained in section 4.1.2 differs by less than 5 % from the one obtained with micromagnetic simulations. Finally, only axial magnetization is allowed, thus at the axis (Figure 4.7f) and, therefore, there is only an impact of surface charges in this curve. The absence of screening is reflected by the higher amplitude of $H_{d,z}$ and also by the larger z distance it takes to reach $H_z = 0$ within the modulation and outside of it. At the center of the modulation $H_z = 0$ at the axis but not on the surface,reflecting the overcompensation of volume charges at the surface due to the lack of them at the axis.

4.4.2 Curling magnetization study vs geometry

Until now, we have described in detail the mechanism that drives curling magnetization at the chemical modulations, exploring the associated decrease of the dipolar field. The validation of our analytical model confirmed that charge screening is the driving force of this phenomenon. The next step is to explore the physics of curling depending on the diameters and chemical modulations length considered. To do so, I have performed this study using FeeLLGood micromagnetic code in a system with a diameter $D = 90\,\mathrm{nm}$ ($D = 130\,\mathrm{nm}$) composed of two Permalloy segments of 100 nm (150 nm) separated by a chemical modulation of variable length ℓ ranging from 10 nm to 120 nm.

In Figure 4.7 we showed micromagnetic simulations of the non-normalized M, H and B/μ_0 along the $\hat{\mathbf{z}}$. In the following, we will see an analogous situation by studying the normalized magnetization component along $\hat{\mathbf{z}}$: m_z. Figure 4.8a shows the surface view of the micromagnetic state at rest for a system with $D = 90\,\mathrm{nm}$ and $\ell = 60\,\mathrm{nm}$. The arrows indicate the direction of magnetization $\mathbf{m}$ and the color code its axial component m_z. The $\hat{\mathbf{z}}$ axis corresponds to the axial direction as indicated in the schematics at the left. As previously anticipated, axial magnetization ($m_z = -1$) is observed in the Permalloy domains whereas a rotation of the magnetization occurs at the chemical modulation (red color). This rotation is maximum at the surface and decreases progressively until it reaches zero at the axis, following the ansatz described in Equation 4.1. The evolution of the curling angle $[\theta(r,z)]$ at the center of the modulation and along the radial direction $\hat{\rho}$ is shown in the cross-section view of Figure 4.8b. For this geometry, the maximum curling angle reached is $\theta(R) \approx 60°$, and $m_z(R) \approx -0.5$. However, these values strongly depend on the geometry of the system.

The longitudinal magnetization $m_z(R,z)$, and the curling angle, $\theta(R,z)$, at the surface of the nanowire

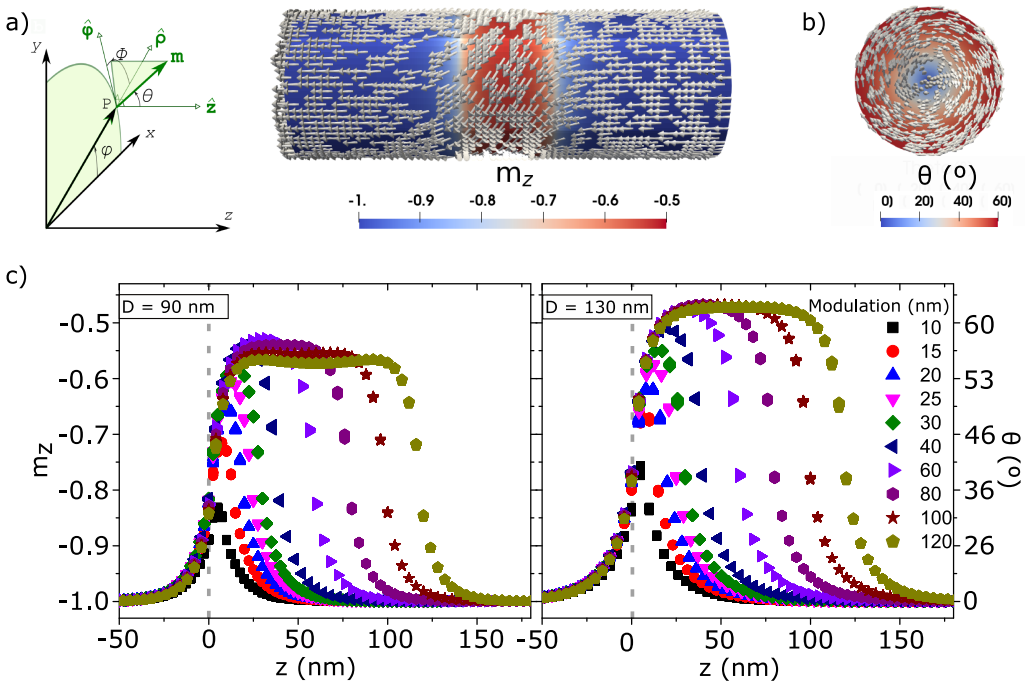

Figure 4.8: Micromagnetic simulations of Permalloy nanowires at rest with a $Fe_{80}Ni_{20}$ chemical modulation at the center. **a)** Outer view and **b)** cross-section view at the center of the modulation, for $D = 90\,\text{nm}$ and $\ell = 60\,\text{nm}$. **c)** Line profiles of unitless longitudinal magnetization $\mathbf{m}_z$ along the **z** direction at the surface of wire with chemical modulation lengths ℓ =10 nm to 120 nm for $D = 90\,\text{nm}$ (left) and $D = 130\,\text{nm}$ (right). The grey dashed line marks the start of the chemical modulation. Adapted from [142].

are shown in Figure 4.8c for two wire diameters [$D = 90\,\text{nm}$ (left figure) and $D = 130\,\text{nm}$ (right figure)], and for ℓ values from 10 nm to 120 nm. The grey dashed line indicates the start of the chemical modulation at $z = 0$. The slope of the curves $[\partial m_z(R,z)/\partial z]$ is equal for all ℓ values. This quantity is directly related to the distribution of volume charges (ρ_{ch}). This shows a characteristic length scale for the screening phenomena, which is of $\Delta_{\text{mod}} = 22\,\text{nm}$, larger than the dipolar exchange length of any of the two materials. This value is defined as $\partial\theta/\partial z = 1/\Delta_{\text{mod}}$, similar to $\Delta_{\text{d}} = \sqrt{\frac{A}{K_{\text{d}}}}$. This length occurs at the distance that would be required to rotate magnetization by 1 rad. Note also that $m_z(R,z)$ curves have nearly an inversion symmetry across each interface, unlike $\theta(R,z)$ curves, implying that screening is largely symmetric. In a general case, magnetization may rotate by 1 rad over a distance $\Delta_{\text{d}} = \sqrt{2A/(\mu_0 M_s^2)}$. However, here magnetization rotates by 1 rad over a distance $\Delta_{\text{mod}} = 22\,\text{nm}$. There are two reasons for the large value of $\Delta_{\text{mod}} = 22\,\text{nm}$. On the one hand, the charges scale with $M_2 - M_1$ and not with the full magnetization. This explains why for short chemical modulation lengths typically from 10 nm to 40 nm, a plateau of curling is not reached due to the associated cost in exchange of the longitudinal variation of magnetization, competing with the gain in magnetostatic energy, which requires a certain distance to rotate magnetization. On the other hand, the screening effect on both sides of the interface further decreases the effective charge and thus the magnetostatic energy.

As the length of the chemical modulation (ℓ) increases, $m_z(R,z)$ increases since there is more z distance to curl. It reaches a plateau at $\ell = 40\,\text{nm}$, consistent with the length scale $\Delta_{\text{mod}} = 22\,\text{nm}$ highlighted above. A maximum curling angle of $\theta = 58°(|m_z| = 0.53)$ is found for $\ell = 60\,\text{nm}$ for $D = 90\,\text{nm}$, and $\theta = 62°(|m_z| = 0.47)$ for $\ell = 80\,\text{nm}$ for $D = 130\,\text{nm}$. Above these ℓ values, the center of the modulations does not have the highest $\theta(R)$ value anymore and becomes the weakest magnetic part. The reason is that, above a certain ℓ value the maximum screening is achieved at z value related to the characteristic length scale. There, at larger z value there is no need to further rotate **m**. This results in the absence of magnetic charges and a

constant $\theta(R)$ is kept, driven by exchange. However, if the ℓ value is very large, a decrease in the curling angle occurs to lower the cost in exchange. This occurs with a very large length scale to avoid a high density of charges, and thus of dipolar energy. An example of this is shown by the light green curve in Figure 4.8c for $\ell = 120\,\text{nm}$. In Sec. 5.5.2 we will see the impact that this weaker region has under a current stimulus.

4.4.3 Case of chemical modulation with lower magnetization

In this section we consider the case of a chemical modulation with lower magnetization than the rest of the nanowire $M_2 = 8\times10^5\,\text{A}\cdot\text{m}^{-1} < M_1 = 14\times10^5\,\text{A}\cdot\text{m}^{-1}$. This situation is beyond the experimental scope of this manuscript. However, we consider it worthwhile to briefly mention the main differences.

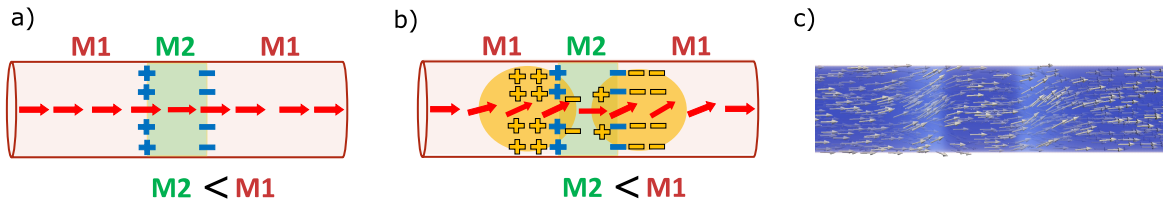

Figure 4.9: **a)** Scheme of magnetic charge distribution for a chemical modulation of lower magnetization ($M_2 < M_1$) for a non-relaxed axially magnetized state. Surface and volume charges are represented in blue and yellow respectively. Red arrows represent the magnetization direction. **b)** Micromagnetic simulations of $D = 90\,\text{nm}$ $Fe_{80}Ni_{20}$ nanowire with $\ell = 100\,\text{nm}$ $Fe_{20}Ni_{80}$ chemical modulation. White arrows represent the magnetization direction and the color code axial magnetization.**c)** Scheme of magnetic charges for the magnetic configuration shown in **b)**. Adapted from [142].

The distribution of magnetic charges for a nanowire with axial magnetization (red arrows) where $M_2 < M_1$ is drawn in Figure 4.9a. In this case, the sign of the surface magnetic charges $\sigma_{ch} = (M_1 - M_2)$ is positive at the first interface and negative at the second one. These signs are opposite to the case studied in this work, where the magnetization is higher at the modulation (see Figure 4.7). This should have a direct consequence of the magnetization distribution. Figure 4.9b shows the outer view micromagnetic simulations performed with *mumax3* code of a system based on a $Fe_{80}Ni_{20}$ nanowire with $D = 90\,\text{nm}$ and $\ell = 100\,\text{nm}$ $Fe_{20}Ni_{80}$ chemical modulation at its center. The color code represents the axial magnetization value, and the arrows represent the direction of magnetization. It displays axial magnetization inside the Ni-rich modulation, curling outside the modulation interfaces and axial magnetization far from the modulation. This magnetic configuration can be understood in terms of the magnetic charges of the system. The curling outside the modulation induces positive magnetic volume charges $\rho_{ch} = -\frac{\partial M_z(z)}{\partial z}$ outside the first modulation, and negative outside the second modulation (see Figure 4.9c). Whereas inside the modulation, opposite volume charges occur next to the interface.We can understand it as follows: to reduce dipolar energy, the volume charges are spread towards the M_1 segments, providing curling magnetization for several tens of nanometers. This phenomenon is similar to the curling at the ends of a nanowire where part of the surface charges are converted into volume charges of the same sign that extend to a certain axial distance instead of just at the interface, leading to a curling state and a decrease of the dipolar energy [300]. Here if M_2 would be zero, this case would be mimicked. For the case of a finite lower magnetization chemical modulation, the repulsion between magnetic charges would extend the cloud of magnetic volume charges outwards of the chemical modulation. In this case, axial magnetization would appear at the modulation and curling magnetization next to the interfaces. Axial magnetization at the modulation is allowed due to the appearance of volume charges of the opposite sign that screen the surface charges.

4.5 Conclusions

In this chapter, we have combined experiments, analytical modeling, and micromagnetic simulations to provide a consistent qualitative and quantitative view of the micromagnetics of high-magnetization longitudinal material modulations in cylindrical nanowires. As a matter of generalization, the conclusions were exposed in terms of reduced magnetic quantities, but we have focused our study on a system based on a Permalloy ($Fe_{20}Ni_{80}$) nanowire with periodic $Fe_{80}Ni_{20}$ chemical modulations. We have considered diameters, D, ranging from 70 nm to 160 nm and chemical modulation lengths, ℓ, ranging from 20 nm to 150 nm.

Firstly, we demonstrated with MFM imaging that magnetic charges of opposite signs occur at the interfaces of the chemical modulations due to the magnetization mismatch. Afterwards, we detected, with electron holography, the in-plane induction field, which showed the stray field arising from the chemical modulation, and inside the wire a tendency to keep a uniform induction flux. Then, the three-dimensional micromagnetic configuration at rest measured with XMCD technique revealed curling magnetization around the wire axis at the chemical modulations and axial magnetization in the Permalloy domains. This configuration was observed for all the geometries considered except for $D = 70\,\text{nm}$ and $\ell = 20\,\text{nm}$ whose size is below the spatial resolution of PEEM microscopy.

Curling magnetization at the modulations occurs to screen the surface charges with the volume charges thus decreasing the dipolar energy of the system. This driving mechanism was proven with an analytical modeling at one interface for an infinitely-long modulation. A limit in the curling angle $\theta(R) \approx 60°$, specific to the M_s values used, was obtained and confirmed quantitatively with micromagnetic simulations. The effectiveness of the screening of magnetic charges was evidenced by the reduction of the dipolar field $H \approx 0$ within the modulation in comparison with $H \approx 3 \times 10^5\,\text{A}\cdot\text{m}^{-1}$ for an axial magnetized case. In terms of geometry dependence, the curling angle θ increases with modulation length, ℓ, until a plateau is reached . Above it, θ decreases with ℓ due to an increasing cost in exchange. This defines a characteristic length scale, $\Delta_{\text{mod}} = 22\,\text{nm}$, a few times larger than the dipolar exchange length of either material and expected to scale with $\sqrt{2A/\mu_0(M_2 - M_1)^2}$.

Chapter 5

Curling in modulations controlled by magnetic fields

In this chapter, we study the micromagnetic response of the curling magnetization at the chemical modulations to a quasi-static external magnetic field or to the Œrsted magnetic field associated with a nanosecond current pulse. This is helpful for further understanding the dynamics of domain walls in this system, which we will consider in Chap. 6. We will start by studying the response of the curling amplitude to an axial magnetic field. To correlate the experimental information with theory, the explanation of a code to quantify the experimental X-rays absorption coefficients, spot size and background intensity will be detailed. This will be followed by the development of a code to quantify the X-ray magnetic circular dichroism (XMCD) contrast into the curling angle $\theta(R)$. This will be used to extract the curling angle reduction under an axial magnetic field. These results will be compared with micromagnetic simulations. The second part of the chapter will focus first, on the experimental evidence of circulation switching driven by the Œrsted field. The switching mechanism is understood by means of time-resolved imaging and micromagnetic simulations. The calculation of the critical current and its dependence on geometrical parameters is provided. This is a required step to later understand the collective interaction of a domain wall and a chemical modulation under this external stimulus.

In this chapter, I have contributed to the X-ray magnetic imaging measurements, performed and post-treated the micromagnetic simulations, created the code to quantify the spot size and background intensity for X-ray absorption spectroscopy (XAS) experimental images, and contacted electrically the nanowires. Regarding time-resolved X-ray imaging I was unable to perform the experiments as they took place during the last stage of the writing period of this manuscript. Therefore, the measurements were performed by OLIVIER FRUCHART and AURÉLIEN MASSEBOEUF. MICHAEL SCHOBITZ wrote the code to quantify the curling angle from the experimental data. DARIA GUSAKOVA and OLIVIER FRUCHART collaborated in the discussions of micromagnetic simulations. OLIVIER FRUCHART contributed to setting the different approaches to quantify X-ray measurements for non-homogeneous magnetization states. AURÉLIEN MASSEBOEUF performed Fresnel and scanning transmission electron microscopy (STEM)-electron energy loss spectroscopy (EELS) imaging and contributed to the electrical contacting of the nanowires. CHRISTOPHE THIRION developed the sample holders for high-frequency pulses and was in charge of all the electronics setup. The main results that are presented are published in [142].

5.1 Reduction of curling angle under axial magnetic field

In this section, we will study the response of the system to an axial magnetic field applied parallel to the magnetization direction **M** ,i.e., no reversal process is desired. Our aim is to experimentally study the reduction of the curling angle under this external stimulus, which may inform us of the system's precise parameters

(geometry, magnetism, anisotropy...). To do so, we performed high-spatial-resolution magnetic imaging by XMCD X-ray ptychography at the HERMES beamline of SOLEIL synchrotron. The magnetic field was applied using a remote permanent magnet perpendicular to the X-ray beam, and thus almost along the nanowire's axis. The sample had a 10° angular offset in order to be sensitive to the magnetization direction in the Permalloy domains. The schematic of the setup is shown in Figure 5.1b. We applied a magnetic field from 1 mT to 90 mT and imaged under field. The ptychographic reconstructed XMCD images under field are shown in Figure 5.1a for a 130 nm diameter Permalloy nanowire with $\ell = 60$ nm modulations. At first sight there is barely any qualitative difference between the images, but it may be noted the decrease of magnetic contrast when increasing the amplitude of the magnetic field.

Figure 5.1c shows the XMCD line profiles across the modulation (yellow line in the inset) for different external fields. With this, we conclude that curling magnetization at the chemical modulation is somehow robust under an axial magnetic field. However, even though curling remains, its strength decreases as H_{ext} increases. Note that the contrast reaches almost 20 %, highlighting the increased spatial resolution obtained with X-ray ptychography (usually for photoemission electron microscopy (PEEM) or scanning transmission X-ray microscopy (STXM) less than 5 % contrast is obtained). The asymmetry of the profiles is due to the

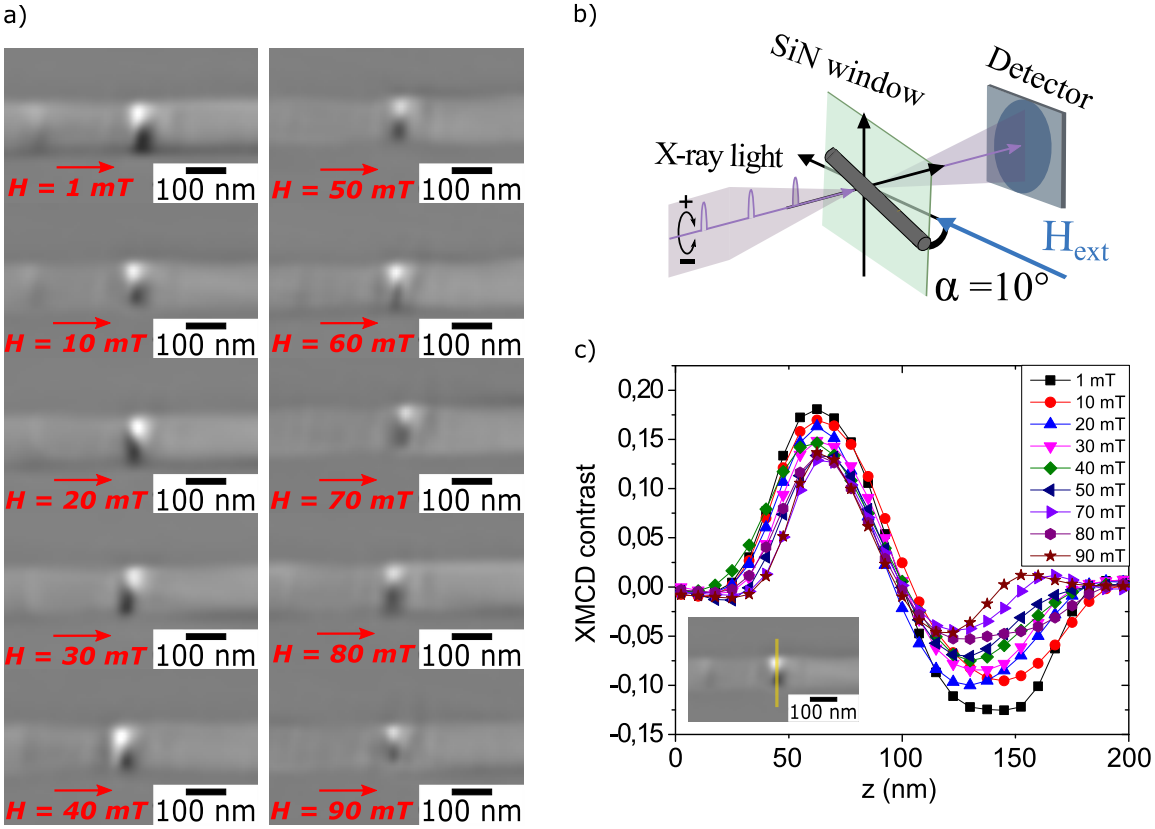

Figure 5.1: Curling angle reduction under axial magnetic field. **a)** Reconstructed XMCD ptychographic images at the Fe L_3 edge under a magnetic field. The system is a 130 nm diameter Permalloy nanowire with a $\ell = 60$ nm $Fe_{80}Ni_{20}$ chemical modulation at the center. The magnetic field was applied with an angular offset of 10° with respect to the axial direction and its amplitude is written in red. **b)** Schematic of X-ray ptychography setup for a 10° rotation of the nanowire with respect to the transverse direction of the X-ray beam. **c)** XMCD contrast line profiles across the modulation for several values of the applied magnetic field. The inset shows the XMCD X-ray ptychography image and the line profile (yellow). Figure adapted from [142].

10° sample rotation that enhances the absorption of one particular direction of magnetization. However, these comments remain qualitative and do not allow us to correlate the magnetic contrast with the angle of curling. This cannot be done directly since the absorption of X-rays is not linear but follows an exponential behavior. To go beyond, in the next sections it is detailed first, how to fit the XAS data, and second, how to fit the XMCD data. Then, the variation of curling angle under axial field will be stimated and compared with micromagnetics simulations.

5.2 Quantitative analysis of X-ray absorption spectroscopy images

5.2.1 Theory of X-ray absorption

In the following, we introduce an analytical model to extract quantitative information from experimental XAS images of magnetic cylindrical objects. First of all, let us define the behavior of X-ray light when traveling through matter. When an incident X-ray beam travels through a material of width l, its intensity decays exponentially with distance. The mean free path of the photons is defined as $\lambda = 1/\mu$, where μ is the linear absorption coefficient. Its value depends on the chemical composition, the X-ray energy, and the projection of the magnetization along the X-ray beam direction ($\hat{\mathbf{k}}$). It is typically expressed as:

$$\mu = \mu_0 + P\frac{\Delta\mu}{2}\left(\hat{\mathbf{k}}\cdot\mathbf{m}\right), \tag{5.1}$$

where μ_0 is the dichroism-independent absorption coefficient for zero beam polarization ($P = 0$), which is equivalent to the average of the absorption coefficients for opposite-handed polarizations [$\mu_0 = (\mu_+ + \mu_-)/2$]. The value of $\Delta\mu$ corresponds to the dichroic signal calculated by the difference between the absorption coefficients for a left (μ_-) and right (μ_+) circularly-polarized X-ray beam when $P = 1$ and the magnetization is parallel to the X-ray beam ($\Delta\mu = \mu_- - \mu_+$). In our case, the materials under study are soft magnetic materials based on FeNi alloys. Since experimentally the highest dichroic signal is obtained at the Fe L_3 edge and our experiments were performed at that edge, we will choose this particular X-ray energy for our analysis. As a reference, we use the experimentally-determined absorption coefficients from the literature [301] that are summarized in Table 5.1. Columns 5 and 6 show the expected absorption coefficients of Permalloy ($Fe_{20}Ni_{80}$) and $Fe_{80}Ni_{20}$ respectively, and calculated as follows:

$$\mu_{\text{th,Permalloy}} = 0.2\mu_{\text{th,Fe}} + 0.8\mu_{\text{th,Ni}} \tag{5.2}$$

$$\mu_{\text{th,Fe}_{80}\text{Ni}_{20}} = 0.8\mu_{\text{th,Fe}} + 0.2\mu_{\text{th,Ni}} \tag{5.3}$$

Returning to the experimental part, we cannot directly measure the absorption of X-rays but the transmitted photon intensity I after traveling across the wire by using the Beer-Lambert law:

$$I(x) = I_0 \exp\left[-\mu l(x)\right] \tag{5.4}$$

where I_0 is the incident intensity and $l(x)$ is the position-dependent length of the path that the X-ray follows across the sample. In our case, this is along the cross-section of the cylindrical nanowire, thus $l(x) = 2\sqrt{F(R^2 - x^2)}$, where R is the radius of the nanowire and $F = 1/\cos(\alpha)$ is a geometrical adjustment made for an angle α of the rotation of the sample holder (see angles representation in Figure 5.1b). Consequently, if we measure I for left (I_-) and right (I_+) circularly-polarized light and we know the projection of magnetization along the X-ray beam ($\mathbf{k}\cdot\mathbf{m}$), it is possible to extract the relative or experimental absorption coefficients, $\Delta\mu$ and μ_0. We call them relative since the value depends on the experimental setup and part of the signal is hidden within background noise and optics limitations. The method to extract these coefficients was provided by MICHAEL SCHÖBITZ and it is well-detailed in the Supplementary Material of [260]. In

this work, we could not apply this method since the $\mathbf{k}\cdot\mathbf{m}$ is unknown due to the curling at the chemical modulations, yet we will describe it briefly.

The methodology considers the experimental line profile of the transmitted intensity through the nanowire and fits it with the profile expected analytically from the Beer Lambert law for the same object properties. Since Eq.(5.4) assumes an infinitely-small X-ray spot size, a convolution of the theoretical profile with a normalized Gaussian is made beforehand, to account for the experimental image blur due to the finite spatial resolution. After the convolution, the maximum theoretical absorption decreases and it increases at the wire edges, such that the integrated absorption remains fixed. The Gaussian describing the experimental spot size is:

$$I_{\text{spot}}(x) = \exp\left(-\frac{x^2}{2\sigma^2}\right) \tag{5.5}$$

where σ is the standard deviation and its value is a measure of the spot size. Therefore, the fit of the experimental XAS profile with the convolution of Eq.(5.4) and Eq.(5.5), in a situation where $\mathbf{k}\cdot\mathbf{m}=0$, gives the diameter, μ and σ as free parameters. This method allows us to calculate the spot size and absorptivity coefficients of a particular experimental dataset. However, as highlighted in [260], the obtained values for μ may be three times smaller than the theoretical predictions due to experimental effects. These include the background intensity signal that reaches the detector without crossing the sample, whose primary sources are higher-order light and leakage of the zone plane center. In addition, the accuracy value of the wire diameter is a source of scattered results. Providing that we are interested in using these results to calculate the tilt angle of magnetization, the accuracy on the determination of σ and μ is a key step.

However, the model explained above cannot be used in a system where the magnetization is not uniform along the X-ray path since knowing the projection of $\hat{\mathbf{m}}$ along the X-ray beam direction $\hat{\mathbf{k}}$ at each point in the path is a prerequisite. In addition, it brings $\Delta\mu$ as a new unknown parameter. This brings to us a more complex situation to be solved since, at the chemical modulation, the magnetization rotates around the axis and the angle of rotation varies along the radius. In the following, I detail the different approaches adopted to determine, with the highest reliability, the values of σ and μ in a $Fe_{80}Ni_{20}$ chemically-modulated Permalloy nanowire. The aim is to provide the most appropriate inputs to the second model where the tilt of magnetization at the chemical modulation will be extracted from the fit. The system under study is a 130 nm diameter Permalloy nanowire with a Fe-rich chemical modulation of 60 nm length as shown in Figure 5.1a. The sample holder has an angular rotation of $\alpha = 10°$.

Edge	μ_{th} (nm^{-1})	Fe	Ni	Py	$Fe_{80}Ni_{20}$	$\Delta\mu_{\text{Py}}$	$\Delta\mu_{Fe_{80}Ni_{20}}$	$\mu_{0,\text{Py}}$	$\mu_{0,Fe_{80}Ni_{20}}$
Fe L_2	μ_-	0.030	≈ 0	0.006	0.024	-0.002	-0.008	0.007	0.028
	μ_+	0.040	≈ 0	0.008	0.032				
Fe L_3	μ_-	0.090	≈ 0	0.018	0.072	0.008	0.032	0.014	0.056
	μ_+	0.050	≈ 0	0.010	0.040				
Ni L_2	μ_-	0.017	0.017	0.017	0.017	-0.003	-0.001	0.019	0.018
	μ_+	0.017	0.021	0.020	0.018				
Ni L_3	μ_-	0.017	0.053	0.046	0.024	0.011	0.002	0.041	0.023
	μ_+	0.017	0.040	0.035	0.022				

Table 5.1: Linear X-ray absorption coefficients (μ) of Fe, Ni, Permalloy (Py) and $Fe_{80}Ni_{20}$ at the L_2 and L_3 edges for circularly left (-) and right (+) polarization. The data for pure elements are extracted from [301]. The value of $\Delta\mu = \mu_- - \mu_+$ corresponds to the dichroic signal and $\mu_0 = (\mu_+ + \mu_-)/2$ corresponds to the non-dichroic signal.

5.2.2 Analysis assuming absence of background intensity

Since the μ and $\Delta\mu$ values from literature do not correspond to the experimental ones, for reasons such as the above mentioned, we proceed to calculate them from the experimental XAS data at the Fe L_3 edge. We will assume that there is no background intensity, which is the added signal that reaches the detector but did not travel through the sample. We will use the model described above, where the μ coefficients are extracted from the fit of the experimental XAS profile with the Gaussian-convoluted theoretical XAS profile. Since magnetization is axial in the Permalloy segments, we will extract the experimental absorption coefficients at this location, where $\mathbf{k}\cdot\mathbf{m}=0$. Then, the experimental absorption coefficients at the chemical modulations, $\Delta\mu_{\mathrm{exp,Fe_{80}Ni_{20}}}$ and $\mu_{0,\mathrm{exp,Fe_{80}Ni_{20}}}$, are calculated as $\Delta\mu_{\mathrm{exp,Fe_{80}Ni_{20}}} = r_1 \times \Delta\mu_{\mathrm{th,Fe_{80}Ni_{20}}}$ and $\mu_{0,\mathrm{exp,Fe_{80}Ni_{20}}} = r_2 \times \mu_{0,\mathrm{th,Fe_{80}Ni_{20}}}$. The ratios are $r_1 = \Delta\mu_{\mathrm{th,Py}}/\Delta\mu_{\mathrm{exp,Py}}$ and $r_2 = \mu_{0,\mathrm{th,Py}}/\mu_{0,\mathrm{exp,Py}}$.

Let us start with the determination of the μ_+ and μ_- experimental coefficients in the Permalloy segment. As mentioned above, the magnetization is axial in this region. However we have to take into account that there is a 10° offset of the sample holder. Thus, the projection of $\hat{\mathbf{m}}$ along $\hat{\mathbf{k}}$ is $\hat{\mathbf{m}}\cdot\hat{\mathbf{k}} = \cos 80^\circ = \sin 10^\circ$. Note that the model based on Eq.(5.4) extracts a μ coefficient that depends on $\mathbf{m}$ as shown in Eq.(5.1). It assumes that $\hat{\mathbf{k}}$ is parallel to $\hat{\mathbf{m}}$, but we are interested in extracting the dichroic-independent coefficient. To solve this, we will call effective coefficients the ones extracted by the model ($\mu_{\mathrm{eff},+}$ and $\mu_{\mathrm{eff},-}$) and from them, we will extract the dichroic-independent coefficients μ_+ and μ_-. Eq.(5.4) comes from the following derivative:

$$\frac{dI}{dl} = -I\left[\frac{1}{2}\mu_+\left(1\pm\mathbf{k}\cdot\mathbf{m}\right)+\frac{1}{2}\mu_-\left(1\mp\mathbf{k}\cdot\mathbf{m}\right)\right] = -I\mu_{eff}, \tag{5.6}$$

which involves that if $\mathbf{k}\cdot\mathbf{m}=0 \Rightarrow \mu_{\mathrm{eff}} = (\mu_+ + \mu_-)/2 = \mu_{\mathrm{eff},+} = \mu_{\mathrm{eff},-}$, and if $\mathbf{k}\cdot\mathbf{m}=\pm 1 \Rightarrow \mu_{\mathrm{eff},+} = \mu_+$ and $\mu_{\mathrm{eff},-} = -\mu_u$, respectively. The effective absorption coefficient for circularly-right polarized light in Eq.(5.6) is

$$\mu_{\mathrm{eff},+} = \frac{1}{2}\left(\mu_+ + \mu_-\right) + \frac{\mathbf{k}\cdot\mathbf{m}}{2}\left(\mu_+ - \mu_-\right), \tag{5.7}$$

and the effective absorption coefficient for circularly left polarized light in Eq.(5.6) is

$$\mu_{\mathrm{eff},-} = \frac{1}{2}\left(\mu_+ + \mu_-\right) - \frac{\mathbf{k}\cdot\mathbf{m}}{2}\left(\mu_+ - \mu_-\right). \tag{5.8}$$

Therefore the sum of Eq.(5.7) and Eq.(5.8) results in

$$\mu_+ + \mu_- = \mu_{\mathrm{eff},+} + \mu_{\mathrm{eff},-} \tag{5.9}$$

and the subtraction of Eq.(5.7) and Eq.(5.8) results in

$$\mu_+ - \mu_- = \frac{\mu_{\mathrm{eff},+} - \mu_{\mathrm{eff},-}}{\mathbf{k}\cdot\mathbf{m}} \tag{5.10}$$

Now we can extract the absorption coefficient by adding Eq.(5.9) and Eq.(5.10) to extract μ_+, and subtracting Eq.(5.9) and Eq.(5.10) to extract μ_-. This results in the following:

$$\mu_+ = \frac{1}{2}\left(\mu_{\mathrm{eff},+} + \mu_{\mathrm{eff},-}\right) + \frac{1}{2}\left(\frac{\mu_{\mathrm{eff},+} - \mu_{\mathrm{eff},-}}{\mathbf{k}\cdot\mathbf{m}}\right) \tag{5.11}$$

$$\mu_- = \frac{1}{2}\left(\mu_{\mathrm{eff},+} + \mu_{\mathrm{eff},-}\right) - \frac{1}{2}\left(\frac{\mu_{\mathrm{eff},+} - \mu_{\mathrm{eff},-}}{\mathbf{k}\cdot\mathbf{m}}\right). \tag{5.12}$$

The inset in Figure 5.2a shows the XAS image of a Permalloy nanowire with $d = 130\,\mathrm{nm}$ and a 60 nm $Fe_{80}Ni_{20}$ chemical modulation. The pink line across the Permalloy segment corresponds to the experimental intensity profile shown by the pink curve in the graph. The theoretical intensity profile obtained from

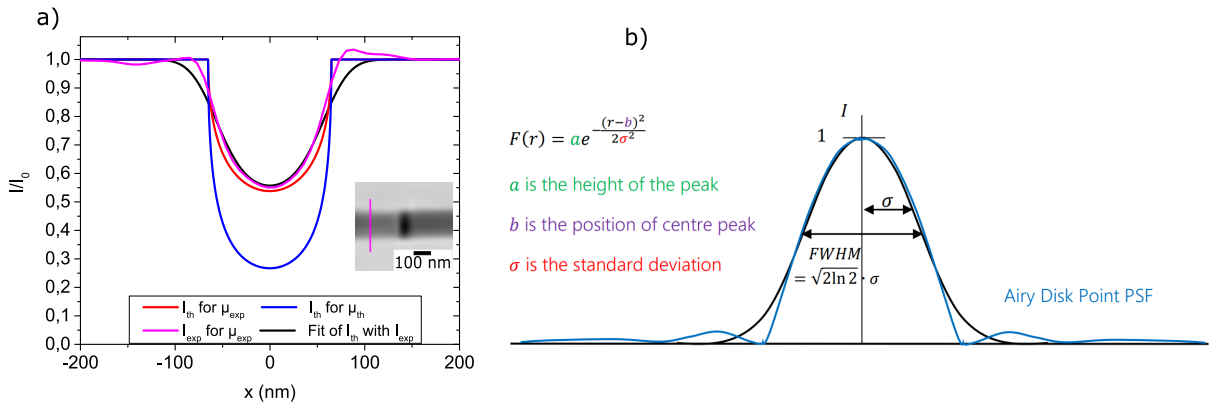

Figure 5.2: **a)** Transmitted intensity profiles across a Permalloy segment in a nanowire. The inset shows a XAS image of a Permalloy nanowire with $d = 130\,\text{nm}$ and a 60 nm $Fe_{80}Ni_{20}$ chemical modulation. The pink line indicates the location and direction of the intensity profile. The pink curve shows the experimental intensity profile (pink line in the inset). The red and blue curves represent the theoretical transmitted intensities obtained for a theoretical (μ_{th}) and experimental fitted (μ_{exp}) absorption coefficient values, respectively. The black curve shows the experimental profile (pink curve) fitted with the Gaussian-convoluted theoretical profile of μ_{exp} (red curve). **b)** The black curve is the Gaussian approximation of the Airy disk, which is shown by the blue curve. The Gaussian function is defined in the top left, with descriptions of the parameters. Adapted from [302].

Eq.(5.4) is shown in blue for the theoretical absorption coefficients ($\mu_{0,\text{th,Py}}$ and $\Delta\mu_{\text{th,Py}}$) and in red for the experimental or effective ones ($\mu_{0,\text{eff,Py}}$ and $\Delta\mu_{\text{eff,Py}}$). The effective values are extracted from the fit (black curve) of the Gaussian-convoluted theoretical profile with the experimental profile. It is important to note that, although the experimental data (pink curve) should overlap with the fit (black curve), this is not the case due to experimental reasons. An artifact at the wire edges due to the algorithm used to reconstruct the X-ray ptychography image leads to a value different from one out of the wire. Thus it is not possible to achieve a proper fit since either the depth of the curve or the edges of the wire may overlap, but not both. There is also a potential problem with the shape of the X-ray beam. We have assumed it follows a Gaussian profile, which is indeed a good approximation but for accuracy, we should have to do the convolution of an Airy pattern (blue curve in Figure 5.2b adapted from [302]) with the theoretical profile. Also note the sinusoidal trend of the Airy pattern that resembles the experimental profile.

Leaving aside these experimental limitations, we extracted the following values: $\mu_{\text{eff},+,\text{Py}} = 0.0044 \pm 0.002\,\text{nm}^{-1}$, $\mu_{\text{eff},-,\text{Py}} = 0.0050 \pm 0.002\,\text{nm}^{-1}$, and a spot size of $\sigma = 22 \pm 3\,\text{nm}$, where the uncertainty is the standard deviation of the data sets. This value is higher than the expected one of $\approx 10\,\text{nm}$. The rotation of $10°$ of the sample holder gives $\mathbf{k}\cdot\mathbf{m} = \sin 10°$, hence Eq.(5.11) and Eq.(5.12) result in $\mu_{+,\text{Py}} = 0.0030 \pm 0.002\,\text{nm}^{-1}$ and $\mu_{-,\text{Py}} = 0.0064 \pm 0.002\,\text{nm}^{-1}$, respectively. This gives $\Delta\mu_{\text{Py}} = 0.0034\,\text{nm}^{-1}$ and $\mu_{0,\text{Py}} = 0.0047\,\text{nm}^{-1}$, whose ratio is $\frac{\Delta\mu_{\text{Py}}}{\mu_{0,\text{Py}}} = 0.72$. If we compare it with the theoretical ratio $\frac{\Delta\mu_{\text{Py,th}}}{\mu_{0,\text{Py,th}}} = 0.57$, we can conclude that ours is 20 % higher. This inequality implies that there is a non-negligible background radiation reaching the detector and consequently we cannot extract the absorption coefficients at the Fe-rich modulation with this method. In addition, the value of the spot size is not accurate due to the non-negligible error of the fit. Finally, what is more striking is the fact that the experimental μ and $\Delta\mu$ values are ≈ 3 times smaller than the theoretical ones. This drives us to the next section, where background signal will be taken into account.

5.2.3 Analysis considering background intensity

In a situation with no background intensity, the ratio $\frac{\Delta\mu_{\mathrm{Py}}}{\mu_{0,\mathrm{Py}}}$ should match the theoretical one. However, we have seen above that the experimental ratio is 20 % higher. Therefore, in the following we proceed to determine the non-negligible background signal. In this second approach we will derive analytically through iterative solving the experimental absorption coefficients μ and background intensity I_{b}. Since the experimental images are obtained at the Fe L_3 edge, we assume that $\mu_{\mathrm{Fe_{80}Ni_{20}}} = 4 \times \mu_{\mathrm{Fe_{20}Ni_{80}}} = 4 \times I_{\mathrm{Py}}$. Considering a dimensionless intensity with $I = I_{\mathrm{wire}} + I_{\mathrm{b}}$, we can assume that

$$\begin{cases} I_{\mathrm{Py}} & = e^{-\mu l} + I_{\mathrm{b}} \\ I_{\mathrm{Fe_{80}Ni_{20}}} & = e^{-4\mu l} + I_{\mathrm{b}} \end{cases} \tag{5.13}$$

Therefore the equation to be solved is $I_{\mathrm{Py}} - I_{\mathrm{Fe_{80}Ni_{20}}} = e^{-\mu l} - e^{-4\mu l}$, which cannot be solved analytically. We proceed to an iterative solving using the variable $X = e^{-\mu l}$, where $X \lesssim 1$ and therefore $X^4 << 1$. For iteration number (0) we have:

$$\Rightarrow \begin{cases} X^{(0)} & \approx I_{\mathrm{Py}} - I_{\mathrm{Fe_{80}Ni_{20}}} \\ I_{\mathrm{b}} & \approx I_{\mathrm{Fe_{80}Ni_{20}}} \end{cases} \tag{5.14}$$

which shows that most of the signal coming from the Fe-rich modulation is background signal. For iteration number (1) where $X^{(1)} - X^{(0)^4} = X^{(1)} - (I_{\mathrm{Py}} - I_{\mathrm{Fe_{80}Ni_{20}}})^4 = I_{\mathrm{Py}} - I_{\mathrm{Fe_{80}Ni_{20}}}$ we obtain:

$$\Rightarrow \begin{cases} X^{(1)} & = e^{-ul} = I_{\mathrm{Py}} - I_{\mathrm{Fe_{80}Ni_{20}}} + (I_{\mathrm{Py}} - I_{\mathrm{Fe_{80}Ni_{20}}})^4 \\ I_{\mathrm{b}}^{(1)} & = I_{\mathrm{Py}} - X^{(1)} = I_{\mathrm{Fe_{80}Ni_{20}}} - (I_{\mathrm{Py}} - I_{\mathrm{Fe_{80}Ni_{20}}})^4 \end{cases} \tag{5.15}$$

from where the extracted value of the absorption coefficients is:

$$\mu = -\frac{1}{l} \ln \left[I_{\mathrm{Py}} - I_{\mathrm{Fe_{80}Ni_{20}}} + (I_{\mathrm{Py}} - I_{\mathrm{Fe_{80}Ni_{20}}})^4 \right] \tag{5.16}$$

and the generalization for iteration number (n) is:

$$\Rightarrow \begin{cases} X^{(n+1)} & = I_{\mathrm{Py}} - I_{\mathrm{Fe_{80}Ni_{20}}} + (X^{(n)})^4 \\ I_{\mathrm{b}}^{(n+1)} & = I_{\mathrm{Fe_{80}Ni_{20}}} - (X^{(n)})^4 \end{cases} \tag{5.17}$$

Now that we have described our methodology, we can proceed to derive values for μ and I_{b} from our experimental data. For circularly-right polarized light (+), the minimum transmitted value at the Permalloy segment is $I_{\mathrm{b},+,\mathrm{Py}} = 0.550$, and the minimum transmitted intensity value at the chemical modulation is $I_{\mathrm{b},+,\mathrm{Fe_{80}Ni_{20}}} = 0.300$. Note that these minimum values are extracted from a line profile at the wire cross section, as shown by the pink curve in Figure 5.2a. Note also that the magnetization is axial at the Permalloy segments, with $\mathbf{k} \cdot \mathbf{m} = \sin 10°$, and curling at the chemical modulation with $\mathbf{k} \cdot \mathbf{m}$ unknown but closer to unity. For iteration number (0) Eq.(5.20) results in:

$$\Rightarrow \begin{cases} X_{+}^{(0)} = 0.250 \\ I_{\mathrm{b},+}^{(0)} = 0.300 \end{cases} \tag{5.18}$$

For iteration number (1) Eq.(5.17) results in:

$$\Rightarrow \begin{cases} X_{+}^{(1)} = 0.246 \\ I_{\mathrm{b},+}^{(1)} = 0.296 \end{cases} \tag{5.19}$$

For iteration number (2) Eq.(5.17) results in:

$$\Rightarrow \begin{cases} X_{+}^{(2)} = 0.246 \\ I_{\mathrm{b},+}^{(2)} = 0.296 \end{cases} \tag{5.20}$$

Thus leading to a absorption coefficient value for a diameter $l = 130\,\mathrm{nm}$ following Eq.(5.16) of:

$$\mu_{\mathrm{eff},+,\mathrm{Py}} = -\frac{1}{l}\ln X^{(2)} = 0.0108\,\mathrm{nm}^{-1}. \tag{5.21}$$

For circularly-left polarized light (-) the transmitted intensity value at the Permalloy segment is $I_{\mathrm{b},+,\mathrm{Py}} = 0.510$ and the transmitted intensity value at the chemical modulation $I_{\mathrm{b},+,\mathrm{Fe_{80}Ni_{20}}} = 0.270$. Following the same iterative procedure this leads to

$$\mu_{\mathrm{eff},-,\mathrm{Py}} = -\frac{1}{l}\ln 0.237 = 0.0111\,\mathrm{nm}^{-1}. \tag{5.22}$$

As explained in the previous section this value depends on magnetization, more specifically on $\mathbf{k}\cdot\mathbf{m}$. Thus the dichroic-independent coefficients is obtained using Eq.(5.11) and Eq.(5.12) resulting in:

$$\mu_{+,Py} = 0.0101\,\mathrm{nm}^{-1}. \tag{5.23}$$

$$\mu_{-,Py} = 0.0119\,\mathrm{nm}^{-1}. \tag{5.24}$$

Thus, at the Permalloy segments the estimated dichroism-independent absorption coefficient is $\mu_{0,Py} = 0.0110\,\mathrm{nm}^{-1}$ and the dichroism-dependent absorption coefficient is $\Delta\mu_{\mathrm{Py}} = 0.0018\,\mathrm{nm}^{-1}$. From Table 5.1, the theoretical coefficients are $\mu_{0,Py} = 0.0140\,\mathrm{nm}^{-1}$ and $\Delta\mu_{\mathrm{Py}} = 0.008\,\mathrm{nm}^{-1}$, which now are closer to the estimated ones. Therefore, we validate that the consideration of the background intensity is indeed important for this quantitative analysis. Regarding the $\mathrm{Fe_{80}Ni_{20}}$ modulation, since we assumed $\mu_{\mathrm{Fe_{80}Ni_{20}}} = 4 \times \mu_{\mathrm{Fe_{20}Ni_{80}}} = 4 \times I_{\mathrm{Py}}$, the analytically calculated dichroism-independent absorption coefficient at the $\mathrm{Fe_{80}Ni_{20}}$ modulation is $\mu_{0,\mathrm{Fe_{80}Ni_{20}}} = 0.0440\,\mathrm{nm}^{-1}$ and the dichroism-dependent absorption coefficient is $\Delta\mu_{\mathrm{Fe_{80}Ni_{20}}} = 0.0072\,\mathrm{nm}^{-1}$. If we compare them with the theoretical values, $\mu_{0,\mathrm{th},\mathrm{Fe_{80}Ni_{20}}} = 0.0560\,\mathrm{nm}^{-1}$ and $\Delta\mu_{\mathrm{th},\mathrm{Fe_{80}Ni_{20}}} = 0.0320\,\mathrm{nm}^{-1}$, we evidence again that now our estimated values are closer to theory. However, we obtained a very large estimated background intensity of $I_{\mathrm{b},+} = 0.296$ and $I_{\mathrm{b},-} = 0.267$, normalized to the beam intensity. Its impact is noticeable in the reduced $\Delta\mu$ values estimated. Therefore, unfortunately, for this data-set we could not use this approach to calculate the absorption coefficients. In addition, as detailed in Sec. 5.2.1, the measured intensity at the wire axis (minimum transmitted intensity) depends strongly on the diameter and spot size. Therefore, we need to make sure that the values we are using are realistic. This will be addressed in the next section.

5.2.4 Analysis by the successive evaluation of the background intensity and probe size

In the following, I will detail the approach I found most reliable for quantifying XAS images. Our starting point is the previously discussed critical impact of the background intensity and spot size, whose accuracy is crucial for the quantification of the curling angle from XMCD images. To address these issues, we decided to work with the theoretical absorption coefficients as inputs in the model and have as free parameters the values of I_{b} and σ.

The estimation of the background signal I_{b} was done by subtracting the minimum value of the experimental profile of the transmitted intensity from the minimum calculated theoretically (pink and blue curves in Figure 5.3a). The value obtained is $I_{\mathrm{b}} = 0.296$, which is equal to the value obtained in the previous section, is added to the theoretical intensity, and then normalized by $1 + I_{\mathrm{b}}$ (Figure 5.3b). Now, both curves share the same depth but not the same edges. This is because of the limited spatial resolution of the experimental data, which must be considered in the theoretical profile. To do so, we perform a convolution of a Gaussian curve

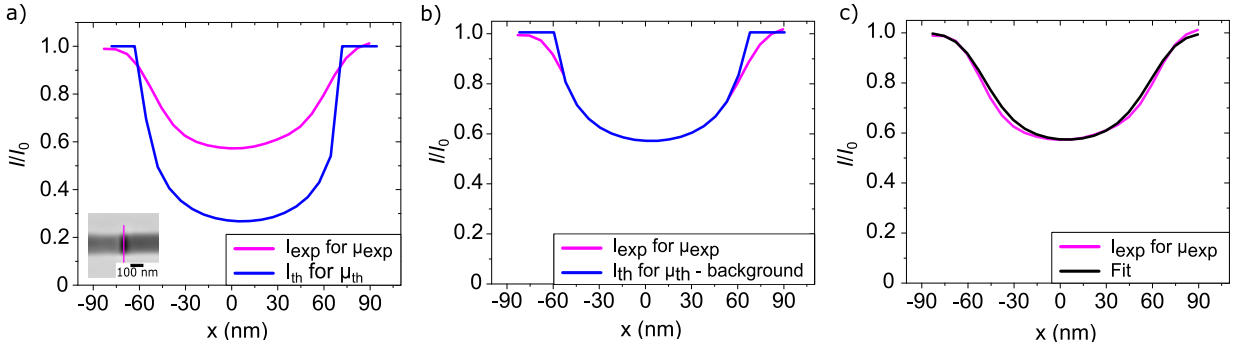

Figure 5.3: XAS normalized intensity profile across the cross-section of the modulation for a nanowire with $d = 130\,\text{nm}$ and $\ell = 60\,\text{nm}$. **a)** The pink curve shows the profile obtained experimentally (pink line in the inset). The theoretical transmitted intensity using the theoretical absorption coefficients is plotted by the blue curve. **b)** Theoretical transmitted intensity with the background signal added (blue). **c)** Fit of the Gaussian-convoluted theoretical intensity of **b)** with the experimental profile (black). The fit gives a spot size of $\sigma = 12\,\text{nm}$. Figure adapted from [142].

with the sum of the theoretical intensity and the background signal (blue curve in Figure 5.3b). The result is shown in Figure 5.3c, where now the depth and edges of the profiles overlap. The Gaussian width is a measure of the spot size and is unknown at this stage. Its value is determined by the best fit (black) with the experimental profile (pink curve). The output gives a Gaussian width or spot size of 12 nm, which is of the order of the measured spatial resolution. This result is very satisfactory since with the previous approaches we obtained a spot size of 22 nm.

5.3 Quantitative analysis of curling from magnetic contrast images

After describing different approaches to quantify the absorption coefficients, spot size and background signal from experimental XAS images, we are now ready to quantify the evolution of the curling angle under an axial magnetic field. However, the reader may wonder why this was not shown previously for the XMCD static images for different geometries shown in Sec. 4.2.2. As mentioned in that section, an ongoing study is estimating the curling angle for these geometries. However, this study takes a relevant amount of time since special care should be taken when moving from one X-ray microscopy to another. For this reason, the study has not been completed and is not shown in this manuscript. In the following, we focus on the study of the curling angle variation in XMCD ptychographic images under an axial magnetic field. The inputs to the model are the experimental XMCD line profiles reported in Figure 5.1c in Sec. 5.1, the theoretical absorption coefficients, the sample diameter ($d = 130\,\text{nm}$), the sample holder rotation ($\alpha = 10°$) and the background intensity and spot size (σ = 12 nm). The background signal was determined by $I_{\text{b, XMCD}} = I_{b,\text{XAS}} \times I_{\text{XMCD,out}} = 0.014$ where $I_{\text{XMCD,out}}$ is the XMCD intensity out of the wire. For higher accuracy in the theoretical absorption coefficients, we measured the chemical composition by STEM-EELS in this particular sample. The atomic percentage of a line profile that crosses the modulation along the axial direction is shown in Figure 5.4b, whose compositional map is shown in Figure 5.4c. This results in a $Fe_{65}Ni_{35}$ chemical modulation. Thus the theoretical absorptivity coefficients to be used are $\mu_{\text{th,Fe}_{65}\text{Ni}_{35}}$ = 0.045 nm $^{-1}$ and $\Delta\mu_{\text{th,Fe}_{65}\text{Ni}_{35}}$ = 0.026 nm^{-1}.

The estimation of the curling angle $\theta(R)$ from the magnetic contrast of the images was done using the post-processing code described in [260]. Figure 5.4a shows in black the selection of three experimental XMCD profiles out of a series of images under an applied axial magnetic field ranging from 1 mT to 90 mT. In red is shown the fit of the theoretically calculated profiles with the experimental data and the curling angle at the surface obtained is written in blue. The summary of this analysis is shown in Figure 5.4d, where the

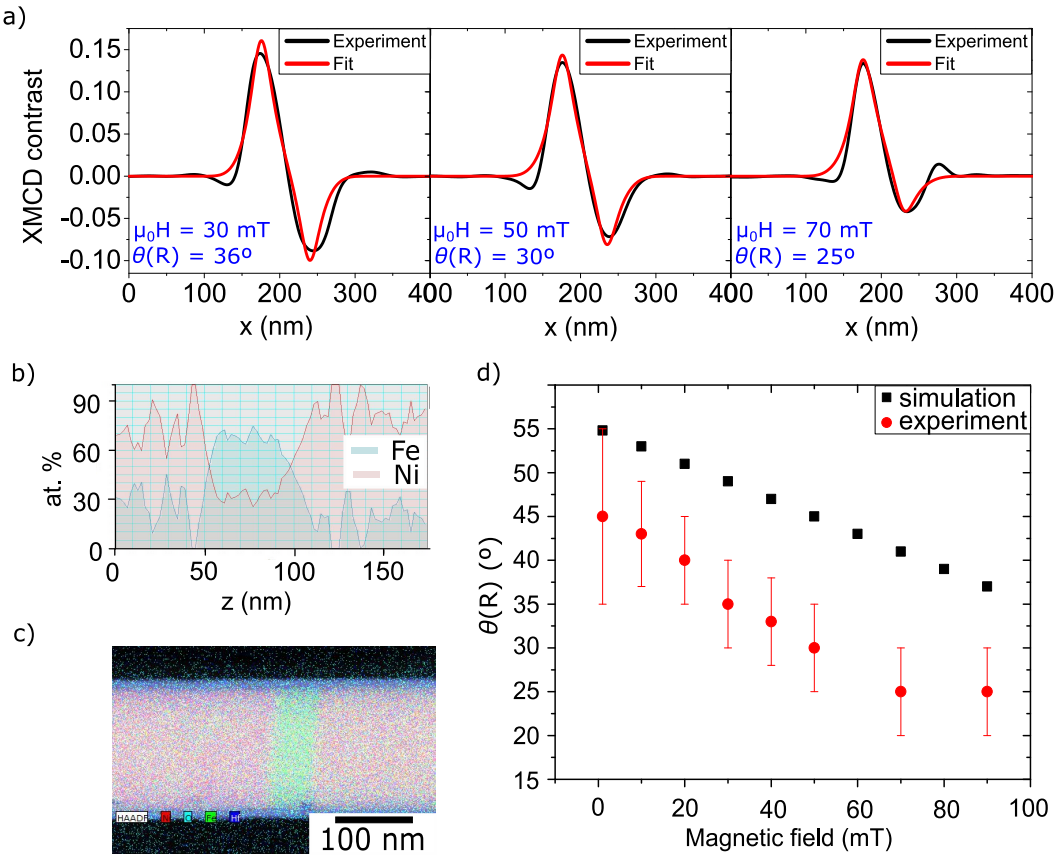

Figure 5.4: Model for quantifying the curling angle reduction under axial magnetic field. **a)** XMCD line profiles across the Fe-rich modulation under an axial magnetic field. The experimental line profiles, shown in Figure 5.1, are shown in black and the theoretical profiles in red. In blue is indicated the axial field applied and curling angle at the surface obtained by the model. **b)** and **c)** STEM-EELS map across the modulation. **d)** Curling angle resulting from the analysis of the line profiles (red) and from micromagnetic simulations (black). Figure adapted from [142].

evolution of the curling angle under an axial magnetic field ranging from 1 mT to 90 mT is shown in red. At 1 mT a curling angle of $\theta(R) = 45°$ is obtained, which decreases linearly until $\theta(R)$ =25° for 90 mT. The error bars were calculated from the standard deviation in $\theta(R)$ after varying slightly the spot size, background intensity and wire diameter.

The $\theta(R)$ expected from micromagnetic simulation is shown by the black symbols in Figure 5.4d. The trend of both curves is the same but the values of the curling angle are around 10° higher with respect to the experimental ones. There may be different explanations for this. First, there is a difference in the exchange stiffness values for the two materials ($A_{\mathrm{Py}} = 1.3 \times 10^{-11}\,\mathrm{J/m}$, $A_{\mathrm{Fe_{65}Ni_{35}}} \approx 1.6 \times 10^{-11}\,\mathrm{J/m}$). In the simulations we considered a uniform exchange stiffness $A_{\mathrm{Py}} = 1.3 \times 10^{-11}\,\mathrm{J/m}$. As a consequence, the simulated system is less stiff, which allows a larger curling angle. Second, in the micromagnetic simulations we have considered zero magnetocrystalline anisotropy in both, the Permalloy section and chemical modulation, but experimentally we may have a non-negligible uniaxial anisotropy also reducing the final curling angle. Third, experimental data may suffer from large uncertainties, coming from the accuracy in the sample diameter, angle of rotation and spot size value. Therefore, in spite of the slight differences between experiment and simulation, arising from the above-mentioned reasons, we have described a model that clearly allows us to extract the curling angle from experimental data.

5.4 Œrsted field-driven circulation switching: experiments

In the second part of this chapter, we will detail the micromagnetic response of a chemically-modulated nanowire to a magnetic field in the azimuthal direction $\hat{\varphi}$. In particular, we will study the response to the Œrsted field associated with a nanosecond current pulse. This is a required step to understand the collective interaction of a domain wall and a chemical modulation under this external stimulus.

First of all, let us recall that curling of magnetization occurring at the chemical modulations may have a positive or negative circulation at rest, as we observed experimentally in Figure 4.3. This is understandable as there is no energy dependence of the chirality of the system, i.e., circulation versus longitudinal magnetization, so that both circulations have the same energy. We expect that this degeneracy is lifted upon the application of an electric current flowing along the wire, which gives rise to an Œrsted magnetic field that couples directly with curling, either parallel or anti-parallel. This situation is analogous to the case of azimuthal curling in a Bloch-point domain wall (BPW) in nanowires, for which the Œrsted field has been proven to be crucial for the dynamic stability and switching [185, 260].

5.4.1 Static X-ray imaging

We experimentally investigate $Fe_{80}Ni_{20}$ chemically-modulated Permalloy nanowires of 90 nm or 130 nm diameter under the stimulus of a current pulse. The nanowires were previously contacted electrically as described in Sec. 2.5 to allow the injection of electric current. Depending on the setup of each X-ray imaging technique, a precise design of the electric contacts was carried out in order to allow the best transmission of the coplanar waveguide, avoiding capacitor effects or signal reflection (see Sec. 2.4). The X-ray beam direction was set perpendicular to the nanowire axis or with a 10° offset in order to image mostly the magnetization components transverse to the wire axis, i.e., revealing curling. The current densities were on the order of $10^{12}\,\mathrm{A\cdot m^{-2}}$ and the pulse width ranged from 0.5 ns to 15 ns. The images were taken under static conditions before and after the application of each current pulse.

Figure 5.5 shows the response of the system to a nanosecond current pulse for three different nanowire geometries. The XAS images (first column), obtained at the Fe L_3 edge, reveal the location of the Fe-rich chemical modulation. Three different X-ray microscopies were used: Figure 5.5a shows a 90 nm diameter nanowire with $\ell = 40$ nm imaged by STXM, Figure 5.5e shows a 130 nm diameter nanowire with $\ell = 100$ nm imaged by TXM and Figure 5.5h shows a 130 nm diameter nanowire with $\ell = 30$ nm imaged by X-ray ptychography. It is worth mentioning that the ptychographic images were not taken with the best parameters, to reduce the acquisition time. See Figure 6.2 for a reconstructed ptychographic image with a spatial resolution below 12 nm.

The corresponding XMCD images in Figure 5.5b, Figure 5.5f, and Figure 5.5i reveal the initial circulation direction of the curling at the modulation (yellow arrow) and an axial direction at the Permalloy segments (black arrows), whose direction we believe is irrelevant for this study. The third column shows the XMCD images after the application of a nanosecond current pulse, whose magnitude and duration are written at the top of the images. The bipolar black and white contrast is reversed after the application of the pulse, revealing a switching of the curling circulation. The final circulation matches with the circulation of the applied Œrsted field (red arrow). Here, we provide evidence of circulation switching driven by the Œrsted field. In addition, a series of images were taken with decreasing current density amplitude. We evidenced a threshold current below which the circulation does not switch. This procedure was repeated several times, below and above the threshold, finding a deterministic behavior. Lastly, we observed no dependence on pulse duration in the range of 0.5 ns to 20 ns.

We observed that the minimum current amplitude for switching depends on the geometry of the system. Specifically for a 90 nm diameter nanowire, we obtained a threshold value for switching of $J_{\mathrm{th}} = 0.9\times10^{12}\,\mathrm{A/m^2}$ and $J_{\mathrm{th}} = 2\times10^{12}\,\mathrm{A/m^2}$ for a chemical modulation length of $\ell = 40$ nm and $\ell = 60$ nm, respectively. For a 130 nm diameter nanowire, the thresholds found were $J_{\mathrm{th}} = 1.2\times10^{12}\,\mathrm{A/m^2}$ and $J_{\mathrm{th}} =$

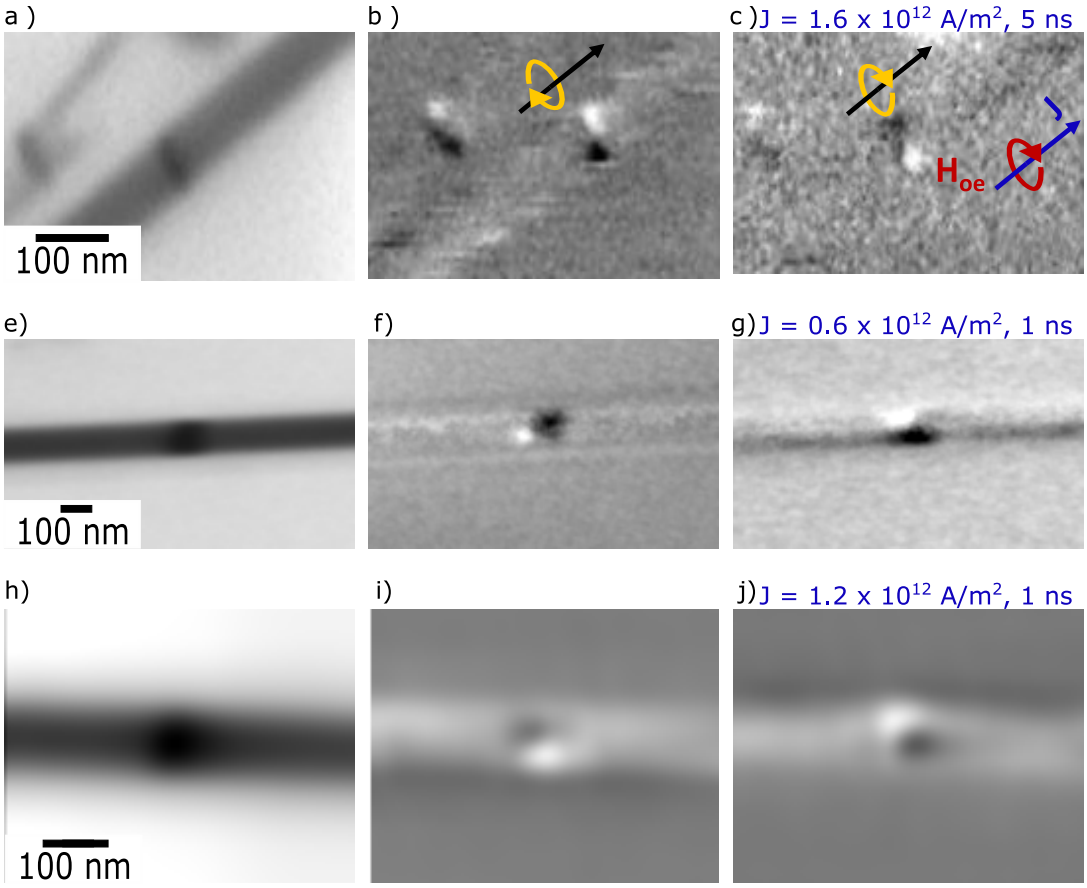

Figure 5.5: Experimental evidence of Œrsted-field-driven circulation switching in the chemical modulation. **a)** XAS Fe L_3 STXM image of a Permalloy nanowire electrically contacted, with $d = 90\,\text{nm}$ and $\ell = 40\,\text{nm}$. The nanowire at the top is not electrically contacted. **b)** XMCD image of **a)** in the initial state, revealing that curling in the modulation has negative circulation $C-$ (yellow arrow) with respect to the axial magnetization (black arrow). **c)** XMCD image after the application of a current pulse with density $J = -1.6 \times 10^{12}\,\text{A/m}^2$ and duration of 5 ns. The circulation switched to positive $C+$ circulation (yellow arrow), which fits the circulation of the Œrsted field during the pulse of current (red arrow). **e)** XAS Fe L_3 TXM image for $d = 130\,\text{nm}$ and $\ell = 100\,\text{nm}$. **h)** Reconstructed-XAS Fe L_3 Ptychographic image for $d = 130\,\text{nm}$ and $\ell = 30\,\text{nm}$. **f)** and **i)** show XMCD image of **e)** and **h)** respectively. **f)** and **i)** show XMCD image after the application of the current pulse described above it.

$0.6 \times 10^{12}\,\text{A/m}^2$ for a chemical modulation length of $\ell = 30\,\text{nm}$ and $\ell = 80\,\text{nm}$, respectively. One can see that the switching current is higher for smaller diameters. While micromagnetic energetics may play a role, the dominant effect may be the magnitude of the Œrsted field, which is lower for the smaller diameters for a given current density. No other geometries were studied due to the complexity and time demand of the X-ray imaging under current pulses. To better understand the switching mechanism and the real-time Œrsted field impact, we performed time-resolved experiments on modulation circulation switching.

5.4.2 Time-resolved X-ray imaging

With conventional X-ray imaging, we probe the magnetization at rest before and after the application of a current pulse. By doing so, we can have a general picture of the phenomenon, but with the drawback of missing the underlying magnetization dynamics. In our case of study, it is highly relevant to have access to the

Œrsted field-driven dynamics during the application of a current pulse. Due to the intrinsically pulsed structure of the X-rays generated in a synchrotron [259], it is possible to perform pump-probe X-ray microscopy. To do so, it is necessary to have a reproducible magnetization dynamics over millions of times.

Time-resolved STXM imaging was performed at MAXYMUS beamline [261] at BESSY II synchrotron. Each time-resolved series had a temporal resolution ranging from 200 ps to 50 ps. As discussed in Sec. 2.4.4, just one circular X-ray polarization is used thus one does not measure XMCD images but differential XAS images, based on the division of an individual XAS image by the average of all the XAS frames. This may make the analysis difficult as the average does not necessarily reflect a static magnetization state. In practice, it is advisable to perform an XMCD image before/after the TR series. Figure 5.6 shows snapshots of the differential XAS contrast images of a time-resolved series on modulation circulation switching. The system is a 111 nm diameter Permalloy nanowire with a 30 nm-long chemical modulation at its center. This sample shows a critical switching current of $0.53 \times 10^{12}\,\mathrm{A \cdot m^{-2}}$. At the top of each subfigure is written the temporal resolution, i.e., the time step between images, and also the current density applied with a duration of 1 ns or 2 ns. The top images correspond to the static differential XAS image at the beginning of the pulsing sequence, where curling at the modulation is evidenced. Once the current pulse is applied, the tilt of the Permalloy domains along the Œrsted field direction is revealed. Its sense is opposed to the initial curling circulation. Then the 1-2 ns-long pulse is stopped, followed by a 10-15 ns waiting time to allow the sample to cool down. Another pulse with opposite polarity is applied to switch back the circulation to its initial state, again followed by the same waiting time. The periodic excitation is repeated about 100 million times per pixel, i.e., a few tens of billions of times per time-resolved image series. Figure 5.6a shows the time-reversal series for a current density of $1.02 \times 10^{12}\,\mathrm{A \cdot m^{-2}}$, with a 50 ps temporal resolution. We evidence that the circulation is completed at $t = 250$ ps. Figure 5.6b shows a circulation switching for $0.68 \times 10^{12}\,\mathrm{A \cdot m^{-2}}$ at $t = 300$ ps. Figure 5.6c shows a circulation switching for $0.57 \times 10^{12}\,\mathrm{A \cdot m^{-2}}$ at $t = 350$ ps. The switching time scale keeps increasing as we reduce the current and approach the critical one for reversal. This is also revealed in Figure 5.6d and Figure 5.6e, where it is applied a very similar current density of $0.54 \times 10^{12}\,\mathrm{A \cdot m^{-2}}$ and $0.53 \times 10^{12}\,\mathrm{A \cdot m^{-2}}$, respectively. The former shows circulation reversal at $t = 1000$ ps, whereas the latter shows reversal at $t = 1200$ ps.

These results can be understood as follows. First, for a current density above $\approx 0.70 \times 10^{12}\,\mathrm{A \cdot m^{-2}}$ the switching mechanism occurs at $t < 250$ ps. Therefore, the dynamics time scale is similar to the rise time of the current pulse at the sample. This ultra-fast magnetization dynamics is driven by the strength of the Œrsted field and dynamic dipolar field in nanowires. Second, we observe an increase in the time scale as the current is reduced, with a value of $t = 1250$ ps for the critical current density for switching of $0.53 \times 10^{12}\,\mathrm{A \cdot m^{-2}}$. This divergence of the switching time scale is consistent with the theoretical and simulations expectations. Therefore, this experimental proof of the divergence of the switching time close to the critical current validates standard methods such as the scaling of a parameter to determine the critical current, where its time scale is set at $t = \infty$. This will be discussed in Sec. 5.5.2. Finally, regarding the switching mechanism, it reveals a shortening of the curling length at the modulation with time. This proves that the modulation reversal is driven from the interfaces towards the modulation center. In addition, a greyish contrast appears at the modulation until the full reversal occurs. This means that an axially magnetized state remains in the modulation before the torque driven by the Œrsted field pushes the magnetization along the opposite azimuthal sense $\hat{\varphi}$, compared with the initial sense. In the following sections, a deeper insight into this mechanism is provided with micromagnetic simulations.

5.5 Œrsted field-driven circulation switching: micromagnetic simulations

In this section, we will study the mechanism of circulation switching in the chemical modulation driven by the Œrsted field, with the *feeLLGood* micromagnetic code. We have chosen an alpha parameter equal to 1 for faster relaxation and a quasi-static dynamics. Even though this value is unphysically large, it is suitable

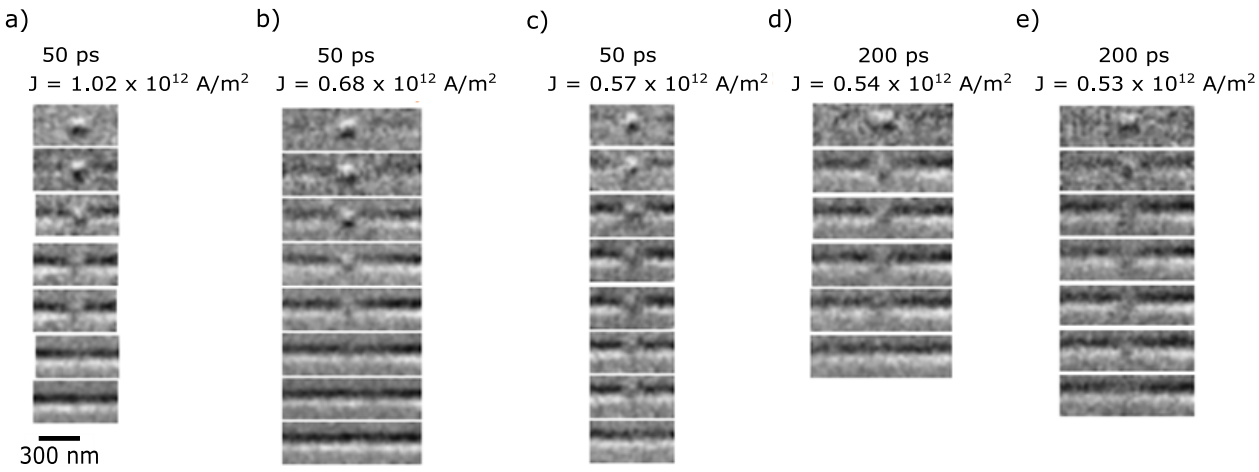

Figure 5.6: STXM time-resolved Œrsted-field driven circulation switching in the chemical modulation. The system is a 111 nm diameter Permalloy nanowire with a 30 nm-long chemical modulation at its center. Subfigures show snapshots of the differential XAS contrast images of a time-resolved series for different current densities. At the top is written the applied current density and temporal resolution. The first image is the initial static differential contrast XAS. The time scale of the dynamics diverges as we approach the critical current density for reversal.

to describe quasistatic situations such as experiments where the rise time of the current pulse is on the order of a few hundred picoseconds. The initial configuration for each geometry consists of its micromagnetically relaxed state at rest, with negative circulation with respect to the axial direction $\hat{\mathbf{z}}$, as shown in Figure 5.7a. Only the Œrsted field is included as an external stimulus since the effect of spin-transfer torque (STT) has been shown to be negligible for similar dynamical processes, such as BPW circulation switching [185]. We also disregarded the effect of Joule heating, which is not expected to play a key role in magnetization dynamics , unless higher current densities or longer pulses are considered. In practice, we estimated experimentally a temperature rise of 250 °C for a current density of magnitude $j = 1.2 \times 10^{12}\,\mathrm{A/m^2}$, pulse duration 8 ns, and 130 nm diameter (see Appendix 8.2).

In the following, the systems considered are based on a cylindrical nanowire made of two Permalloy segments of 100 nm (for $D = 90$ nm) or 150 nm (for $D = 130$ nm) length, separated by a $Fe_{80}Ni_{20}$ chemical modulation with length ℓ varied between 10 and 100 nm. In order to mimic an infinite wire, the magnetic charges at the wire ends are removed numerically. The tetrahedrons that compose the meshes have a characteristic size of 4 nm. The following material parameters were used: spontaneous magnetization $M_1 = 8 \times 10^5\,\mathrm{A/m}$ for the Permalloy segments, $M_2 = 14 \times 10^5\,\mathrm{A/m}$ for the $Fe_{80}Ni_{20}$ modulation, single exchange stiffness for all materials $A = 1.3 \times 10^{-11}\,\mathrm{J/m}$ and zero magnetocrystalline anisotropy. We provide first a qualitative description of the switching mechanism, followed by the study of the threshold current to produce the switch as a function of the diameter and chemical modulation length.

5.5.1 Mechanism of the circulation switching

In this section, we describe step by step the response of the system to an Œrsted field of antiparallel circulation with respect to the initial one at the chemical modulation. Just to remind that in this case rotational symmetry is preserved, which makes irrelevant the initial and final circulation senses. We define the sign of the circulation with respect to the axial direction $\hat{\mathbf{z}}$. Figure 5.7a shows the surface view of the micromagnetic state at rest of a 90 nm diameter Permalloy nanowire with a $\ell = 40$ nm chemical modulation. The color code represents the absolute value of the curling angle at the surface of the nanowire $\theta(R)$, and the white arrows

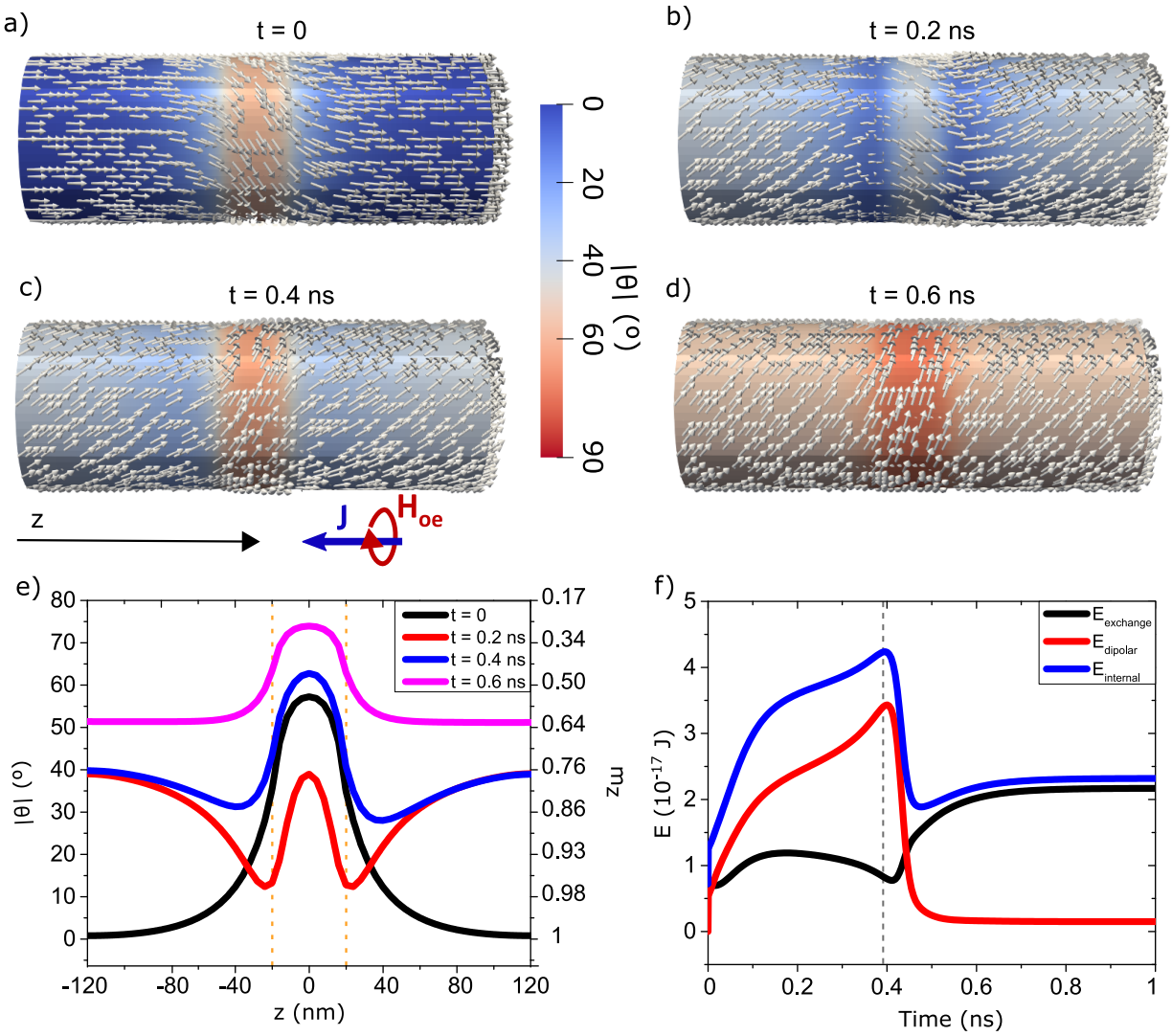

Figure 5.7: Micromagnetic simulations of Œrsted-field driven circulation switching in the chemical modulation. **a)-d)** Outer view of the micromagnetic configuration of a 90 nm Permalloy nanowire with $\ell = 40$ nm. The color code represents the absolute value of the curling angle at the surface $\theta(R)$. White arrows indicate the local direction of magnetization. **a)** Initial state at rest reveals curling at the modulation with positive circulation with respect to $\hat{\mathbf{z}}$. **b)**, **c)** and **d)** outer view configuration under a current pulse of amplitude $J = -2.5 \times 10^{12}\,\mathrm{A/m^2}$ at $t = 0.2$ ns, $t = 0.4$ ns and $t = 0.6$ ns, respectively. The Œrsted field has negative circulation $C-$. **e)** Surface $\theta(R)$ vs z line profiles at the different time steps. Orange dashed lines set locations of the modulation interfaces. **f)** Evolution over time during the switching mechanism of the internal energy E_{int} (blue), which is the sum of the dipolar energy E_{d} (red) and the exchange energy E_{ex} (black). The grey dashed line indicates the moment of switching ($m_\phi = 0$).

indicate the direction of magnetization at the surface, showing axial Permalloy domains and curling state at the modulation. The schematics of the cylindrical coordinates and the curling angle θ can be found in Figure 4.8a. The initial curling circulation is positive ($C+$) with respect to the $\hat{\mathbf{z}}$-axis.

Figure 5.7b shows the magnetization configuration at $t = 0.2$ ns after the start of application of a current pulse of magnitude $J = -2.5 \times 10^{12}\,\mathrm{A/m^2}$ and thus, with negative Œrsted field circulation $C-$. The impact of the Œrsted field in the Permalloy segments can be noticed by the curling of magnetization. Curling has

a magnitude of $\theta(R) \approx 40°$ at the edges, decreasing progressively close to the material interfaces (dark blue clouds), before it tilts again along the opposite azimuthal direction until it reaches $\theta(R) \approx 40°$ at the center of the modulation, whereas at rest it was $\theta(R) \approx 57°$. The curling angle at the modulation keeps decreasing until it reaches $\theta(R) = 0°$ at the moment of switching. The micromagnetic configuration just after the switching is shown in Figure 5.7c. At $t = 0.4\,\text{ns}$, the curling in the modulation is along the Œrsted field $C-$ and its magnitude is $\theta(R) = 64°$. Finally, at $t = 0.6\,\text{ns}$, the curling magnitude is $\theta(R) = 75°$ (Figure 5.7d). When the current is switched off, the circulation at rest remains negative $C-$.

The $\theta(R)$ vs z line profiles over time at the surface of the nanowire are shown in Figure 5.7e. The orange dashed lines show the location of the interfaces. The black curve shows the $\theta(R)$ profile at rest, which reveals that the maximum curling occurs at the center of the modulation. This will have a direct impact on the switching mechanism that will be explained at the end of this section. For larger modulations, a curling plateau is reached where the curling angle is equal throughout the modulation, and even weaker at its center (see Sec. 4.4.2). The red curve illustrates the progressive reduction of the curling angle prior to switching its circulation. It can be seen that this reduction starts from the interfaces towards the center of the modulation, driven by the exchange torque applied on the modulation by the domains due to the different curling senses. This also supports our experimental findings on STXM time-resolved circulation switching shown in Sec. 5.4.2. The blue curve shows the profile during the switching so that the Œrsted field direction is parallel to the circulation in the modulation. This allows an increase of the curling angle throughout the system reaching its maximum for $\theta(R) = 73°$ and $\theta(R) = 51°$ at the chemical modulation and Permalloy segments, respectively (pink curve).

In terms of energetics, the states before switching show a progressive increase of the dipolar energy and a non-monotonic decrease of the exchange energy (red and black curves, respectively, in Figure 5.7e). This behavior is different from the case of BPW switching reported in [185] for a Permalloy nanowire of $D = 90\,\text{nm}$. In that case, the dipolar energy decreases while the exchange energy increases before the BPW reversal. In our case we may understand the energetics evolution as follows: the states before switching show a nearly axial magnetization at the interfaces (dark blue clouds in Figure 5.7b) which enhances the magnitude of surface charges and thus the dipolar energy E_d. Once the circulation has switched, E_d drops since screening can again set in and the amount of surface charges reaches a minimum. However, the increase in the curling angle θ leads to a rise in the associated exchange energy. We understand the non-monotonous variation of E_ex in the following way: first, curling first develops in the domains within $\approx 100\,\text{ps}$. This leads to an increase of E_ex via its radial contribution. In a second step, curling in the modulation shrinks and decreases its amplitude, inducing a decrease of E_ex. After the circulation reversal, the curling angle rises to screen the magnetic charges and decrease E_d, which induces an increase in E_ex. Therefore, this study has provided us insight into the switching mechanism. Nevertheless, since simulation time is finite and long, we cannot directly guess which is the critical current density j_c to switch since at this value $\tau_\text{c} \to \infty$.

5.5.2 Critical current density of the switching mechanism

In the following, we will discuss a method to determine with a good accuracy the critical current density j_c required to switch the circulations with a finite computation time. A standard method in micromagnetism to address this issue is to rely on the scaling of a parameter, such as the susceptibility below the threshold [303, 304] or the switching time t_sw above the threshold [305, 306], versus the driving parameter, in this case, the current density j. We expect and indeed evidence that $1/\tau_\text{c}$ scales almost linearly with $|j - j_\text{c}|$ [185], from which j_c can be determined.

First, we need to determine the critical time for switching τ_c above the threshold current density. To do so, we need to decide on a criterion. To search for the most suitable one, we studied the evolution over time of the maximum and minimum values of m_z, m_ρ and m_ϕ at the surface of the nanowire during the switching process. The results are shown in Figure 5.8a for a system with $D = 90\,\text{nm}$ and $\ell = 60\,\text{nm}$ and a current density of $j = 3 \times 10^{12}\,\text{A/m}^2$. By circulation switching, we imply going from $C+$ to $C-$, and so

from $m_\phi) > 0$ to $m_\phi) < 0$. Therefore, setting the switching time at $m_\phi) = 0$ is coherent. In addition, $m_\phi) = 0$ seems the easiest to track, through a simple linear intercept between the points before and after switching. This τ_c value corresponds to the maximum E_{int} (grey line in Figure 5.7f). In Figure 5.8a, τ_c is at max(m_ϕ) = 0 (orange circle).

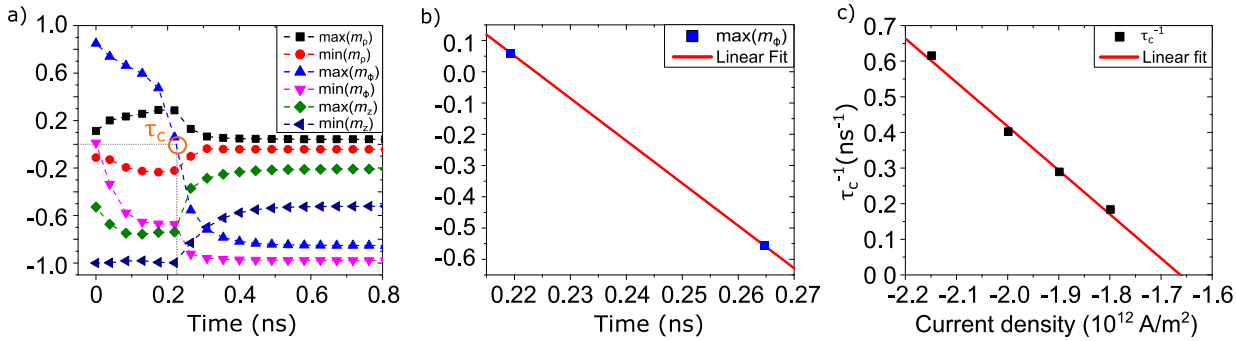

Figure 5.8: Standard method to extract the threshold current density j_c of switching. a) Maximum and minimum value of m_z, m_ρ and m_ϕ over time at the surface of the wire during the circulation switching process. The nanowire diameter is $D = 90$ nm and $\ell = 60$ nm and the current density is $j = 3 \times 10^{12}$ A/m^2. The switching time τ_c is determined by max(m_ϕ) = 0 (orange circle). b) Linear interpolation between the values before and after max(m_ϕ) = 0 to extract the exact value of τ_c. c) Linear interpolation of the values of τ_c^{-1} as a function of j. Interception with the horizontal axis (τ_c^{-1} = 0) gives the threshold current density j_c. Figure adapted from [142].

This procedure is applied to several current densities j for which circulation switching occurs, to obtain several values of τ_c. Then, the threshold current density j_c is obtained from the intercept at 0 of the linear interpolation of the τ_c^{-1} values, as displayed in Figure 5.8c. Note that in the present situation, a linear interpolation seems relevant at least for j values close to the threshold. However, for higher j values or more complex dynamical processes such as BPW switching, a phenomenological power scaling law should be used to take into account the curvature of τ_c^{-1} [185].

I applied this method to calculate the critical current densities for two different diameters ($D = 90$ nm and $D = 130$ nm) and for ℓ ranging from 10 nm to 100 nm. The results are summarized in Figure 5.9a, where the values of j_c vs chemical modulation length are shown, along with the experimental results. From this graph, there are two main remarks to mention. First, j_c values are higher for smaller diameters. One reason could be that curling has a higher cost in E_{ex}, which requires a stronger external stimulus to rotate the magnetization. However, we believe that the dominant effect is the amplitude of the Œrsted field, which rises linearly with radius for a given j. To illustrate this, the Œrsted field value associated with each for each j_c is mentioned in the right y-axis for $D = 90$ nm (black) and $D = 130$ nm (red). Second, the shape of the curves shows non-monotonous behavior as the length of the chemical modulation increases. There is a maximum current density value of $j \approx 2.1 \times 10^{12}$ A/m^2 for $\ell = 40$ nm and $D = 90$ nm and $j \approx 1.3 \times 10^{12}$ A/m^2 for $\ell = 30$ nm and $D = 130$ nm. These values are located within the green region which sets a limit between two different switching regimes, which we describe below.

5.5.3 Coherent versus incoherent circulation switching

We identify a first regime of switching for short chemical modulations, or in other words, for lengths where the plateau or maximum curling angle has not been reached. This was mentioned in Sec. 4.4.2 where a characteristic length scale of the screening of magnetic charges was calculated, limiting the slope of m_z vs z. Specifically, the characteristic length scale estimated is $\Delta_{mod} \approx 22$ nm. This means that magnetization may rotate by 180° over a distance of $\approx \pi\Delta_{mod}$. As the plateau for curling reaches $60° = \pi/3$ rad, so that the total

rotation is twice this value, we expect that the length required is $(2*\pi/3)\Delta_{\text{mod}} \approx 46\,\text{nm}$. This is consistent with the modulation length giving rise to the maximum of switching current obtained in Figure 5.9a, which confirms the relevance of a specific length scale for modulations, Δ_{mod}.

Therefore, a smaller curling angle makes it easier for the circulation switching, allowing a low critical current. In the first regime, the curling angle increases with modulation length (see Figure 4.8c), explaining the increase of j_c with modulation length. In addition, since the maximum curling angle is reached at the center of the chemical modulation, the reversal process starts from the interfaces towards the center of the modulation. In practice, the switching mechanism can be named a coherent process in cylindrical coordinates, in terms of $\theta(z)$. This is evidenced by examining the profiles at the surface of the wire of m_z vs z at different time steps, which are shown in Figure 5.9b for the case of $D = 90\,\text{nm}$ and $\ell = 40\,\text{nm}$ under the application of a current pulse of $j = -2.10 \times 10^{12}\,\text{A/m}^2$. The profile in the modulation remains similar with a hat shape for every time step, supporting the evidence of a coherent switching mechanism. In addition, the

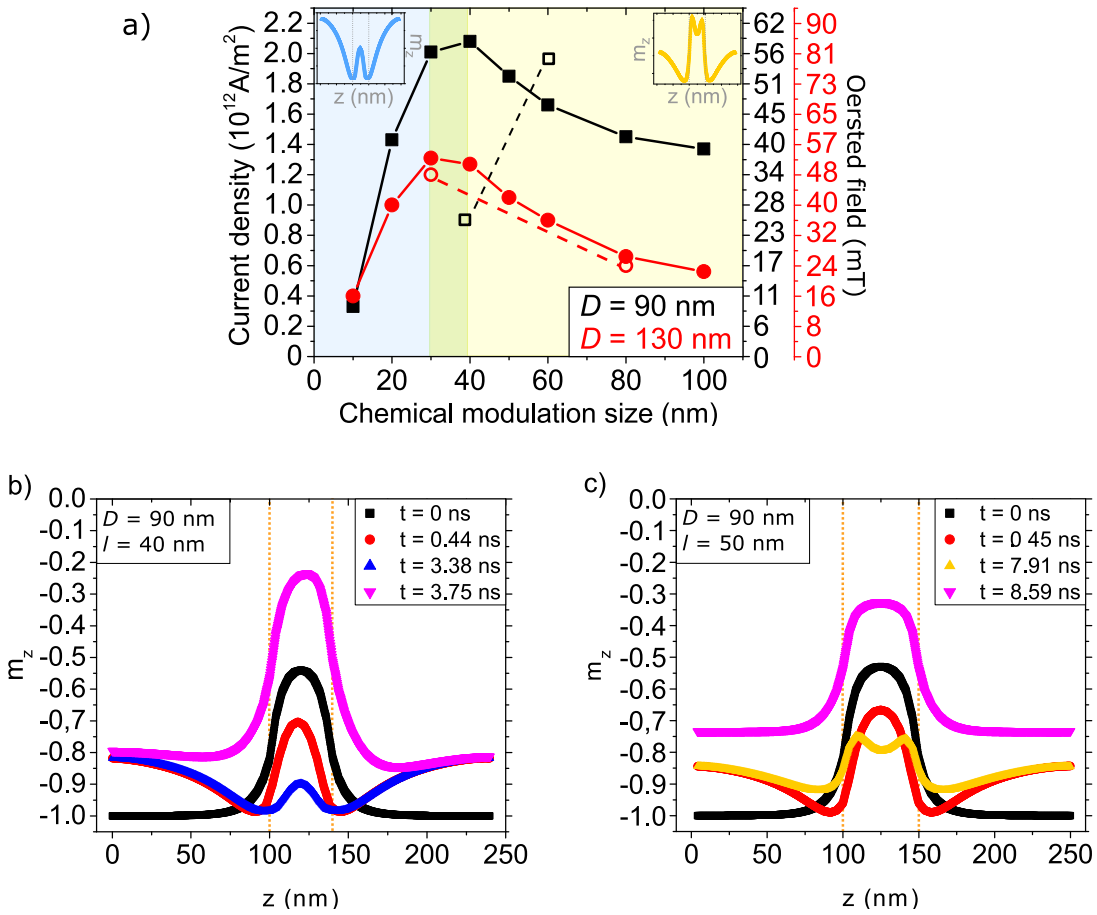

Figure 5.9: **a)** Critical current density j_c for switching circulation, versus length of the chemical modulation ℓ. Simulation and experimental data are displayed with full and open symbols, for a system with $D = 90\,\text{nm}$ (black) and $D = 130\,\text{nm}$ (red) respectively. The y-axis on the right shows the corresponding Œrsted field at the external surface for $D = 90\,\text{nm}$ (values in black) and $D = 130\,\text{nm}$ (values in red). The green background separates two regimes of switching. The insets in the first and second regimes (blue and yellow background) show m_z vs z at the periphery of the wire before switching the circulation. This is displayed better in **b)** for a nanowire with $D = 90\,\text{nm}$ nanowire with $\ell = 40\,\text{nm}$ and in **c)** for a $D = 90\,\text{nm}$ nanowire with $\ell = 50\,\text{nm}$ under the application of a current pulse of $j = -2.10 \times 10^{12}\,\text{A/m}^2$. The orange dashed line sets the location of the interfaces. Figure adapted from [142].

blue curve shows that just before switching, m_z decreases more rapidly at the edges of the peak than at the center. This evidences once more that the center of the modulation is the most magnetically stiff region. Note that the value of m_z outside the modulation reflects the tilt of the magnetization at the Permalloy segments.

We identify a second regime of switching for lengths of the chemical modulation above the one for which the maximum switching current is reached (yellow background in Figure 5.8a). These long modulations correspond to the situation for which a maximum curling angle is reached (Figure 4.8c). In this regime, the maximum screening of magnetic charges has been achieved at both interfaces, and curling is maintained throughout the modulation thanks to longitudinal exchange.This implies that for a very long modulation the magnetization will turn axial at the center of the wire. For this reason, the interfaces are magnetically stiffer, where the tilt of magnetization is driven by magnetostatics and charge screening. The curling at the center of the modulation is magnetically weaker, even more so as the modulation length increases. The examination of the m_z vs z profiles at the surface of the nanowire reveals a non-coherent switching process with a profile $\theta(\phi,z)$ that indicates a nucleation at the center of the modulation. This is clear on the yellow curve in Figure 5.9c, which shows the m_z profile at the moment before switching the circulation for the case of $D = 90\,\text{nm}$ and $\ell = 50\,\text{nm}$ under the application of a current pulse of $j = -2.10\times10^{12}\,\text{A/m}^2$. It is clear that the lowest value of the curling angle $\theta(R)$ is reached at the center of the modulation, opposite to the case of short modulations (blue curve in Figure 5.9b) where the highest value is reached at this point.

5.5.4 Comparison with experiments

Regarding the experimental j_c values, the order of magnitude is consistent with the one obtained by micromagnetic simulations. However, while the experimental trend for $D = 130\,\text{nm}$ is consistent with the situation described above, the measurements carried out with a diameter of $D = 90\,\text{nm}$ followed an opposite behavior. Several reasons may explain this. First, we have not considered in the simulations a different value for exchange stiffness in the Fe-rich modulation, while a larger exchange is expected in practice for $Fe_{80}Ni_{20}$, which shall increase Δ_{mod}. Second, we have neglected thermal activation (expected to have more impact for shorter modulations and smaller diameters, associated with a lower energy barrier) as well as heating during the current pulse. Third, in terms of the experimental samples, the ones with $D = 90\,\text{nm}$ were synthesized at the start of this thesis work, thus they do not have all the material optimization and quality obtained for the ones with $D = 130\,\text{nm}$ (Chap. 3). In particular, they suffer from branches or ramifications, slight changes in the diameter and lower quality of the electric contact and they do not have the 20 nm alumina atomic layer deposition (ALD) coating to improve heat flow. In addition, the exact length of the chemical modulation could not be measured after the experiment since the wire was exploded at this location, which explains once more the weakness of this batch of samples. Due to this, we believe that the experimental values are shifted to the right of the graph but correspond to the first regime.

Finally, time-resolved experiments revealed a switching time scale of $\approx 200\,\text{ps}$ for a current pulse reasonably above the critical one (Figure 5.6b), with a sharp slowing down of the dynamics for currents close to the critical, down to $\approx 1200\,\text{ps}$ (Figure 5.6e). Regarding micromagnetic simulations, the switching times cannot be compared directly with the experiments because, to mimic a quasistatic situation, we used a parameter of $\alpha = 1$. Therefore, new simulations with $\alpha = 0.02$ are ongoing to perform a future comparison. Nevertheless, we evidenced also with micromagnetic simulations, as in experiments, the divergence of the switching time as we approach the critical current. One example is the case of a 90 nm diameter nanowire with a 40 nm-long chemical modulation. The critical switching current of this system is $2.05\times10^{12}\,\text{A}\cdot\text{m}^{-2}$. For a current density of $2.5\times10^{12}\,\text{A}\cdot\text{m}^{-2}$ a reversal time of 0.38 ns is obtained (Figure 5.7e). However, for a current density of 2.1×10^{12} a reversal time of 3.50 ns is obtained (Figure 5.9b). The choice of $\alpha = 1$ to mimic a quasistatic situation does not allow reflecting the actual switching time. Finally, experiments revealed a shortening of the curling length during the switching mechanism for a 111 nm diameter nanowire with 30 nm-long chemical modulations (Figure 5.6e). This revealed that curling is induced by the torque of the adjacent Permalloy domains. This has been also demonstrated with micromagnetic simulations for the

coherent switching regime that occurs for short modulations (Figure 5.9b).

5.6 Conclusions

In this chapter, we have reviewed the micromagnetic behavior of the curling of magnetization at the $Fe_{80}Ni_{20}$ chemical modulations within a Permalloy nanowire under the stimulus of magnetic fields of various types. The experimental investigations rely on X-ray magnetic imaging (PEEM, TXM, STXM or X-ray ptychography).

We reported the experimental study of the reduction of the magnetic contrast at the chemical modulation when an increasing axial magnetic field is applied. By setting the X-ray beam nearly perpendicular to the wire axis, the magnetic contrast arises mostly from curling at the modulations. The applied field induces a reduction of the curling angle $\theta(R)$, evidenced by the reduction of the XMCD contrast. We proposed and assessed various analysis processes to quantify the reduction of the curling angle under field, taking into account the various instrumental effects that contribute to the imaging.

In order to translate the XMCD contrast into a degree of tilting of the magnetization, it is required to have the most accurate inputs to the model. In our particular case, we found that the background incoherent intensity plays a major role, leading us to make use of the theoretical absorption coefficients and using as inputs the background signal, the spot size, the sample holder rotation and the wire diameter. The resulting analysis reveals a linear decrease of the curling angle under field, which is in reasonable quantitative agreement with micromagnetic simulations. However, the estimated curling is $\approx 10°$ lower. Possible reasons include the presence of two exchange stiffness values that are not considered in the simulations and the uncertainties of the parameters used in the model.

The second part of the chapter focused on the response of the system to a nanosecond current pulse, where the dominating stimulus is the Œrsted field associated with the current. We evidenced experimentally a deterministic Œrsted-field driven circulation switching above a certain density of current. We found that the critical current j_c depends on the wire diameter and chemical modulation size. In addition, time-resolved STXM imaging revealed a time scale of switching of ≈ 200 ps for current values above the critical one and time scales of ≈ 1200 ps for current values near the critical one. This divergence of the switching time was used to calculate the critical current with micromagnetic simulations using a standard method based on the scaling of a parameter. The switching time τ_c was defined at $\max(m_\phi) = 0$, and the value of j_c was obtained from the intercept at $\tau_c^{-1} = 0$. The j_c vs ℓ curves show a non-monotonous behavior, from which we identify two switching regimes. For modulations shorter than typically $2\Delta_{mod}$ the charge screening is partial, and curling in the entire modulation is driven by the screening of surface charges. This leads to a coherent switching process driven by the Œrsted field. This was also confirmed experimentally with time resolved imaging , since a shortening of the curling length during switching was imaged, revealing the torque that the Permalloy domains exert on the modulation interfaces. For modulations longer than this, the charge screening is nearly full, and the plateau of curling at the center of the modulation is driven by longitudinal exchange. Switching of the curling occurs incoherently, nucleating from the center of the modulation and expanding towards its interfaces. The switching current reaches its maximum at the crossover between the two regimes.

Chapter 6

Interplay of curling at modulations and domain walls

This last chapter examines the interaction of magnetic Domain wall (DW)s and chemical modulations: at rest, under a quasistatic magnetic field, and under nanosecond pulses of Œrsted field. Experimental evidence and micromagnetic simulations will be provided to show a complete and realistic picture of the phenomena. The first part of the chapter will show the modification of the energy profiles that a chemical modulation induces on a DW. This will be followed by the study of DW propagation through a chemical modulation under a quasistatic axial magnetic field, considering the cases of parallel ($C+C+$) and antiparallel ($C+C-$) circulations. Then, DW transformations induced by an axial field will be detailed from a topological point of view. The second part of the chapter focuses on Œrsted field-driven DW transformations in a homogeneous and in a modulated nanowire. X-ray imaging experiments in static and time-resolved modes are combined with micromagnetic simulations and a post-processing tool that tracks volume (Bloch Point (BP)) and surface (vortex-antivortex) singularities. Some of these transformations include Bloch-point domain wall (BPW) circulation switching, BPW to transverse-vortex domain wall (TVW) transformation, TVW to BPW transformation, BPW expulsion from modulation. Lastly, we will show the experimental evidence of long-distance DW motion from one modulation to the adjacent one.

In this chapter, I have contributed to all the X-ray magnetic imaging measurements, their post-treatment, and the analysis of the data. Regarding, time-resolved X-ray imaging, I was unable to perform the experiments as they took place during the last stage of the writing period of this manuscript. Therefore, the measurements were performed by OLIVIER FRUCHART and AURÉLIEN MASSEBOEUF. I have performed and post-treated the micromagnetic simulations with the *mumax3* code. The micromagnetic simulations by *FeeLLGood* were launched by DARIA GUSAKOVA and post-treated by the two of us. DARIA GUSAKOVA and OLIVIER FRUCHART collaborated in the discussions of micromagnetic simulations. JÉRÔME HURST wrote the post-treatment code to detect singularities from a *FeeLLGood* output. AURÉLIEN MASSEBOEUF performed Fresnel, scanning transmission electron microscopy (STEM)-electron energy loss spectroscopy (EELS) and transmission electron microscopy (TEM) imaging under current pulses. Also, AURÉLIEN MASSEBOEUF and I performed the electrical contacting of the nanowires. CHRISTOPHE THIRION developed the sample holders for high-frequency pulses and was in charge of all the electronics setup. The main results that are presented are in preparation for two upcoming publications.

6.1 Physics of domain wall pinning at the chemical modulations

In Chap. 4, the micromagnetic behavior at rest of $Fe_{80}Ni_{20}$ chemically-modulated Permalloy nanowires was explored, detailing the physics of curling in the chemical modulations. The curling response to an external magnetic field or a nanosecond current pulse was detailed in Chap. 5, delving into the Œrsted field-driven

circulation switching. Once the system of study is understood, we have the knowledge to integrate a DW into it. In the simulations we are considering a BPW, since it is the energetically favorable DW for the diameters considered and, in addition, it is favored under a current pulse due to the Œrsted field [181].

In the following we will explore the mechanism driving the pinning of a BPW at a chemical modulation. The modification of the energy landscape on the BPW induced by the chemical modulations will be explored, along with the impact of the relative circulations of the BPW and modulation. Finally, the experimental observations of different types of DW pinning will be presented and discussed in the light of the predictions of the simulations.

6.1.1 Simulation of the energy landscape at rest

To study the energy modification that a chemical modulation induces in the system, we performed micromagnetic simulations with *mumax3* code. The system considered is a cylindrical Permalloy nanowire of 90 nm diameter and 2046 nm length, with a 20 nm-long $Fe_{80}Ni_{20}$ chemical modulation at its center. In order to mimic an infinite wire, the magnetic charges at the wire ends were removed numerically. The mesh size used was 2 nm. The following material parameters were used: spontaneous magnetization $M_1 = 8\times10^5\,\mathrm{A/m}$ for the Permalloy segments, $M_2 = 14\times10^5\,\mathrm{A/m}$ for the chemical modulation, single exchange stiffness for all materials $A = 1.3\times10^{-11}\,\mathrm{J/m}$ and zero magnetocrystalline anisotropy.

The initial configuration was set analytically to define a system with a BPW of a particular circulation and at a desired location. In particular, we use the following to initialize a BPW with positive circulation $C+$:

$$m_z = -\tanh\left[\frac{(z-z_{DW})}{a}\right] \tag{6.1}$$

for a head-to-head configuration, where z_{DW} is the initial position of the center of BPW and a is the DW parameter. In most cases we used $z_{DW} = \pm500\,\mathrm{nm}$ and $a = 50\,\mathrm{nm}$. As regards the transversal components:

$$m_x = \frac{-1}{\cosh(z/a)}\times\sin[\mathrm{Arctan2}(y,x)] \tag{6.2}$$

$$m_y = \frac{1}{\cosh(z/a)}\times\cos[\mathrm{Arctan2}(y,x)] \tag{6.3}$$

where $\phi = \mathrm{Arctan2}(y,x)$ is the azimuthal angle.

Then, we use the following at the location of the modulation to define curling with a positive sense of circulation $C+$ at the chemical modulation, with respect to the axial direction $\hat{\mathbf{z}}$.

$$m_z = 0 \tag{6.4}$$

$$m_x = -\sin[\mathrm{Arctan2}(y,x)] \tag{6.5}$$

$$m_y = \cos[\mathrm{Arctan2}(y,x)] \tag{6.6}$$

The system was relaxed by solving numerically the Landau-Lifshitz-Gilbert (LLG) equation (Sec. 1.2.6). To obtain the internal energy $E_0 = E_d + E_{ex}$ at different DW positions z_{DW}, due to the non-monotonous energy landscape, as we will see, we cannot rely on the drift of the DW free of external forces, as described in [131]. Instead, we applied a longitudinal external magnetic field to move the DW. Therefore, in order to move the DW along the wire and simultaneously be as close to equilibrium as possible, we established the following approach: first, a linearly increasing magnetic field along the axial direction was applied, such that the DW will move at the critical field. Second, an $\alpha = 1$ was set in order to have a quasistatic situation. In [131], it has been shown to deliver results very close to those when using free drift.

Figure 6.1a shows the internal energy as a function of the BPW position (z_{DW}. This position was calculated at the intersection of three isosurfaces of the magnetization field: $m_x = 0$, $m_y = 0$ and $m_z = 0$ [174]. The orange dashed lines indicate the interfaces of the modulation, which is centered at $z = 0$. The initial position of the BPW was $z_{DW} = -500\,\text{nm}$ for $z_{DW} < 0$. Therefore, a positive magnetic field was applied to move the wall towards the modulation. Then, the opposite was set for $z_{DW} > 0$ values where the initial position of the BPW was $z_{DW} = 500\,\text{nm}$ and a negative axial magnetic field was applied to drive the wall towards the modulation. Therefore, for the moment the DW does not cross the modulation, it just moves towards it. The blue curve corresponds to the case where the BPW and modulation have parallel and positive circulations $C+C+$ with respect to the sense of motion in the axial direction $\pm\hat{\mathbf{z}}$. In this case, the modulation acts as an energy well, being the minimum energy when the BPW is at the chemical modulation. On the other hand, the red curve shows the case of antiparallel circulations of the BPW ($C+$) and modulation ($C-$), where the energy landscape shows the opposite behavior: an energy barrier (Figure 6.1a).

A more illustrative view is shown in Figure 6.1b and Figure 6.1c, where the micromagnetic simulated outer views are shown for the different wall positions (z_{DW}) marked with a letter in Figure 6.1a. The color-code corresponds to axial magnetization (m_z) and the orange dashed line to the interfaces of the modulation. In particular, Figure 6.1b shows the case of parallel circulations, $C+C+$, where we observe the shrinking of the DW width when it is at the modulation (letter b). Also, note in the inset the clarification on the notation of positive $C+$ or negative $C-$ circulation depending on the sense of wall motion along the axial direction $\pm\hat{\mathbf{z}}$. This is the reason why letters c and d show another sense of rotation but still positive circulation. Figure 6.1c reflects the case of antiparallel circulations $C+C-$. In this case the system has the highest energy when the BPW is next to the modulation (letter f). At that stage, the DW shrinks until a depinning field is reached and it propagates through the chemical modulation. This phenomenon brings new rich physics and will be described later in this chapter.

The physics provided in Figure 6.1 can be understood as follows: (i) at long distances between the BPW and the modulation, both energy profiles overlap. This means that the interaction of both micromagnetic objects is independent of their relative circulations. It results in a repulsive interaction governed by magnetostatics, i.e., by the interaction of a positively charged head-to-head BPW with the positively charged

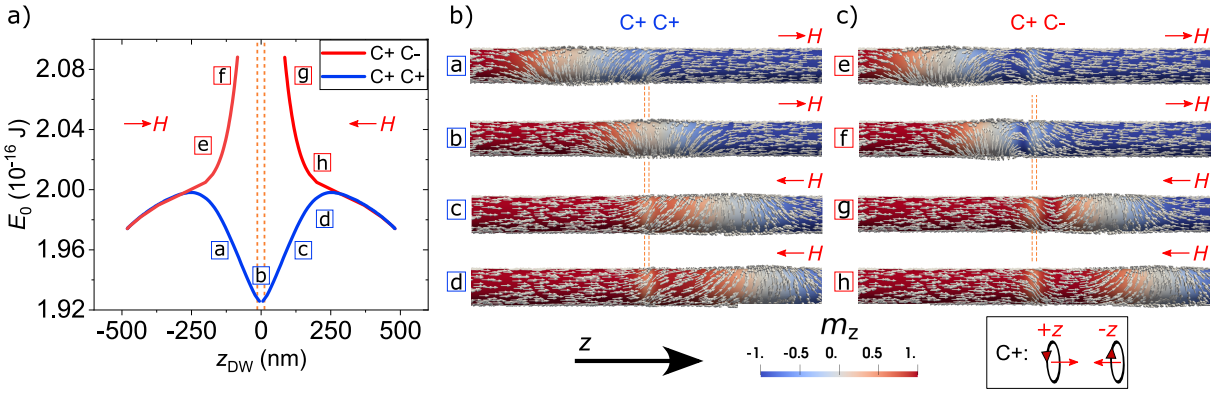

Figure 6.1: **a)** Internal energy E_0 versus BPW position (z_{DW}) of a 90 nm diameter Permalloy nanowire with a 20 nm-long chemical modulation at $z = 0$. Orange dashed lines indicate interfaces of the modulation. The wall is drifted towards the modulation under an axial quasistatic magnetic field. In blue it is shown the case of parallel circulations $C+C+$ between BPW (always $C+$ with respect to the axial direction of motion $\pm\hat{\mathbf{z}}$) and modulation $C+$. In red, it is shown the case of antiparallel circulations $C+C-$ between BPW ($C+$) and modulation $C-$. **b)** and **c)** show outer view configurations obtained with micromagnetic simulations at different wall positions (z_{DW}) for parallel and antiparallel circulations, respectively. The color-code represents m_z.

modulation interface (see Sec. 4.3.2). (ii) At short distances, the relative circulation determines the energy profile: a well for parallel circulations and a barrier for antiparallel circulations. This is also direct evidence that the energetics is governed by exchange and magnetostatics. The exchange interaction strongly depends on the relative circulations [307]. This is reflected by the gain in exchange energy when curling occurs, i.e., when the BPW is at the modulation for the $C+C+$ situation. On the other hand, for antiparallel configurations $C+C-$, we found two metastable states at both sides of the modulation separated by an energy barrier. The only way to overcome the barrier is by increasing the dipolar energy E_d with the shrinking of the wall as shown in letter f in Figure 6.1c.

6.1.2 Imaging of domain wall pinning at modulations

We conducted different types of microscopy techniques to investigate experimentally the role of the chemical modulations as effective pinning sites. The most convenient technique in terms of the speed of acquisition and availability of the setup is TEM microscopy. With it, we can nucleate DWs by applying a quasistatic pulse of a transverse magnetic field up to 1 T and correlate the location of the DW with that of the chemical modulations. Also, I performed the same study with magnetic force microscopy (MFM) by demagnetizing previously the samples. However, in these cases, the magnetization is probed indirectly. Therefore, conducting dichroism-based X-ray imaging is complementary and often more conclusive to comprehensively characterize the system.

Figure 6.2a shows a reconstructed amplitude ptychographic XAS image at the Fe L_3 edge of a 130 nm-diameter Permalloy nanowire with periodic 60 nm-long $Fe_{80}Ni_{20}$ chemical modulations. The image is composed of 2 µm width images. The Fe-rich chemical modulations show a darker contrast due to the higher absorption. Their locations are indicated by orange dashed lines. This particular sample had a 5 nm HfO_2 atomic layer deposition (ALD) coating of the alumina pores, which made difficult the synthesis process as described in Chap. 3 Sec. 3.2.5. However, the issues related to the synthesis were not detected until we observed in detail the reconstructed XAS images (Figure 6.2f). XAS reveals a slight depletion in the content of Fe at the left of the chemical modulation, followed by a short Fe rich segment (see modulation #4).

Figure 6.2b shows the corresponding ptychographic reconstructed XMCD image with no tilt of the sample holder, i.e., the wire is perpendicular to the X-ray beam. Accordingly, there is no contribution from the axial magnetization components, thus the Permalloy domains show a uniform gray magnetic contrast. This sample was previously demagnetized within the TEM chamber by applying 1 T magnetic field along the transverse direction. The reason to do so was to nucleate DWs before the ptychography experiment. Since these wires were not electrically contacted, the DWs could not be nucleated in-situ with electric pulses. Therefore, the only option is to nucleate them by applying a high amplitude transversal field, which demagnetizes the sample and relaxes the system, hopefully with at least one DW within it. Due to the presence of chemical modulations, the DWs get easily pinned at the chemical modulations, as predicted by micromagnetic simulations in Figure 6.1. This initial state (Figure 6.2b) shows curling magnetization at the chemical modulations with various circulations ($C+$ or $C-$). We also observe one BPW pinned at modulation #2 and another BPW at modulation #4. Since the BPW and modulation show parallel circulations, the DW has relaxed on the modulation where the equilibrium state occurs (see Figure 6.1a). The XMCD range of contrast in the image is 20 %, whereas in other techniques such as photoemission electron microscopy (PEEM) or scanning transmission X-ray microscopy (STXM) it is usually less than 3 %. Figure 6.2b shows information about the transverse magnetization components. However, it can be desirable to have also information on the axial domains, e.g., to know if the DWs are of head-to-head or of tail-to-tail nature. We found that a 10° sample holder tilt is a good compromise to probe the three-dimensional magnetization components. This is shown in the ptychographic reconstructed XMCD image in Figure 6.2c, where now we can distinguish the axial domains but still have high magnetic contrast coming from the transversal magnetization components.

Micromagnetic simulations shown in Figure 6.1a predict different pinning configurations depending on the relative circulation between the BPW and modulation. For the case of parallel circulations, a similar

mechanism should occur for a TVW, which has also an associated curling magnetization. The XMCD image shown in Figure 6.2e shows a TVW pinned at a chemical modulation. The system is a 120 nm diameter Permalloy nanowire with a 30 nm-long $Fe_{80}Ni_{20}$ chemical modulation. Now, we can notice that the wall is not exactly centered at the modulation as in the case of a BPW. Probably, this is due to the fact that the center of a TVW has not the largest curling since at this location there is a strong transverse magnetization component. On the other hand, since each side of a TVW has opposite curling circulations, we may encounter also the case of antiparallel circulations ($C+C-$) between a TVW and a modulation. This is displayed in Figure 6.2g, where the ptychographic XMCD contrast shows a TVW pinned next to the chemical modulation. Note that this sample shows the second Fe-rich modulation impurity due to a synthesis issue, which is at the location of the center of the DW. For the antiparallel configuration case ($C+C-$), the repulsion between both micromagnetic objects is driven by the magnetic charges, as in the case of a BPW pinned next to a chemical modulation shown in Figure 6.2i. The distance between the wall and the modulation is < 100 nm which is in agreement with micromagnetic simulations (Figure 6.1a). Finally, note that the nucleation of the DWs shown in Figure 6.1 was performed by applying a transverse field within the TEM chamber, previous to X-ray imaging. With this, we show that both walls (BPW and TVW) can be

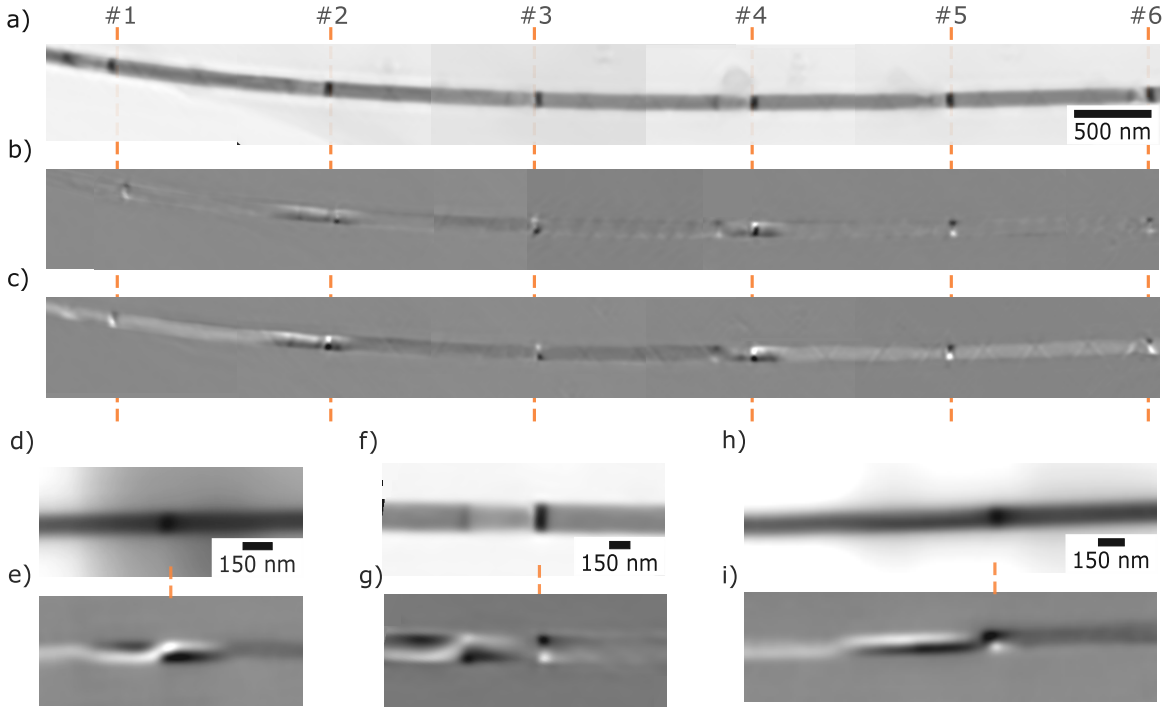

Figure 6.2: Ptychography experiments of DW pinning at chemical modulations. **a)** Reconstructed amplitude ptychographic XAS image at the Fe L_3 edge of a 130 nm diameter Permalloy nanowire with periodic 60 nm-long $Fe_{80}Ni_{20}$ chemical modulations. Orange dashed lines indicate the location of the chemical modulations. **b)** and **c)** show reconstructed amplitude ptychographic XMCD image of **a)** for a 0° and 10° tilt of the sample holder, respectively. BPWs are displayed at modulations #2 and #4. **d)** XAS image of a 120 nm diameter Permalloy nanowire with a 30 nm-long $Fe_{80}Ni_{20}$ chemical modulation at its center. **e)** Shows the corresponding XMCD image where a TVW is pinned on the modulation. **f)** XAS image of a 130 nm diameter Permalloy nanowire with a 60 nm-long $Fe_{80}Ni_{20}$ chemical modulation. **g)** Shows corresponding XMCD image where a TVW is pinned next to the modulation. Chemical defect is shown at the left of the modulation. **h)** XAS image at the Fe L_3 edge of a 120 nm diameter Permalloy nanowire with a 30 nm-long $Fe_{80}Ni_{20}$ chemical modulation at its center. **i)** Shows corresponding XMCD image where a BPW is pinned next to the modulation.

stabilized and pinned on the modulations.

Next, we show experimental electron holography images of a TVW at a chemical modulation. The top image in Figure 6.3a shows a high angle annular dark field (HAADF) image of a 130 nm-diameter Permalloy nanowire with a 20 nm-long $Fe_{80}Ni_{20}$ chemical modulation at its center. The bottom shows a EELS compositional map of Ni (green) and Fe (red). The orange dashed lines indicate the location of the material interfaces. In order to nucleate DWs in the system, a transverse magnetic field of 1 T was applied and then switched off to image at remanence. The nucleated wall was a TVW pinned at the chemical modulation. Its corresponding amplified magnetic phase image is shown in Figure 6.3b, displayed as $\cos(20 \times \Phi)$. The simulated magnetic phase-shift map obtained from [308] in Figure 6.3c shows that the obtained contrast corresponds to a TVW with a transverse component along $-\hat{\boldsymbol{z}}$. After the application of an external field with a 4 mT axial component, the TVW moves slightly to the left and turns its transverse component along $\hat{\boldsymbol{x}}$. The amplified magnetic phase image is shown in Figure 6.3d, which shows a different shape than the previous one. Its related simulated magnetic phase-shift map obtained from [308] is shown in Figure 6.3e. These results highlight the importance of combining electron holography experiments with micromagnetic simulation to determine the type of DW and determine its inner structure. In correlation with the ptychographic image of a TVW on a modulation (Figure 6.2e), here we also show that the TVW is not centered at the modulation.

To conclude this section on DW pinning at chemical modulations, we recall that a demagnetization transversal field of 1 T was used to nucleate DWs. These walls were then imaged at the location of the chemical modulations. When the wall and modulation circulations are parallel, the BPW or TVW relaxes on the modulation, following the energy well profile predicted by micromagnetic simulations. On the other hand, when the circulations are antiparallel, the walls relax next to the modulation due to a repulsion that arises from the magnetic charges of both objects. Finally, we also evidenced that a TVW does not sit centered on the modulation, but instead it is displaced by ≈ 10 nm to the point where the highest curling occurs.

6.2 BPW propagation through a chemical modulation under magnetic field

In Sec. 6.1, the physics of DW at modulations was described at rest. In the following, we investigate the physics of a BPW propagating through a chemical modulation, depending on their relative circulations. We will reveal a complex mechanism involving the BP [163], which is a magnetic singularity at the core of the BPW (see Sec. 1.3.2). This study is performed by combining experiments with micromagnetic simulations.

6.2.1 BPW propagation for parallel circulations

We first consider the simplest case, which is when the BPW and the chemical modulation have parallel and positive ($C+$) sense of circulation with respect to the axial direction $\hat{\boldsymbol{z}}$. The parameters used within *mumax3* code are the same as the ones mentioned section Sec. 6.1.1. The chemical modulation lengths considered are: 20 nm and 100 nm. The initial state is a 90 nm diameter BPW at $z_{DW} = -500$ nm and a modulation centered at $z = 0$, both with $C+$. An increasing amplitude magnetic field of 2 ns duration is applied along the axial direction $\hat{\boldsymbol{z}}$, to mimic a quasi-static situation.

Figure 6.4a shows the evolution of the internal energy $E_0 = E_d + E_{ex}$ as a function of the position of the BPW. Open symbols correspond to a chemical modulation length of 20 nm, whereas full symbols correspond to a chemical modulation length of 100 nm. The y-axis in red shows the linearly increasing magnetic field with plateaus of 2 ns. Both profiles show an energy well even after crossing the chemical modulation. The nearly symmetric shapes on both sides of the modulation prove that a larger $\vec{H}_{ext}$ does not substantially modify the DW. For the larger modulation, the internal energy is higher due to the cost associated to curl a longer segment. Note also that the energy well is deeper for larger modulations. This makes sense since now most of the curling of the BPW can fit within the modulation. In addition, the depinning field is higher for

the larger modulation, which we believe is related to the deeper well. Specifically, the depinning fields for a 20 nm and 100 nm long chemical modulation are 10 mT and 14 mT, respectively.

In this study, the DW position (z_{DW}) was calculated by tracking the BP position with *Paraview* software at the point where $m_x = m_y = m_z = 0$. Figure 6.4b shows the micromagnetic configurations for selected values of z_{DW} values identified with a letter. At the left, the outer view is shown along $\hat{\boldsymbol{z}}$. The color code represents the magnetization along the radial direction m_ρ. Note that the color scale is not centered at zero, being red for $m_\rho = 0.26$ and blue for $m_\rho = -0.038$. This scale was chosen to highlight the radial component, since the BPW has a non-negligible radial component whose sign depends on the wall polarity. In this case, for a head-to-head configuration, the radial component is outwards (positive). The black square below corresponds to the position of the BP, whereas the light blue rectangle shows the chemical modulation. The interfaces of the modulation are indicated by the orange dashed lines. On the right, we can observe the inside view through the nanowire, where the color code also represents m_ρ. This view is shown to detect any motion of the BP along $\hat{\boldsymbol{x}}$. Note that a smaller m_ρ occurs at the modulation, in both situations: when the wall reaches the modulation (letters *a* and *b*) and when the wall is on the modulation (letter *c*). We believe the reason is that for a modulation length below the wall width, the head-to-head positive charges

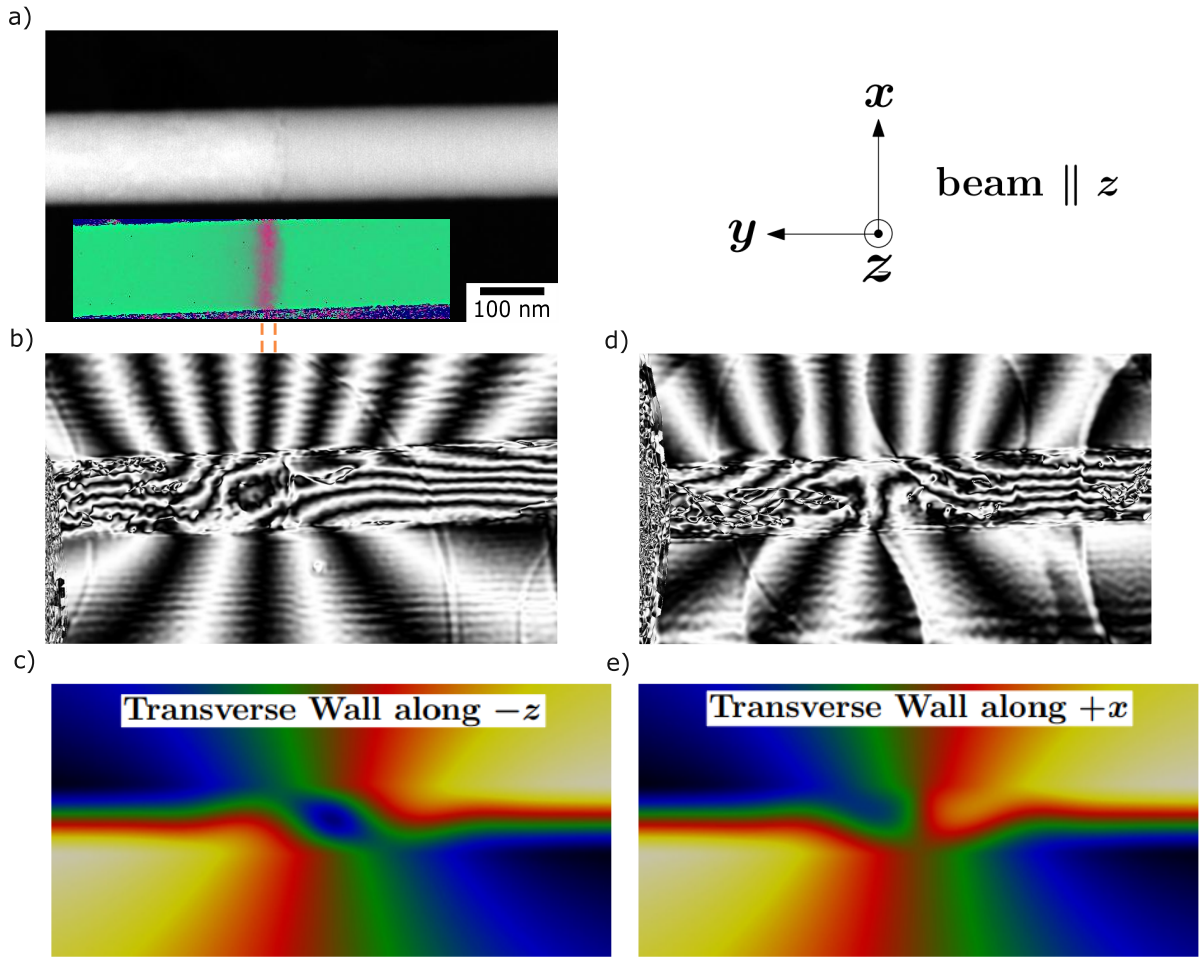

Figure 6.3: Electron holography of a TVW with two transverse orientations. **a)** HAADF image of a 130 nm-diameter Permalloy nanowire with a 20 nm-long $Fe_{80}Ni_{20}$ chemical modulation at its center. Orange dashed lines indicate the location of the material interfaces. **b)** and **d)** Amplified magnetic phase images displayed as $\cos(20 \times \Phi)$. These reveal a TVW with a transverse component along $-\hat{\boldsymbol{z}}$ and along $\hat{\boldsymbol{x}}$, respectively. **c)** and **e)** show simulated magnetic phase-shift maps obtained from [308].

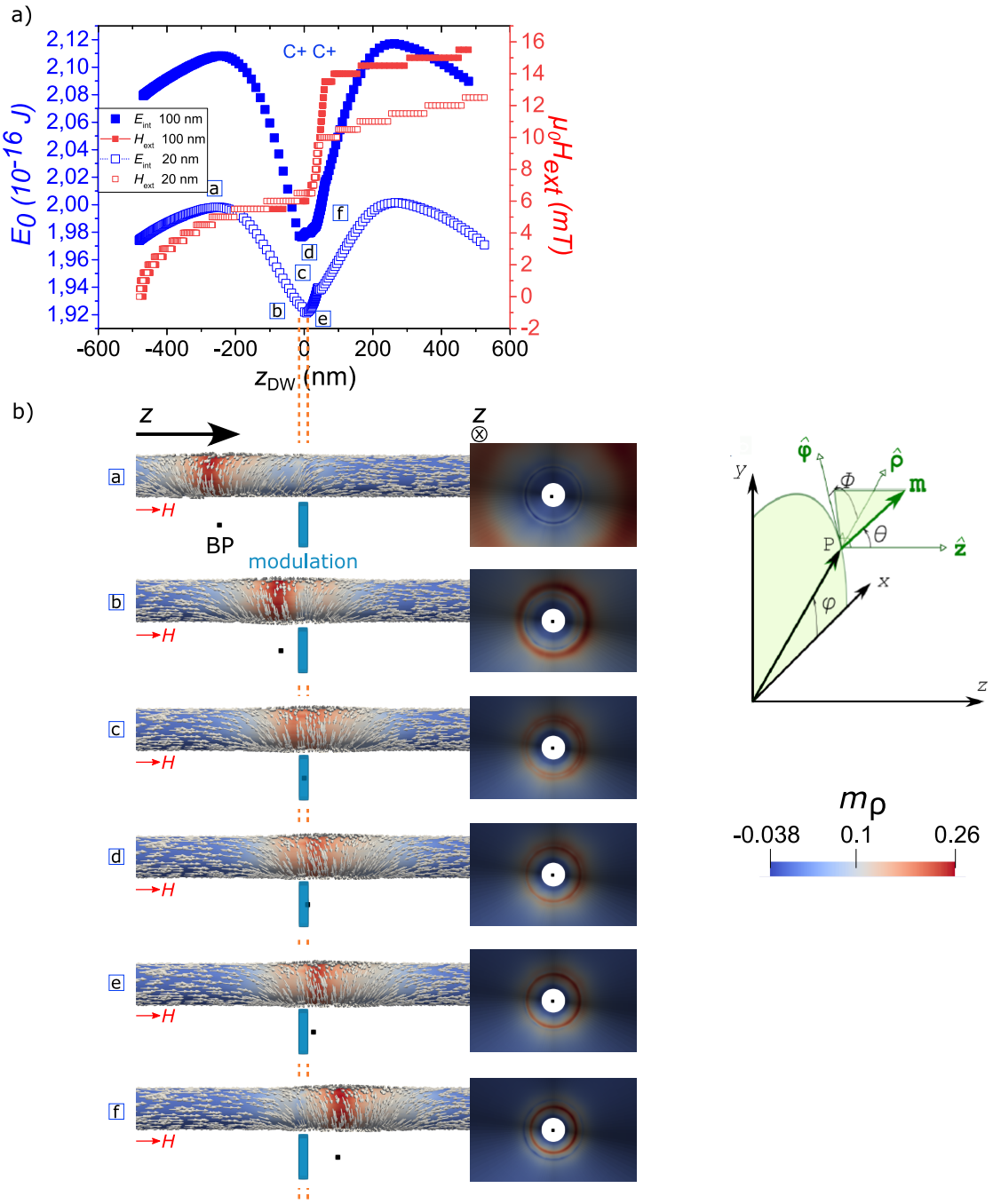

Figure 6.4: BPW propagation through a chemical modulation of a 90 nm diameter Permalloy nanowire for parallel and positive circulations $C+C+$ with respect to $\hat{\mathbf{z}}$. **a)** Internal energy E_0 versus BPW position (z_{DW}). Open and full blue symbols correspond to a chemical modulation length of 20 nm and 100 nm, respectively. Red symbols show the magnitude of the 2 ns plateaus of the axial magnetic field applied. **b)** Outer (left) and inside (right) micromagnetic views at different z_{DW}, for a modulation length of 20 nm. Each configuration is identified with a letter in **a)**. The black square corresponds to the BP position and the elongated light blue rectangle to the position of the chemical modulation, whose interfaces are indicated by the orange dashed lines. Color code represents m_ρ.

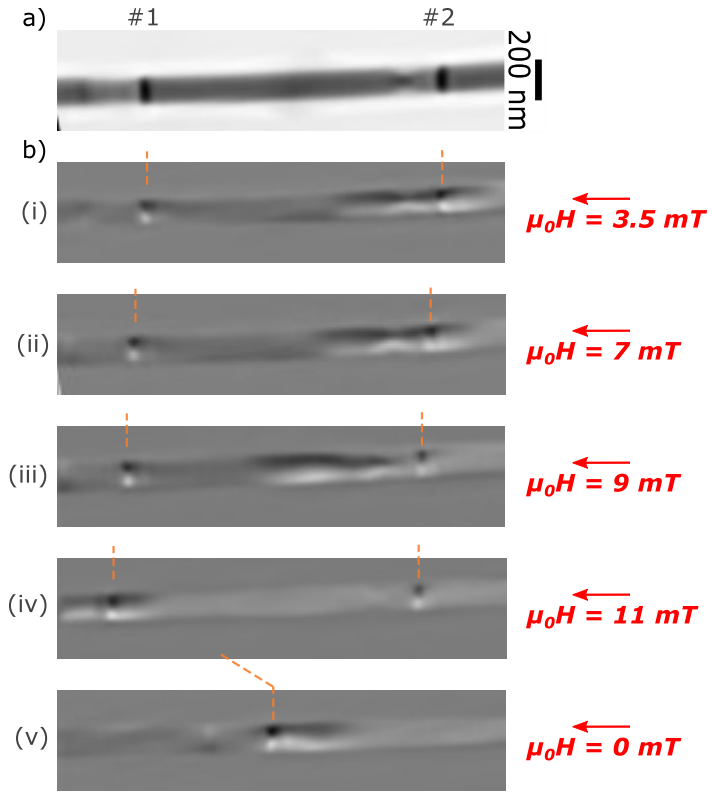

Figure 6.5: BPW depinning, propagation and pinning under magnetic field. **a)** Reconstructed amplitude ptychographic XAS image at the Fe L_3 edge of a 130 nm diameter Permalloy nanowire with periodic 60 nm-long $Fe_{80}Ni_{20}$ chemical modulations. Orange dashed lines indicate locations of the chemical modulations. **b)** Reconstructed amplitude ptychographic XMCD images under a constant magnetic field indicated in red.

are largely linked with M_s, which is limited by M_2 at the modulation. As $M_2 > M_1$, m_ρ is smaller in the modulation. This also supports the wall width contraction when it is on the modulation (letter *c*). In letter *d*, the BP is pinned at the interface of the chemical modulation until the depinning field is reached, and it leaves the modulation (letter *e*). Afterwards, the BPW keeps propagating steadily. Additionally, we confirm that the BP remains at the core of the wire during propagation. Therefore, we may conclude that a progressive and smooth propagation of the BPW takes place when its circulation and the circulation of the chemical modulation are parallel ($C+C+$).

Let us illustrate the above expectations with experimental results obtained on BPW depinning and propagation from a chemical modulation. Figure 6.5 considers a 130 nm diameter Permalloy nanowire with two 60 nm-long $Fe_{80}Ni_{20}$ chemical modulations. Figure 6.5a shows a reconstructed amplitude ptychographic XAS image at the Fe L_3 edge and its corresponding reconstructed XMCD image is shown at the top of Figure 6.5b. The magnetic configuration shows a parallel circulation sense of the chemical modulations and the BPW, which is pinned at modulation number #2 (i). The image was acquired under the application of a constant magnetic field of 3.5 mT along $-\hat{\mathbf{z}}$, which is the reason why the BPW is shifted to the left. However, this shift may also come from the chemical defect at the left of the modulation. As a material defect, we refer to the depletion of Fe at the left of the modulation followed by a very thin second Fe-rich modulation (see Sec. 3.2.5). The depinning field in this case was of 9 mT, field at which the BPW leaves the modulation and propagates a distance of $\approx$ 200 nm towards the left side (iii). The DW notably remains pinned on the material defect at the left side. At 11 mT axial field, the DW propagates until the next modulation, and it gets pinned on it, reflecting once more the effective pinning (iv). When the magnetic field is removed, the BPW relaxes to the right side of the modulation, as shown in (v). We believe this is because the material defect at

the left of the chemical modulation #1 has an opposite sense of circulation.

6.2.2 BPW propagation and circulation switching for antiparallel circulations

In this section we consider DW propagation when the BPW (C+) and the chemical modulation (C−) have initial antiparallel circulations with respect to the axial direction $\hat{\mathbf{z}}$. First, let's look at the internal energy profiles obtained with *mumax3* code using the same parameters as in Sec. 6.2.1 for a 90 nm diameter Permalloy nanowire (Figure 6.6a). The initial state is a BPW $C+$ at $z_{DW} = -500$ nm, that propagates towards the modulation $C-$ along $\hat{\mathbf{z}}$ by applying linearly increasing magnetic field plateaus of 2 ns (red symbols). Grey open symbols correspond to a $Fe_{80}Ni_{20}$ chemical modulation of 20 nm length. The energy profile is complex since it combines an initial repulsive part (letter a), followed by an attractive part (letters $b-h$). Also, it is non-symmetric for $z_{DW} < 0$ and $z_{DW} > 0$. This shows that non-trivial behavior occurs, which is not associated with the relative circulations. With regard to the depinning field, a value of 18 mT was obtained for a 20 nm-long modulation. For the case of a modulation of 100 nm length (in blue), the depinning field is 32 mT. Therefore, both systems show a larger depinning field than in the case of $C+C+$. The internal energy profiles suggest that circulation switching occurs when the BPW crosses the modulation. However, they do not provide a complete understanding of the phenomenon, which requires a deep analysis of $\mathbf{M}$ at different time steps. Also, this can be checked by studying the surface maps before (letters $a-d$) and after (letters $e-i$) the modulation.

Figure 6.6b shows the outer views micromagnetic simulated of a 90 nm diameter Permalloy nanowire with a 20 nm-long chemical modulation at its center. The letters on the left correspond to the configurations at selected z_{DW} values in Figure 6.6a. The black square below corresponds to the BP position, and the light blue rectangle corresponds to the location of the chemical modulation. When inspecting over time all the configurations we can conclude the following: first, the BP starts approaching the chemical modulation (letter b), then a strong radial component appears at one specific location on the wire surface (letter c). Unrolled m_ρ maps of surface magnetization allow to describe such locations as surface vortex-antivortex of positive polarity (Figure 6.6d). Note that the unrolled maps show a view from inside the wire, which is why the arrows show upward direction for positive circulation $C+$. Later on, a strong negative radial component appears, revealing the existence of a surface antivortex of negative polarity, location at which the magnetization is fully pointing inwards $m_\rho = -1$ (letter d). Later, the surface vortex-antivortex of opposite polarity merge (letter g) and a BP with opposite polarity re-enters in the volume (letter h). The BPW remains at the chemical modulation until the depinning field is reached and it propagates to the right (letter i). Therefore, we demonstrate here that a chemical modulation drives the switching of a BPW under propagation driven by an external axial magnetic field. This may seem surprising at first sight, since the BPW is a more massive object than the modulation. We believe that what matters is the energy barrier separating the two circulations for each object. When probed by the application of an Œrsted field, switching has been shown to occur at lower thresholds for the BPW [185] than for modulations [142], which makes the present switching process understandable.

The nucleation of surface vortex-antivortex pairs and their interaction with a BP to reverse its polarity, or to transform a TVW into a BPW, has already been predicted by the group through micromagnetic simulations in the work of ARNAUD DE RIZ [185]. To explore the similarities and differences with the present case, let us examine in more detail the dynamics of the BP, the vortex and the antivortex. It is helpful to follow the radial magnetization m_ρ in the volume and at the surface, for which two visualization approaches have been used. Figure 6.6c shows the inside view of the surface m_ρ configuration obtained with the *Paraview* software. This way, we can visualize any BP in the volume and correlate it with the presence of vortex-antivortex, and their polarity via the isolines $m_\rho = 1$ (red) and $m_\rho = -1$ (blue). The surface view is displayed in Figure 6.6d, where the unrolled m_ρ surface maps are extracted using a post-treatment code. In letter a the BP is at the core of the wire, and at the surface one vortex (V) - antivortex (AV) pair is nucleated and shown by the two red contours in the intersection of $m_\varphi = 0$ with $m_z = 0$. Since topology must be conserved, this pair shares

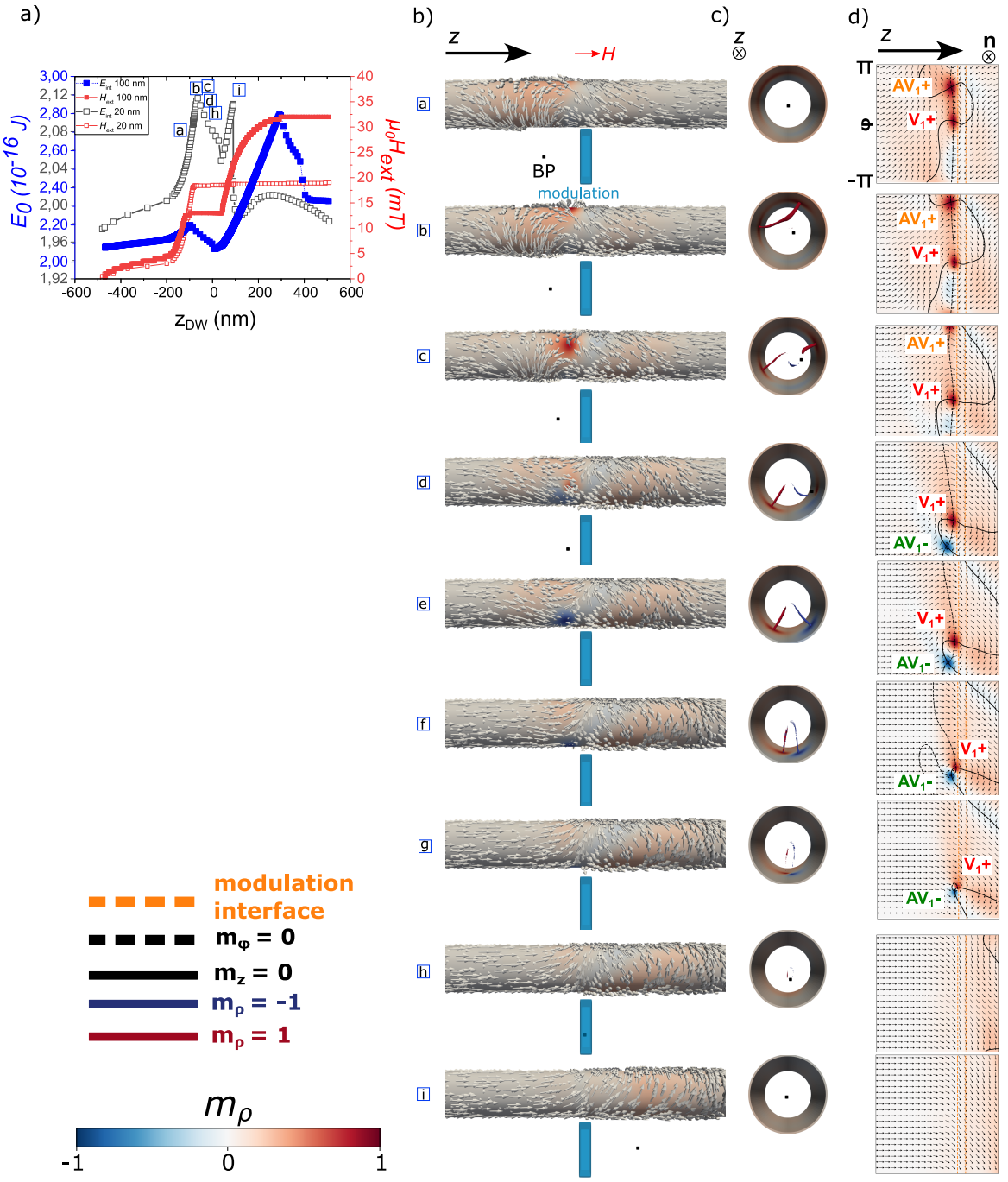

Figure 6.6: BPW circulation switching before crossing a chemical modulation of opposite circulation under a linearly-increasing magnetic field. The switching process involves one vortex-antivortex pair. **a)** Internal energy E_0 versus BPW position z_{DW} for a 90 nm diameter Permalloy nanowire. Grey and blue symbols correspond to a chemical modulation length of 20 nm and 100 nm respectively. Red symbols belong to the amplitude of the axial magnetic field pulses with 2 ns plateaus applied. **b)** Outer view configuration of the micromagnetic simulations at selected z_{DW}. The black square corresponds to the BP position and the elongated blue rectangle corresponds to the position of the chemical modulation. The color-code represents m_ρ. **c)** Inside surface view through the nanowire showing the location of vortex, antivortex and BP. Red and blue isolines correspond to $m_\rho = 1$ and $m_\rho = -1$, respectively. **d)** Unrolled m_ρ maps at the wire surface. Black arrows indicate the direction of magnetization. Orange dashed lines indicate the interfaces of the modulation. Black and dashed black lines correspond to $m_z = 0$ and $m_\varphi = 0$, respectively. The normal **n** indicates the direction of the outer normal to the wire surface.

the same m_ρ sign and thus the positive same polarity, thus we will use the notation V_1^+ - AV_1^+ (we will look later into the conservation of the topological charge). In letter *b*, the V_1^+ - AV_1^+ pair at the surface moves away from each other. In the volume view, we can see the extent of the radial components in the red isolines $m_\rho = 1$, that connect the V_1^+ - AV_1^+ pair. When, the V_1^+ - AV_1^+ pair are far enough from each other, the red isoline has reached the BP (letter *c*). At later stages, the BP moves along the isoline towards the surface. When the BP reaches the surface (letter *d*), it is annihilated from the volume. This comes with a change in the antivortex polarity AV_1^-, as the BP was connected with the portion of the isoline with $m_\rho = -1$ (letter *e*). This is reflected by the appearance of a blue cloud corresponding to $m_\rho = -1$ on the surface map. At this stage, there is no BPW in the system but a TVW, as usual characterized by a line of flux going through the wire. Then, the V_1^+ - AV_1^- pair keeps moving azimuthally towards the side opposite to the one they were nucleated (letters *f* and *g*), until they merge and a BP enters again in the volume (letter *h*). The BPW has now a negative circulation $C-$, i.e., the same as the initial one in the modulation. Therefore, when the depinning field is reached, the BPW propagates to the right side of the chemical modulation (letter *i*).

This BPW circulation switching when crossing a chemical modulation under magnetic field has never been reported before. However, the just-explained underlying mechanism is the same as the one reported in [185] for Œrsted field driven BPW switching in a Permalloy nanowire, for a current density above but close to the critical one. We can draw an analogy between this phenomenon and coherent reversal versus nucleation- propagation mechanisms. The switching of circulation of the BPW via the rise of m_ρ to ± 1 on the wire periphery may have been expected. However, it would be very costly in dipolar energy. Instead, an area with $m_\rho = -1$ nucleates locally and propagates around the perimeter via the motion of the surface vortex-antivortex along opposite azimuthal directions. Consequently, we can conclude that the switching mechanism is independent of the external driving force. Although it remains to be studied whether equivalent dynamics would occur under the spin-transfer torque (STT) stimulus, we suspect that this will be the case. One particular feature that we have observed is that vortex-antivortex pairs nucleate only at the right of the BPW, between the BPW and the chemical modulation. Indeed, if we take a closer look at the letter *a* unrolled map in Figure 6.6d, we notice that there is only one green isoline $m_\varphi = 0$ at the right of the DW. This is not the case for a BPW that is on a plain wire (no modulation), where one $m_\varphi = 0$ isolines occurs at each side of the DW.

With a view to describing a more realistic situation, we conducted the same simulation again but with $\alpha = 0.02$ under a constant $H_{\text{ext}} = 50\,\text{mT}$. All the other parameters were kept the same. The simulations were now conducted with the *FeeLLGood* code for the following reasons. In order to track the positions of volume and surface singularities (such as BP or vortex-antivortex), we used the in-home post-processing tool developed by JÉRÔME HURST. This code is specifically for *FeeLLGood* code output data, as it is adapted to the finite elements data generated for tetrahedron-based mesh. The singularity tracking tool analyzes the magnetization vector field topology. It is capable of detecting whether the magnetic distribution contains singularities. It also calculates their coordinates and determines the singularity type. The tool is based on conventional vector field analysis, implying the calculation of the eigen-values of the so-called Jacobian matrix which contains magnetization component derivatives over the spatial coordinates at a given point. The procedure is divided into three steps: (i) detection of singularity using $m_x = m_y = m_z = 0$ condition for BP or $m_\varphi = m_\rho = 0$condition at the tangent to wire surface for vortex-antivortex, (ii) the construction of the Jacobian matrix at the singularity position, and (iii) analysis of the sign of the real and imaginary parts of the Jacobian matrix eigen-values.

The three-dimensional graph in Figure 6.7a shows the evolution along $\hat{\boldsymbol{x}}$, $\hat{\boldsymbol{y}}$ and $\hat{\boldsymbol{z}}$ of the BP and surface vortex-antivortex. The black color corresponds to a BP, the red one to a vortex with positive polarity V_1^+ and the orange one to an antivortex with positive polarity AV_1^+. The blue and green colors correspond to a vortex V_2^- and an antivortex AV_2^- with negative polarity. The interfaces of the 20 nm-long chemical modulation are indicated by the orange dashed lines. The initial state is a BPW at $z = -500\,\text{nm}$ with positive circulation $C+$ with respect to $\hat{\boldsymbol{z}}$. In order to better understand the dynamics of the vortex-antivortex pairs, we studied their time evolution along z (Figure 6.7b) and their time evolution on the unrolled m_ρ surface maps (Figure 6.7c).

Initially, the BP propagates along $\hat{\boldsymbol{z}}$ with a spiraling motion [171]. Just before reaching the modulation, we notice the growth of two areas along the wire perimeter with $m_\varphi = 1$ and $m_\varphi = -a$. The former leads first to the creation of a V_1^+ - AV_1^+ pair of positive polarity (red and orange lines), whereas the latter leads to the

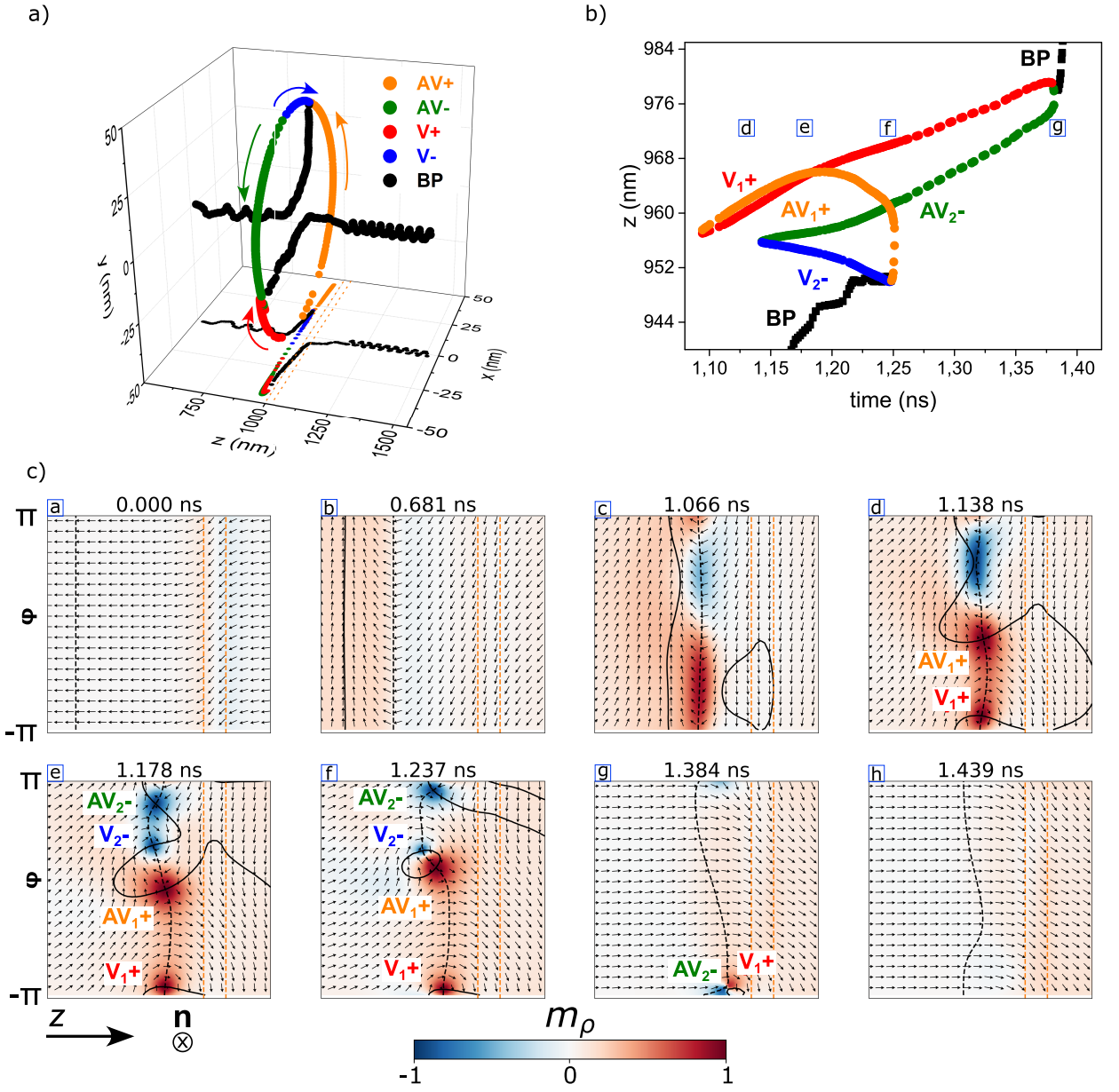

Figure 6.7: BPW circulation switching before crossing a chemical modulation of opposite circulation under a constant axial external field of 50 mT. The switching process involves two vortex-antivortex pairs. The system is a 90 nm diameter Permalloy nanowire with a 20 nm long chemical modulation. **a)** A three-dimensional graph shows evolution along $\hat{\boldsymbol{x}}$, $\hat{\boldsymbol{y}}$, and $\hat{\boldsymbol{z}}$ of the BP (black) and the vortex-antivortex pairs with positive V_1^+ (red) - AV_1^+ (orange) and negative V_2^- (blue) - AV_2^- (green) polarity. The orange dashed lines indicate the location of the modulation interfaces. **b)** Time evolution of the singularities shown in **a)**. **c)** Unrolled m_ρ surface maps of the switching mechanism. The color code corresponds to m_ρ, the black dashed line to $m_\varphi = 0$ and the black line to $m_z = 0$. The normal **n** indicates the direction of the outer normal to the wire surface.

nucleation of a V_2^- - AV_2^- second pair of negative polarity (blue and green lines). Within each V-AV pair, the vortex and antivortex move away from each other along the azimuthal direction. Note that the polarity of the first pair matches with the polarity of the head-to-head BPW, and also the one favored by the chirality of the LLG equation via $\mathbf{H} \times \mathbf{M}$. The reason for the opposite polarity of this second pair is probably to reduce the global magnetostatic energy. Therefore, in the end, the switching process involves now two pairs of vortex-antivortex. During the vortex-antivortex pair formation and motion, the BP moves from the core of the wire towards the surface. It reaches the surface at the moment when the vortex with negative polarity V_2^- (blue) and the antivortex with positive polarity AV_1^+ (orange) merge. At this precise moment, only V_1^+ and AV_2^- remain in the system far from each other. Later, a BP with positive polarity re-enters in the volume at the moment the V_1^+ and AV_2^- annihilate. Afterward, this BP propagates through the chemical modulation and moves along $\hat{\boldsymbol{z}}$ with a different frequency.

Let us now describe this transformation using topology. During the first nanosecond, a BPW with positive circulation approaches the modulation, resulting in the formation of red and blue m_ρ contours between the BPW and modulation (letters *b* and *c* in Figure 6.7c). This results firstly in the nucleation of the first pair V_1^+ - AV_1^+ (letter *d*), followed by a second pair with the opposite polarity V_2^- - AV_2^- (letter *e*). When the BP reaches the surface it annihilates with V_2^- and AV_1^+ (letter *f*). From a topological point of view, the topological charge of a vortex in a 2D system (the surface) is $q = +1$, whereas the one of an antivortex is $q = -1$. The winding number, which should be conserved by topology Sec. 1.2.4), of a vortex or an antivortex is $w = qp/2$, where $p = +1$ is positive polarization and $p = -1$ is negative polarization. Thus the total winding number of the V_1^+ - AV_1^+ pair with positive polarization is $w = 0$. The winding number of the BP is $w = \pm 1$, being positive for a tail-to-tail BP and negative for a head-to-head BP. Thus, since the conservation of topology implies $\Delta w_{\text{surf}} = \Delta w_{\text{vol}}$, let's check if this is fulfilled. The initial winding number in the volume is that of the head-to-head BP ($w_{\text{vol,i}} = -1$), and after its annihilation, $w_{\text{vol,f}} = 0$. This makes $\Delta w_{\text{vol}} = 1$. The initial winding number at the surface is the sum of the V_1^+ - AV_1^+ pair and the V_2^- - AV_2^- pair and thus $w_{\text{surf,i}} = 0$. After the annihilation of V_2^- and AV_1^+, the final winding number at the surface is that of the remaining V_1^+ ($w = 1/2$) plus the remaining AV_2^- ($w = 1/2$), and thus $w_{\text{surf,f}} = 1$, which makes $\Delta w_{\text{surf}} = 1 = \Delta w_{\text{vol}}$, thus topology is conserved. The same rule is applied when the remaining V_1^+ and AV_2^- annihilate and a BP with opposite polarity re-enters in the volume (letter *g*).

6.2.3 BPW transformation into TVW at modulations

DW transformations in cylindrical nanowires in motion by a magnetic field have been explored in the last decades. For small diameters ($d \approx 65$ nm to 30 nm), it has been reported with simulations that when a BPW propagates under a magnetic field through a narrower section, it becomes unstable and transforms into a TVW [133]. In addition, it has been reported that in curved nanowires, the TVW becomes even more stable, enhancing the collapse of a BPW into a TVW [309]. For larger diameters, the opposite transformation has been reported experimentally and by simulations under a magnetic field, showing that a TVW transforms into a BPW after a fraction of a nanosecond [180]. In the following, we will detail a new case of DW transformation.

In Sec. 6.2.2, we detailed the BPW circulation switching mechanism that occurs before a BPW C+ propagates through a chemical modulation C-. This phenomenon involves the formation of at least one pair of surface vortex-antivortex and the annihilation of the BP. At a later stage, the BP re-enters in the volume, and the DW is a BPW with opposite circulation to the initial one. However, during the lapse of time with no BPW in the wire, the topology of the system is that of a TVW. We may wonder what would happen if the external stimulus is stopped during that lapse of time. Its duration is ≈ 0.13 ns under a 50 mT and $\alpha = 0.02$ (Figure 6.7), and up to several nanoseconds at smaller fields and larger α (Figure 6.6).

Figure 6.8a shows the time evolution along $\hat{\boldsymbol{z}}$ of the BP (black), the surface vortex-antivortex pairs with positive polarity V_1^+ (red) - AV_1^+ (orange) and with negative polarity V_2^- (blue) - AV_2^- (green). The initial state is a BPW with positive circulation $C+$ next to a chemical modulation $C-$. The wall is set in motion

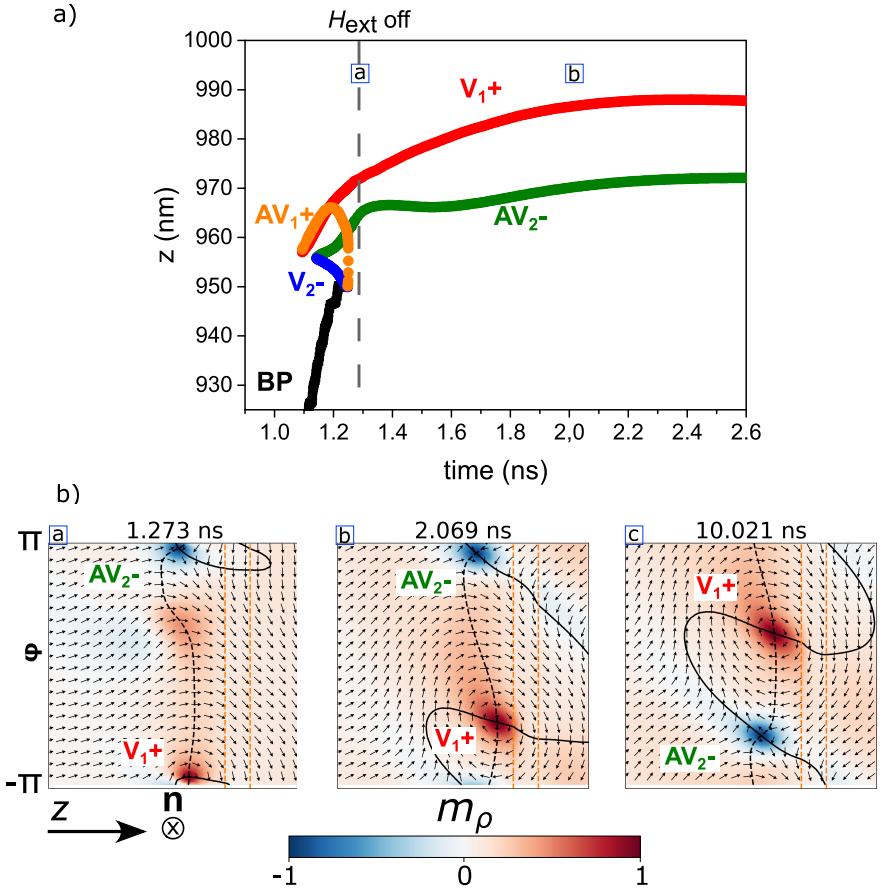

Figure 6.8: BPW transformation to TVW under a magnetic field in a 90 nm diameter Permalloy nanowire with a 20 nm-long chemical modulation. **a)** Time evolution along $\hat{\mathbf{z}}$ of the BP (black) and the surface vortex-antivortex pairs. The initial state is a BPW of positive circulation $C+$ pinned at the left side of the chemical modulation with negative circulation $C-$. An axial magnetic field of 50 mT is applied along $\hat{\mathbf{z}}$ and is turned off at $t = 1.27$ ns. A value of $\alpha = 0.02$ value is used. **b)** Unrolled m_ρ surface maps of the TVW stabilization. The color code corresponds to m_ρ, the black dashed line to $m_\varphi = 0$ and the black line to $m_z = 0$. The normal **n** indicates the direction of the outer normal to the wire surface.

under a magnetic field of 50 mT along $\hat{\mathbf{z}}$ and an alpha value of 0.02. The circulation switching mechanism is similar to the one described in Sec. 6.2.2. However, now we turn off the external field after the first annihilation, that of V_2^- (blue) with AV_1^+ (orange), at $t = 1.27$ ns. Then, the remaining V_1^+ (red) and AV_2^- (green) remain in a TVW configuration (Figure 6.8b). Note that the vortex-antivortex remains seated next to the modulation instead of at its center. We believe that this occurs to allow uniform curling at the modulation. This was also evidenced experimentally in Figure 6.2e, where the XMCD ptychographic image shows a TVW whose core is next to the modulation interface.

6.2.4 Curling response to magnetization reversal

In the following, we experimentally study DW propagation along the wire and through the chemical modulations, i.e., magnetization reversal.

Magnetization reversal in nanowires

Magnetization reversal process in arrays or in individual magnetic nanowires has been widely studied experimentally and theoretically. In short, the reversal process starts at the wire ends where the dipolar field is the highest [310, 311]. Therefore a magnetic field applied anti parallel to magnetization will give rise to the nucleation of a domain wall at the wire end, which will propagate throughout the nanowire. The initial magnetic configuration at the wire end will determine the type of nucleated DW: a transverse configuration will nucleate a TVW and a curling configuration will nucleate a BPW [312, 313]. Usually, for diameters below $7\Delta_d$ a TVW is nucleated, and for larger diameters a BPW. One of the first experimental reports in arrays of nanowires was performed by using superconducting quantum interference device (SQUID) technique to measure the angular variation of the nucleation field [314]. Other reports by micromagnetic simulations on individual nanowires review in detail the different reversal modes as a function of the exchange correlation length, diameter and anisotropy direction [102]. Recent experimental reports with magnetic imaging in individual nanowires modulated in diameter [117, 136, 315, 316] or composition [141, 291] show DW pinning at the modulations during the reversal process. This sets two nucleation fields to continue the propagation of the wall [133]. In the following, we investigate experimentally in a single nanowire the impact of magnetization reversal on the curling circulation at the modulations.

Axial magnetic field

We conducted X-ray imaging experiments under quasistatic magnetic field pulses using PEEM microscopy (Sec. 2.4.2). Figure 6.9a and Figure 6.9d show a XAS PEEM image at the Fe L_3 edge of a 120 nm diameter Permalloy nanowire with 40 nm-long $Fe_{80}Ni_{20}$ chemical modulations. The positions of the wire and its shadow are indicated, with the focus set at the shadow. The location of the chemical modulations is highlighted by the bright segments in the nanowire (more photoemitted electrons in these Fe-rich regions). The corresponding XMCD images are shown in Figure 6.9b and Figure 6.9e, respectively. Each chemical modulation shows a given sense of the curling circulation. After the application of an axial magnetic field pulse, the axial domain reverses its magnetization, as expected. Some of the chemical modulations reversed their circulation from $C+$ to $C-$ or viceversa, while the others remain with the same circulation. Specifically, 8 out of 11 modulations are switched. This is shown in Figure 6.9c for an axial magnetic field of 82 mT. Two orange dashed lines indicate two positions of the chemical modulations, one of which has reversed its circulation, and the other remains with the same circulation. A similar behavior is shown in Figure 6.9f, but for a lower axial field of 30 mT. In this case, changes in the axial component are less visible to the eye since the X-ray beam is nearly transverse to the wire axis. Also, we have access to the wire end, where the circulation reversal is evidenced. In terms of modulations, 4 out of 9 are reversed. We may conclude that the propagation of a DW under axial magnetic field from one wire end to the other termination does not lead to homogeneous circulation switching at the chemical modulations. However, since the images are acquired before and after the external stimulus, we do not have access to the magnetization dynamics in between. This implies that several DWs may have propagated, even transformed, or switched as suggested by micromagnetic simulations. Nevertheless, simulations predicted that it should be the BPW the micromagnetic object reversing its circulation, while the modulation remains with the same circulation. This was not obtained in the experimental data shown in Figure 6.9. Reasons may be the following: first, the Permalloy segments separating the chemical modulation have a length <500 nm. This length may be below the DW width, which will bring new unexplored magnetization dynamics. Also, these samples were the first ones synthesized in this work, thus they do not have the material optimization detailed in Chap. 3. Therefore, they may suffer from slight variations in the diameter at the location of the chemical modulations, which will also affect the physics.

With the aim of probing the minimum magnetic field required for magnetization reversal in an individual chemically-modulated nanowire, we performed Lorentz microscopy in Fresnel mode (defocus mode). Compared to electron holography, this technique is quick and provides a larger field of view, which is useful for

detecting the presence of DWs or magnetization tilting. For this study, the sample was first saturated along the axial direction with a magnetic field of 0.8 T, to achieve a system free of DWs. Figure 6.9g shows the end of a Permalloy nanowire with $d = 130\,\text{nm}$ and $\ell = 60\,\text{nm}$ $Fe_{80}Ni_{20}$ chemical modulations. The longitudinal lines are electrostatic fringes that occur at the edges of the wire and these lines are shifted upwards or downwards, depending on the sign of the induction field of the sample. At the end of the wire, the lines return to the location they should be in the absence of magnetization. Axial magnetic field pulses of increasing amplitude in the ms range were applied until the nucleation field for reversal of the axial domain was obtained. This was achieved for an amplitude of 4.2 mT, evidenced by the upwards shift at the termination as shown in Figure 6.9h. This value was expected, confirming that the presence of chemical modulations does not rise strongly the reversal field.

Non-axial magnetic field

Next, we will study the micromagnetic behavior of the system under the application of a non-axial magnetic field, i.e., with a transverse component with respect to the wire axis. In this case, there will be a large projection of the external field along the curling magnetization at the modulations, which we expect to have an impact on the sense of circulation. Figure 6.10a shows a XAS PEEM image at the Fe L_3 edge of a 120 nm diameter Permalloy nanowire with $\ell = 40\,\text{nm}$ modulations. The position of the wire and the shadow are indicated, and the focus is set at the shadow. The chemical modulations indicated by the orange dashed line

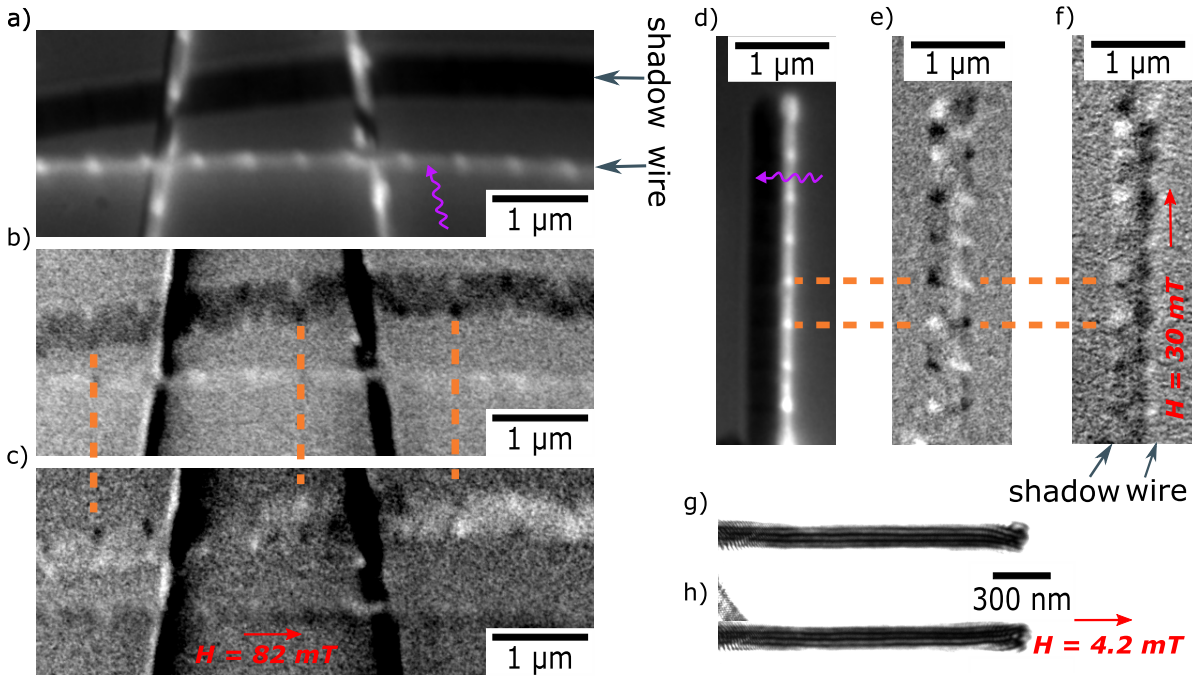

Figure 6.9: X-Ray imaging of Permalloy cylindrical nanowires with $Fe_{80}Ni_{20}$ chemical modulations after the application of quasistatic axial magnetic field pulses. **a)**, **d)** XAS image at the Fe L_3 edge obtained by PEEM for a wire with $d = 120\,\text{nm}$ and $\ell = 40\,\text{nm}$. The microscope focus is set at the shadow, and the X-ray direction is almost perpendicular to the wire axis (purple arrow). The orange dashed lines show the location of chemical modulations. **b)**, **e)** XMCD images of **a)** and **d)** respectively, reveal axial magnetization in the Permalloy segments, while the bipolar contrast at the chemical modulations reveals curling magnetization. **c)**, **f)** XMCD images after the application of a magnetic field pulse along the axial direction of 82 mT and 30 mT respectively. **g)** Fresnel microscopy image at remanence of a modulated nanowire with $d = 130\,\text{nm}$ and $\ell = 60\,\text{nm}$. **h)** Magnetization reversal of **g)** after the application of an axial magnetic field of 4.2 mT.

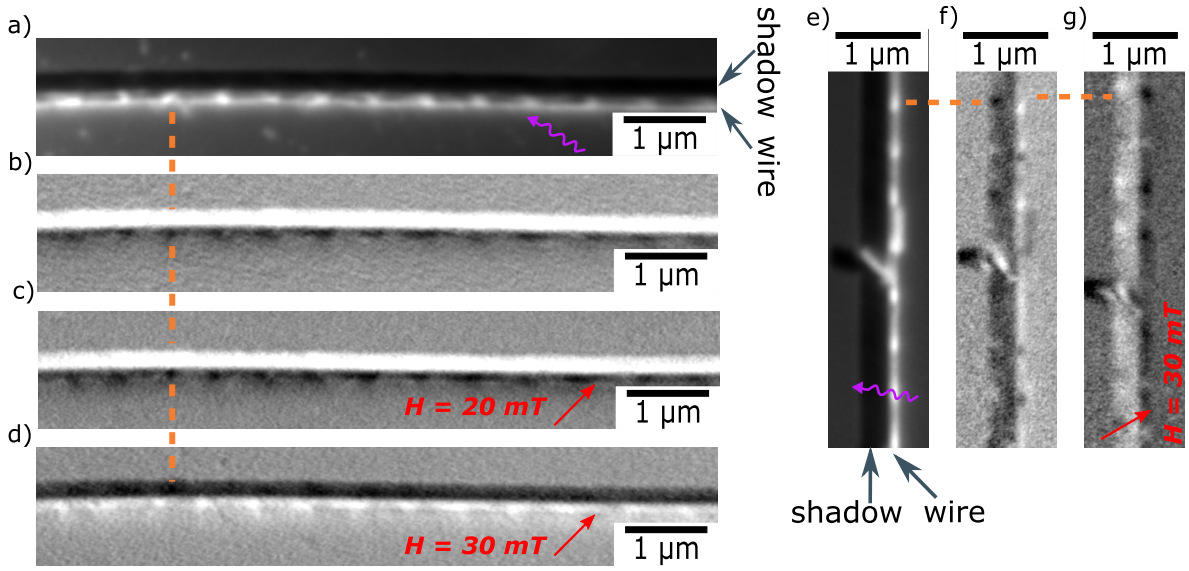

Figure 6.10: X-Ray imaging of Permalloy cylindrical nanowires with $Fe_{80}Ni_{20}$ chemical modulations after the application of non-axial magnetic field pulses. **a)**, **e)** XAS image at the Fe L_3 edge obtained by PEEM for a wire with $d = 120\,\text{nm}$ and $\ell = 40\,\text{nm}$. The microscope focus was set at the shadow and the X-ray direction is indicated by the purple arrow. The orange dashed line guides the location of a chemical modulation (bright segments at the wire position). **b)**, **f)** XMCD images of **a)** and **e)** respectively. **c)**, **d)** XMCD images after the application of a magnetic field pulse with a 45° offset with respect to the axial direction of 20 mT and 30 mT respectively. **g)** XMCD image after the application of a magnetic field pulse of 30 mT with a 30° offset with respect to the axial direction.

appear bright in the wire. The X-ray beam has an incident angle of 45° with respect to the nanowire axis. This has an extreme impact on the dichroic image shown in Figure 6.10b, where the axial components of the magnetization hide the curling at the modulation in the shadow, and an homogeneous bright contrast is obtained. This is the reason why it is more advisable to work with a lower tilt so that we do not lose information. Nevertheless, at the wire location, a darker contrast is observed at the chemical modulations , highlighting curling in a particular sense of circulation for all the modulations. However, to confirm this, sample rotation is required. This is because, if the magnetization were longitudinal at the modulation, we would also observe a darker contrast at the modulation since they are Fe-rich. After the application of a magnetic field pulse of 20 mT with an angle of 45° with respect to the axis, nothing changes (Figure 6.10b). However, for a higher field of 30 mT amplitude, not only the axial domain is reversed, but also the sign of circulation of each modulation. This is shown in Figure 6.10c, where the shadow now shows dark contrast and the chemical modulations show bright contrast at the wire location.

With this, we may conclude that deterministic circulation switching in the chemical modulations and axial magnetization reversal may be achieved by means of a magnetic field with a high transverse component (30 mT amplitude and 45° tilt). For a lower transverse component for the same system size displayed in Figure 6.10g, not all the modulations were reversed. In this case, the X-ray beam direction (purple arrow) is nearly transverse, making the curling circulation visible as shown in Figure 6.10f. Therefore, more measurements are needed to clarify the impact of magnetization reversal at different angles.

6.3 Œrsted field driven DW transformations: homogeneous nanowire

In the remainder of this chapter, we will focus on the Œrsted field impact on magnetization dynamics in cylindrical nanowires. The role of the Œrsted field was at first not considered compared to the STT one. However, a recent experimental report on current-induced DW motion revealed the strong influence of the Œrsted field [181]. First, it stabilizes the BPW, and then, above a critical value, it deterministically sets its sense of circulation. This was confirmed by micromagnetic simulations, providing more details on the switching mechanism and its sub-ns timescale [185]. Time-resolved imaging experiments revealed the breathing or shrinking of the BPW when an Œrsted field is applied, either parallel or antiparallel to the BPW circulation [184]. Regarding long-distance motion, velocities above $2400\,\mathrm{m\cdot s^{-1}}$ were experimentally reached, however, with a stochastic direction of motion [181]. Therefore, the impact of the Œrsted field on the propagation direction remains to be clarified. In addition, the propagation has been predicted to become unstable if the BPW circulation is antiparallel to the applied Œrsted field [317]. Finally, the Œrsted field is also thought to induce the TVW transformation to BPW [318]. With all of this in mind, in the following, we will first delve into the DW transformation induced by the Œrsted field in a homogeneous wire, and second in Sec. 6.4, we will explore how its impact is modified in a chemically modulated nanowire.

6.3.1 BPW circulation switching

The Œrsted field-induced BPW switching mechanism in a Permalloy cylindrical nanowire has been described in detail in [185]. For a 90 nm diameter wire, the critical current density obtained with micromagnetic simulations was $0.80\times10^{12}\,\mathrm{A\cdot m^{-2}}$. The switching process involves the nucleation and annihilation of a vortex-antivortex pair, as described in Sec. 6.2.2. For a current density close to the critical one ($1.20\times10^{12}\,\mathrm{A\cdot m^{-2}}$), only one vortex-antivortex pair was reported [185]. The underlying mechanism turned out to be similar to that described in Sec. 6.2.2 for BPW switching under a magnetic field before crossing a modulation of antiparallel circulation (see Figure 6.6). In that case, the external magnetic field was also close to the critical one, and only one vortex-antivortex pair was involved. In addition, it was also reported that the exact mechanism depends on the current density. For higher fields, we have previously described the case of a switching process involving two vortex-antivortex pairs of opposite polarity nucleated between the BPW and the modulation (see Figure 6.7). Note that we have emphasized on the sign of the polarity. This is because we have found that in the presence of a modulation, two vortex-antivortex pairs have opposite polarity, and in a homogeneous wire they have the same polarity. Below, we will detail the BPW circulation reversal under Œrsted field, involving also two vortex-antivortex pairs of the same polarity.

This study was performed using the *FeeLLGood* micromagnetic code. A post-treatment code was used to identify the nature of the volume (BPs) and surface (vortex-antivortex) singularities, an analysis that has never been done before for this physics. This identification allows for a more detailed understanding of the switching mechanism. The system studied was a 90 nm diameter Permalloy nanowire of 1 µm length, with a 4 nm mesh size, $M=8\times10^{5}\,\mathrm{A/m}$, $A=1.3\times10^{-11}\,\mathrm{J/m}$, and zero magnetocrystalline anisotropy. An alpha value of 1 was used to better track singularities. In order to mimic an infinite wire, the magnetic charges at the wire ends were removed numerically. Only the Œrsted field was included as an external stimulus, since it has been demonstrated that the impact of STT is not the main driving force for BPW switching phenomenon [318]. The initial state was a tail-to-tail BPW relaxed configuration with positive circulation $C+$ with respect to the axial direction $\hat{\mathbf{z}}$. Figure 6.11a shows the time evolution of the singularities along the axial direction z under a current pulse of $-1.50\times10^{12}\,\mathrm{A\cdot m^{-2}}$, corresponding to an Œrsted field of 42.5 mT at the periphery. The current direction is along $-\hat{\mathbf{z}}$ and thus the associated Œrsted field has a negative circulation with respect to $\hat{\mathbf{z}}$. The black color represents the BP, the red one a vortex with positive polarity V^{+}, the blue one a vortex with negative polarity V^{-} and the orange one an antivortex with positive polarity AV^{+}. To better understand the switching mechanism we may look at Figure 6.11c, where the unrolled m_ρ surface maps at different time steps are shown. The color code corresponds to m_ρ, the black dashed line to $m_\varphi=0$ and the black line to

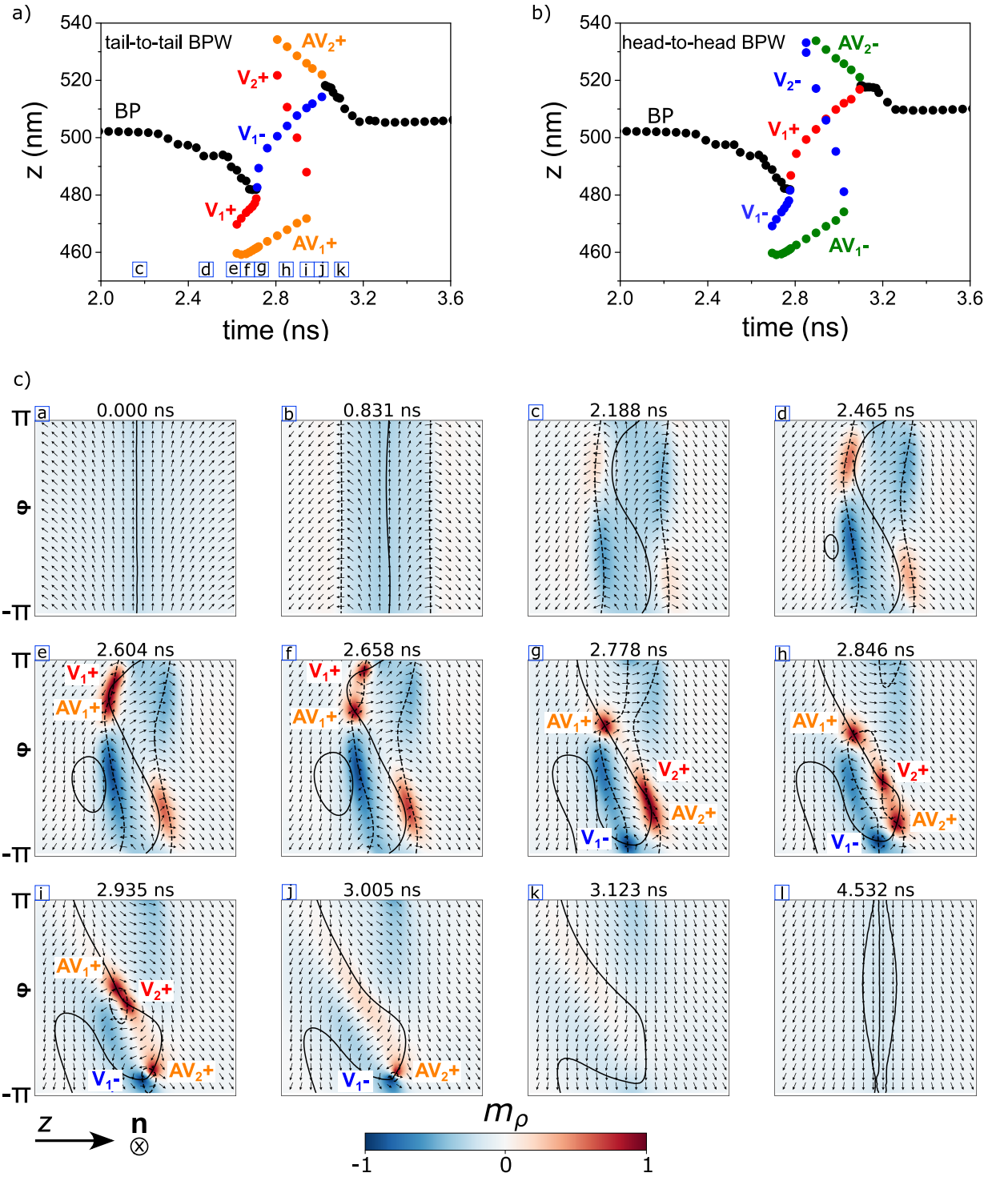

Figure 6.11: Œrsted field induced BPW circulation switching mechanism involving two vortex-antivortex pairs of the same polarity. The initial state is a homogenous 90 nm diameter Permalloy nanowire with a BPW with positive circulation. A current pulse of $-1.50 \times 10^{12}\,\mathrm{A \cdot m^{-2}}$ along z is applied. **a)** Time evolution along z for a tail-to-tail configuration of the BP (black), the vortex V^{+} (red) and antivortex AV^{+} (orange) pairs of positive polarity, and the vortex with negative polarity V^{-} (blue). **b)** Time evolution along z for a head-to-head configuration of the BP (black), the vortex V^{-} (blue) and antivortex AV^{-} (green) pairs of negative polarity, and the vortex with positive polarity V^{+} (red). **c)** Unrolled m_ρ surface maps of the different time steps of the tail-to-tail BPW switching. The color code corresponds to m_ρ, the black dashed line to $m_\varphi = 0$ and the black line to $m_z = 0$. The normal **n** indicates the direction of the outer normal to the wire surface.

$m_z = 0$. When these isolines get closer it implies that a strong radial component is occurring at that location. At the moment they cross, a vortex or an antivortex will have formed $m_\rho = \pm 1$. The different letters correlate the unrolled maps with selected time events in Figure 6.11a. Letter *a* shows the initial surface unrolled map of a BPW of positive circulation. Letter *b* illustrates the shrinking of the DW width after the application of a current pulse. The shrinkage of the wall continues while out-of-plane radial components start to appear on both sides of the wall (letters *c* and *d*), until a first vortex-antivortex pair of positive polarity V_1^+ - AV_1^+ is formed (letter *e*). The V_1^+ separates from the AV_1^+ along the azimuthal direction $\hat{\varphi}$ until the BP reaches V_1^+ at the surface. At that moment, the BP is annihilated and V_1^+ changes polarity to V_1^- (letter g). Afterward, a second V_2^+ - AV_2^+ pair of positive polarity is formed (letters *g* and *h*), and then an annihilation of V_2^+ with AV_1^+ occurs (letter *i*). Finally, V_1^- annihilates with AV_2^+ and a BP with negative polarity enters in the volume (letter *k*). The final state shows a BPW with negative circulation (letter *l*). The same mechanism occurs for a head-to-head BPW, but in this case, the polarity of the wall is the opposite. This leads to the opposite polarity of the vortex-antivortex pairs occurs, such as the total out-of-plane radial component is minimized. This is shown in Figure 6.11b, where now two vortex-antivortex pairs of negative polarity are nucleated. Regarding the timescale of the dynamics, the switching occurs at 2.7 ns, which is rather slow. The reasons may be the following: first, an alpha value equals to 1 is used to track in detail the vortex-antivortex dynamics but with the drawback of a very high damping term leading to slow dynamics. Second, the current density is rather close to the threshold, and as we studied in Sec. 4.4, the time-scale of the dynamics diverges as we approach the critical current.

From a topological point of view, we may note the conservation of the variation of the winding number at the surface and at the volume such that $\Delta w_{\text{surf}} = \Delta w_{\text{vol}}$. The topological charge of a vortex is $q = +1$, whereas that of an antivortex is $q = -1$. The winding number of a vortex or an antivortex is $w = qp/2$, where $p = +1$ is a positive polarization, and $p = -1$ is a negative polarization. Therefore, for the first event (letter *f*), the initial winding number in the volume is the one corresponding to a tail-to-tail BP, $w_{\text{vol,i}} = 1$ and after its annihilation, $w_{\text{vol,f}} = 0$, thus $\Delta w_{\text{vol}} = -1$. The initial winding number at the surface is the sum of the V_1^+ - AV_1^+ pair and thus $w_{\text{surf,i}} = 0$. The final (letter *g*) winding number at the surface is the one of V_1^- ($w = -1/2$) and AV_1^+ ($w = -1/2$), thus $w_{\text{surf,f}} = -1$, which makes $\Delta w_{\text{surf}} = -1 = \Delta w_{\text{vol}}$. The second event, is the annihilation of V_2^+ with AV_1^+. Here, since there is not BP, $w_{\text{vol,i}} = 0 = w_{\text{vol,f}} = \Delta w_{\text{vol}}$ (letter *h*). At the surface, the initial state is the sum of the winding numbers of V_1^-, AV_1^+, V_2^+ and AV_2^+, and thus $w_{\text{surf,i}} = -1$. The final state is the sum of the winding numbers of V_1^- ,and AV_2^+ and thus $w_{\text{surf,i}} = -1$, thus $\Delta w_{\text{surf}} = 0 = \Delta w_{\text{vol}}$ (letter *j*). The last event is the nucleation of a BP. Therefore, in the volume, we have $w_{\text{vol,i}} = 0$ in the initial state (letter *j*) and $w_{\text{vol,f}} = 1$ for a tail-to-tail BP (letter *k*). At the surface, we have $w_{\text{surf,i}} = -1$ initially and $w_{\text{surf,f}} = 0$ after the annihilation of V_1^- with AV_2^+, thus $\Delta w_{\text{surf}} = 1 = \Delta w_{\text{vol}}$.

In the following, we describe the experimental observations. The first experimental evidence of current-induced BPW circulation switching was provided by the group in 2019 using the XMCD-PEEM technique [181]. In this case a critical current density of $1.4 \times 10^{12}\,\text{A}\cdot\text{m}^{-2}$ was obtained for a 90 nm diameter $Co_{30}Ni_{70}$ nanowire. In our case, even though the system contains chemical modulations, we also studied BPW switching in a Permalloy segment far from the modulation. The system studied is made up of a 130 nm diameter Permalloy nanowire with 100 nm-long periodic $Fe_{80}Ni_{20}$ chemical modulations separated by a distance $\approx$ 4 µm. We performed transmission X-ray microscopy (TXM) at MISTRAL beamline at ALBA synchrotron on electrically-contacted samples, being the first users to implement current pulses in this set up. The corresponding XAS image at the Fe L_3 edge is shown in Figure 6.14d. The location of the chemical modulation interfaces is indicated by the orange dashed lines. The initial state for this study is shown in Figure 6.14f, where the XMCD image displays a BPW in the Permalloy segment, whose circulation is positive $C+$ with respect to $\hat{\boldsymbol{z}}$. This state was obtained after a current pulse of $2.04 \times 10^{12}\,\text{A}\cdot\text{m}^{-2}$ of 1 ns duration along $\hat{\boldsymbol{z}}$, whose Œrsted field circulation is also positive. The magnetic configuration after the application of a 1 ns pulse of $-2.27 \times 10^{12}\,\text{A}\cdot\text{m}^{-2}$ shows a BPW with negative circulation $C-$ with respect to the $\hat{\boldsymbol{z}}$ direction, which matches with the circulation of the associated Œrsted field. We evidenced deterministic BPW circulation reversal above a current density of $0.4 \times 10^{12}\,\text{A}\cdot\text{m}^{-2}$ for 130 nm diameter Permalloy nanowires. Since

the Si_3N_4 membrane where the wires were dispersed had a thickness of 20 nm, in order to allow correlative TEM measurements, we sputtered 100 nm of Al on the backside and performed 20 nm of alumina ALD on the topside. This increased the thermal diffusion path and improve the management of Joule heating in the samples. However, since the current densities required for dynamics are on the order of a few $10^{12}\,\mathrm{A\cdot m^{-2}}$, the impact of heating is non-negligible. This impact will be described with temperature calculations in Appendix 8.2. For the moment, we would like to mention that above a current density of $3.5\times10^{12}\,\mathrm{A\cdot m^{-2}}$, non-deterministic BPW switching was obtained due to the strong demagnetization of the samples induced by the Joule heating.

Time-resolved imaging of BPW switching

The above experimental results characterized the BPW switching with static imaging, i.e., before and after the application of the electric pulse. This allows us to characterize the critical current for switching but not to study the dynamics during the application of the pulse. This is only possible through pump-probe experiments, which can be done by phase-locking the X-ray frequency with the electric pulse frequency. A recent publication by the group reported time-resolved STXM imaging of the so-called breathing of the BPW under the application of a current pulse [184]. The system was a 90 nm diameter $Co_{30}Ni_{70}$ cylindrical nanowire. The experiments evidenced the expansion of the BPW width when the Œrsted field is parallel to the wall circulation, and its shrinking when the Œrsted field is antiparallel. Since time-resolved experiments require a series of repetitive dynamics over billions of times, such repetitive events could not be obtained above the critical current for switching, which is around $1\times10^{12}\,\mathrm{A\cdot m^{-2}}$. For these current densities, Joule heating or STT contributed to the depinning of the wall, thus a single event could not be repeated over billions of times, which did not allow performing time-resolved imaging of BPW switching.

In this work, time-resolved STXM imaging was performed at theMAXYMUS beamline [261] at BESSY II synchrotron. This time it was possible since larger diameter wires show a lower critical current density, which in our case was $\approx 0.3\times10^{12}\,\mathrm{A\cdot m^{-2}}$. Each time-resolved series had a temporal resolution ranging from 200 ps to 50 ps. As discussed in Sec. 2.4.4, just one circular X-ray polarization is used, thus one does not measure XMCD images but differential XAS images, displayed as the division of an individual XAS image by the average of all the XAS frames. This may make the analysis difficult as the average does not necessarily reflect a static magnetization state. In practice, it is advisable to perform an XMCD image before/after the TR series. The sample was a 111 nm diameter Permalloy nanowire with 30 nm-long chemical modulations. In order to study BPW switching without the impact of a modulation, we considered an initial state where the BPW is relatively far from the modulation. Figure 6.12a shows a series of differential XAS images of BPW switching for a current density of $0.30\times10^{12}\,\mathrm{A\cdot m^{-2}}$. This current is very close to the critical one in this system. This explains the rather large switching time of t =5600 ps. In addition, we may note that the core of the wall moves slightly to the left during the switching process (red dashed line indicates the initial center of the wall). When the current density is increased to $0.53\times10^{12}\,\mathrm{A\cdot m^{-2}}$, the dynamics time scale drops. This is displayed in Figure 6.12b where a full BPW switching is obtained slightly above t =2150 ps. Here, the evolution of the shrinking of the wall prior to the reversal of magnetization is better displayed. In addition, the lack of contrast at the center of the wall for such long periods is probably the signature of a rather complex dynamics that may be different during the successive pulses. Figure 6.12b shows two consecutive BPW reversals, i.e., from $C+$ to $C-$ and from $C-$ to $C+$. This evidences more clearly the slight drift of the wall towards the right if a negative pulse is applied, and to the left if a positive pulse is applied. This drift may be due to the chirality of the LLG equation, but also to other effects such as STT, thermal gradient, due to the nearby modulation, etc., thus it needs to be studied in more detail. These results were obtained by the end of December 2022, and thus at the last stage of the writing of this manuscript. Therefore, a complete study is not provided here. However, we expect that a comparison with micromagnetic simulations will provide, among others, an insight on the experimental damping term, an interesting aspect as it depends on the magnetization gradient.

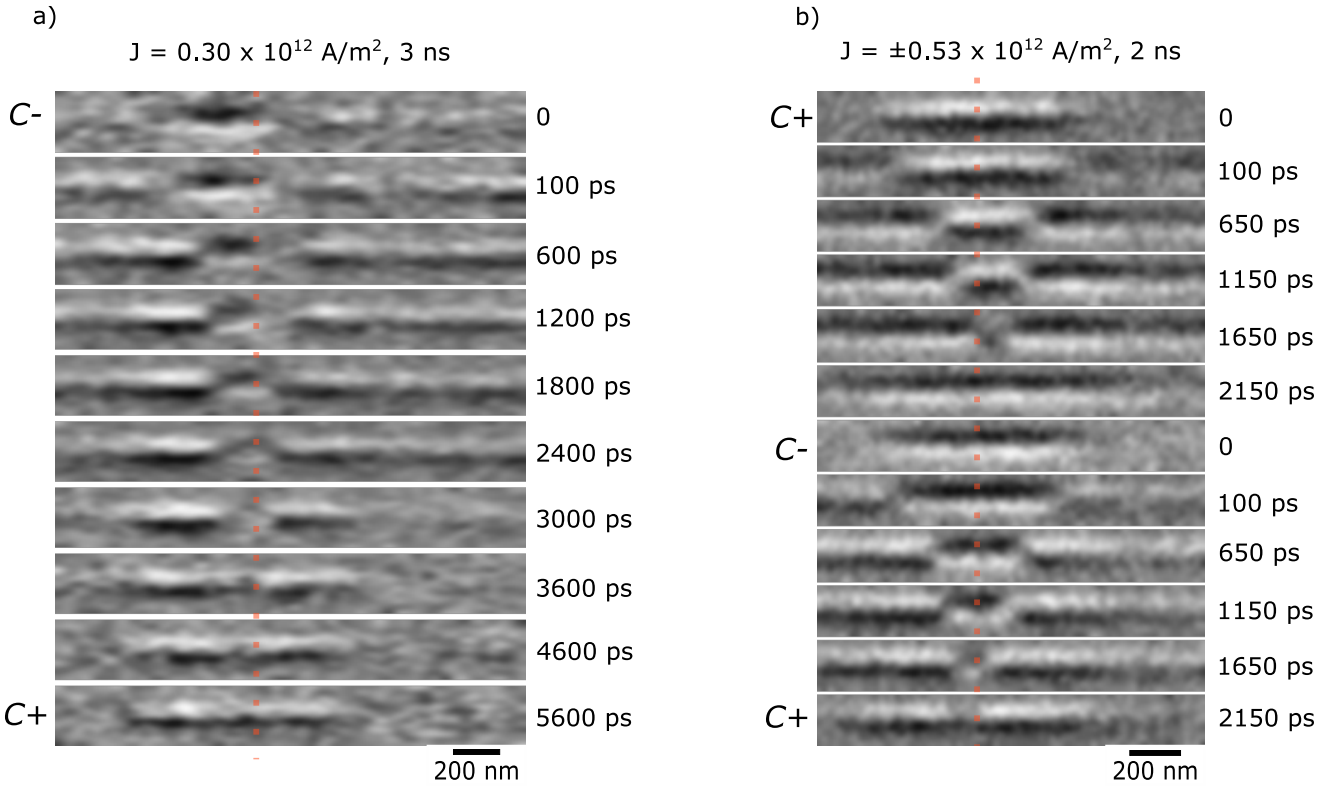

Figure 6.12: STXM time-resolved imaging of BPW circulation switching on a 111 nm diameter Permalloy nanowire. **a)** Differential XAS contrast images of a time-resolved series for a current density of $0.30 \times 10^{12}\,\mathrm{A \cdot m^{-2}}$ and pulse duration of 3 ns. The corresponding time of each subfigure is mentioned. Figure size $2 \times 0.25\,\mu\mathrm{m}^2$. **b)** Differential XAS contrast images of a time-resolved series showing two consecutive circulation reversals, for a current density of $0.53 \times 10^{12}\,\mathrm{A \cdot m^{-2}}$ and pulse duration of 2 ns. Figure size $1.5 \times 0.2\,\mu\mathrm{m}^2$. Vertical red dotted lines are a guide to the eye of the initial core of the BPW.

6.3.2 BPW transformation to TVW

In Sec. 6.2.3, we described a never-reported DW transformation under a magnetic field. The initial state consisted of a BPW of positive circulation $C+$ with respect to the axial direction $\hat{\mathbf{z}}$, pinned next to a chemical modulation of negative circulation $C-$. Above the depinning field, the BPW switches its circulation to allow its propagation through the chemical modulation. This switching mechanism is similar to the one described above under an Œrsted field, involving the nucleation, motion and annihilation of surface vortex-antivortex pairs. In Sec. 6.2.3, we observed that if the external field is stopped during the vortex-antivortex transient state, the system relaxes to a state that preserves the vortex-antivortex pair, i.e., to a TVW. This was observed for alpha values of 1 and 0.02. Since the time scales of the switching mechanism correspond to the timescale of the experimental nanosecond current pulses, we will again study theoretically the impact of a sub-nanosecond Œrsted field pulse in a system without a chemical modulation.

Figure 6.13 shows the unrolled m_ρ surface maps of a BPW during a sub-nanosecond current pulse. The initial state corresponds to a BPW with positive circulation $C+$ with respect to the axial direction $\hat{\mathbf{z}}$. Afterward, a current pulse of $-1.2 \times 10^{12}\,\mathrm{A \cdot m^{-2}}$ along $\hat{\mathbf{z}}$ is applied. The Œrsted field associated has negative $C-$ circulation. At $t = 0.676\,\mathrm{ns}$, out-of-plane radial components start to appear on both sides of the DW, which results in the formation of a V_1^+ - AV_1^+ pair at $t = 0.851\,\mathrm{ns}$. This pair moves away from each other along the azimuthal direction ($t = 0.983\,\mathrm{ns}$). Inside the wire, the vorticity line that links the vortex-antivortex pairs

catches the BP, which moves along it towards the surface. When it reaches AV_1^+, it changes its polarity to negative (AV_1^-) and the BP is annihilated ($t = 1.210\,\text{ns}$). At this stage, the DW is of TVW type. If the current pulse were to continue we have seen in Figure 6.11 that a BP re-enters in the volume after the annihilation of the vortex-antivortex pair of opposite polarities. Here we stop the external stimulus at $t = 1.210\,\text{ns}$, as it could be experimentally for a 1 ns pulse. The V_1^+ - AV_1^- pair remains, and the system relaxes to a TVW, as observed at $t = 13.688\,\text{ns}$. Therefore, here we show that a BPW can be transformed into a TVW under a very short Œrsted field stimulus of antiparallel circulation with respect to the BPW circulation.

In the following, we will show the experimental evidence of BPW transformation into a TVW under a short current pulse stimulus. We will prove experimentally that this phenomenon is independent of the presence of a chemical modulation, as opposed to the case under a magnetic field. The system studied was a 130 nm diameter Permalloy nanowire with periodic $Fe_{80}Ni_{20}$ chemical modulations of 100 nm length. Its TXM-XAS image at the Fe L_3 edge is shown in Figure 6.14a, where a defect-free sample with a homogeneous diameter is observed. The chemical modulation shows darker contrast due to its higher absorption. The orange dashed lines are guides that indicate the material interfaces. In the initial state, the BPW is situated $\approx 1\,\mu\text{m}$ away from a chemical modulation, such that no interaction occurs. This configuration was obtained by applying nanosecond current pulses to drift a DW pinned next to a chemical modulation. The corresponding XMCD image in Figure 6.14b shows a BPW at the center of the image, with negative cir-

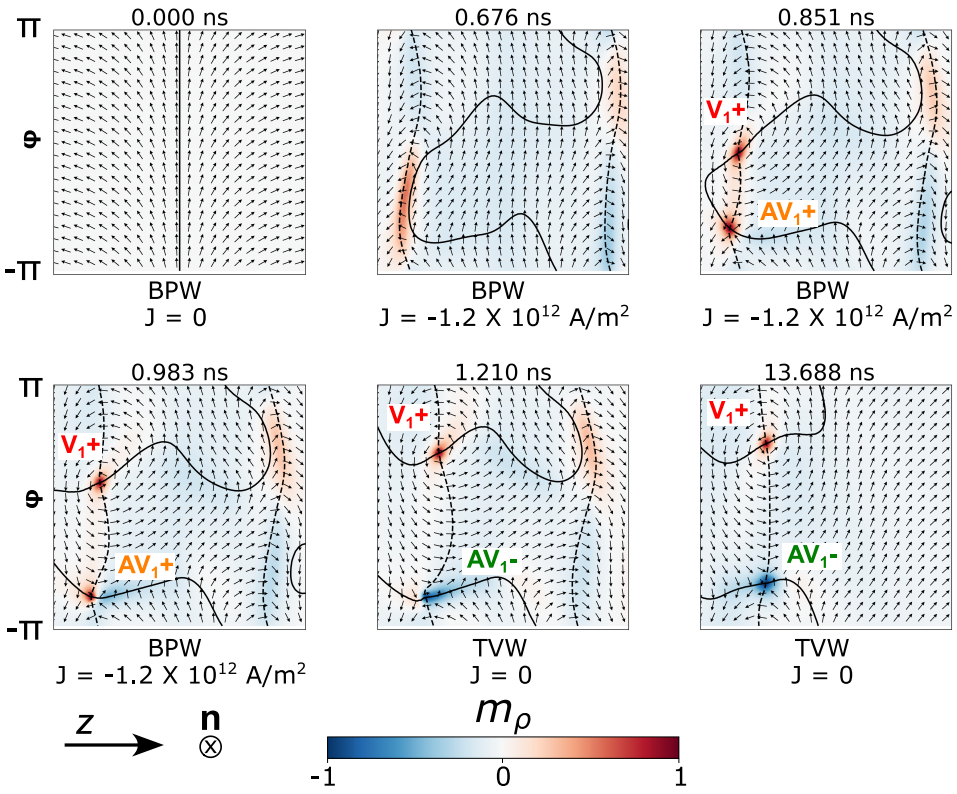

Figure 6.13: BPW transformation to TVW induced by a sub-nanosecond Œrsted field pulse. Unrolled m_ρ surface maps of the different time steps. The color code corresponds to m_ρ, the black dashed line to $m_\varphi = 0$ and the black line to $m_z = 0$. The normal **n** indicates the direction of the outer normal to the wire surface. The initial configuration shows a BPW of positive circulation $C+$ with respect to $\hat{\mathbf{z}}$. Afterward, a current density pulse of $-1.2 \times 10^{12}\,\text{A}\cdot\text{m}^{-2}$ is applied along $\hat{\mathbf{z}}$, whose Œrsted field circulation is negative $C-$. At $t = 0.851\,\text{ns}$, the formation of a V_1^+ - AV_1^+ pair occurs. Before $t = 1.210\,\text{ns}$, AV_1^+ changes polarity to AV_1^- and the BP is annihilated. At $t = 1.210\,\text{ns}$, the current pulse is stopped and the system relaxes to a TVW.

culation $C-$ with respect to the axial direction $\hat{\mathbf{z}}$. At the Fe-rich chemical modulation, there is barely any magnetic contrast since most photons are absorbed and the contrast is artificially reduced by the background level (see Sec. 5.2). To confirm this, we imaged at the Ni L_3 edge and obtained a clear magnetic contrast at the chemical modulations. Another solution would had been to shift the energy out the peak of the Fe L_3 edge. To obtain sensitivity to the axial component, we tilted the sample holder by $\approx 10°$. Figure 6.14c shows the magnetic configuration after the application of a 2 ns current pulse with amplitude $2.62 \times 10^{12}\ \mathrm{A \cdot m^{-2}}$ along $\hat{\mathbf{z}}$ (blue arrow). The associated Œrsted field has positive circulation $C+$ with respect to the axial direction $\hat{\mathbf{z}}$. After the pulse, the magnetic image reveals a TVW instead of a BPW with reversed circulation. This result supports the findings obtained with micromagnetic simulations. However, we also observed BPW to TVW transformations when the Œrsted field direction was parallel to the initial configuration and the current density was rather high. We believe that the mechanism driving this involves significant demagnetization of the sample resulting from Joule heating.

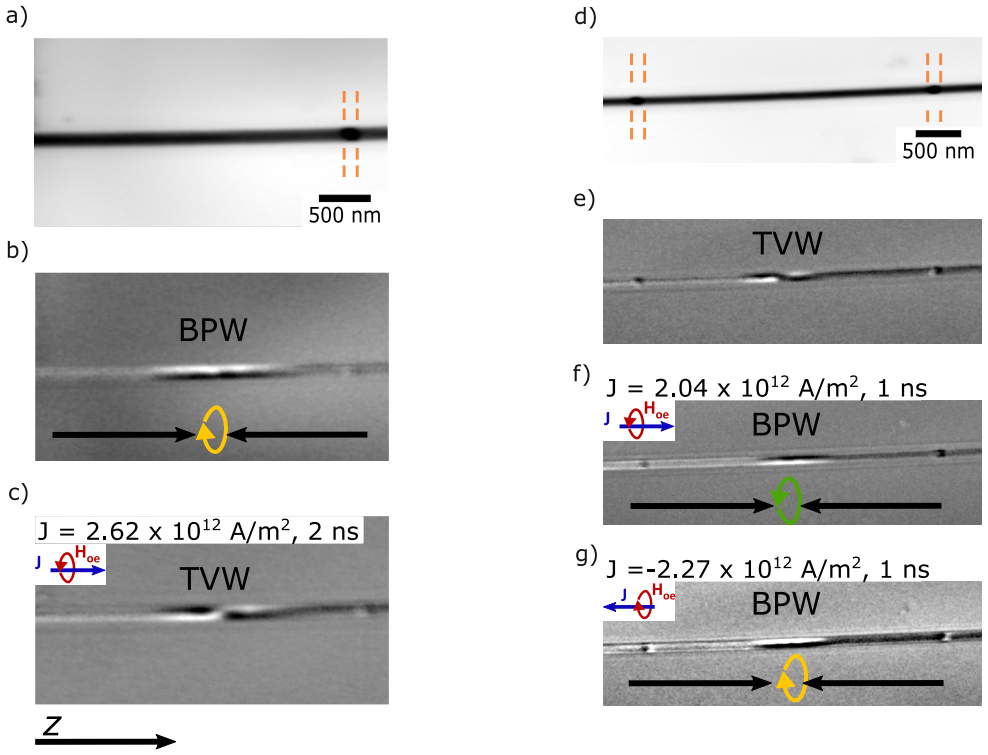

Figure 6.14: X-ray imaging of DW transformations induced by the Œrsted field in a Permalloy segment. **a)** and **d)** show a XAS-TXM image at the Fe L_3 edge of a Permalloy nanowire with $Fe_{80}Ni_{20}$ periodic chemical modulations. Orange dashed lines indicate the interfaces of the modulations. The sample holder was rotated 10° to obtain a small contrast from the axial domains. **b)** XMCD image of **a)** shows a BPW in the Permalloy segment with negative circulation $C-$ relative to the axial direction $\hat{\mathbf{z}}$. Black arrows indicate the direction of magnetization of the axial domains, and yellow indicates the direction of the BPW. **c)** XMCD shows a transformation to TVW after the application of a 2 ns current pulse of $2.62 \times 10^{12}\ \mathrm{A \cdot m^{-2}}$ amplitude along $\hat{\mathbf{z}}$ (blue arrow), whose associated Œrsted field with positive $C+$ circulation. **e)** XMCD of **d)** shows the initial state of a TVW in the middle of the Permalloy segment. **f)** XMCD shows a transformation to BPW after the application of a 1 ns current pulse of $2.04 \times 10^{12}\ \mathrm{A \cdot m^{-2}}$ along $\hat{\mathbf{z}}$, whose associated Œrsted field has positive $C+$ circulation. **g)** XMCD shows a circulation switching of BPW to $C-$ after the application of a 1 ns current pulse of $-2.27 \times 10^{12}\ \mathrm{A \cdot m^{-2}}$ along $-\hat{\mathbf{z}}$, whose associated Œrsted field has negative $C-$ circulation.

6.3.3 TVW transformation to BPW

In section Sec. 6.2.3, we described the mechanism of BPW transformation to TVW under a magnetic field when the BPW propagates through a chemical modulation of opposite circulation. It was mentioned that the underlying mechanism is similar to the one experimentally and theoretically reported for a homogeneous Permalloy nanowire [180]. For the case under current, it has been reported that the Œrsted field above a certain threshold drives the transformation of a TVW to a BPW [185]. The process is similar to the one under field, involving the motion of the surface vortex-antivortex pair until they annihilate and a BP is nucleated and moves radially towards the axis. The final circulation of the BPW matches the one of the Œrsted field applied. However, so far this transformation has not been evidenced experimentally.

Figure 6.14d shows a XAS image at the Fe L_3 edge of a 130 nm diameter Permalloy nanowire with periodic 100 nm-long chemical modulations. The interfaces of two modulations are indicated by the orange dashed lines. The corresponding XMCD image is shown in Figure 6.14e, where a TVW is evidenced at the center of the Permalloy segment. The axial domains show darker and lighter contrast thanks to the $\approx 10°$ tilt of the sample holder. After the application of 1 ns current pulse of amplitude $2.04 \times 10^{12}\,\mathrm{A \cdot m^{-2}}$ along $\hat{\boldsymbol{z}}$, the DW transforms into a BPW, whose circulation is positive and parallel to the Œrsted field applied. We evidence this transformation for current densities above $0.2 \times 10^{12}\,\mathrm{A \cdot m^{-2}}$ and independently of the pulse duration.

6.4 Œrsted field driven DW transformations: modulated nanowire

Once we have explored the important role that the Œrsted field plays in cylindrical nanowires made of a homogeneous material, we will now move to its impact on a chemically-modulated nanowire. The interplay between a chemical modulation and a DW under an Œrsted field is not straight forward. The reasoning is based on the different nature of the micromagnetic objects. Firstly, the chemical modulation is based on an abrupt material change in a fixed position, with opposite magnetic charges located at each interface, whereas a DW is a moving entity with variable width and a single magnetic charge. On the other hand, there is an important common feature, which is that both objects show deterministic circulation switching induced by the Œrsted field. The critical current density for switching depends on the diameter and on the chemical modulation length, thus it may differ largely between both objects. In addition, the different dynamics timescales may have an important impact on their collective behavior. With all of this in mind, in the last part of this chapter we will delve into the theoretical and experimental observations of current-induced DW dynamics in chemically-modulated nanowires.

6.4.1 DW transformations on the chemical modulation: high damping

In the following, we will address DW transformations on a chemical modulation induced by the Œrsted field. We will start with the most common one, which is BPW and modulation collective switching. The system studied by *FeeLLGood* micromagnetic code is a 90 nm diameter Permalloy nanowire with a 20 nm-long $Fe_{80}Ni_{20}$ chemical modulation. An alpha parameter of 1 and a moderate Œrsted field are used to better track singularities and to approach a quasistatic situation. In the next section Sec. 6.4.2, we will see the case of a low damping term and a higher Œrsted field amplitude. The initial state considered is a head-to-head BPW of positive circulation with respect to $\hat{\boldsymbol{z}}$, pinned on a chemical modulation. A current pulse of amplitude $-2 \times 10^{12}\,\mathrm{A \cdot m^{-2}}$ is applied along $\hat{\boldsymbol{z}}$, whose Œrsted field circulation is negative. The STT is not included. The temporal evolution along $\hat{\boldsymbol{z}}$ of the singularities is shown in Figure 6.15a. To better understand the dynamics, we may also look at the unrolled m_ρ surface maps of the different time steps shown in Figure 6.15b. The color code corresponds to m_ρ, the black dashed line to $m_\varphi = 0$ and the black line to $m_z = 0$. The switching mechanism is similar to the one shown in Figure 6.7 for a BPW switching under a magnetic field before crossing a modulation of opposite circulation: two vortex-antivortex pairs of

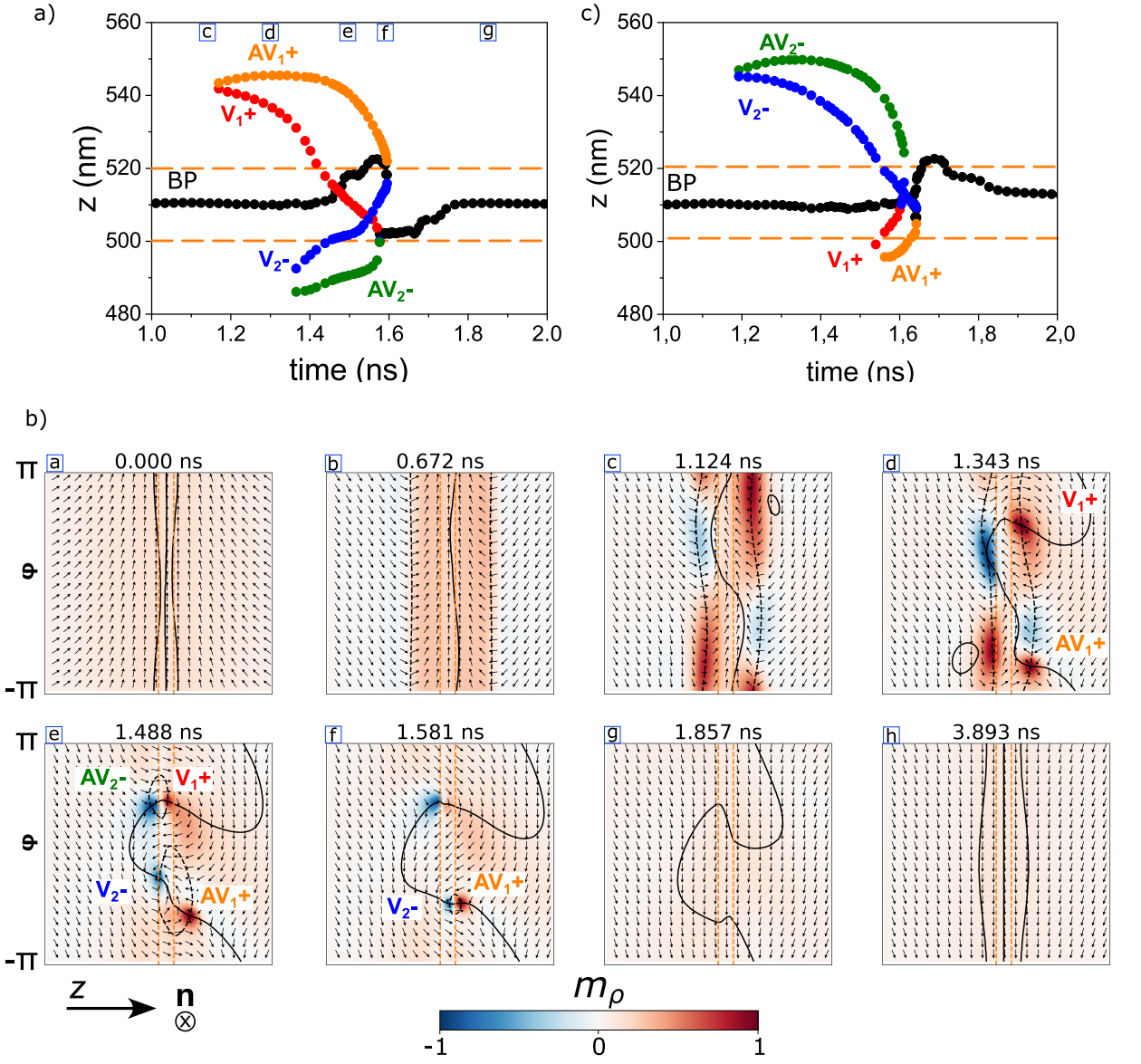

Figure 6.15: Œrsted field-induced BPW switching on a chemical modulation under a current density of $-2\times10^{12}\,\mathrm{A\cdot m^{-2}}$ and alpha equals to 1. The system is a 90 nm diameter Permalloy nanowire with a 20 nm-long $Fe_{80}Ni_{20}$ chemical modulation. Orange dashed lines indicate the location of the modulation interfaces. **a)** Time evolution along $\hat{\mathbf{z}}$ of the BP (black), a vortex V_1^+ (red) - antivortex AV_1^+(orange) pair of positive polarity and a vortex V_2^- (blue) antivortex AV_2^-(green) pair of negative polarity. **b)** Unrolled m_ρ surface maps of the different time steps. The color code corresponds to m_ρ, the black dashed line to $m_\varphi = 0$ and the black line to $m_z = 0$. Orange dashed lines indicate the location of the modulation interfaces. The normal **n** indicates the direction of the outer normal to the wire surface.

opposite polarity, V_1^+-AV_1^+ and V_2^--AV_2^-, are formed, contrary to the case of a homogeneous wire shown in Figure 6.11, where two vortex-antivortex pairs of the same polarity are formed. In this case, since the BPW is centered at the modulation, each V-AV pair nucleates at one modulation interface. Specifically, the first V_1^+-AV_1^+ pair forms at the right modulation interface (letter *d*), and the V_2^--AV_2^- pair forms at the left modulation interface (letter *e*). We may note that the BP reaches the surface and annihilates outside the modulation interface (see t =1.6 ns) and re-enters in the volume also outside of the modulation. This implies that even though the BPW is switching on the modulation, the BP leaves the modulation to reverse polarity and then re-enters again. This may be due to the higher M_s content at the modulation, which makes it more energetically favorable to have the V-AV pair outside of it. We will see a more drastic BP expulsion in Sec. 6.4.2 for a lower damping term and longer modulation length. On the contrary and as expected, for the case of tail-to-tail BPW, the temporal evolution of the singularities starts with the formation of a V_1^--AV_1^- term of negative polarity, as shown in Figure 6.15c. If we compare the singularities' evolution of the head-to-head and tail-to-tail case, we may notice subtle differences. The reason comes from the fact that the relaxed initial configurations were extracted at different times, leading to an initial system less relaxed for the tail-to-tail case. With this, we would like to put emphasis on the fact that the details of the initial configuration dramatically affect the switching dynamics. Finally, regarding the switching time scales found with micromagnetic simulation in a 90 nm diameter nanowire with $\alpha = 1$, they are: $\approx t$ =1.6 ns for BPW switching on a modulation (Figure 6.15), $\approx t$ =3.1 ns for BPW switching on a homogeneous wire (Figure 6.11) and $\approx t$ =0.2 ns for modulation circulation switching (Figure 5.8). The different time scales result from the different switching dynamics. While for the case of BPW switching $m_\rho = \pm 1$ needs to be reached, for the case of a modulation $m_z = 1$ and $m_\rho = 0$ need to be accomplished.

Regarding the experimental evidence, we will first show different types of DW transformations on a chemical modulation induced by a low amplitude nanosecond current pulse, i.e., close to the threshold value. As shown in Figure 5.8, as we get closer to the critical switching current, the timescale of the dynamics increases. Therefore, to some extent, we may compare experiments close to the critical field with simulations with a high damping term. The system studied is a 120 nm-diameter Permalloy nanowire with periodic 100 nm-long $Fe_{80}Ni_{20}$ chemical modulations. Figure 6.16a shows a XAS-TXM image at the Fe L_3 edge of a nanowire with two chemical modulations 4 µm apart. The orange dashed lines indicate the location of the modulation interfaces. Figure 6.16b shows the corresponding XMCD image where modulation #1 shows negative curling circulation with respect to $\hat{\boldsymbol{z}}$ and modulation #2 shows a BPW with negative circulation pinned on it. Black arrows indicate the direction of axial magnetization, whereas yellow arrows indicate the direction of azimuthal magnetization. Note that the magnetic contrast at modulation #2 is weak because the modulation now has a 90° curling angle and thus maximum x-ray absorption. Therefore, the differential contrast for right and left circularly polarized light is below the background signal. To confirm the aforementioned effect of magnetic contrast saturation at the chemical modulation, we may look at Figure 6.16e, an XMCD image at the Fe L_2 edge that shows opposite contrast to Figure 6.16d and a non-saturated signal at the modulation.The subsequent XMCD image in Figure 6.16c shows a transformation to TVW after the application of a 5 ns current pulse of $-0.20 \times 10^{12}\,\mathrm{A\cdot m^{-2}}$ along $\hat{\boldsymbol{z}}$ (blue arrow). On the other hand, modulation #1 remains with negative circulation. To explain this transformation, we may recall to Sec. 6.3, where the critical current densities obtained experimentally for DW transformations on a homogeneous 130 nm diameter wire were reported. Specifically, the transformation from BPW to TVW and vice versa showed a critical current of $0.20 \times 10^{12}\,\mathrm{A\cdot m^{-2}}$, which is below the critical value obtained for BPW circulation switching ($0.40 \times 10^{12}\,\mathrm{A\cdot m^{-2}}$). Therefore, for current densities below the threshold of BPW switching, we obtain BPW to TVW transformation, as shown in Figure 6.16c, and a TVW to BPW transformation as shown in Figure 6.16d. In addition we may comment that the 100 nm-long chemical modulation shows an experimental switching critical current of $0.60 \times 10^{12}\,\mathrm{A\cdot m^{-2}}$ (Figure 5.9), which is the reason why it does not switch. Lastly, for a 5 ns current pulse of $-0.40 \times 10^{12}\,\mathrm{A\cdot m^{-2}}$, BPW switching on a modulation occurred as shown in Figure 6.16e. Therefore, we conclude that the collective BPW and modulation switching follow quantitatively and qualitatively the switching process of a BPW, although we have seen in Sec. 6.2.2 that the

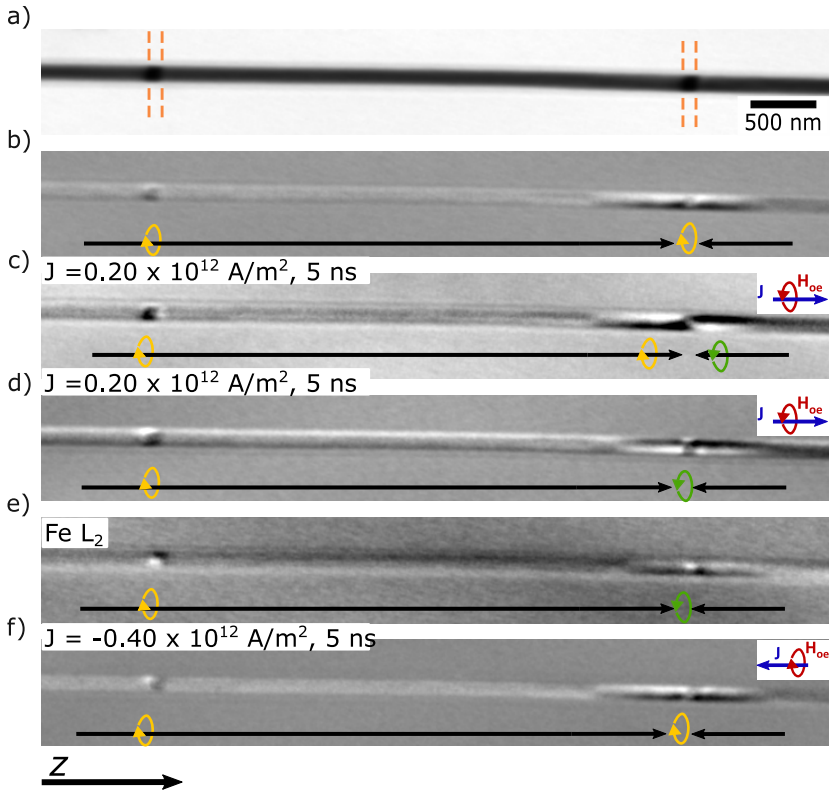

Figure 6.16: X-ray imaging of DW transformation on a chemical modulation induced by a moderate current density pulse. The system is based on a 120 nm diameter Permalloy nanowire with 100 nm long periodic $Fe_{80}Ni_{20}$ chemical modulations. **a)** XAS-TXM image at the Fe L_3 edge. Orange dashed lines indicate the location of the modulation interfaces. **b)** The corresponding XMCD image shows a BPW of negative circulation with respect $\hat{\boldsymbol{z}}$ pinned on modulation number #2. Black arrows indicate the direction of axial magnetization and yellow arrows indicate the direction of curling. **c)** XMCD shows the transformation to a TVW after the application of a 5 ns pulse of amplitude $0.20\,\mathrm{A}\cdot\mathrm{m}^{-2}$ along $\hat{\boldsymbol{z}}$ (blue arrow) with positive Œrsted field circulation (red arrow). **d)** XMCD shows further transformation to a BPW after the application of a 5 ns pulse of amplitude $0.20\,\mathrm{A}\cdot\mathrm{m}^{-2}$ along $\hat{\boldsymbol{z}}$ (blue arrow) with positive Œrsted field circulation (red arrow). **e)** XMCD image at the Fe L_2 edge showing consistently opposite magnetic contrast. **f)** XMCD shows BPW circulation switching after the application of a 5 ns pulse of amplitude $-0.40\,\mathrm{A}\cdot\mathrm{m}^{-2}$ along $\hat{\boldsymbol{z}}$ (blue arrow), thus with negative Œrsted field circulation (red arrow).

circulation of the modulation induces BPW switching upon propagation.

6.4.2 DW transformations on the chemical modulation: low damping

Here, we consider a more realistic situation in which a DW on a chemical modulation is subjected to a high Œrsted field amplitude under a low damping term, implying precession of the magnetization components and also faster magnetization dynamics. The reason to study this relies on the fact that the current densities required for long-distance DW motion are usually above $2\times10^{12}\,\mathrm{A}\cdot\mathrm{m}^{-2}$ [181], which has an associated Œrsted field at the periphery above 56 mT or 81 mT for a diameter of 90 nm or 130 nm, respectively. First, we will show the experimental results, and then this will be supported with micromagnetic simulations. Figure 6.17a shows a XAS-TXM image at the Fe L_3 edge of a 120 nm diameter Permalloy nanowire with a 100 nm-long $Fe_{80}Ni_{20}$ chemical modulation at its center. The orange dashed lines indicate the modulation interfaces. The corresponding XMCD in Figure 6.17b shows a head-to-head BPW on the chemical

modulation with collective negative circulation with respect to $\hat{\mathbf{z}}$. Black arrows indicate the direction of axial magnetization and yellow and green arrows indicate the direction of azimuthal magnetization. The axial magnetization components are visible due to the 10° tilt of the sample holder. Figure 6.17c shows the XMCD image after the application of a 2 ns pulse of current density $2.50 \times 10^{12}\,\mathrm{A \cdot m^{-2}}$ (blue arrow), whose Œrsted field circulation is positive (red arrow). The micromagnetic state after the pulse shows a BPW with positive circulation at the right side of the modulation opposite to the electron flow, the latter remaining with negative circulation (Figure 6.17c). It is surprising that the modulation did not reverse its circulation for such a high amplitude pulse. However, we should remember that the 2 ns duration of the pulse is of the order of or even below the DW switching dynamics. Therefore, it is possible that the external stimulus was stopped during a transient state. After the application of a current pulse of the same characteristics, the modulation reverses its circulation to positive and the BPW moves and pins on it (see Figure 6.17d). For another pulse of the same characteristics, with parallel Œrsted field and BPW circulation, the BPW is expelled at the right side of the modulation in the direction opposite to the electron flow (Figure 6.17e). This small motion is not led by the STT but by the Œrsted field, highlighting its important contribution. Finally, for a pulse in the opposite direction, the BPW reverses its circulation and pins on the chemical modulation, as displayed in Figure 6.17f.

These experimental results cannot be explained solely on the basis of our existing knowledge of an isolated modulation (Sec. 5.5), an isolated DW (Sec. 6.3.1), or with the energy landscape of the DW induced by the modulation (Sec. 6.1). In order to understand the impact that a high amplitude Œrsted field has on a BPW pinned on a chemical modulation, micromagnetic simulations using the *mumax3* code were carried out. The system is based on a 90 nm diameter Permalloy nanowire with a 100 nm $Fe_{80}Ni_{20}$ chemical modulation at its center. In Figure 6.15, we already discussed the BPW switching on a chemical modulation for a quasistatic stimulus (damping term $\alpha = 1$) with a 20 nm $Fe_{80}Ni_{20}$ chemical modulation, and a current density of $2 \times 10^{12}\,\mathrm{A \cdot m^{-2}}$. The slow dynamics provided by the high damping term, stabilized a homogeneous BPW circulation switching on the modulation, where the BP moves towards the modulation interface to join the V-AV, annihilates and re-enters in the volume with opposite polarity. In that case, due to the short 20 nm width of the chemical modulation length, the V-AV pair had to be formed outside of the modulation interface, leading to BP expulsion towards them. However, when the modulation length is longer, we have identified two possible phenomena: BPW switching on the modulation or BPW expulsion from the modulation, switching, and return to the modulation. By closely examining these phenomena, we have observed that the polarity of the first V-AV pair is not stochastic and it sets the subsequent behavior of the wall. The V-AV polarity deterministically depends on the damping term and on the DW charge. In the following, we will detail the micromagnetic conditions that set these two different types of behaviors.

Figure 6.18 summarizes the Œrsted field-induced BPW switching dynamics, initially on a 100 nm-long modulation, for all possible types of BPW configurations (head-to-head or tail-to-tail, and $C+$ or $C-$), and for a high ($\alpha = 1$) and a low ($\alpha = 0.1$) damping parameter. The initial state is a BPW on a chemical modulation, whose characteristics are indicated in the first column. A current density of amplitude $2 \times 10^{12}\,\mathrm{A \cdot m^{-2}}$ is applied, with an associated Œrsted field antiparallel to the corresponding initial state. In each subfigure, two unrolled m_ρ surface maps are shown: the first one corresponds to the time event where the first V-AV forms and the second one to the time event where the last V-AV pair annihilates and the BP re-enters in the volume, i.e., when the reversal process is completed. The color code corresponds to m_ρ, the black dashed line to $m_\varphi = 0$ and the black line to $m_z = 0$. The orange dashed line corresponds to the location of the modulation interfaces. The black square sets the location in $\hat{\mathbf{z}}$ of the BP, which is always initially at the center of the modulation. Figure 6.18 can be understood as follows. The main overall message is that for $\alpha = 0.1$, the same sign of m_ρ is shared between the BPW and the V-AV pair, which leads to a high radial component favoring wall expulsion out of the modulation. Then after the reversal, the BPW returns to the modulation. For high $\alpha = 1$, opposite m_ρ signs between the V-AV and the BPW occur, thus the overall radial component is offset and BPW switching occurs within the modulation. Here are some important and more specific points: (i) For the case of $\alpha = 0.1$, the four types of systems (letters $a-d$) show BP switching

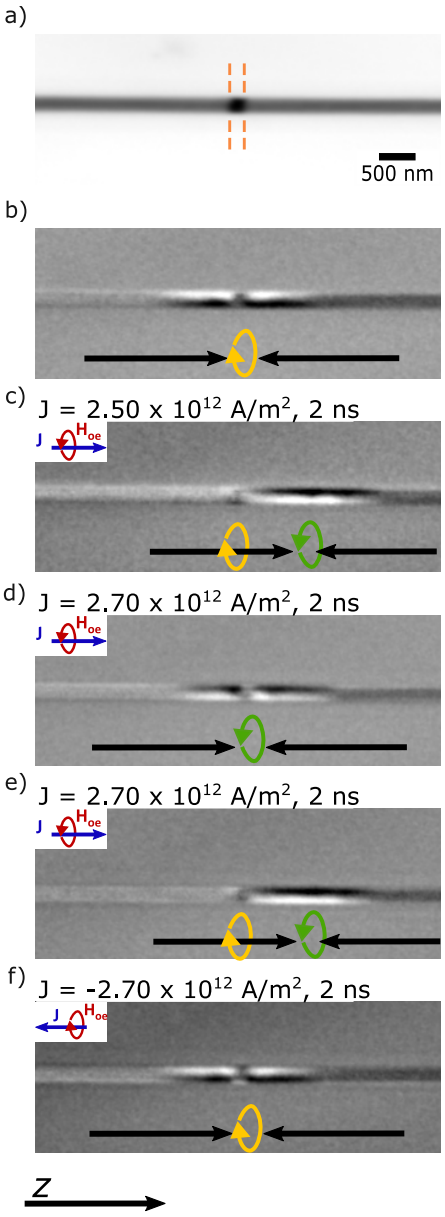

Figure 6.17: X-ray imaging of BPW switching and expulsion from modulation induced by high amplitude current density pulses. **a)** XAS-TXM image at the Fe L_3 edge of a 120 nm diameter Permalloy nanowire with a 100 nm-long $Fe_{80}Ni_{20}$ chemical modulation at its centered. The orange dashed line indicates the location of the modulation interfaces. **b)** Corresponding XMCD image shows a BPW with negative circulation with respect to $\hat{\boldsymbol{z}}$, pinned on the modulation. The black arrow indicates the direction of axial magnetization, and yellow arrow indicates the direction of azimuthal magnetization. **c)** XMCD image after the application of a 2 ns pulse of amplitude $2.50\,\mathrm{A}\cdot\mathrm{m}^{-2}$ along $\hat{\boldsymbol{z}}$ (blue arrow) with positive Œrsted field circulation (red arrow). BPW has switched to positive circulation (green arrow) and expelled from the modulation, which remains with negative circulation (yellow arrow). **d)** XMCD image after the application of a 2 ns pulse of amplitude $2.70\,\mathrm{A}\cdot\mathrm{m}^{-2}$ along $\hat{\boldsymbol{z}}$ shows BPW motion and pinning on the modulation. **e)** XMCD image after the application of a 2 ns pulse of amplitude $2.70\,\mathrm{A}\cdot\mathrm{m}^{-2}$ along $\hat{\boldsymbol{z}}$ shows BPW expulsion from modulation. **f)** XMCD image after the application of a 2 ns pulse of amplitude $-2.70\,\mathrm{A}\cdot\mathrm{m}^{-2}$ along $\hat{\boldsymbol{z}}$ shows BPW switching to negative circulation and pinning on the modulation.

outside of the modulation. For the case of $\alpha = 1$, the four types of systems (letters $e-h$) show BP switching inside the modulation. The four equal dynamics for a fixed α value highlight the symmetry of the system, which can be understood as follows. A tail-to-tail $C+$ and a tail-to-tail $C-$ configuration are equivalent by a 180° rotation around an axis perpendicular to the wire axis. The same applies to a head-to-head $C+$ and a head-to-head $C-$. A tail-to-tail $C+$ and a head-to-head $C-$ can be obtained by time-reversal symmetry. Also we observe that for $\alpha = 0.1$, vortex-antivortex pairs with $m_\rho = 1$ for a head-to-head BPW, and with a $m_\rho = -1$ for a tail-to-tail BPW. The associated charge of a head-to-head BPW is positive, whereas for a tail-to-tail configuration it is negative. Therefore, even though $\mathrm{d}m_\rho/\mathrm{d}t$ remains the same, because of the different BPW charges the m_ρ components of the V-AV shares the same radial component as the BPW. Nevertheless, $\mathrm{d}m_\rho/\mathrm{d}t$ has mirror symmetry with the median plane of the BPW, which inverts the left and right. (ii) If we focus on a specific situation, e.g. a head-to-head BPW $C+$, with $\mathrm{H_{OE}}$ $C-$ (letter a). Since m_ρ has mirror symmetry, the torque $m_\rho \hat{\rho} \times \mathbf{H}$ sets the wall in motion along $\hat{\mathbf{z}}$. In addition, m_z has mirror symmetry, so that $\mathrm{d}m_\rho/\mathrm{d}t$ has opposite signs on the two sides of the wall. Due to the influence of the existing head-to-head charge, this is the second reason to make the dynamics different for $z > 0$ and $z < 0$. Therefore, we can conclude that the dependence of the direction of motion on the circulation is based on the chirality of the LLG equation. This was proven also for the case of BPW switching on a homogeneous wire, showing that an inertia drift of the wall occurs when the external field is turned off. The direction of the drift was found to be to the right for positive circulation $C+$ and to the left for negative BPW circulation $C-$. (iii) We observe that for high damping ($\alpha = 1$), the vortex-antivortex pair has an opposite m_ρ sign than the BPW, which remains inside the modulation for switching. Since by setting high alpha we are close to a quasistatic situation, i.e., a flux closure state to reduce magnetostatics, opposite m_ρ components allow for this energy minimization. For the case of low damping ($\alpha = 0.1$), we observe that equal m_ρ signs are shared between the BPW and the vortex-antivortex pair, and the BPW switches its circulation outside of the modulation. In this case, since precession dominates the effect is similar to the preferred dynamical circulation, for which $\mathrm{d}m_\rho/\mathrm{d}t > 0$ induces $|m_\rho| = 1$ easier than $\mathrm{d}m_\rho/\mathrm{d}t < 0$ for a head-to-head BPW. The increase in the out-of-plane components along the radial direction, combined with the higher magnetization at the modulation and the reduced BPW width when it is on it, leads to the expulsion of the BPW out of the modulation. This causes the BPW to expand its width, resulting in a reduction of the magnetic charge density. (iv) The same behavior was observed for BPW switching in a homogeneous nanowire for $\alpha = 1$. V-AV pairs were found with $m_\rho = 1$ for a tail-to-tail BPW (Figure 6.11a), while V-AV pairs were found with $m_\rho = -1$ for a head-to-head BPW (Figure 6.11b), in agreement with the literature [185]. However, for $\alpha = 0.1$, new physics arise due to the precessional dynamics, which give rise to longitudinal DW motion and fast dynamics. Furthermore, in the presence of a modulation, expulsion out of it, transformations and return to modulation occur.

In Sec. 6.3.2, we presented the theoretical and experimental evidence of BPW switching in a homogeneous nanowire, where we addressed the impact of pulse width. In Figure 6.18 and Figure 6.17, we explored, with simulations and experimentally, the case of BPW switching on a chemical modulation, where we observed a longitudinal wall motion out of the modulation. Next, we proceed to study the impact of pulse width on this phenomenon. The studied system with *mumax3* code is based on a 90 nm diameter Permalloy nanowire with a 100 nm-long $\mathrm{Fe_{80}Ni_{20}}$ chemical modulation at its center, and a damping $\alpha = 0.1$. The initial state is a BPW $C+$ pinned on the chemical modulation, as shown in the first unrolled m_ρ surface maps in Figure 6.19a at t =0 ns. The color code corresponds to m_ρ, the black dashed line to $m_\varphi = 0$, and the black line to $m_z = 0$. The orange dashed lines indicate the location of the modulation interfaces. The first column of unrolled maps shown in Figure 6.19 corresponds to different time events under the application of an Œrsted field $C-$ of amplitude $-2 \times 10^{12}\,\mathrm{A \cdot m^{-2}}$. The second column of unrolled m_ρ surface maps corresponds to the relaxed configuration obtained after turning off the Œrsted field at the corresponding time event of the first column. The third column shows the micromagnetic outer view of the relaxed configuration, where the color code corresponds to m_φ. If the external stimulus is stopped when only the first $\mathrm{V_1^+}$-$\mathrm{AV_1^+}$ pair is formed, as shown at t =0.56 ns in Figure 6.19b, the system relaxes to a TVW pinned on the modulation. Note that a TVW has opposite circulations on both sides of the wall, thus the part overlapping with the modulation

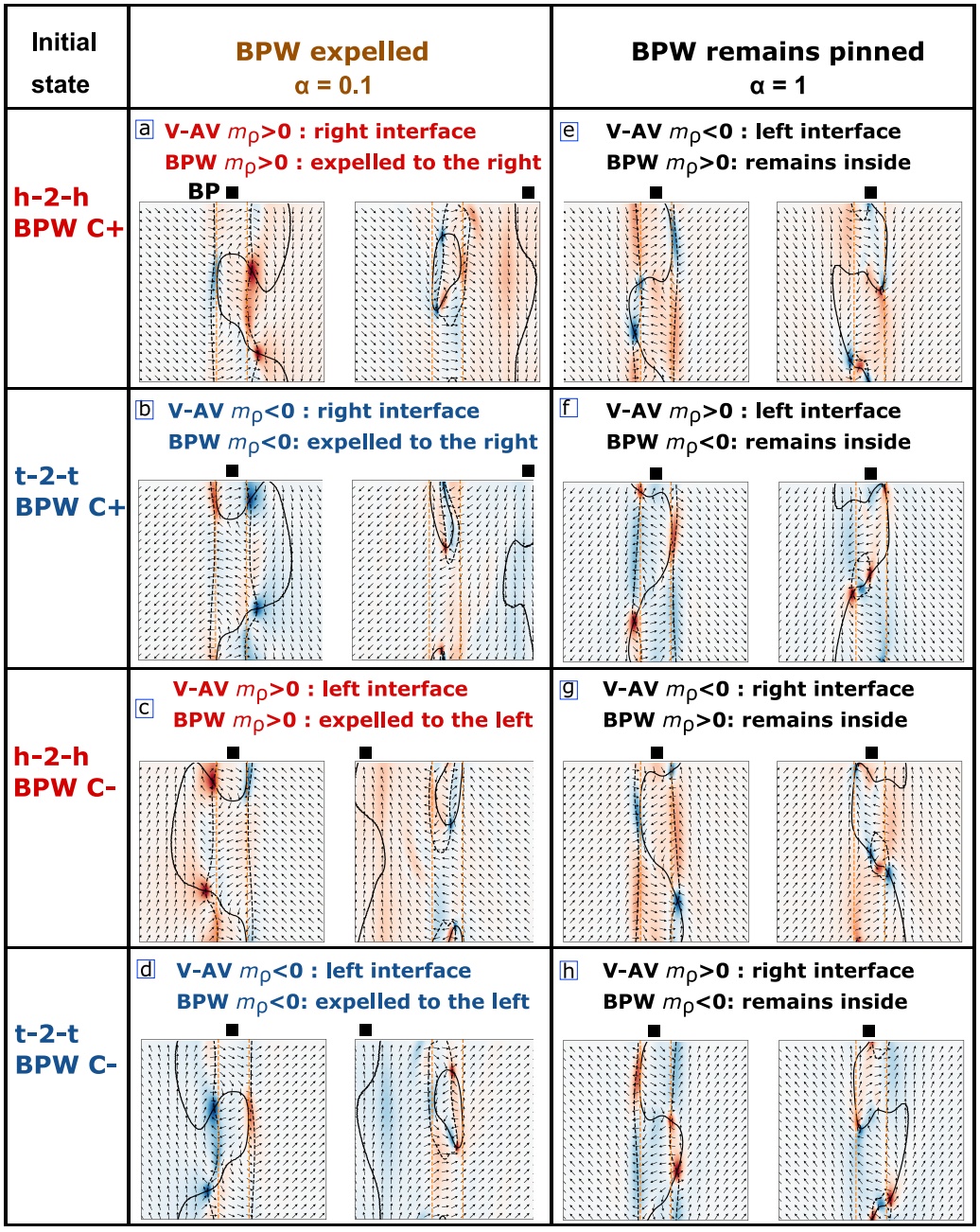

Figure 6.18: Characterization of Œrsted field induced BPW switching on modulation for the case of slow dynamics ($\alpha = 1$) or expulsion and switching outside of modulation for the case of fast dynamics ($\alpha = 0.1$) for a current density of $2 \times 10^{12}\,\mathrm{A \cdot m^{-2}}$. The initial configuration is based on a 90 nm diameter Permalloy nanowire with a BPW on the 100 nm-long chemical modulation. The two unrolled m_ρ surface maps per subfigure show the state of the first vortex-antivortex formation and the state of the last vortex-antivortex annihilation, i.e., when the BPW switching is completed. The first column for $\alpha = 0.1$ shows the same m_ρ signs of the BPW (positive for head-to-head and negative for tail-to-tail) and the V-AV pair, which leads to BPW expulsion towards the side where the vortex-antivortex pair is formed. After the switching process, the BPW returns to the modulation. The second column for $\alpha = 1$ shows opposite m_ρ signs of the BPW and V-AV pair, leading to a BPW switching inside the modulation. The chirality of the LLG equation sets the side where the V-AV pairs are formed.

has $C-$, which can be understood as a partial BPW switching. If the stimulus is stopped at t =0.68 ns when the BP has been already expelled from the modulation and the second V_2^--AV_2^- pair has been formed, then the system relaxes into a BPW with reversed circulation $C-$ located outside the chemical modulation, which remains $C+$ (Figure 6.19c) . This occurs because the modulation did not have time enough to reverse its circulation, which is inconsistent with the faster modulation dynamics versus the wall. This highlights that there is a collective dynamics with a new associated time scale. Finally, if the stimulus is stopped after the full collective switching mechanism (t =0.86 ns Figure 6.19d), this leads to a relaxation state where a BPW $C-$ is pinned on the chemical modulation also $C-$. With this, we reflect on the impact that the pulse duration has on the DW dynamics on a modulation.

Next, we provide experimental evidence of the different possible final states. As mentioned before, the two previously reported experimental evidences of current-driven DW dynamics [181, 184] were done for pulse durations above 5 ns on a homogeneous CoNi nanowire. This could explain why no BPW to TVW transformation was evidenced. In the experiments performed in my thesis electric pulses duration down to 500 ps were applied, allowing us to approach the timescale of the dynamics predicted by simulations to lead to a variety of final states. In the following, we show three types of experimental final states after sending the same 2 ns pulse of amplitude $-2\times10^{12}\,\mathrm{A\cdot m^{-2}}$ to the initial state shown in Figure 6.19a. The third column shows a ptychographic reconstructed XAS image at the Fe L_3 edge of a 120 nm diameter Permalloy nanowire with a 20 nm-long chemical modulation at its center. The orange dashed lines set the location of the modulation interfaces. The corresponding XMCD image below shows a BPW of positive circulation $C+$ pinned on the chemical modulation. Black and green arrows indicate the direction of axial and azimuthal magnetization, respectively. After the application of the current pulse, the first type of behavior is the BPW transformation to a TVW pinned on the chemical modulation, as displayed in the XMCD image in Figure 6.19b. However, if we send the same pulse to the same initial state, we also obtain the micromagnetic configuration shown in Figure 6.19c. In this case, the BPW is outside the modulation with reversed circulation $C-$, and the modulation did not switch and remains $C+$. Lastly, another type of final state is a BPW pinned on the modulation with a collective $C-$ reversed circulation. Therefore, we may conclude that experimentally it is not trivial to have deterministic behaviors since for the same initial state and pulse characteristics, different final states may occur. We should highlight several things: first, even though there is no DW motion, the STT impact should be considered for such high current densities. In addition, the Joule heating adds stochasticity to the dynamics, which we cannot control. Then, the rest of the nanowire of $\approx$ 20 µm length also undergoes a micromagnetic modification since several DWs are usually present within the same nanowire. To sum up, we have identified the mechanism driving the different DW dynamics, which is based on the Œrsted field, however there are several experimental parameters that does not allow a full control on the dynamics.

6.5 Ultra-fast and long distance DW motion: STT, Œrsted and heating.

To conclude this chapter, we will focus our attention on long-distance current-driven DW motion. So far, we have explored the high impact that the Œrsted field has on DW transformations in a homogeneous and modulated nanowire. When it comes to long-distance DW motion, we would expect that it is the STT that pushes the wall in the direction of the electron flow. However, this is not always the case as was reported in 2019 by the group [181]. This first experimental evidence on current-driven DW motion on cylindrical nanowires showed that the main driving force does not seem to be STT. In addition, it reported velocities up to $2400\,\mathrm{m\cdot s^{-1}}$, which sets a record and opens the door towards the magnonic regime. Theory has predicted BPW velocities above $1000\,\mathrm{m\cdot s^{-1}}$, with an absence of Walker breakdown. These high speeds may be achieved if the BPW circulation is clock wise with respect to the direction of motion. In the previous sections, no long DW motions were obtained for current densities up to $2\times10^{12}\,\mathrm{A\cdot m^{-2}}$, which are already rather large. This reflects that the material's intrinsic pinning is high. In addition, we may highlight that the

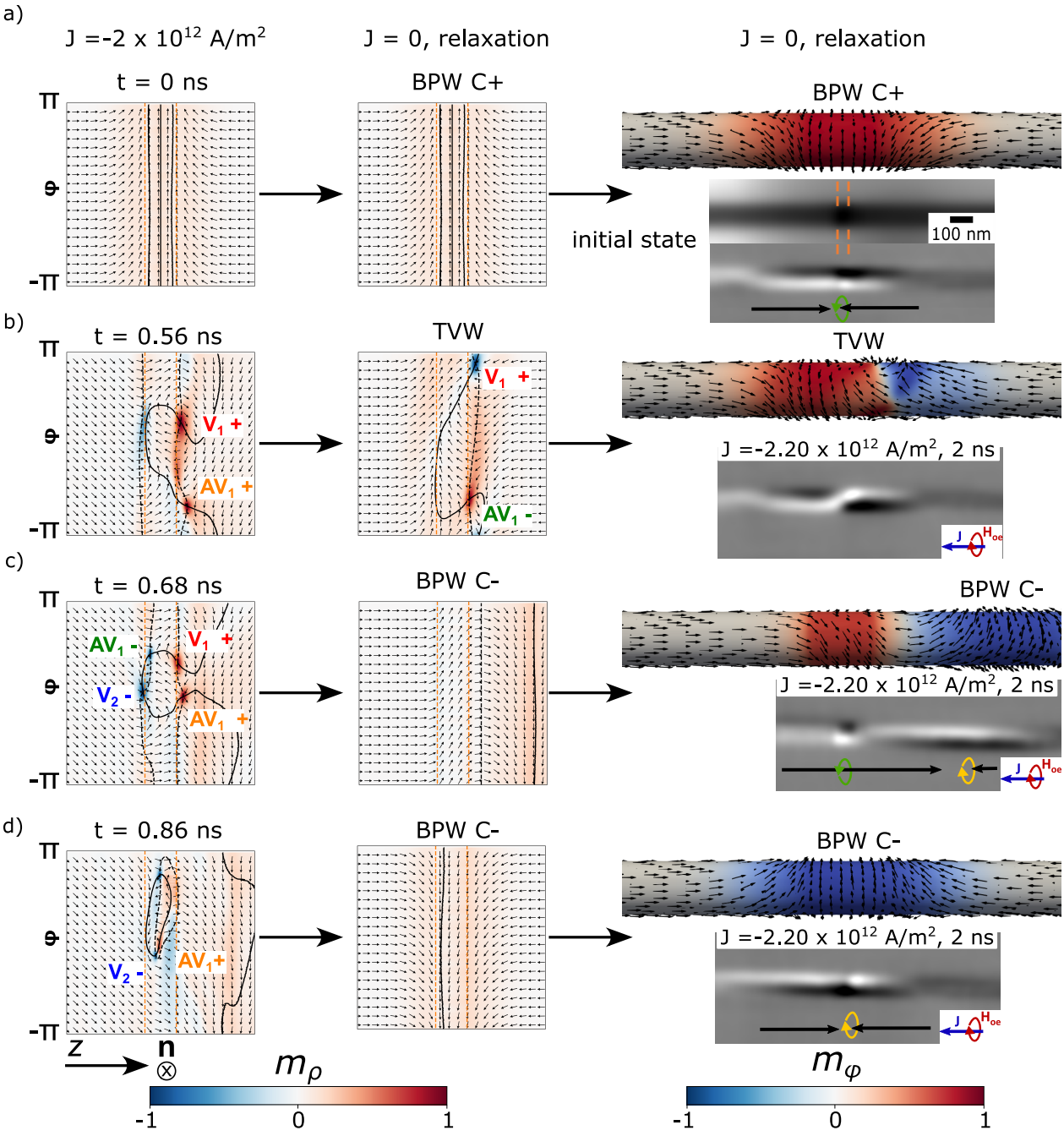

Figure 6.19: BPW on modulation switching dynamics when the Œrsted field is turned off at different times. The simulated system is a 90 nm diameter Permalloy nanowire with a 100 nm-long chemical modulation, and a damping term of $\alpha = 0.1$. The first column of unrolled m_ρ surface maps shows the micromagnetic state at specific time events under the application of an Œrsted field $C-$, arising from a current of amplitude $-2 \times 10^{12}\,\mathrm{A \cdot m^{-2}}$. The second column shows unrolled m_ρ surface maps after the relaxation of the micromagnetic state shown in the first column. The third column shows the simulated micromagnetic outer view of the relaxed configuration. The color code corresponds to m_φ. Below, the ptychographic reconstructed XMCD image at the Fe L_3 edge of a 120 nm diameter Permalloy nanowire with a 20 nm-long $Fe_{80}Ni_{20}$ chemical modulation at its center. The common initial state is shown in **a)** where a BPW $C+$ is pinned on the modulation. **b)** shows a TVW final state. Note that it is not equivalent to the final state obtained with simulations, as in the experiment the modulation has switched its circulation. **c)** shows as final state a BPW $C-$ outside of the chemical modulation $C+$. **d)** shows a BPW $C-$ on the chemical modulation as a final state.

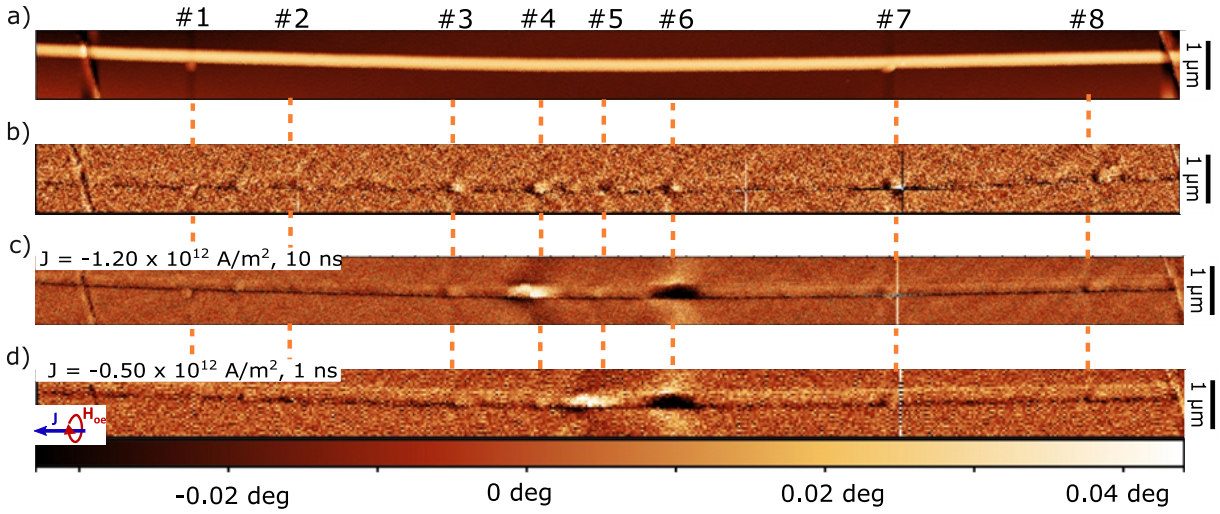

Figure 6.20: MFM imaging of current-induced DW motion. **a)** AFM image of an electrically contacted Permalloy nanowire with 130 nm of diameter and 100 nm-long $Fe_{80}Ni_{20}$ periodic chemical modulation. Orange dashed lines indicate the interfaces of the chemical modulations. **b)** MFM image of **a)**, which shows stray field arising from the modulations. **c)** MFM image after the application of a 10 ns pulse of $1.20 \times 10^{12}\,\mathrm{A \cdot m^{-2}}$ amplitude applied to nucleate DWs. One DW is nucleated and pinned on modulation #4 and another one on modulation #6. **d)** MFM image after the application of a 1 ns pulse of $0.50 \times 10^{12}\,\mathrm{A \cdot m^{-2}}$ to nucleate DWs. DW motion from modulation #4 to #5.

calculation of the current density was extracted from the maximum signal of the transmitted pulse, taking into account the attenuation and reflections of the pulse. Therefore, it may be slightly over estimated. In Sec. 2.6.4, it is detailed the procedure to calculate the current density through a nanowire. In the following, I will detail different microscopies techniques that I used to characterize DW motion. Before, I would like to address that in all of them, DW speeds above $1000\,\mathrm{m \cdot s^{-1}}$ were estimated, with a preferential pinning location at or next to the chemical modulations. However, the direction of motion was stochastic, i.e., not always along the STT direction. All the samples had a 20 nm alumina ALD coating on the top to decrease Joule heating. In addition, based on temperature calculations described in Sec. 8.2, we do not expect to demagnetize the sample since $T << T_C$. In addition, due to the short pulse duration we do not expect to have thermal gradients between the Au pads.

Depending on the experimental objective, several techniques are feasible for studying current-driven DW motion. Regarding in-lab techniques, a common one is possibly MFM imaging using a dedicated sample holder suitable for sending high-frequency (HF) pulses. With this technique, there are no constraints in terms of long cabling, high vacuum, and connections, allowing for pulses durations above 0.5 ns. The main complexity in this case arises from the three-dimensional shape of the nanowire, leading to an interplay of electrostatic forces with topography. In addition, the sub-miniature push-on (SMP) cables connected to the sample holder add an additional vibration that can be minimized but not avoided. Once good imaging conditions are set, high-quality AFM and MFM images are obtained, as shown in Figure 6.20a and Figure 6.20b, respectively. In this case, the system is a 130 nm of diameter nanowire with 100 nm-long $Fe_{80}Ni_{20}$ chemical modulations. Orange dashed lines indicate the interfaces of the chemical modulations. A bipolar magnetic contrast arises from the chemical modulations, allowing us to detect their location. In order to send current pulses, the feedback loop must be turned off, and the tip retracted. Once this is done, we apply a current pulse to nucleate DW in the system. The pulse characteristics were 10 ns of duration and $-1.20 \times 10^{12}\,\mathrm{A \cdot m^{-2}}$ of amplitude. Figure 6.20c shows the MFM image after the pulse, where two DWs have been nucleated, one on modulation #4 and another one on modulation #6. With the phase convention of the microscope and the polarity of the magnet used to magnetize the tip, white magnetic contrast corresponds to a repulsive force

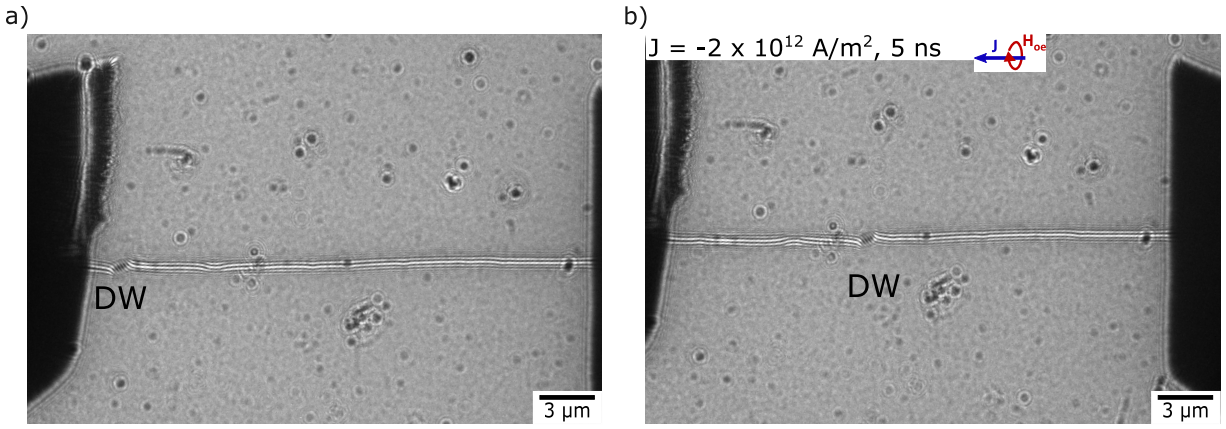

Figure 6.21: TEM imaging of current-induced DW motion. **a)** Defocus fresnel imaging of an electrically contacted Permalloy nanowire with 130 nm diameter and 100 nm long $Fe_{80}Ni_{20}$ periodic chemical modulations. The location of the DW is indicated. **b)** Imaging after the application of a 5 ns pulse of amplitude $-2\times10^{12}\,\mathrm{A\cdot m^{-2}}$ along $\hat{\mathbf{z}}$. Long-distance DW motion above 6 µm to the right is evidenced.

and thus a head-to-head DW (positively charged). Black contrast corresponds to an attractive force and thus a tail-to-tail DW (negatively charged). Consecutive 1 ns pulses of increasing amplitude were sent. DW motion was obtained from modulation #4 to #5, for an amplitude of $-0.50\times10^{12}\,\mathrm{A\cdot m^{-2}}$ along $\hat{\mathbf{z}}$. The distance between modulations is 1.5 µm, which suggests a speed of $1500\,\mathrm{m\cdot s^{-1}}$. However, the low depinning current may be induced by the interacting stray fields of DW and modulations due to the short distance between them and the large DW width. Specifically, the stray field $\mu_0 H = \mu_0 MR^2/2l^2$ at a distance $l = 1.5\,\mu$m is 1.6 mT, and at a distance $l = 3\,\mu$m is 0.4 mT. In order to disentangle possible interactions between the modulations, a distance of3.50 µm was set between them. This also allows for longer and faster DW motion. Another in-lab technique to study DW motion is by performing TEM imaging in defocus Fresnel mode. In this case, a dedicated sample holder that allows HF pulses is required. In our experiment at CEMES the connection between the Au pads and the cabling was not possible to make it through microbonding, since the sample holder had dedicated metallic clips. This increased the impedance mismatch of the circuit with the drawback of a non-square shape of the pulse. However, a correct transmitted signal was obtained even for very short pulses of 1 ns. This technique has the fastest acquisition rate and does not require post-treatment of the data. Therefore, it is very beneficial to acquire a big amount of data in order to do statistics on the direction of motion and pinning sites. In addition, correlative crystallinity or holographic measurements can be done. However, the sense of circulation cannot be detected, which does not allow a full picture of the situation. Next, we will show an example of long-distance DW motion evidenced by TEM. Figure 6.21a shows a defocused fresnel image with the initial state of an electrically-contacted Permalloy nanowire of 130 nm diameter and 100 nm-long $Fe_{80}Ni_{20}$ periodic chemical modulations separated by a distance of 3.50 µm. The distorted contrast at the left side of the wire indicates the location of the DW. The state after the application of a 5 ns pulse along $\hat{\mathbf{z}}$ of current density $-2\times10^{12}\,\mathrm{A\cdot m^{-2}}$ is shown in Figure 6.21b. A 7.5 µm DW displacement towards the right side is evidenced. The direction of motion is along the STT direction. Also, the DW is moved from modulation #1 to #3, over modulation #2. This results in a DW speed of $1500\,\mathrm{m\cdot s^{-1}}$. However, with MFM and TEM, the lack of information on the circulation of the DW does not allow to achieve the full picture of the DW's inner structure. Therefore, we focused on obtaining a large number of DW motions in order to get statistics. However, we found no clear relation between the DW direction of motion and the direction of the electron flow, highlighting once more the impact of the Œrsted field and Joule heating. In the following, we will see an example of DW motion obtained by XMCD, thus showing the full picture.

Figure 6.22a shows a reconstructed ptychographic amplitude XAS image at the L_3 edge of a 120 nm diameter Permalloy nanowire with periodic 20 nm-long $Fe_{80}Ni_{20}$ chemical modulations separated by a dis-

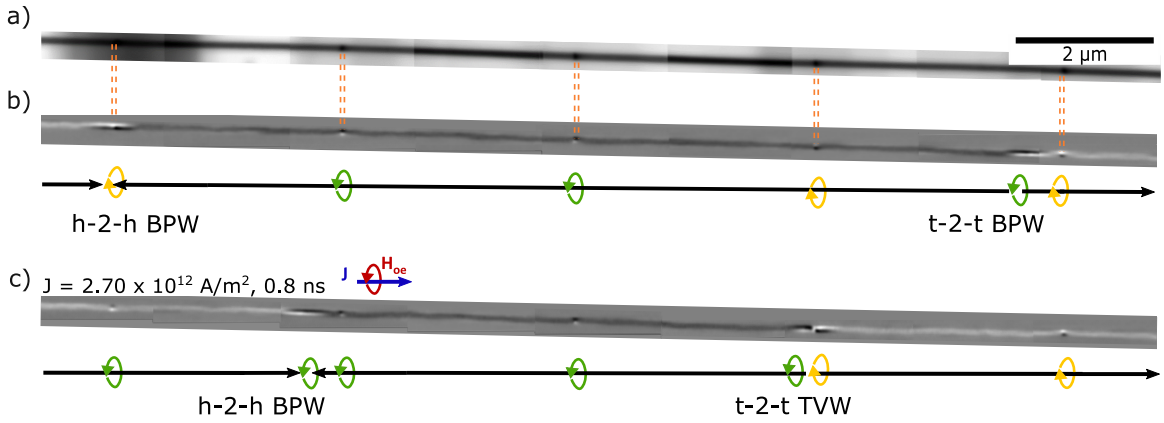

Figure 6.22: X-ray imaging of current-driven DW motion. **a)** Ptychographic reconstructed amplitude XAS image at the Fe L_3 edge of a 120 nm diameter Permalloy nanowire with periodic 20 nm long $Fe_{80}Ni_{20}$ chemical modulations separated by a distance of $\approx 3.5\,\mu m$. Orange dashed lines indicate the location of the modulations interfaces. **b)** Ptychographic reconstructed amplitude XMCD image of **a)**. A head-to-head BPW is located on modulation #1 and a tail-to-tail BPW next to modulation #5. Black arrows indicate the direction of axial magnetization and yellow and green arrows indicate the direction of azimuthal magnetization. **c)** Ptychographic reconstructed amplitude XMCD image after sending a 0.8 ns current pulse density of $2.70 \times 10^{12}\,A \cdot m^{-2}$. The first BPW moved to modulation #2 and the second BPW moved to modulation #4 and transformed into a TVW.

tance of $\approx 3.5\,\mu m$. Orange dashed lines indicate the location of the modulation interfaces. The continuous scanning on the same nanowire can be evidenced by the rectangles of carbon contamination. The image is constructed from a series of 2 µm-long images. The corresponding XMCD image is shown in Figure 6.22b. The axial magnetic domains are evidenced thanks to the $\approx 10°$ sample holder tilt. This initial state shows a head-to-head BPW with negative circulation $C-$ with respect to $\hat{\boldsymbol{z}}$ at modulation #1, and a tail-to-tail BPW with positive circulation $C+$ next to modulation #5, which has the opposite circulation. Black arrows indicate the direction of axial magnetization. Yellow and green arrows indicate the direction of azimuthal magnetization. In Figure 6.22c is shown the state after the application of a 0.8 ns pulse along $\hat{\boldsymbol{z}}$ of $2.70 \times 10^{12}\,A \cdot m^{-2}$ amplitude. The associated Œrsted field has positive circulation $C+$. The XMCD images shows that the BPW on modulation #1 has switched its circulation to positive $C+$ and moved to modulation #2. Therefore, two wall transformations occurred: switching and long-distance motion against the direction of the electron flow. On the right side of the nanowire, the BPW has moved from modulation #5 to #4 along the electron flow and transformed to TVW. This example illustrates that current driven BPW motion in cylindrical nanowires is not trivial. Firstly, even though we achieved to control the DW location of pinning, the sense of the motion seems stochastic. For the moment, it still requires to look carefully at all the data gathered together with new micromagnetic simulations, in order to disentangle the impact of STT, Œrsted field and heating. Moreover, the mechanism driving the Œrsted field driven DW transformation from BPW to TVW and from TVW to BPW has been identified within the above sections with micromagnetic simulations. These transformations were not considered before since the Œrsted field was thought to be negligible. However, the high current densities required for motion come with a very high Œrsted field amplitude and temperature rise. Therefore, a big effort is now required to disentangle the three of them. Future experiments, would be ideally based on materials with a lower pinning threshold and a reduced diameter.

6.6 Conclusions

In this last chapter, I have tried to provide a broad overall view of the DW behavior in a chemically-modulated nanowire. The presence of chemical modulations induces a modification of the energy landscape for the DW. Specifically, micromagnetic simulations suggested an energy well or energy barrier for the case of parallel ($C+C+$) or antiparallel ($C+C-$) circulation between the BPW and the chemical modulation, respectively. These predictions are supported by X-ray magnetic imaging, where DW locations at or next to the chemical modulations are evidenced. BPWs are often found on the modulation for the case of $C+C+$, and next to the modulation for the case of $C+C-$. In addition, we also evidenced TVW on or next to the chemical modulations.As regards DW motion for the $C+C+$ case, BPW depinning and propagation through the chemical modulation under axial field occurs above a certain depinning field in a smooth manner, i.e with continuous BP motion through the material interfaces. However, for the case of $C+C-$, we found that the circulation of the BPW switches before propagation through the chemical modulation. We attribute this to the larger energy barrier to switch the circulation of a BPW compared to a modulation. The mechanism behind BPW circulation switching under axial field was found to be similar to the one under Œrsted field detailed in [185]. This consists first in the formation of at least one vortex-antivortex pair at the surface, then the isoline $m_\rho = 1$ that connects them in the volume extends until they are diametrically opposed. More or less at this point, these lines attach to the BP, which leaves the core of the wire towards the surface until it annihilates via the antivortex polarity switching. Later on, the vortex annihilates with the antivortex of opposite polarity and the BP re-enters the volume, ending in a BPW with reversed circulation. In addition, we found that if the external stimulus is stopped during the vortex-antivortex transient state, the DW relaxes into a TVW. Regarding the experimental data, magnetization reversal under an axial quasistatic magnetic field resulted in a final state where some circulations were reversed. This implies that a more complex procedure occurs when the DW is traveling through the nanowire, implying switching of circulation of the DW and/or the modulation, or even transformations. In addition, this does not support our micromagnetic simulations since they predict only the BPW reversal, but not modulation one. However, we observed that when the magnetization reversal occurs under a magnetic field with an angular offset of 45° or higher with respect to the axis, a deterministic switching of the curling occurs along the direction parallel to the external field.

The second part of the chapter detailed DW transformations under an Œrsted field. Firstly, we detailed the case of BPW circulation switching in a homogeneous nanowire. We reported the case of a switching mechanism involving two vortex-antivortex pairs of the same polarity, using a high damping $\alpha = 1$ to better track the singularities. The sign of the polarity of the nucleated vortex-antivortex pair is the opposite of the wall charge: positive polarity for a tail-to-tail BPW and negative polarity for a head-to-head BPW. Similarly to the above, if the applied Œrsted field is stopped during the vortex-antivortex transient state the system relaxes to a TVW. We supported these predictions with experimental evidence of BPW transformation to TVW under a current pulse. Time-resolved STXM experiments of BPW allowed us to better understand the switching mechanism, characterize the time scale of the dynamics, and will provide a value of the experimental damping. As regards BPW switching on a chemical modulation, the same mechanisms occur but with subtle differences. First, the two vortex-antivortex pairs have opposite polarity between each other, which is formed at the modulation interfaces. Depending on wether a high ($\alpha = 1$) or low ($\alpha = 0.1$) damping term is used, the polarity of the first vortex-antivortex pair has opposite or same m_ρ components as the BPW, respectively. We studied the dynamics of the four types of BPW systems, i.e., head-to-head, tail-to-tail, $C+$ or $C+$. For a fixed α value, the four configurations showed the same dynamics, highlighting the symmetry of the system. For the case of high damping, as we approach a quasistatic situation, the overall m_ρ components are nearly offset, which allows BPW switching within the modulation. For the case of low damping, the rise in the overall m_ρ components along one radial direction has an associated non-negligible magnetic charge. This added up to the higher magnetization in the modulation and reduced DW width when it is on it, leads to a BPW expulsion and switching aside the modulation, followed by a return to it after the reversal

process. The sense of the BPW expulsion is determined by the chirality of the LLG equation. Finally, we evidenced that depending on the pulse direction different micromagnetic final states may be achieved for a shared initial state. These predictions were supported with experiments, where we evidenced events such as collective circulation switching, BPW expulsion aside the modulation or BPW transformation to TVW on a modulation. We also identified other events that at this stage cannot be explained, such as BPW transformation to TVW under a parallel Œrsted field. Since at this stage, experimentally, the Œrsted field cannot be disentangled from STT and homogeneous heating and stochastic thermal excitations, it remains unclear the driving physics of them.

Finally, regarding long-distance DW motion, we experimentally observed BPW motion from modulation to modulation for pulse durations even below 1 ns at speeds above $1000\,\mathrm{m}\cdot\mathrm{s}^{-1}$. However, the direction of motion was in both the direction of the electron flow and opposite to it. Therefore, we conclude that in our system, for such high current densities required for motion ($> 2.50\times10^{12}\,\mathrm{A}\cdot\mathrm{m}^{-2}$), the STT is not the sole driving force. Even though heating was optimized by performing alumina coating to increase the thermal path, it is not enough to take it out of the equation since a considerable voltage drop is still measured in the transmitted signal. To conclude, future experiments and simulations should focus on the disentanglement of STT, Œrsted field and heating in order to achieve a control direction of motion at lower depinning currents.

Chapter 7

Conclusions and perspectives

7.1 Conclusions

In the past 20 years, many theoretical and micromagnetic simulations reports have focused on the impact of curvature on magnetization dynamics. Cylindrical nanowires, whose diameter size can be close to the characteristic length scales of micromagnetism, are a text-book platform for the study of these phenomena. In addition, a one-dimensional model can be applied to study processes such as magnetization reversal or Domain wall (DW) dynamics. Regarding the experiments, the synthesis of template-assisted electrodeposited nanowires is easy to perform and affordable, allowing for a wide range of possibilities. In particular, a vertical array of nanowires could serve as the building blocks of a magnetic race track memory device. However, before this, the magnetization dynamics on an individual nanowire should be addressed. DW dynamics in this system have been studied in-depth by theory and simulations during the past two decades, but experiments are beginning to emerge. The main experimental complexity arises from imaging the magnetization not only at the nanowire surface but also at its core, such a three-dimensional characterization is obtained, with the added constraint of coupling it to a high-frequency (HF) electronics.

A specific aspect of cylindrical nanowires is the existence of a unique type of DW, known as the Bloch-point domain wall (BPW). Its magnetization rotates along the azimuthal direction at the periphery, and at the core, a Bloch Point (BP) magnetic singularity is located. The topology of this DW allows ultra-fast speeds above $1000\,\mathrm{m\cdot s^{-1}}$, delaying the Walker breakdown. Its experimental evidence was confirmed in 2014 by shadow-X-ray magnetic circular dichroism (XMCD)-photoemission electron microscopy (PEEM) by the host group, who also provided the first experimental current-induced DW motion in 2019. There, velocities above $600\,\mathrm{m\cdot s^{-1}}$ were measured, although with a stochastic direction of motion, and non-controlled pinning locations. In addition, the high impact of the Œrsted field was also reported, that stabilizes the BPW and sets deterministically its circulation. At the start of this PhD work, there were several open questions. The most relevant were the following: *"Which type of system could control DW pinning sites?"*, *"How is the micromagnetic behavior of this new system?"*, *"How does it interact with DWs?"*, *"What is the Œrsted impact in it?"*, *"Does it allow long-distance DW motion?"*, *"What is the main driving force of the dynamics?"*, etc.

To answer these questions, among others, this thesis has explored a new micromagnetic system based on Permalloy ($Fe_{20}Ni_{80}$) nanowires with periodic $Fe_{80}Ni_{20}$ chemical modulations. The diameters considered range from 90 nm to 130 nm, and the chemical modulation lengths range from 20 nm to 120 nm. These nanowires were synthesized by electrodeposition inside home-made porous anodised aluminium oxide (AAO) templates. The synthesis parameters have a direct impact on the micromagnetics of the sample, some of them include grain size, strain, composition, oxidation, crystallinity or curvature. A crucial step in this work was the optimization of defect-free modulations, a process described in Chap. 3. The starting point was the use of pulse plating for the synthesis of the nanowires, with pulses of -1.5 V to plate Permalloy (with a growth rate of $\approx 100\,\mathrm{nm/s}$), and short pulses ($\approx 8$ s) of -1 V to plate $Fe_{80}Ni_{20}$ (with a growth

rate of $\approx 4\,\mathrm{nm/s}$). However, several unexpected issues were encountered, the most unforeseen involving a sharp reduction in diameter at the location of the chemical modulations. The research conducted suggests that the cause lies in the different growth rates, which are directly related to different growth regimes. To minimize this effect, the plating of Permalloy was performed at $-1.35\,\mathrm{V}$, reducing the difference between the two growth potentials. In addition, a rest potential was set between pulses to ensure that we reach a steady state more rapidly. This resulted in defect-free chemically-modulated wires. Finally, we observed a drastic change in the crystal structure at the start of the chemical modulation, shifting from a single-crystal structure to a polycrystalline one. This was undesired since it could have a non-negligible impact on micromagnetics. Nevertheless, it could not be avoided since it arises from the strain associated with the change of potential.

The insertion of high-magnetization chemical modulations has a direct impact on the micromagnetics of the system. This is discussed in Chap. 4, where magnetic imaging, analytical modeling and micromagnetic simulations are combined to provide a broad picture of the phenomenon. An initial in-lab characterization performed by magnetic force microscopy (MFM) imaging and electron holography revealed stray field arising from the modulation interfaces. The three-dimensional magnetic characterization, performed by XMCD technique coupled to different X-ray microscopies (PEEM, transmission X-ray microscopy (TXM), scanning transmission X-ray microscopy (STXM) and X-ray ptychography), revealed curling of magnetization at the chemical modulations and axial magnetization in the Permalloy segments. The physics of curling was studied with analytical modeling and micromagnetic simulations, suggesting that the driving force is the screening of the interfacial surface magnetic charges by the volume charges. This screening was proven to reduce the dipolar field nearly to zero within the chemical modulations. We found an associated characteristic length scale of the screening phenomenon of $\Delta_{\mathrm{mod}} = 22\,\mathrm{nm}$, which is larger than the dipolar exchange length of either of the two materials. With regard to geometry dependence, the curling angle θ increases with the diameter and modulation length, being the maximum curling at the center of the modulation. For modulation lengths above $2\Delta_{\mathrm{mod}}$, a plateau of curling angle occurs throughout the modulation. The reason is that, after a certain z-distance, the curling is not driven by screening, which has already been achieved, but instead by longitudinal exchange, which makes the center of the modulation the least magnetically stiff region.

In Chap. 5, I explore the curling response to a quasi-static external magnetic field or to the Œrsted magnetic field associated with a nanosecond current pulse. This study is important because it forms the basis for later understanding of the interaction with DWs. First, I performed XMCD-X-ray ptychography imaging under an increasing axial magnetic field from 1 mT to 90 mT. A reduction of the magnetic contrast was detected, which translates into a reduction of the curling angle θ. The estimated curling angles decrease linearly with the field, in reasonable quantitative agreement with micromagnetic simulations. To quantify the XMCD contrast in terms of the degree of tilting of the magnetization, several analysis processes were described, considering the various instrumental effects contributing to the image. In our case of study, the incoherent background intensity plays a major role. Finally, X-ray imaging associated with nanosecond current pulses revealed switching of the curling circulation along the associated Œrsted field direction above a critical current. Time resolved STXM imaging revealed divergence of the switching time when approaching the critical current. This divergence was used to estimate the critical current density for switching above j_c from micromagnetic simulations. For the case of short modulation lengths (below $2\Delta_{\mathrm{mod}}$), j_c increases with length. We believe that this is because the modulation has a higher curling angle as the length increases, thus, a higher Œrsted field is required. We draw an analogy between this switching regime and a coherent reversal process where the switching occurs from the interfaces towards the center of the modulation. This was also supported by time resolved STXM imaging, where a shortening of the curling length while switching reflected the torque created by Permalloy domains on the modulation interfaces. A second switching regime was identified for larger modulations, where in this case the center of the modulation is the less magnetically stiff region. In this regime, j_c decreased with modulation length. We believe that this is because switching occurs incoherently, nucleating from the center of the modulation and expanding towards both interfaces.

Having provided a fairly complete study of the micromagnetics at rest, under a magnetic field or a

nanosecond current pulse in Chap. 6, we proceeded to study its interaction with DWs. First, micromagnetic simulations predict that the presence of chemical modulations induces an energy well for the BPW, if circulations are parallel $C+C+$, and an energy barrier for the BPW if circulations are antiparallel $C+C-$. This was supported with X-ray imaging, where deterministic DW pinning at the modulations was evidenced. Specifically, for the $C+C+$ case, BPW or transverse-vortex domain wall (TVW) were often found at the chemical modulations, whereas for the $C+C-$ configuration, they were often found next to the modulation. Under axial field, for the $C+C+$ case, we predict a BPW smooth propagation through the chemical modulation, with continuous BP motion through the interfaces. On the other hand, for the $C+C-$ case, BPW circulation switching occurs before crossing the modulation. We attribute this to the lower energy barrier associated with BPW switching compared to a modulation. The switching mechanism is similar to the one described in literature for a BPW switching under an Œrsted field. The process involves at least one vortex-antivortex pair and the annihilation and re-nucleation of the BP. Regarding Œrsted field-induced dynamics, we first described in a homogeneous Permalloy nanowire a new BPW switching mechanism involving two vortex-antivortex pairs with the same polarity. I identified that the system can be relaxed to a TVW if the Œrsted field is stopped during the transient vortex-antivortex state. This finding is in agreement with X-ray imaging experiments since a nanosecond pulse duration is of the order of the switching time scale of the simulations. This was confirmed with time-resolved STXM imaging revealing a BPW switching time of $\approx 6600\,\mathrm{ps}$ for a current near the critical one. However, there may be discrepancies with the experimental switching dynamics due to a different damping term. Switching times of $\approx 2000\,\mathrm{ps}$ were found for a current slightly above the critical. Therefore, these results agree that the switching dynamics have a similar duration to the HF applied pulses. When modulations come into play, a similar BPW switching dynamics on a modulation is identified. A curious difference is that the vortex-antivortex pairs show opposite polarity between each other, contrary to the homogeneous wire case where the same polarity was shared. In addition, I found out that the polarity of the first pair selects the type of dynamics ahead. If the vortex-antivortex pair has the same polarity/charge as the BPW, the wall is expelled out of the modulation during the reversal mechanism such that the out-of-plane radial components are spread. On the other hand, if the polarities are opposite, the BPW switches within the modulation. This behavior was also identified in experiments, where both final states were found. Finally, regarding long-distance motion, we evidenced BPW long distance motion from modulation to modulation for pulse durations below 1 s and velocities above $1000\,\mathrm{m\cdot s^{-1}}$. However, the current densities required for motion are above $2.50\times10^{12}\,\mathrm{A\cdot m^{-2}}$, which implies that spin-transfer torque (STT) is not the sole driving force, but also the Œrsted field and Joule heating. Experimentally, it was not possible to disentangle the three contributions. Therefore, future work on micromagnetic simulations may focus on this.

To conclude, in this thesis, I have provided a solid foundation for the micromagnetics of chemically-modulated nanowires and the interaction between modulations and DWs. This includes the first experimental evidence of Œrsted field-induced curling reversal of the chemical modulations, along with its time-resolved imaging and micromagnetic simulations. Also, it includes the first experimental evidence of time-resolved BPW circulation switching, along with imaging of its transformation to TVW and vice versa, all of this supported by micromagnetic simulations. The impact of the Œrsted field on the curling textures was highlighted. Finally, controlled DW long-distance motion was successfully achieved with the drawback of an uncontrolled direction of motion due to the combined effects of STT, Œrsted field, and Joule heating.

7.2 Perspectives

One of the major challenges with three-dimensional nanostructures is their handling for magnetic imaging and characterization under HF pulses. However, during the last five years, progress has been made in the field, and adaptation of different microscopies setup has allowed for advances in experimental research, including my own research. Still, several challenges remain, which I will briefly discuss.

First, regarding chemical synthesis, it remains an open question whether it is possible to synthesize a material with very low intrinsic pinning. This would have a drastic impact on deterministic DW motion driven by STT. The reason is that a lower depinning current, ideally of a few $10^{11}\,\mathrm{A\cdot m^{-2}}$, would be required for motion. This would result in a very low amplitude associated with the Œrsted field and also a low increase in temperature, which would make STT the sole driving force. Another type of platform to study would be ratchet-type nanowires, where the composition is gradually decreased, setting a preferential DW motion sense.

In my work, I have shown that the Œrsted field plays a key role in the dynamics. However, it does not drive it. To achieve a driving force for DW motion from Œrsted fields, azimuthal magnetization domains are required. This occurs normally for nanowires with a large diameter, above 250 nm. This is the topic of the PhD thesis of LUCIA GÓMEZ CRUZ, who will pioneer the study of DW motion in this type of system.

Another remaining challenge is to quantify the impact of Joule heating on magnetization dynamics. So far, we have estimated the temperature rise in a nanowire during a current pulse, and also decreased it by depositing 20 nm of alumina by atomic layer deposition (ALD). However, due to the high current densities required for motion in this work, this step is not enough. Therefore, new approaches remain to be study to increase heat dissipation in the system. This comes along with another concept, which is DW inertia. This effect was not considered throughout this work, but it may have an important impact on DW motion and also on the estimation of DW speed.

Finally, based on the record speeds above $1000\,\mathrm{m\cdot s^{-1}}$, the door to the magnonic regime in cylindrical nanowires is closer than ever. Therefore, time-resolved experiments are at hand to test this regime, and whether spin-waves can be detected from DW motions.

Chapter 8

Appendix

8.1 Electrical pulses shapes

In this section, we describe the expected electrical pulse shape measured in the oscilloscope depending on the configuration of the electrical circuits. The objective is to provide a general picture of the effect of cable length, oscilloscope coupling, transformers, attenuators, resistances, etc on the pulse shape. In all the described situations, a pulse generator with a 50 Ω impedance delivers an output pulse of 2 V amplitude and 10 ns duration.

Oscilloscope coupling

We first show the example of a pulse generator connected to an oscilloscope. The electronics and the cables are prepared to be coupled in 50 Ω to avoid impedance mismatches in high-frequency (HF) pulses. Therefore, a pulse generator (with a 50 Ω impedance) is designed to be coupled to an electronic device that has also 50 Ω impedance. This means that it will provide twice the asked voltage in anticipation of a 50 Ω-terminated load. Thus, when the oscilloscope is coupled to 1 MΩ, the signal will be fully reflected back to the pulse generator, adding the input and reflected signal. This results in a 4 V amplitude read at the oscilloscope as shown in Figure 8.1a. When the oscilloscope is coupled to a 50 Ω resistance, no reflections will occur, and a squared-pulse with the 2 V voltage will be read at the oscilloscope (Figure 8.1b).

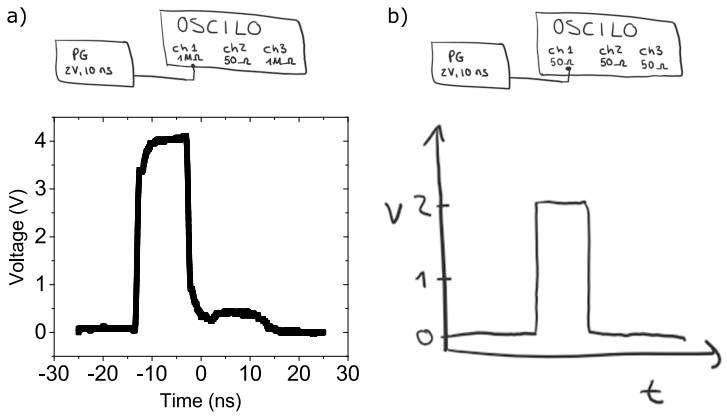

Figure 8.1: Shape of the electric pulse when the oscilloscope is coupled to **a)** 1 MΩ and **b)** 50 Ω.

Load terminations

Let us analyze the signal from a circuit closed by a zero-Ω load with the oscilloscope coupled to 1 MΩ. In a naive approach, this could be seen as the reflected signal reflected going through the ground of the load to the ground of the cable until the oscilloscope, where a negative amplitude is read. This is shown in Figure 8.2a where the input and reflected signals show the same amplitude but opposite sign. If a 50 Ω load termination is set, there are no reflections since there is a perfect impedance match, so a 2 V pulse is read Figure 8.2b.

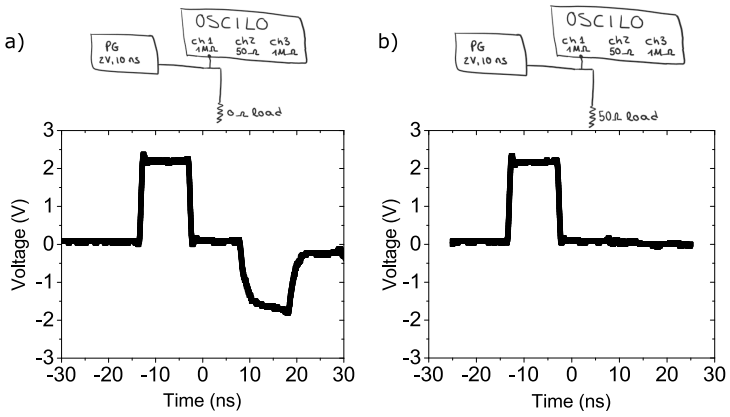

Figure 8.2: Electric pulse shape of the displayed circuit when the oscilloscope is coupled to 1 MΩ and **a)** zero-Ω load or **b)** 50 Ω load termination is set.

Open vs closed circuit

We could leave the circuit open instead of closing it with a termination load. In this case, signal reflections will not occur through the ground of the cables but through the transmission line or what we so-called "live". Therefore, a positive reflected amplitude will be measured as shown in Figure 8.3a. However, if the length of the *open* cable is shorter, the reflected signal will overlap with the input signal as shown in Figure 8.3b.

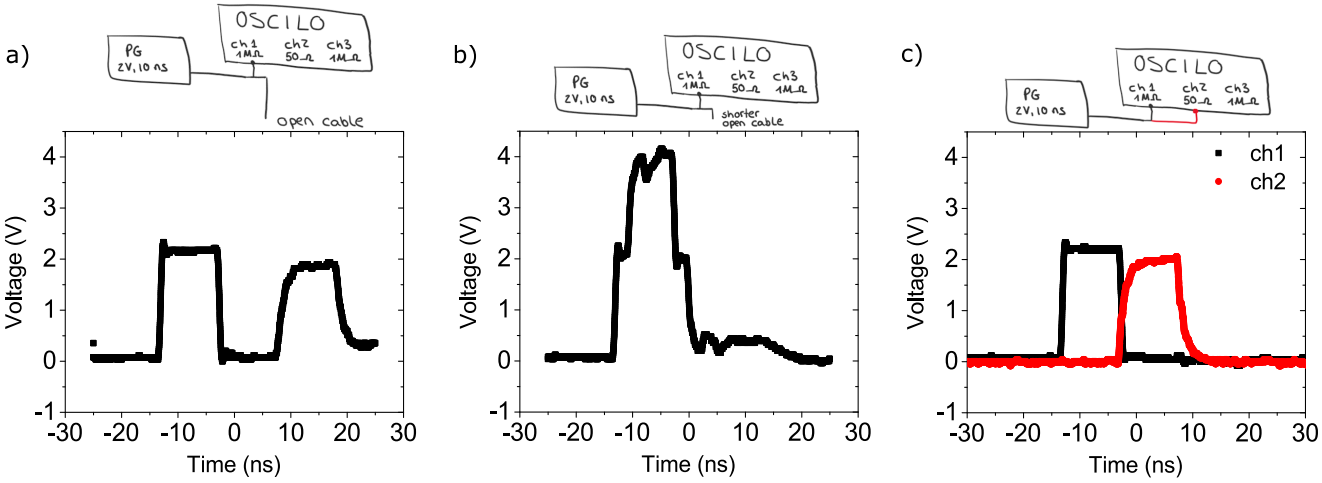

Figure 8.3: Shape of the electric pulses when the oscilloscope is coupled to 1 MΩ and **a)** the circuit is open, **b)** the circuit is open with a shorter cable and **c)** the circuit is closed by connecting the cable to another channel in the oscilloscope coupled to 50 Ω.

We may also connect the cable to another channel in the oscilloscope coupled to 50 Ω, which will measure a 2 V pulse (Figure 8.3c).

Attenuators

Let us analyze the behavior of attenuators. Will test the same circuit as in Figure 8.3c but with an attenuator before channel 2. The attenuation of the signal is clearly evidenced in Figure 8.4a, where a 20 dB attenuator is used. The signal is less attenuated for a 10 dB attenuator as displayed in Figure 8.4b.

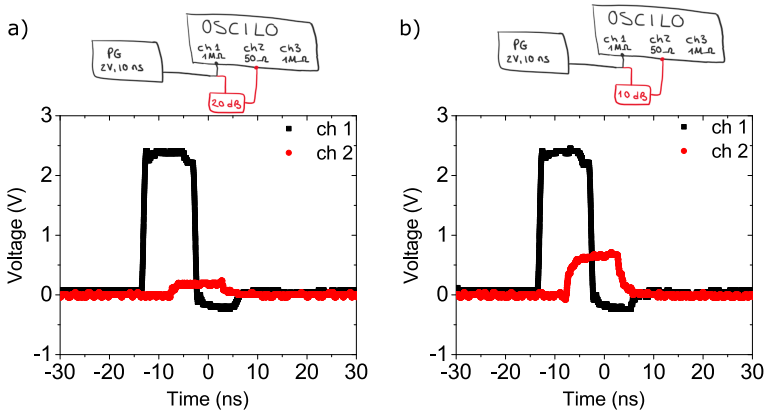

Figure 8.4: Shape of electric pulses when a **a)** 20 dB or a **b)** 10 dB attenuator is introduced in the circuit.

Transformers

As discussed in Sec. 2.4.2, photoemission electron microscopy (PEEM) imaging requires to have the electronics at high voltage. Therefore, electronics need to be protected from electrical discharges. To do so, two transformers are used after the input pulse and before the transmitted pulse reaches the oscilloscope. Transformers allow only transmitted frequencies in the range $0.2 - 500$ MHz, and thus block high voltage discharges. These transformers do not add signal reflections but just decrease slight the read voltage. This is displayed in Figure 8.5a for one transformer and Figure 8.5b for two transformers.

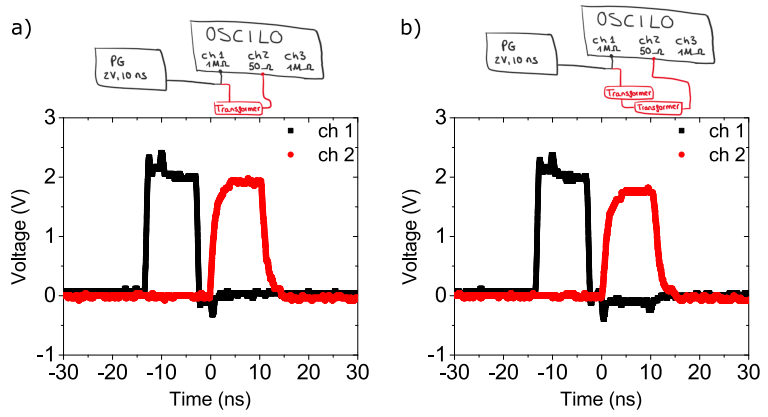

Figure 8.5: Shape of the electric pulse when **a)** one transformer or **b)** two transformers are included in the displayed circuit.

Resistance and transformers

Finally, it is also possible to add a resistance, which would mimic a real sample. We chose a 600 Ω resistance, which is the typical one obtained in our samples. Here we see clearly the impact of impedance mismatch on signal reflections and low signal transmission. This is displayed in Figure 8.6a, where the input pulse shows the expected 2 V amplitude, the reflected pulse shows a 1.7 V amplitude and the transmitted pulse a 0.3 V amplitude. In addition, further signal reflections are also evidenced for $t > 10$ ns. If we also add a transformer before the resistance (Figure 8.6b), or one before and another one after the resistance (Figure 8.6c), the transmitted pulse (red) suffers small modifications in its shape due to the signal reflections.

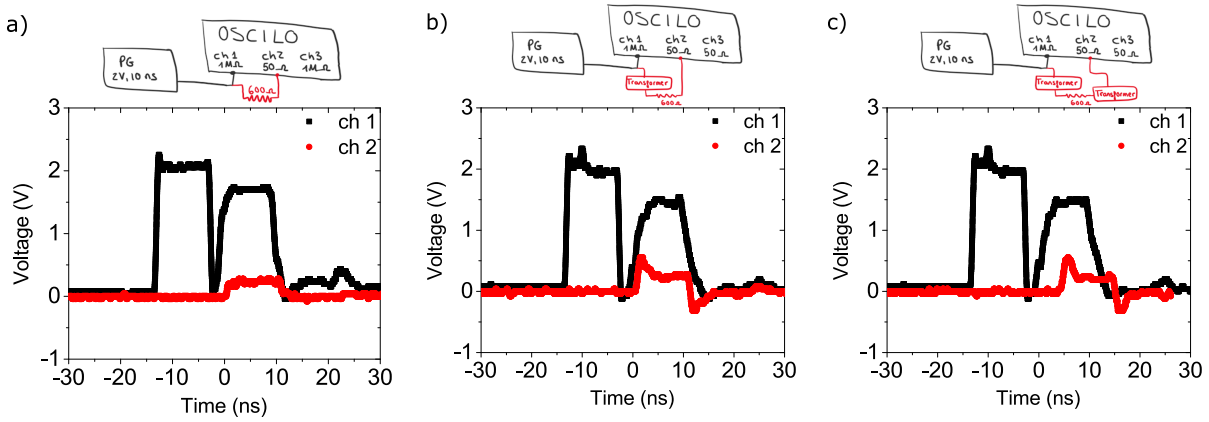

Figure 8.6: Electric pulse shape of the displayed circuits for a **a)** 600 Ω resistance, **b)** one transformer before the resistance or **c)** one transformer before and after the resistance.

8.2 Temperature calculations in a nanowire

As mentioned throughout this manuscript, Joule heating is one of the main issues faced when injecting current pulses in nanowires. The current densities required in this work for domain wall motion are above $2.50 \times 10^{12}\,\mathrm{A \cdot m^{-2}}$, which dramatically increases temperature in the nanowire. This increase in temperature is proportional to the voltage drop displayed in the transmitted pulse at the oscilloscope (due to the increase in sample resistance). As mentioned in the introduction, most of the experiments on domain wall motion have been carried out in nanostripes (nanowires with rectangular cross-section), which are in direct contact with the substrates. However, in the case of nanowires, the amount of material in contact with the substrate is really smaller. We have found that 20 nm of alumina coating, by atomic layer deposition (ALD), increases the thermal paths and reduces thermal gradients along the nanowire's cross-section by expanding the surface area of heat-loss. We need to convert the measured voltage to a temperature value to prove it.

There are different approaches in the literature to correlate temperature and resistance for flat strips in [319–321]. In the case of nanowires, a code developed by MICHAEL SCHÖBITZ, based on the relation between the resistance of a metal and its temperature, links both parameters. This approach allows estimating the increase of temperature in a nanowire due to the application of a current pulse. The resistance, R, of a metal is directly related to its temperature:

$$\Delta T = \frac{R/R_0 - 1}{\alpha} \tag{8.1}$$

being R_0 the resistance before heating and α the temperature coefficient of resistance. This coefficient is $0.0013\,\mathrm{K^{-1}}$ for $Fe_{20}Ni_{80}$ nanowires [322, 323], which is much smaller than for bulk FeNi alloys. However, it is important to take into account that this value, extracted from literature, should be only considered as a starting point because the temperature coefficient α strongly depends on the wire diameter, presence of grain

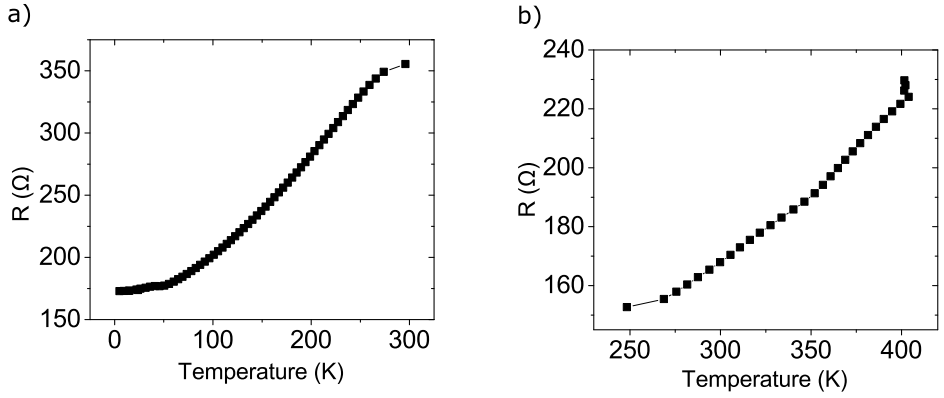

Figure 8.7: Variation of the sample resistance vs temperature for **a)** an AC current of 10 µA and **b)** an AC current of 50 µA measured by PPMS. Sample is a 130 nm diameter Permalloy nanowire with periodic 100 nm-long $Fe_{80}Ni_{20}$ chemical modulations

boundaries, grain size and scattering rates of the conduction electrons with phonons and lattice defects. This motivates us to measure this coefficient in the nanowires grown for this thesis work. To do so, transport measurements were done in a wide temperature range with a Physical property measurement system (PPMS). The sample chosen was a 130 nm diameter Permalloy nanowire with periodic 100 nm- long $Fe_{80}Ni_{20}$ chemical modulations. The nanowire resistance at room temperature was 350 Ω, which means a resistivity of $2.14 \times 10^{-7}\,\Omega \cdot m$. Figure 8.7a shows the thermal evolution of the resistance for an AC current of 10 µA. The temperature ranges from 5 K to 300 K. At 0 K the residual resistance is 172 Ω (ρ =$1.06 \times 10^{-7}\,\Omega \cdot m$). The calculation of the temperature coefficient α at temperature T_1 follows:

$$\alpha = \frac{R_2 - R_1}{R_1(T_2 - T_1)} = \frac{slope}{R_1} \tag{8.2}$$

Therefore, the slope in Figure 8.7a is 0.85 and the resistance at room temperature (T=298 K) is R =355.62 Ω. This leads to a temperature coefficient at room temperature of $\alpha = 0.0024$, which almost doubles the one from temperature.

We have also performed the same study for a higher AC current of 50 µA such that heating effects are noticeable. The result is shown in Figure 8.7b for a temperature range 250 K to 400 K. In this case, the slope is 0.44 and the resistance at room temperature 167.18 Ω, which gives $\alpha = 0.0026$. The measured α is twice the one reported in the literature, reflecting once more the importance of its calculation. However, it remains unclear why the resistance at room temperature is smaller in this case.

Once we have obtained an accurate experimental value of α, we can move to calculate the increase of temperature in nanowires with and without alumina ALD coating following Eq.(8.1). We have performed the experiments in 130 nm diameter Permalloy nanowires with periodic-100 nm long $Fe_{80}Ni_{20}$ chemical modulations. The measurements are shown Figure 8.8a, where the time evolution of the increase of temperature (black) and transmitted current density (blue) is shown. The initial current density is $\approx 1.2 \times 10^{12}\,A \cdot m^{-2}$ and the final is $\approx 0.75 \times 10^{12}\,A \cdot m^{-2}$, due to Joule heating. This translates into an increase of temperature of 250 K. When the nanowire is coated with 20 nm of alumina there is a smother increase of temperature for the same applied current density (see Figure 8.8b), with a maximum variation of ≈ 150 K. Therefore, the coating of an electrically contacted nanowire effectively reduces Joule heating by enhancing heat dissipation.

8.3 Azimuthal magnetic domains

All the nanowires studied in this manuscript, with diameters ranging from 90 nm to 135 nm, have axial magnetization along the Permalloy segments, with curling magnetization at the chemical modulations. However, above this range, azimuthal domains start to appear in the system due to the reduced exchange energy cost. We have experimentally found that, for samples with diameter close to the limit, that azimuthal domains start to appear, effect that it is enhanced after sending several pulses of high amplitude. This is due to the high associated Œrsted field, but also a clear evidence on the material degradation and changes in its resistivity.

Azimuthal domains in Permalloy nanowires with chemical notches have been previously reported in [141, 281], for nanowires with diameter above 200 nm. This previous work studied the domain wall dynamics under magnetic field, reporting the robust stabilization of the Domain wall (DW) at the chemical notches. Up to now, there is not an experimental report on current-driven DW motion on azimuthal domains. In this section, we show some preliminary results of this.

Figure 8.9a shows a reconstructed amplitude X-ray magnetic circular dichroism (XMCD) ptychographic image at the Fe L_3 edge of a 135 nm Permalloy nanowire with a 20 nm-long $Fe_{80}Ni_{20}$ chemical modulation (orange dashed line). Curling of magnetization occurs at the chemical modulation, whereas magnetization is axial in the immediate surroundings. However, azimuthal domains with opposite rotational senses are evidenced 200 nm away from the modulation. The change in the XMCD contrast reflects different curling angles, being the strongest contrast closer to $\theta = 90°$.

Azimuthal domains can be directly coupled to the Œrsted field associated to a current pulse. This opens the door to new unexplored physics. Figure 8.9b shows the corresponding XMCD image after the application of a nanosecond current pulse of amplitude $-2.50 \times 10^{12}\ \mathrm{A \cdot m^{-2}}$. The blue dashed line indicates the location of the DWs. It can be noticed that two walls were displaced in opposite senses in order to favor the enlargement of the azimuthal domains along the direction of the Œrsted field (see arrows). If a pulse with an opposite sign is sent, the favored domains are the opposite ones (black at the top), as shown in Figure 8.9c. This shows that the Œrsted field is the main driving force of DW motion in systems with azimuthal domains.

In addition, large azimuthal domains over several microns were also observed, as shown in Figure 8.10a. In this case the modulations were within the azimuthal domains. Note also that some segments, as at the left of the second modulation, show stronger contrast. This again implies a higher degree of tilt of the magnetization along the azimuthal direction. After the application of a nanosecond current pulse of amplitude $-2.50 \times 10^{12}\ \mathrm{A \cdot m^{-2}}$, the domains with white contrast at the top are favored and enlarged. After the application of a nanosecond current pulse of amplitude $2.50 \times 10^{12}\ \mathrm{A \cdot m^{-2}}$, the long domains with black contrast

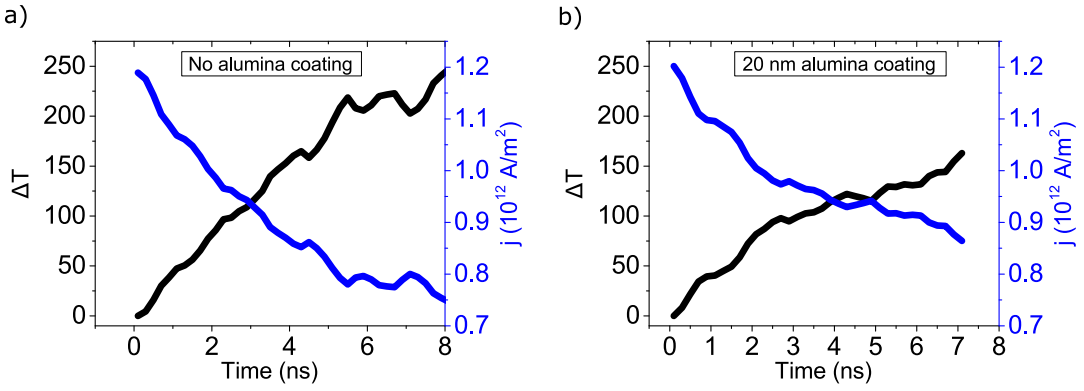

Figure 8.8: Temporal evolution of the temperature variation under a current pulse in a 130 nm diameter Permalloy nanowire with periodic 100 nm long $Fe_{80}Ni_{20}$ chemical modulations. Temperature (black) is calculated following Eq.(8.1) and the measured applied current density is shown in blue. **a)** sample without alumina coating. **b)** Sample with 20 nm alumina coating.

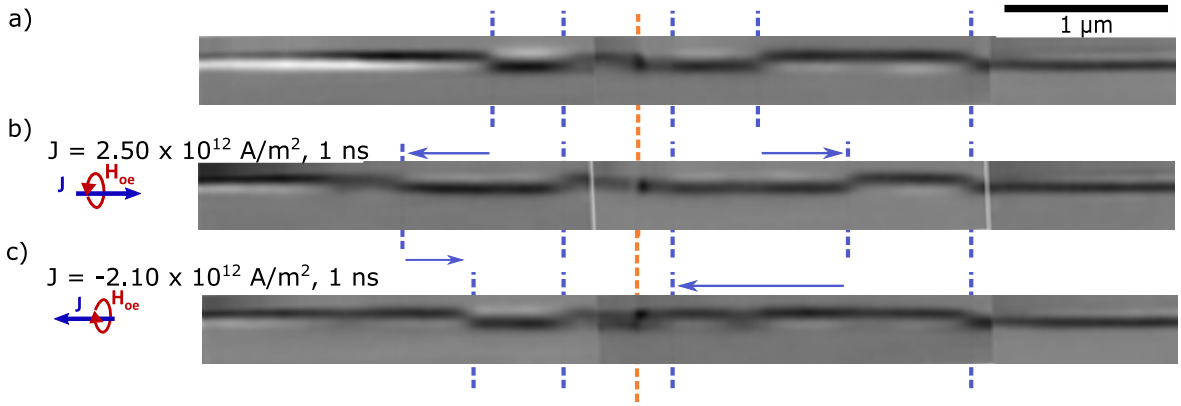

Figure 8.9: DW motion in a nanowire with short azimuthal domains. **a)** Reconstructed amplitude XMCD ptychographic image at the Fe L_3 edge of a 135 nm Permalloy nanowire with a 20 nm-long $Fe_{80}Ni_{20}$ chemical modulation (orange dashed line). Corresponding XMCD image of a nanosecond current pulse of amplitude **b)** $2.50 \times 10^{12}\ \mathrm{A \cdot m^{-2}}$ and **c)** $-2.10 \times 10^{12}\ \mathrm{A \cdot m^{-2}}$. The blue dashed line indicate the location of the DWs. Domains favored by the Œrsted field are enlarged.

at the top are favored and enlarged. Even though more measurements are needed to provide a more detailed analysis, this experimental data serves as a starting basis for future works. Specifically, LUCIA GOMEZ CRUZ PhD thesis is focused on exploring current-induced DW motion on azimuthal domains in nanowires and nanotubes.

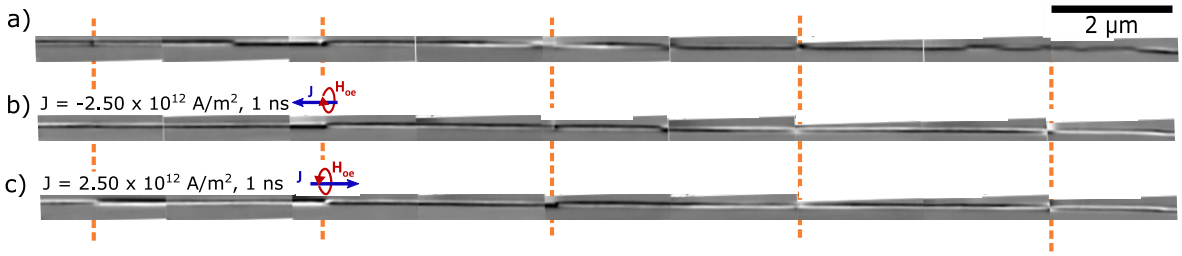

Figure 8.10: DW motion in a nanowire with long azimuthal domains. **a)** Reconstructed amplitude XMCD ptychographic image at the Fe L_3 edge of a 135 nm Permalloy nanowire with a 20 nm-long $Fe_{80}Ni_{20}$ chemical modulation (orange dashed line). Corresponding XMCD image of a nanosecond current pulse of amplitude **b)** $-2.50 \times 10^{12}\ \mathrm{A \cdot m^{-2}}$ and **c)** $2.50 \times 10^{12}\ \mathrm{A \cdot m^{-2}}$. Domains favored by the Œrsted field are enlarged.

List of abbreviations

AAO anodised aluminium oxide. 2, 21–25

ABF annular bright field. 26

ADF annular dark field. 26

AFM atomic force microscopy. 25, 27

ALD atomic layer deposition. 23, 45

BF bright field. 26

BNC A commonly used type of co-axial cable. 28, 46

BP Bloch Point. 48

BPW Bloch-point domain wall. 33

CCD charge-coupled device. 36, 38

CDI coherent diffraction imaging. 38, 40

DW Domain wall. 21, 26, 27, 32, 33, 45

EDX energy dispersive X-ray analysis. 25

EELS electron energy loss spectroscopy. 26

FZP Fresnel zone plate. 37, 38, 40

HAADF high angle annular dark field. 26

HF high-frequency. 21, 26–28, 33, 34, 36–38, 45–47

IBE ion beam etching. 45

LLG Landau-Lifshitz-Gilbert. 48

LPCVP low pressure chemical vapor deposition. 44

MFM magnetic force microscopy. 21, 27, 28, 47

OSA order separating aperture. 37, 38

PCB printed circuit board. 33, 34, 36–38, 41, 43, 46, 47

PEEM photoemission electron microscopy. 21, 25, 31–37, 40, 43–45

RIE reactive-ion etching. 44

sCMOS scientific complementary metal oxide semiconductor. 42

SEM scanning electron microscopy. 21–23, 25, 33, 34, 38, 41, 44–46

SMA sub-miniature version A. 28, 33, 34, 36–38, 47

SMP sub-miniature push-on. 28, 33, 34, 36–38, 41, 47

STEM scanning transmission electron microscopy. 26

STT spin-transfer torque. 3

STXM scanning transmission X-ray microscopy. 21, 31, 37–44

TEM transmission electron microscopy. 21, 26, 36, 37, 44

TXM transmission X-ray microscopy. 21, 31, 36–38, 40, 43, 44

X-ray ptychography A combination of scanning transmission X-ray microscopy with coherent diffraction imaging. 21, 31, 38, 40–44

XAS X-ray absorption spectroscopy. 29, 30, 39

XMCD X-ray magnetic circular dichroism. 21, 28–33, 37, 39, 42

Bibliography

[1] A. Kloss. *Geschichte des Magnetismus*. vde-Verlag Berlin, 1994.

[2] W. Gilbert. De magnete. Transl. PF Mottelay, 1958.

[3] J. Howard. Faraday, M-experimental researches in electricity, 1967.

[4] J. C. Maxwell. *A treatise on electricity and magnetism*, volume 1. Oxford: Clarendon Press, 1873.

[5] J. P. Joule. XVII. on the effects of magnetism upon the dimensions of iron and steel bars. *The London, Edinburgh, and Dublin Philosophical Magazine and Journal of Science*, 30(199):76–87, 1847.

[6] W. Thomson. XIX. on the electro-dynamic qualities of metals:—effects of magnetization on the electric conductivity of nickel and of iron. *Proc. R. Soc. London*, (8):546–550, 1857.

[7] J. Kerr. XLIII. on rotation of the plane of polarization by reflection from the pole of a magnet. *The London, Edinburgh, and Dublin Philosophical Magazine and Journal of Science*, 3(19):321–343, 1877.

[8] J. A. Ewing. *Magnetic induction in iron and other metals*. D. Van Nostrand Company, 1900.

[9] P. Curie. *Propriétés magnétiques des corps a diverses températures*, volume 3. Taylor & Francis, 1877.

[10] S. Tomonaga et al. *The story of spin*. University of Chicago Press.

[11] J. M. D. Coey. *Magnetism and magnetic materials*. Cambride University Press, 2010.

[12] L. H. Thomas. The motion of the spinning electron. *Nature*, 117(2945):514–514, 1926.

[13] L. H. Thomas. I. the kinematics of an electron with an axis. *The London, Edinburgh, and Dublin Philosophical Magazine and Journal of Science*, 3(13):1–22, 1927.

[14] F. Bloch. Zur theorie des ferromagnetismus. *Zeitschrift für Physik*, 61(3-4):206–219, 1930.

[15] P. Marage and G. Wallenborn. *Les Conseils Solvay et les débuts de la physique moderne*. Université libre de Bruxelles, 1995.

[16] J. M. D. Coey and S. S. P. Parkin, editors. *Handbook of Magnetism and Magnetic Materials*. Springer International Publishing, 2021.

[17] W. F. Brown. Micromagnetics: domain walls. *J. Appl. Phys.* , 30(4):62S, 1959.

[18] W. F. Brown. *Micromagnetics*. Wiley, 1963.

[19] S. Blundell. *Magnetism in condensed matter*. Oxford University Press, 2001.

[20] R. Skomski. *Simple models of magnetism*. Oxford, 2008.

[21] C. L. Dennis, R. P. Borges, L. D. Buda, U. Ebels, J. F. Gregg, M. Hehn, E. Jouguelet, K. Ounadjela, I. Petej, I. L. Prejbeanu, and M. J. Thornton. The defining length scales of mesomagnetism: a review. *J. Phys.: Condens. Matter* , 14:R1175–R1262, 2002.

[22] R. Skomski. Nanomagnetics. *J. Phys.: Condens. Matter* , 15:R841–896, 2003.

[23] A. Hubert and R. Schäfer. *Magnetic domains. The analysis of magnetic microstructures*. Springer, Berlin, 1999.

[24] A. P. Guimaraes. *Principles of Nanomagnetism*. Springer, 2009.

[25] A. Layadi, J. O. Artman, B. O. Hall, R. A. Hoffman, C. L. Jensen, D. J. Chakrabarti, and D. A. Saunders. FMR in evaporated single and multilayer thin Fe films. *J. Appl. Phys.*, 64(10):5760–5762, 1988.

[26] C. Wilts and S. Lai. Spin wave measurements of exchange constant in Ni-Fe alloy films. *IEEE Transactions on Magnetics*, 8(3):280–281, 1972.

[27] A. Michels, J. WeissmÜller, A. Wiedenmann, J.S. Pedersen, and J.G. Barker. Measuring the exchange-stiffness constant of nanocrystalline solids by elastic small-angle neutron scattering. *Philos. Mag. Lett.*, 80(12):785–792, 2000.

[28] R. Moreno, R. F. L. Evans, S. Khmelevskyi, M. C. Muñoz, R. W. Chantrell, and O. Chubykalo-Fesenko. Temperature-dependent exchange stiffness and domain wall width in Co. *Phys. Rev. B*, 94(10):104433, 2016.

[29] J. Li, J. Huang, Y. Qin, and F. Ma. Magnetic and microwave properties of cobalt nanoplatelets. *Materials Science and Engineering: B*, 138(3):199–204, 2007.

[30] P Talagala, Petru S Fodor, D Haddad, R Naik, LE Wenger, PP Vaishnava, and VM Naik. Determination of magnetic exchange stiffness and surface anisotropy constants in epitaxial Ni 1- x Co x (001) films. *Phys. Rev. B*, 66(14):144426, 2002.

[31] R. Schäfer. Magnetic domains. In *Handbook of Magnetism and Magnetic Materials*, pages 391–434. Springer International Publishing, 2021.

[32] A. E. LaBonte. Two-dimensional bloch-type domain walls in ferromagnetic films. *J. Appl. Phys.*, 40(6):2450–2458, 1969.

[33] M. Schabes and A. Aharoni. Magnetostatic interaction fields for a three-dimensional array of ferromagnetic cubes. *IEEE Transactions on Magnetics*, 23(6):3882–3888, 1987.

[34] G. Rowlands. *Magnetising energies and domain structures in ferromagnetics*. PhD thesis, University of Leeds, Leeds, 1956.

[35] D. A. Goode and G. Rowlands. The demagnetizing energies of a uniformly magnetized cylinder with an elliptic cross-section. *J. Magn. Magn. Mater.* , 267:373–385, 2003.

[36] B. Borca, O. Fruchart, E. Kritsikis, F. Cheynis, A. Rousseau, P. David, C. Meyer, and J.C. Toussaint. Tunable magnetic properties of arrays of Fe(110) nanowires grown on kinetically grooved W(110) self-organized templates. *J. Magn. Magn. Mater.* , 322(2):257, 2010.

[37] G. Rowlands. On the calculation of acoustic radiation impedance of polygonal-shaped apertures. *J. Acoust. Soc. Am.* , 92(5):2961–2963, 1992.

[38] M. Beleggia and M. De Graef. On the computation of the demagnetization tensor field for an arbitrary particle shape using a fourier space approach. *J. Magn. Magn. Mater.* , 263:L1–9, 2003.

[39] M. Beleggia, M. De Graef, and Y. T. Millev. Magnetostatics of the uniformly polarized torus. *Proc. Roy. Soc. Lond. A* , 465:3581, 2009.

[40] A. Hubert and W. Rave. Systematic analysis of micromagnetic switching processes. *Phys. Stat. Sol. (b)* , 211(2):S815–829, 1999.

[41] F. Bloch. Zur theorie des austauschproblems und der remanenzerscheinung der ferromagnetika. In *Zur Theorie des Austauschproblems und der Remanenzerscheinung der Ferromagnetika*, pages 295–335. Springer Berlin Heidelberg, 1932.

[42] L. Landau and E. Lifshitz. On the theory of the dispersion of magnetic permeability in ferromagnetic bodies. In *Perspectives in Theoretical Physics*, pages 51–65. Elsevier, 1992.

[43] Louis Néel. Energie des parois de bloch dans les couches minces. *Cr Hebd Acad Sci*, 241(6):533–537, 1955.

[44] K. Ramstöck, W. Hartung, and A. Hubert. The phase diagram of domain walls in narrow magnetic strips. *Phys. Stat. Sol. (a)* , 155:505, 1996.

[45] H. J. Williams and R. C. Sherwood. Magnetic domain patterns on thin films. *J. Appl. Phys.*, 28(5):548–555, 1957.

[46] M. J. Freiser. On the zigzag form of charged domain walls. *IBM Journal of Research and Development*, 23(3):330–338, 1979.

[47] A. Wachowiak, J. Wiebe, M. Bode, O. Pietzsch, M. Morgenstern, and R. Wiesendanger. Direct observation of internal spin structure of magnetic vortex cores. *Science*, 298(5593):577–580, 2002.

[48] J. Miltat and A. Thiaville. Vortex cores–smaller than small. *Science*, 298(5593):555–555, 2002.

[49] R. Hertel and C. Andreas. *Magnetic Nano- and Microwires*, chapter Multiscale simulation of Bloch point dynamics in thick nanowires, page 653. Woodhead, 2015.

[50] A. S. Arrott, B. Heinrich, and A. Aharoni. Point singularities and magnetization reversal in ideally soft ferromagnetic cylinders. *IEEE Trans. Magn.* , 15:1228, 1979.

[51] A. Drews. *Dynamics of magnetic vortices and antivortices*. PhD thesis, Staats-und Universitätsbibliothek Hamburg Carl von Ossietzky, 2009.

[52] L. Landau and E. M. Lifschitz. On the theory of the dispertion of magnetic permeability in ferromagnetic bodies. *Phys. Z. Sowjetunion* , 8:153–159, 1935.

[53] T. L Gilbert. A lagrangian formulation of the gyromagnetic equation of the magnetization field. *Phys. Rev.*, 100:1243, 1955.

[54] T. L Gilbert. A phenomenological theory of damping in ferromagnetic materials. *IEEE transactions on magnetics*, 40(6):3443–3449, 2004.

[55] S. M. Bhagat and P. Lubitz. Temperature variation of ferromagnetic relaxation in the 3d transition metals. *Phys. Rev. B*, 10(1):179–185, 1974.

[56] M. A. W. Schoen, D. Thonig, M. L. Schneider, T. J. Silva, H. T. Nembach, O. Eriksson, O. Karis, and J. M. Shaw. Ultra-low magnetic damping of a metallic ferromagnet. *Nat. Phys.*, 12(9):839–842, 2016.

[57] C. H. Back, R. Allenspach, W. Weber, S. S. P. Parkin, D. Weller, E. L. Garwin, and H. C. Siegmann. Minimum field strength in precessional magnetization reversal. *Science*, 285:864–867, 1999.

[58] N. L. Schryer and L. R. Walker. The motion of 180° domain walls in uniform dc magnetic fields. *J. Appl. Phys.* , 45(12):5406–5421, 1974.

[59] M. D. Stiles and J. Miltat. *Magnetization dynamics in confined magnetic structures*, chapter Spin transfer torque and dynamics. Springer, 2006.

[60] D.C. Ralph and M.D. Stiles. Spin transfer torques. *J. Magn. Magn. Mater.* , 320(7):1190–1216, 2008.

[61] J. C. Slonczewski. Current-driven excitation of magnetic multilayers. *J. Magn. Magn. Mater.* , 159:L1–L7, 1996.

[62] A. Thiaville and Y. Nakatani. *Nanomagnetism and Spintronics*, chapter Micromagnetic simulation of domain wall dynamics in nanostrips, pages 231–276. Elsevier, 2009.

[63] A. Thiaville, Y. Nakatani, J. Miltat, and Y. Suzuki. Micromagnetic understanding of current-driven domain wall motion in patterned nanowires. *Europhys. Lett.* , 69(6):990–996, 2005.

[64] G.S.D. Beach, M. Tsoi, and J.L. Erskine. Current-induced domain wall motion. *J. Magn. Magn. Mater.* , 320(7):1272–1281, 2008.

[65] G. S D. Beach, C. Knutson, M. Tsoi, and J. L. Erskine. Field- and current-driven domain wall dynamics: An experimental picture. *J. Magn. Magn. Mater.* , 310:2038–2040, 2007.

[66] S. Zhang and Z. Li. Roles of nonequilibrium conduction electrons on the magnetization dynamics of ferromagnets. *Phys. Rev. Lett.* , 93(12):127204, 2004.

[67] E. Martinez, G. Finocchio, L. Torres, and L. Lopez-Diaz. The influence of the spin-orbit torques on the current-driven domain wall motion. *AIP Advances*, 3(7):072109, 2013.

[68] E. Martinez, S. Emori, and G. S. D. Beach. Current-driven domain wall motion along high perpendicular anisotropy multilayers: The role of the rashba field, the spin hall effect, and the dzyaloshinskii-moriya interaction. *Appl. Phys. Lett.*, 103(7):072406, 2013.

[69] A. Thiaville, S. Rohart, E. Jué, V. Cros, and A. Fert. Dynamics of Dzyaloshinskii domain walls in ultrathin magnetic films. *Europhys. Lett.* , 100:57002, 2012.

[70] O. Boulle, S. Rohart, L. D. Buda-Prejbeanu, E. Jué, I. M. Miron, S. Pizzini, J. Vogel, G. Gaudin, and A. Thiaville. Domain wall tilting in the presence of the dzyaloshinskii-moriya interaction in out-of-plane magnetized magnetic nanotracks. *Phys. Rev. Lett.*, 111(21):217203, 2013.

[71] J. A. Katine, F. J. Albert, R. A. Buhrman, E. B. Myers, and D. C. Ralph. Current-driven magnetization reversal and spin-wave excitations in co/cu/co pillars. *Phys. Rev. Lett.* , 84(14):3149, 2000.

[72] A. Thiaville and Y. Nakatani. *Spin dynamics in confined magnetic structures III*, volume 101 of *Topics Appl. Physics*, chapter Domain-wall dynamics in nanowires and nanostrips, pages 161–205. Springer, Berlin, 2006.

[73] R. McMichael and M. Donahue. Head to head domain wall structures in thin magnetic strips. *IEEE Trans. Magn.* , 33:4167, 1997.

[74] A. Thiaville, Y. Nakatani, F. Piéchon, J. Miltat, and T. Ono. Transient domain wall displacement under spin-polarized current pulses. *Eur. Phys. J. B* , 60:15–27, 2007.

[75] Z. Li and S. Zhang. Domain-wall dynamics and spin-wave excitations with spin-transfer torques. *Phys. Rev. Lett.*, 92(20):207203, 2004.

[76] Z. Li and S. Zhang. Domain-wall dynamics driven by adiabatic spin-transfer torques. *Phys. Rev. B*, 70(2):024417, 2004.

[77] A. Thiaville, Y. Nakatani, J. Miltat, and N. Vernier. Domain wall motion by spin-polarized current: a micromagnetic study. *J. Appl. Phys.* , 95(11):7049–7051, 2004.

[78] G. Meier, M. Bolte, R. Eiselt, B. KrÃ¼ger, D. -H. Kim, and P. Fischer. Direct imaging of stochastic domain-wall motion driven by nanosecond current pulses. *Phys. Rev. Lett.* , 98(18):187202, 2007.

[79] M. Hayashi, L. Thomas, C. Rettner, R. Moriya, Y. B. Bazaliy, and S. S. P. Parkin. Current driven domain wall velocities exceeding the spin angular momentum transfer rate in permalloy nanowires. *Phys. Rev. Lett.* , 98(3):037204, 2007.

[80] J. -Y. Lee, K. S. Lee, S. Choi, K. Y. Guslienko, and S. K. Kim. Dynamic transformations of the internal structure of a moving domain wall in magnetic nanostripes. *Phys. Rev. B* , 76(18):184408, 2007.

[81] R. L Stamps, S. Breitkreutz, J. Åkerman, A. V Chumak, Y. Otani, G. E W Bauer, J. -U. Thiele, M. Bowen, S. A. Majetich, M. Kläui, I. L. Prejbeanu, B. Dieny, N. M. Dempsey, and B. Hillebrands. The 2014 magnetism roadmap. *J. Phys. D: Appl. Phys.*, 47(33):333001, 2014.

[82] S. Villain-Guillot, R. Dandoloff, and A. Saxena. Heisenberg spins on an infinite cylinder: a geometrical effect of anisotropy. *Phys. Lett. A*, 188(4-6):343–346, 1994.

[83] R. Dandoloff, S. Villain-Guillot, A. Saxena, and A. R. Bishop. Violation of self-duality for topological solitons due to soliton-soliton interaction on a cylindrical geometry. *Phys. Rev. Lett.*, 74(5):813–815, 1995.

[84] R. Streubel, P. Fischer, F. Kronast, V. P Kravchuk, D. D Sheka, Y. Gaididei, O. G Schmidt, and D. Makarov. Magnetism in curved geometries. *J. Phys. D: Appl. Phys.*, 49(36):363001, 2016.

[85] R. Streubel, L. Han, F. Kronast, A A. Unal, O G. Schmidt, and D. Makarov. Imaging of buried 3d magnetic rolled-up nanomembranes. *Nano Lett.* , 14(7):3981–3986, 2014.

[86] R. Streubel, J. Lee, D. Makarov, M. -Y Im, D. Karnaushenko, L. Han, R. Schäfer, P. Fischer, S. -K. Kim, and O G. Schmidt. Magnetic microstructure of rolled-up single-layer ferromagnetic nanomembranes. *Adv. Mater.* , 26:316, 2014.

[87] Y. Gaididei, V P. Kravchuk, and D. D. Sheka. Curvature effects in thin magnetic shells. *Phys. Rev. Lett.* , 112(25), 2014.

[88] D. D Sheka, V. P Kravchuk, and Y. Gaididei. Curvature effects in statics and dynamics of low dimensional magnets. *J. Phys. A: Math. Theor.*, 48(12):125202, 2015.

[89] A. Fernández-Pacheco, R.Streubel, O. Fruchart, R. Hertel, P. Fischer, and R. P. Cowburn. Three-dimensional nanomagnetism. *Nat Commun*, 8(1), 2017.

[90] D. Makarov and D D. Sheka, editors. *Curvilinear Micromagnetism*. Springer International Publishing, 2022.

[91] R. Hertel. Curvature-induced magnetochirality. *SPIN*, 03(03):1340009, 2013.

[92] D. A. Allwood, G. Xiong, M. D. Cooke, C. C.Faulkner, D. Atkinson, N. Vernier, and R. P. Cowburn. Submicrometer ferromagnetic not gate and shift register. *Science* , 296:2003–2006, 2002.

[93] S. S. P. Parkin. U.s. patents 6834005, 6898132, 6920062, 2004.

[94] Stuart S. P. Parkin, Masamitsu Hayashi, and Luc Thomas. Magnetic domain-wall racetrack memory. *Science* , 320:190, 2008.

[95] M. Hayashi, L. Thomas, Ch. Rettner, R. Moriya, and S. S. P. Parkin. Direct observation of the coherent precession of magnetic domain walls propagating along permalloy nanowires. *Nat. Phys.* , 3(1):21, 2007.

[96] G A. Ozin. Nanochemistry: Synthesis in diminishing dimensions. *Adv. Mater.*, 4(10):612–649, 1992.

[97] C R. Martin. Nanomaterials: A membrane-based synthetic approach. *Science*, 266(5193):1961–1966, 1994.

[98] S. Anantharaj, H. Sugime, S. Yamaoka, and S. Noda. Pushing the limits of rapid anodic growth of CuO/Cu (OH) 2 nanoneedles on cu for the methanol oxidation reaction: anodization pH is the game changer. *ACS Appl. Energy Mater.*, 4(1):899–912, 2021.

[99] J. C. Hulteen and C. R. Martin. A general template-based method for the preparation of nanomaterials. *J Mater Chem*, 7(7):1075–1087, 1997.

[100] A. Fert and J. L. Piraux. Magnetic nanowires. *J. Magn. Magn. Mater.* , 200:338–358, 1999.

[101] K. D Sattler, editor. *Handbook of nanophysics: nanotubes and nanowires*. CRC press, 2010.

[102] Y. P Ivanov, M Vázquez, and O Chubykalo-Fesenko. Magnetic reversal modes in cylindrical nanowires. *J. Phys. D: Appl. Phys.* , 46(48):485001, 2013.

[103] M. Vazquez, editor. *Magnetic Nano- and Microwires*, volume 80 of *Woodhead Publishing Series in Electronic and Optical Materials*. Woodhead publishing, Cambridge, 2015.

[104] M. Staňo and O. Fruchart. *Handbook of Magnetic Materials*, volume 27, chapter Magnetic nanowires and nanotubes. Elsevier, 2018.

[105] L. Piraux. Magnetic nanowires. *Applied Sciences*, 10(5):1832, 2020.

[106] L. Skoric, D. Sanz-Hernández, F. Meng, C. Donnelly, S. Merino-Aceituno, and A. Fernández-Pacheco. Layer-by-layer growth of complex-shaped three-dimensional nanostructures with focused electron beams. *Nano Lett.*, 20(1):184–191, 2019.

[107] L. Skoric, C. Donnelly, A. Hierro-Rodriguez, M. A. Cascales Sandoval, S. Ruiz-Gómez, M. Foerster, M. A. Niño, R. Belkhou, C. Abert, D. Suess, and A. Fernández-Pacheco. Domain wall automotion in three-dimensional magnetic helical interconnectors. *ACS Nano*, 16(6):8860–8868, 2022.

[108] H. Masuda and H. Fukuda. Ordered metal nanohole arrays made by a two-step replication of honeycomb structures of anodic alumina. *Science* , 268:1466–1468, 1995.

[109] C. T. Sousa, D. C. Leitao, M. P. Proenca, J. Ventura, A. M. Pereira, and J. P. Araujo. Nanoporous alumina as templates for multifunctional applications. *Appl. Phys. Rev.*, 1(3):031102, 2014.

[110] Dusan Losic, Mickael Lillo, and Dusan Losic Jr. Porous alumina with shaped pore geometries and complex pore architectures fabricated by cyclic anodization. *-journal*, 5(12):1392, 2009.

[111] P Yu Apel and S N Dmitriev. Micro- and nanoporous materials produced using accelerated heavy ion beams. *Adv. Nat. Sci.: Nanosci. Nanotechnol.*, 2(1):013002, 2011.

[112] M. Paunovic, M. Schlesinger, and D. D Snyder. Fundamental considerations. *Modern Electroplating*, 5, 2010.

[113] H. Zeng, R. Skomski, L. Menon, Y. Liu, S. Bandyopadhyay, and D. J. Sellmyer. Structure and magnetic properties of ferromagnetic nanowires in self-assembled arrays. *Phys. Rev. B* , 65:134426, 2002.

[114] T. Thurn-Albrecht, J. Schotter, G. A. Kästle, N. Emley, T. Shibauchi, L. Krusin-Elbaum, K. Guarini, C. T. Black, M. T. Tuominen, and T. P. Russell. Ultrahigh-density nanowire arrays grown in self-assembled diblock copolymer templates. *Science*, 290(5499):2126–2129, 2000.

[115] T. Wang, Y. Wang, Y. Fu, T. Hasegawa, H. Oshima, K. Itoh, K. Nishio, H. Masuda, F. S. Li, H. Saito, and S. Ishio. Magnetic behavior in an ordered Co nanorod array. *Nanotechnology* , 19:455703, 2008.

[116] J. Xu and K. Wang. Pulsed electrodeposition of monocrystalline ni nanowire array and its magnetic properties. *Appl. Surf. Sci.*, 254(20):6623–6627, 2008.

[117] K. Pitzschel, J. Bachmann, S. Martens, J. M. Montero-Moreno, J. Kimling, G. Meier, J. Escrig, K. Nielsch, and D. Görlitz. Magnetic reversal of cylindrical nickel nanowires with modulated diameters. *J. Appl. Phys.* , 109:033907, 2011.

[118] A.S. Samardak, F. Nasirpouri, M. Nadi, E.V. Sukovatitsina, A.V. Ognev, L.A. Chebotkevich, and S.V. Komogortsev. Conversion of magnetic anisotropy in electrodeposited Co-Ni alloy nanowires. *J. Magn. Magn. Mater.* , 383:94–99, 2015.

[119] M. S. Salem, P. Sergelius, R. Zierold, J. M. Montero Moreno, D. Görlitz, and K. Nielsch. Magnetic characterization of nickel-rich nife nanowires grown by pulsed electrodeposition. *J Mater Chem*, 22(17):8549–8557, 2012.

[120] Z. Chen, Q. Zhan, D. Xue, F. Li, X. Zhou, H. Kunkel, and G. Williams. Mössbauer study of Fe-Co nanowires. *J. Phys.: Condens. Matter*, 14(3):613–620, 2002.

[121] B. Ozkale, N. Shamsudhin, G. Chatzipirpiridis, M. Hoop, F. Gramm, X. Chen, X. Marti, J. Sort, E. Pellicer, and S. Pane. Multisegmented FeCo/Cu nanowires: electrosynthesis, characterization, and magnetic control of biomolecule desorption. *ACS applied materials & interfaces*, 7(13):7389–7396, 2015.

[122] F.E. Atalay, H. Kaya, V. Yagmur, S. Tari, S. Atalay, and D. Avsar. The effect of back electrode on the formation of electrodeposited CoNiFe magnetic nanotubes and nanowires. *Appl. Surf. Sci.*, 256(8):2414–2418, 2010.

[123] N. Yasui, A. Imada, and T. Den. Electrodeposition of 001 oriented CoPt L10 columns into anodic alumina films. *Appl. Phys. Lett.*, 83(16):3347–3349, 2003.

[124] Y Dahmane, L Cagnon, J Voiron, S Pairis, M Bacia, L Ortega, N Benbrahim, and A Kadri. Magnetic and structural properties of electrodeposited CoPt and FePt nanowires in nanoporous alumina templates. *J. Phys. D: Appl. Phys.*, 39(21):4523–4528, 2006.

[125] M. S. Salem, P. Sergelius, R. M. Corona, J. Escrig, D. Görlitz, and K. Nielsch. Magnetic properties of cylindrical diameter modulated Ni80Fe20 nanowires: interaction and coercive fields. *Nanoscale* , 2013.

[126] M. S. Salem, F. Tejo, R. Zierold, P. Sergelius, J. M. Montero Moreno, D. Görlitz, K. Nielsch, and J. Escrig. Composition and diameter modulation of magnetic nanowire arrays fabricated by a novel approach. *Nanotechnology* , 29:065602, 2018.

[127] C. Bran, E. Berganza, E. M. Palmero, J. A. Fernandez-Roldan, R. P. Del Real, L. Aballe, M. Foerster, A. Asenjo, A. Fraile Rodríguez, and M. Vazquez. Spin configuration of cylindrical bamboo-like magnetic nanowires. *J. Mater. Chem. C* , 4(5):978–984, 2016.

[128] C. Bran, J. A. Fernandez-Roldan, R. P. del Real, A. Asenjo, O. Chubykalo-Fesenko, and M. Vazquez. Magnetic configurations in modulated cylindrical nanowires. *Nanomaterials*, 11(3):600, 2021.

[129] J. A. Fernandez-Roldan, R. P. del Real, C. Bran, M. Vazquez, and Oksana Chubykalo-Fesenko. Magnetization pinning in modulated nanowires: from topological protection to the "corkscrew" mechanism. *Nanoscale* , 10:5923, 2018.

[130] L. A. Rodríguez, C. Bran, D. Reyes, E. Berganza, M. Vázquez, C. Gatel, E. Snoeck, and A. Asenjo. Quantitative nanoscale magnetic study of isolated diameter-modulated FeCoCu nanowires. *ACS Nano*, 10(10):9669–9678, 2016.

[131] A. De Riz, B. Trapp, J.A. Fernandez-Roldan, Ch. Thirion, J.-Ch. Toussaint, O. Fruchart, and D. Gusakova. Domain wall pinning in a circular cross-section wire with modulated diameter. In *Magnetic Nano- and Microwires*, pages 427–453. Elsevier, 2020.

[132] F. Nasirpouri, S.-M. Peighambari-Sattari, C. Bran, E. M. Palmero, E. Berganza Eguiarte, M. Vazquez, A. Patsopoulos, and D. Kechrakos. Geometrically designed domain wall trap in tri-segmented nickel magnetic nanowires for spintronics devices. *Sci. Rep.* , 9:1–11, 2019.

[133] S. Allende, D. Altbir, and K. Nielsch. Magnetic cylindrical nanowires with single modulated diameter. *Phys. Rev. B* , 80(17):174402, 2009.

[134] Voicu O. Dolocan. Domain wall pinning and interaction in rough cylindrical nanowires. *Appl. Phys. Lett.* , 105(16):162401, 2014.

[135] S. Bochmann, D. Döhler, B. Trapp, M. Staňo, A. Wartelle, O. Fruchart, and J. Bachmann. Preparation and physical properties of soft magnetic nickel-cobalt nanowires with modulated diameters. *J. Appl. Phys.* , 124(16):163907, 2018.

[136] E. Berganza, C. Bran, M. Vazquez, and A. Asenjo. Domain wall pinning in FeCoCu bamboo-like nanowires. *Sci. Rep.* , 6:29702, 2016.

[137] M. Méndez, S. González, V. Vega, J. Teixeira, B. Hernando, C. Luna, and V. Prida. Ni-Co alloy and multisegmented Ni/Co nanowire arrays modulated in composition: Structural characterization and magnetic properties. *Crystals*, 7(3):66, 2017.

[138] Y. P. Ivanov, A. Chuvilin, S. Lopatin, and J. Kosel. Modulated magnetic nanowires for controlling domain wall motion: Toward 3D magnetic memories. *Am. Chem. Soc. Nano* , 10(5):5326, 2016.

[139] S. Bochmann, A. Fernandez-Pacheco, M. Mačkovič, A. Neff, K. R. Siefermann, E. Spiecker, R. P. Cowburn, and J. Bachmann. Systematic tuning of segmented magnetic nanowires into three-dimensional arrays of 'bits'. *RCS Adv.* , 7:37627, 2017.

[140] M. Chen, C.-L. Chien, and P. C. Searson. Potential modulated multilayer deposition of multisegment Cu/Ni nanowires with tunable magnetic properties. *Chem. Mater.* , 18(6):1595–1601, 2006.

[141] S. Ruiz-Gómez, M. Foerster, L. Aballe, M. P. Proenca, I. Lucas, J. L. Prieto, A. Mascaraque, J. de la Figuera, A. Quesada, and L. Pérez. Observation of a topologically protected state in a magnetic domain wall stabilized by a ferromagnetic chemical barrier. *Sci. Rep.* , 8(1):16695, 2018.

[142] L. Álvaro-Gómez, S. Ruiz-Gómez, C. Fernández-González, M. Schöbitz, N. Mille, J. Hurst, D. Tiwari, A. De Riz, I. M. Andersen, J. Bachmann, L. Cagnon, M. Foerster, L. Aballe, R. Belkhou, J.-C. Toussaint, C. Thirion, A. Masseboeuf, D. Gusakova, L. Pérez, and O. Fruchart. Micromagnetics of magnetic chemical modulations in soft-magnetic cylindrical nanowires. *Phys. Rev. B*, 106(5):054433, 2022.

[143] F. Beron, L.-P. Carignan, D. Menard, and A. Yelon. Magnetic behavior of Ni/Cu multilayer nanowire arrays studied by first-order reversal curve diagrams. *IEEE Transactions on Magnetics*, 44(11):2745–2748, 2008.

[144] M Susano, M P Proenca, S Moraes, C T Sousa, and J P Araújo. Tuning the magnetic properties of multisegmented Ni/Cu electrodeposited nanowires with controllable ni lengths. *Nanotechnology*, 27(33):335301, 2016.

[145] S. Moraes, D. Navas, F. Béron, M. Proenca, K. Pirota, C. Sousa, and J. Araújo. The role of cu length on the magnetic behaviour of Fe/Cu multi-segmented nanowires. *Nanomaterials*, 8(7):490, 2018.

[146] E. M Palmero, C. Bran, R. P del Real, and M. Vázquez. Synthesis and magnetism of modulated FeCo-based nanowires. *J. Phys.: Conf. Ser.*, 755:012001, 2016.

[147] A. J. Grutter, K. L. Krycka, E. V. Tartakovskaya, J. A. Borchers, K. S. M. Reddy, E. Ortega, A. Ponce, and B. J. H. Stadler. Complex three-dimensional magnetic ordering in segmented nanowire arrays. *ACS Nano*, 11(8):8311–8319, 2017.

[148] C Bran, Y. P Ivanov, J Kosel, O Chubykalo-Fesenko, and M Vazquez. Co/Au multisegmented nanowires: a 3d array of magnetostatically coupled nanopillars. *Nanotechnology* , 28(9):095709, 2017.

[149] J. García, V. M. Prida, L. G. Vivas, B. Hernando, E. D. Barriga-Castro, R. Mendoza-Reséndez, C. Luna, J. Escrig, and M. Vázquez. Magnetization reversal dependence on effective magnetic anisotropy in electroplated Co–Cu nanowire arrays. *J. Mater. Chem. C* , 3(18):4688–4697, 2015.

[150] D. Reyes, N. Biziere, B. Warot-Fonrose, T. Wade, and C. Gatel. Magnetic configurations in Co/Cu multilayered nanowires: Evidence of structural and magnetic interplay. *Nano Lett.* , 16(2):1230–1236, 2016.

[151] A. Tekgül, H. Kockar, H. Kuru, and M. Alper. Electrochemical deposition of CoCu/cu multilayers: Structural and magnetic properties as a function of non-magnetic layer thickness. *Zeitschrift für Naturforschung A*, 73(2):127–133, 2018.

[152] S. Valizadeh, J.M. George, P. Leisner, and L. Hultman. Electrochemical synthesis of Ag/Co multilayered nanowires in porous polycarbonate membranes. *Thin Solid Films*, 402(1-2):262–271, 2002.

[153] C.H. Peng, T.-Y. Wu, and C.-C. Hwang. A preliminary study on the synthesis and characterization of multilayered Ag/Co magnetic nanowires fabricated via the electrodeposition method. *The Scientific World Journal*, 2013:1–5, 2013.

[154] S. Lucatero, W. H. Fowle, and E. J. Podlaha. Electrodeposited au/FeAu nanowires with controlled porosity. *Electrochem. Solid-State Lett.*, 12(12):D96, 2009.

[155] N U Saidin, K Y Kok, I K Ng, and S H Ilias. Fabrication of Au/Ni multilayered nanowires by electrochemical deposition. *J. Phys.: Conf. Ser.*, 431:012006, 2013.

[156] J. rak Choi, S. J. Oh, H. Ju, and J. Cheon. Massive fabrication of free-standing one-dimensional Co/Pt nanostructures and modulation of ferromagnetism via a programmable barcode layer effect. *Nano Lett.*, 5(11):2179–2183, 2005.

[157] Y.-Kun Su, D.-H. Qin, H.-Li. Zhang, H. Li, and H.-L. Li. Microstructure and magnetic properties of bamboo-like CoPt/pt multilayered nanowire arrays. *Chem. Phys. Lett.*, 388(4-6):406–410, 2004.

[158] K. Nielsch, R. Hertel, R. B. Wehrspohn, J. Barthel, J. Kirschner, U. Gösele, S. F. Fischer, and H. Kronmüller. Switching behavior of single nanowires inside dense nickel nanowire arrays. *IEEE Trans. Magn.* , 38(5):2571, 2002.

[159] H. Forster, T. Schrefl, D. Suess, W. Scholz, V. Tsiantos, R. Dittrich, and J. Fidler. Domain wall motion in nanowires using moving grids. *J. Appl. Phys.* , 91(10):6914, 2002.

[160] H. Forster, T. Schrefl, W. Scholz, D. Suess, V. Tsiantos, and J. Fidler. Micromagnetic simulation of domain wall motion in magnetic nano-wires. *J. Magn. Magn. Mater.* , 249:181, 2002.

[161] S. Jamet, N. Rougemaille, J. C. Toussaint, and O. Fruchart. *Magnetic Nano- and Microwires: Design, synthesis, properties and applications*, chapter Head-to-head domain walls in one-dimensional nanostructures: an extended phase diagram ranging from strips to cylindrical wires, pages 783–811. Woodhead, 2015.

[162] R. Hertel. Computational micromagnetism of magnetization processes in nickel nanowires. *J. Magn. Magn. Mater.* , 249:251, 2002.

[163] R. Feldtkeller. Mikromagnetisch stetige und unstetige magnetisirungsverteilungen. *Z. Angew. Physik* , 19:530, 1965.

[164] A. Thiaville, J. M. Garcìa, R. Dittrich, J. Miltat, and T. Schrefl. Micromagnetic study of Bloch-point-mediated vortex core reversal. *Phys. Rev. B* , 67:094410, 2003.

[165] R. Hertel and J. Kirschner. Magnetization reversal dynamics in nickel nanowires. *Physica B* , 343:206, 2004.

[166] A. Mougin, M. Cormier andJ.P. Adam, P.J. Metaxas, and J. Ferré. Domain wall mobility, stability and walker breakdown in magnetic nanowires. *Europhys. Lett.* , 78:57007, 2007.

[167] M. Yan, A. Kákay, S. Gliga, and R. Hertel. Beating the Walker limit with massless domain walls in cylindrical nanowires. *Phys. Rev. Lett.* , 104(5):057201, 2010.

[168] R. Wieser, E. Y. Vedmedenko, P. Weinberger, and R. Wiesendanger. Current-driven domain wall motion in cylindrical nanowires. *Phys. Rev. B* , 82:144430, 2010.

[169] N. Biziere, C. Gatel, R. Lassalle-Balier, M. C. Clochard, J. E. Wegrowe, and E. Snoeck. Imaging the fine structure of a magnetic domain wall in a Ni nanocylinder. *Nano Lett.* , 13:2053, 2013.

[170] S. Da Col, S. Jamet, N. Rougemaille, A. Locatelli, T. O. Menteş, B. Santos Burgos, R. Afid, M. Darques, L. Cagnon, J. C. Toussaint, and O. Fruchart. Observation of bloch-point domain walls in cylindrical magnetic nanowires. *Phys. Rev. B* , 89:180405, 2014.

[171] R. Hertel. Ultrafast domain wall dynamics in magnetic nanotubes and nanowires. *J. Phys.: Condens. Matter* , 28(48):483002, 2016.

[172] M. Yan, C. Andreas, A. Kakay, F. Garcia-Sanchez, and R. Hertel. Fast domain wall dynamics in magnetic nanotubes: Suppression of Walker breakdown and Cherenkov-like spin wave emission. *Appl. Phys. Lett.* , 99(12):122505, 2011.

[173] D. Bouzidi and H. Suhl. Motion of a bloch domain wall. *Phys. Rev. Lett.*, 65(20):2587–2590, 1990.

[174] C. Andreas, A. Kákay, and R. Hertel. Multiscale and multimodel simulation of bloch-point dynamics. *Phys. Rev. B* , 89(13):134403, 2014.

[175] R. Hertel and J.Kirschner. Magnetic drops in a soft-magnetic cylinder. *J. Magn. Magn. Mater.* , 278:L291, 2004.

[176] W. Döring. Point singularities in micromagnetism. *J. Appl. Phys.* , 39(2):1006, 1968.

[177] A. P. Malozemoff and J. C. Slonczewski. *Magnetic domain walls in bubble materials*. Academic press, 1979.

[178] M. Yan, A. Kákay, C. Andreas, and R. Hertel. Spin-cherenkov effect and magnonic mach cones. *Phys. Rev. B* , 88(22):1–5, 2013.

[179] R. Hertel, W. Wulfhekel, and J. Kirschner. Domain-wall induced phase shifts in spin waves. *Phys. Rev. Lett.* , 93:257202, 2004.

[180] A. Wartelle, B. Trapp, M. Staňo, C. Thirion, S. Bochmann, J. Bachmann, M. Foerster, L. Aballe, T. O. Menteş, A. Locatelli, A. Sala, L. Cagnon, J.C. Toussaint, and O. Fruchart. Bloch-point-mediated topological transformations of magnetic domain walls in cylindrical nanowires. *Phys. Rev. B* , 99:024433, 2019. arXiv:1806.10918.

[181] M. Schöbitz, A. De Riz, S. Martin, S. Bochmann, C. Thirion, J. Vogel, M. Foerster, L. Aballe, T. O. Menteş, A. Locatelli, F. Genuzio, S. Le Denmat, L. Cagnon, J.C. Toussaint, D. Gusakova, J. Bachmann, and O. Fruchart. Fast domain walls governed by topology and œsted fields in cylindrical magnetic nanowires. *Phys. Rev. Lett.* , 123(21):217201, 2019.

[182] S. Da Col, S. Jamet, M. Staňo, B. Trapp, S. Le Denmat, L. Cagnon, J. C. Toussaint, and O. Fruchart. Nucleation, imaging, and motion of magnetic domain walls in cylindrical nanowires. *Appl. Phys. Lett.* , 109(6):062406, 2016.

[183] David Aurelio, A. Giordano, L. Torres, G. Finocchio, and E. Martinez. The role of the Oersted field on the current-driven domain wall dynamics along wires with square cross section. *IEEE Transactions on Magnetics*, 49(7):3211–3214, 2013.

[184] M. Schöbitz, S. Finizio, A. De Riz, J. Hurst, C. Thirion, D. Gusakova, J.-C. Toussaint, J. Bachmann, J. Raabe, and O. Fruchart. Time-resolved imaging of Oersted-field inducxed magnetization dynamics in cylindrical magnetic nanowires. *Appl. Phys. Lett.* , 118(17):172411, 2021.

[185] A. De Riz, J. Hurst, M. Schöbitz, C. Thirion, J. Bachmann, J. C. Toussaint, O. Fruchart, and D. Gusakova. Mechanism of fast domain wall motion via current-assisted bloch-point domain wall stabilization. *Phys. Rev. B* , 103(5):054430, 2021.

[186] H. Masuda and M. Satoh. Fabrication of gold nanodot array using anodic porous alumina as an evaporation mask. *Jpn. J. Appl. Phys.*, 35(Part 2, No. 1B):L126–L129, 1996.

[187] G. E. Thompson, Y. Xu, P. Skeldon, K. Shimizu, S. H. Han, and G. C. Wood. Anodic oxidation of aluminium. *Philos. Mag. B*, 55(6):651–667, 1987.

[188] C. Fernández González. *Electrodeposited magnetic nanostructures: newgeometries and applications*. PhD thesis, Universidad Complutense de Madrid, 2022.

[189] W. Lee and S.-J. Park. Porous anodic aluminum oxide: Anodization and templated synthesis of functional nanostructures. *Chem. Rev.*, 114(15):7487–7556, 2014.

[190] H. Masuda, H. Yamada, M. Satoh, H. Asoh, M. Nakao, and T. Tamamura. Highly ordered nanochannel-array architecture in anodic alumina. *Appl. Phys. Lett.* , 71(19):2770, 1997.

[191] S. Z. Chu, K. Wada, S. Inoue, M. Isogai, Y. Katsuta, and A. Yasumori. Large-scale fabrication of ordered nanoporous alumina films with arbitrary pore intervals by critical-potential anodization. *J Electrochem Soc*, 153(9):B384, 2006.

[192] J. Zhang, J. E. Kielbasa, and D. L. Carroll. Controllable fabrication of porous alumina templates for nanostructures synthesis. *Mater Chem Phys*, 122(1):295–300, 2010.

[193] H. Masuda, H. Asoh, M. W. K. Nishio, M. Nakao, and T. Tamamura. Square and triangular nanohole array architectures in anodic alumina. *Adv. Mater.* , 13(3):189, 2001.

[194] W. Lee, R. Ji, U. Gösele, and K. Nielsch. Fast fabrication of long-range ordered porous alumina membranes by hard anodization. *Nat. Mater.*, 5(9):741–747, 2006.

[195] Y. Li, M. Zheng, L. M., and W. Shen. Fabrication of highly ordered nanoporous alumina films by stable high-field anodization. *Nanotechnology*, 17(20):5101–5105, 2006.

[196] C. Bae, H. Shin, and K. Nielsch. Surface modification and fabrication of 3d nanostructures by atomic layer deposition. *MRS Bulletin*, 36(11):887–897, 2011.

[197] H.C.M. Knoops, S.E. Potts, A.A. Bol, and W.M.M. Kessels. Atomic layer deposition. In *Handbook of Crystal Growth*, pages 1101–1134. Elsevier, 2015.

[198] M. Ritala and M. Leskelä. Atomic layer deposition. In *Handbook of Thin Films*, pages 103–159. Elsevier, 2002.

[199] M. Paunovic, M. Schlesinger, and D. D. Snyder. Fundamental considerations. In *Modern Electroplating*, pages 1–32. John Wiley & Sons, Inc., 2011.

[200] M. Paunovic and M. Schlesinger. *Fundamentals of electrochemical deposition*. john wiley & sons, 2006.

[201] S. Chen. Practical electrochemical cells. In *Handbook of Electrochemistry*, pages 33–56. Elsevier, 2007.

[202] A. J Bard, L. R. Faulkner, et al. Fundamentals and applications. *Electrochemical methods*, 2(482):580–632, 2001.

[203] S. Ruiz-Gómez, C. Fernández-González, and L. Perez. Electrodeposition as a tool for nanostructuring magnetic materials. *Micromachines*, 13(8):1223, 2022.

[204] M. Aliofkhazraei, F. C. Walsh, G. Zangari, H. Köçkar, M. Alper, C. Rizal, L. Magagnin, V. Protsenko, R. Arunachalam, A. Rezvanian, A. Moein, S. Assareh, and M. H. Allahyarzadeh. Development of electrodeposited multilayer coatings: A review of fabrication, microstructure, properties and applications. *Applied Surface Science Advances*, 6:100141, 2021.

[205] W. Schwarzacher and D.S. Lashmore. Giant magnetoresistance in electrodeposited films. *IEEE Transactions on Magnetics*, 32(4):3133–3153, 1996.

[206] I. Bakonyi and L. Péter. Electrodeposited multilayer films with giant magnetoresistance (GMR): Progress and problems. *Prog Mater Sci*, 55(3):107–245, 2010.

[207] L. M. Goldman, C. A. Ross, W. Ohashi, D. Wu, and F. Spaepen. New dual-bath technique for electrodeposition of short repeat length multilayers. *Appl. Phys. Lett.*, 55(21):2182–2184, 1989.

[208] A. Brenner. *Electrodeposition of alloys: principles and practice*. Elsevier, 2013.

[209] Pandey. *Handbook of Semiconductor Electrodeposition*. CRC Press, 2017.

[210] E Budevski, V Bostanov, and G Staikov. Electrocrystallization. *Annu. Rev. Mater. Sci.*, 10(1):85–112, 1980.

[211] A.M. Rashidi and A. Amadeh. The effect of current density on the grain size of electrodeposited nanocrystalline nickel coatings. *Surf. Coat. Technol.*, 202(16):3772–3776, 2008.

[212] Y. Li, H. Jiang, W. Huang, and H. Tian. Effects of peak current density on the mechanical properties of nanocrystalline Ni–Co alloys produced by pulse electrodeposition. *Appl. Surf. Sci.*, 254(21):6865–6869, 2008.

[213] A. Ibañez and E. Fatás. Mechanical and structural properties of electrodeposited copper and their relation with the electrodeposition parameters. *Surf. Coat. Technol.*, 191(1):7–16, 2005.

[214] F Ebrahimi, G.R Bourne, M.S Kelly, and T.E Matthews. Mechanical properties of nanocrystalline nickel produced by electrodeposition. *Acs Sym Ser*, 11(3):343–350, 1999.

[215] S. Riemer, J. Gong, M. Sun, and I. Tabakovic. Influence of solution pH and concentration of saccharin on electrodeposition and properties of 2.4 t CoFe alloys. *J Electrochem Soc*, 156(10):D439, 2009.

[216] F Ebrahimi and Z Ahmed. The effect of current density on properties of electrodeposited nanocrystalline nickel. *J. Appl. Electrochem.*, 33:733–739, 2003.

[217] H. Natter and R. Hempelmann. Nanocrystalline copper by pulsed electrodeposition: the effects of organic additives, bath temperature, and pH. *The Journal of Physical Chemistry*, 100(50):19525–19532, 1996.

[218] A.M. Rashidi and A. Amadeh. The effect of saccharin addition and bath temperature on the grain size of nanocrystalline nickel coatings. *Surf. Coat. Technol.*, 204(3):353–358, 2009.

[219] Sh. Hassani, K. Raeissi, M. Azzi, D. Li, M.A. Golozar, and J.A. Szpunar. Improving the corrosion and tribocorrosion resistance of ni–co nanocrystalline coatings in NaOH solution. *Corros. Sci.*, 51(10):2371–2379, 2009.

[220] Y. Zhu, editor. *Modern Techniques for Characterizing Magnetic Materials*. Springer US, 2005.

[221] M. De Graef. *Magnetic imaging and its applications to materials*. Academic Press, 2000.

[222] A. Tonomura. Applications of electron holography. *Rev. Modern Phys.*, 59(3):639–669, 1987.

[223] A. Tonomura. *Electron Holography*. Springer Berlin Heidelberg, 1999.

[224] H. Lichte. Gottfried m llenstedt and his electron biprism: four decades of challenging and exciting electron physics. *J. Electron Microsc.*, 47(5):387–394, 1998.

[225] J.N. Chapman and M.R. Scheinfein. Transmission electron microscopies of magnetic microstructures. *J. Magn. Magn. Mater.*, 200(1-3):729–740, 1999.

[226] F. Monroy. *Holography: Different Fields of Application*. BoD–Books on Demand, 2011.

[227] P. Eaton and P. West. *Atomic force microscopy*. Oxford university press, 2010.

[228] H. Hopster and H. P. Oepen. *Magnetic microscopy of nanostructures*. Springer Science & Business Media, 2006.

[229] P. Grütter, H. J. Mamin, and D. Rugar. Magnetic force microscopy (MFM). In *Scanning Tunneling Microscopy II*, pages 151–207. Springer Berlin Heidelberg, 1992.

[230] L Belliard, J Miltat, A Thiaville, S Dubois, J.L Duvail, and L Piraux. Observing magnetic nanowires by means of magnetic force microscopy. *J. Magn. Magn. Mater.*, 190(1-2):1–16, 1998.

[231] S. Da Col, S. Jamet, M. Staňo, B. Trapp, S. Le Denmat, L. Cagnon, J. C. Toussaint, and O. Fruchart. Nucleation, imaging, and motion of magnetic domain walls in cylindrical nanowires. *Appl. Phys. Lett.*, 109(6):062406, 2016.

[232] T Wang, Y Wang, Y Fu, T Hasegawa, F S Li, H Saito, and S Ishio. A magnetic force microscopy study of the magnetic reversal of a single Fe nanowire. *Nanotechnology*, 20(10):105707, 2009.

[233] Sandrine da Col. *Parois magnétiques dans les nanofils cylindriques*. Theses, Université de Grenoble, 2014.

[234] Michael Schöbitz. *Current-induced of magnetic Bloch-point domain wall dynamics in cylindrical nanowires*. Theses, Université Grenoble Alpes [2020-....] ; Friedrich-Alexander-Universität Erlangen-Nürnberg, 2021.

[235] J. Als-Nielsen and D. McMorrow. *Elements of modern X-ray physics*. John Wiley & Sons, 2011.

[236] J. Stöhr and H. C. Siegmann. Magnetism. *Solid-State Sciences. Springer, Berlin, Heidelberg*, 5:236, 2006.

[237] P. Fischer. Exploring nanoscale magnetism in advanced materials with polarized x-rays. *Materials Science and Engineering: R: Reports*, 72(5):81–95, 2011.

[238] F Baudelet. X-ray magnetic circular dichroism. *Neutron and X-ray Spectroscopy*, pages 103–130, 2006.

[239] P. Fischer and H. Ohldag. X-rays and magnetism. *Rep. Progr. Phys.*, 78(9):094501, 2015.

[240] J. M.D. Coey. *Magnetism and magnetic materials*. Cambridge university press, 2010.

[241] J. Stöhr, Y. Wu, B. D. Hermsmeier, M. G. Samant, G. R. Harp, S. Koranda, D. Dunham, and B. P. Tonner. Element-specific magnetic microscopy with circularly polarized x-rays. *Science*, 259(5095):658–661, 1993.

[242] L. Aballe, M. Foerster, E. Pellegrin, J. Nicolas, and S. Ferrer. The ALBA spectroscopic LEEM-PEEM experimental station: layout and performance. *J. Synchrotron Radiat.*, 22(3):745–752, 2015.

[243] S. Jamet, S. Da Col, N. Rougemaille, A. Wartelle, A. Locatelli, T. O. Menteş, B. Santos Burgos, R.Afid, L. Cagnon, J. Bachmann, S. Bochmann, O. Fruchart, , and J. C. Toussaint. Quantitative analysis of shadow x-ray magnetic circular dichroism photo-emission electron microscopy. *Phys. Rev. B* , 92:144428, 2015.

[244] X M Cheng and D J Keavney. Studies of nanomagnetism using synchrotron-based x-ray photoemission electron microscopy (x-PEEM). *Rep. Progr. Phys.*, 75(2):026501, 2012.

[245] L. Aballe, M. Foerster, E. Pellegrin, J. Nicolas, and S. Ferrer. The ALBA spectroscopic LEEM-PEEM experimental station: layout and performance. *J. Synchro. Radiat.* , 22:745–752, 2015.

[246] M. Foerster, J. Prat, V. Massana, N. Gonzalez, A. Fontsere, B. Molas, O. Matilla, E. Pellegrin, and L. Aballe. Custom sample environments at the ALBA XPEEM. *Ultramicr.* , 171:63–69, 2016.

[247] J. Kimling, F. Kronast, S. Martens, T. Böhnert, M. Martens, J. Herrero-Albillos, L. Tati-Bismaths, U. Merkt, K. Nielsch, and G. Meier. Photoemission electron microscopy of three-dimensional magnetization configurations in core-shell nanostructures. *Phys. Rev. B*, 84(17):174406, 2011.

[248] P. Fischer. Magnetic imaging with polarized soft x-rays. In *Springer Proceedings in Physics*, pages 155–183. Springer International Publishing, 2013.

[249] V. Franco and B. Dodrill, editors. *Magnetic Measurement Techniques for Materials Characterization*. Springer International Publishing, 2021.

[250] E. Pereiro, J. Nicolás, S. Ferrer, and M. R. Howells. A soft x-ray beamline for transmission x-ray microscopy at ALBA. *J. Synchrotron Radiat.*, 16(4):505–512, 2009.

[251] J. Kirz and H.Rarback. Soft x-ray microscopes. *Rev. Sci. Instrum.*, 56(1):1–13, 1985.

[252] R. Belkhou, S. Stanescu, S. Swaraj, A. Besson, M. Ledoux, M. Hajlaoui, and D. Dalle. Hermes: a soft x-ray beamline dedicated to x-ray microscopy. *J. Synchro. Radiat.* , 22(4):968–979, 2015.

[253] E. Beaurepaire, J.-C. Merle, A. Daunois, and J.-Y. Bigot. Ultrafast spin dynamics in ferromagnetic nickel. *Phys. Rev. Lett.*, 76(22):4250–4253, 1996.

[254] H. Stoll, A. Puzic, B. van Waeyenberge, P. Fischer, J. Raabe, M. Buess, T. Haug, R. Höllinger, C. Back, D. Weiss, and G. Denbeaux. High-resolution imaging of fast magnetization dynamics in magnetic nanostructures. *Appl. Phys. Lett.*, 84(17):3328–3330, 2004.

[255] J. Vogel, W. Kuch, M. Bonfim, J. Camarero, Y. Pennec, F. Offi, K. Fukumoto, J. Kirschner, A. Fontaine, and S. Pizzini. Time-resolved magnetic domain imaging by x-ray photoemission electron microscopy. *Appl. Phys. Lett.*, 82(14):2299–2301, 2003.

[256] M. Bonfim, G. Ghiringhelli, F. Montaigne, S. Pizzini, N. B. Brookes, F. Petroff, J. Vogel, J. Camarero, and A. Fontaine. Element-selective nanosecond magnetization dynamics in magnetic heterostructures. *Phys. Rev. Lett.*, 86(16):3646–3649, 2001.

[257] F.-U. Stein, L. Bocklage, M. Weigand, and G. Meier. Time-resolved imaging of nonlinear magnetic domain-wall dynamics in ferromagnetic nanowires. *Sci. Rep.*, 3(1), 2013.

[258] C. Donnelly, S. Finizio, S. Gliga, M. Holler, A. Hrabec, M. Odstrčil, S. Mayr, V. Scagnoli, L. J. Heyderman, M. Guizar-Sicairos, and J. Raabe. Time-resolved imaging of three-dimensional nanoscale magnetization dynamics. *Nat. Nanotechnology*, 15(5):356–360, 2020.

[259] A. Puzic, T. Korhonen, B. Kalantari, J.Raabe, C. Quitmann, P. Jüllig, L.Bommer, D. Goll, G. Schütz, S. Wintz, T. Strache, M. Körner, D.Markó, C. Bunce, and J. Fassbender. Photon counting system for time-resolved experiments in multibunch mode. *Synchrotron Radiation News*, 23(2):26–32, 2010.

[260] M. Schöbitz, S. Finizio, A. De Riz, J. Hurst, C. Thirion, D. Gusakova, J.-C. Toussaint, J. Bachmann, J. Raabe, and O. Fruchart. Time-resolved imaging of œrsted field induced magnetization dynamics in cylindrical magnetic nanowires. *Appl. Phys. Lett.* , 118(17):172411, 2021.

[261] R. Follath, J. S. Schmidt, M. Weigand, K. Fauth, R. Garrett, I. Gentle, K. Nugent, and S. Wilkins. The x-ray microscopy beamline UE46-PGM2 at BESSY. In *AIP Conference Proceedings*. AIP, 2010.

[262] S. Eisebitt, J. Lüning, W. F. Schlotter, M. Lörgen, O. Hellwig, W. Eberhardt, and J. Stöhr. Lensless imaging of magnetic nanostructures by x-ray spectro-holography. *Nature*, 432(7019):885–888, 2004.

[263] E. Guehrs, A. M Stadler, S. Flewett, S. Frömmel, J. Geilhufe, B. Pfau, T. Rander, S. Schaffert, G. Büldt, and S. Eisebitt. Soft x-ray tomoholography. *New J. Phys.*, 14(1):013022, 2012.

[264] P.Thibault, M. Guizar-Sicairos, and A. Menzel. Coherent imaging at the diffraction limit. *J. Synchrotron Radiat.*, 21(5):1011–1018, 2014.

[265] J.M. Rodenburg. Ptychography and related diffractive imaging methods. In *Advances in Imaging and Electron Physics*, pages 87–184. Elsevier, 2008.

[266] R. Hegerl and W. Hoppe. Dynamische theorie der kristallstrukturanalyse durch elektronenbeugung im inhomogenen primärstrahlwellenfeld. *Berichte der Bunsengesellschaft für physikalische Chemie*, 74(11):1148–1154, 1970.

[267] P. Thibault, Ma. Dierolf, A. Menzel, O. Bunk, C. David, and F. Pfeiffer. High-resolution scanning x-ray diffraction microscopy. *Science*, 321(5887):379–382, 2008.

[268] F. Pfeiffer. X-ray ptychography. *Nat. Photonics*, 12(1):9–17, 2017.

[269] A. Björling, S. Kalbfleisch, M. Kahnt, S. Sala, K. Parfeniukas, U. Vogt, D. Carbone, and U. Johansson. Ptychographic characterization of a coherent nanofocused x-ray beam. *Opt. Express*, 28(4):5069, 2020.

[270] A. M. Maiden and J. M. Rodenburg. An improved ptychographical phase retrieval algorithm for diffractive imaging. *Ultramicroscopy*, 109(10):1256–1262, 2009.

[271] M. Guizar-Sicairos and P. Thibault. Ptychography: A solution to the phase problem. *Phys. Today*, 74(9):42–48, 2021.

[272] K. Desjardins, H.Popescu, P. Mercère, C. Menneglier, R. Gaudemer, K. Thånell, and N. Jaouen. Characterization of a back-illuminated CMOS camera for soft x-ray coherent scattering. In *AIP Conference Proceedings*. Author(s), 2019.

[273] T. Harada, N. Teranishi, T. Watanabe, Q. Zhou, J. Bogaerts, and X. Wang. High-exposure-durability, high-quantum-efficiency (> 90%) backside-illuminated soft-x-ray cmos sensor. *Appl. Phys. Express*, 13(1):016502, 2019.

[274] K. Desjardins, K. Medjoubi, M. Sacchi, H. Popescu, R. Gaudemer, R. Belkhou, S. Stanescu, S. Swaraj, A. Besson, J. Vijayakumar, S. Pautard, A. Noureddine, P. Mercère, P. D. Silva, F. Orsini, C. Menneglier, and N. Jaouen. Backside-illuminated scientific CMOS detector for soft x-ray resonant scattering and ptychography. *J. Synchrotron Radiat.*, 27(6):1577–1589, 2020.

[275] V. Favre-Nicolin, G. Girard, S. Leake, J. Carnis, Y. Chushkin, J. Kieffer, P. Paleo, and M.-I. Richard. PyNX: high-performance computing toolkit for coherent x-ray imaging based on operators. *J. Appl. Cryst.* , 53(5):1404–1413, 2020.

[276] I. Bykova. High-resolution x-ray ptychography for magnetic imaging, 2018.

[277] A. Vansteenkiste, J. Leliaert, M. Dvornik, M. Helsen, F. Garcia-Sanchez, and B. V. Waeyenberge. The design and verification of MuMax3. *AIP Advances*, 4(10):107133, 2014.

[278] http://feellgood.neel.cnrs.fr.

[279] E. Berganza, M. Jaafar, C. Bran, J. A. Fernández-Roldán, O. Chubykalo-Fesenko, M. Vázquez, and A. Asenjo. Multisegmented nanowires: a step towards the control of the domain wall configuration. *Sci. Rep.* , 7(1):11576, 2017.

[280] Y. Rheem, B. Yoo, B. K. Koo, and N. V. Myung. Electrochemical synthesis of compositionally modulated NiFe nanowires. *Phys. Stat. Sol. (a)* , 204(12):4021–4024, 2007.

[281] S. Ruiz-Gómez, C. Fernández-González, E. Martínez, V. Raposo, A. Sorrentino, M. Foerster, L. Aballe, A. Mascaraque, S. Ferrer, and L. Pérez. Helical surface magnetization in nanowires: the role of chirality. *Nanoscale*, 12(34):17880–17885, 2020.

[282] The morphology and mechanism of formation of porous anodic films on aluminium. *Proceedings of the Royal Society of London. A. Mathematical and Physical Sciences*, 317(1531):511–543, 1970.

[283] A. Brenner. *Electrodeposition of alloys: principles and practice*. Elsevier, 2013.

[284] Á. Llavona, L. Pérez, M. C. Sánchez, and V. de Manuel. Enhancement of anomalous codeposition in the synthesis of Fe–Ni alloys in nanopores. *Electrochim. Acta*, 106:392–397, 2013.

[285] N. Zech, E. J. Podlaha, and D. Landolt. Anomalous codeposition of iron group metals: II. mathematical model. *J Electrochem Soc*, 146(8):2892–2900, 1999.

[286] S. Hessami and C. W. Tobias. A mathematical model for anomalous codeposition of nickel-iron on a rotating disk electrode. *J Electrochem Soc*, 136(12):3611–3616, 1989.

[287] D. Gangasingh and J. B. Talbot. Anomalous electrodeposition of nickel-iron. *J Electrochem Soc*, 138(12):3605–3611, 1991.

[288] W. C. Grande and J. B. Talbot. Electrodeposition of thin films of nickel-iron: II . modeling. *J Electrochem Soc*, 140(3):675–681, 1993.

[289] K. Nielsch, F. Müller, A.-P. Li, and U. Gösele. Uniform nickel deposition into ordered alumina pores by pulsed electrodeposition. *Adv. Mater.* , 12(8):582, 2000.

[290] H. Mohammed, E. Vilanova Vidal, Y. P. Ivanov, and J. Kosel. Magnetotransport measurements of domain wall propagation in individual multisegmented cylindrical nanowires. *IEEE Trans. Magn.* , 52(7):1–5, 2016.

[291] C. Bran, E. Berganza, J. A. Fernandez-Roldan, E. M. Palmero, J. Meier, E. Calle, M. Jaafar, M. Foerster, L. Aballe, A. F. Rodriguez, R. P. del Real, A. Asenjo, O. Chubykalo-Fesenko, and M. Vazquez. Magnetization ratchet in cylindrical nanowires. *Am. Chem. Soc. Nano* , 12(6):5932–5939, 2018.

[292] Y. P. Ivanov, Andrey Chuvilin, Sergei Lopatin, Hanan Mohammed, and Jurgen Kosel. Direct observation of current-induced motion of a 3d vortex domain wall in cylindrical nanowires. *ACS Appl. Mater. Interfaces* , 9(20):16741–16744, 2017.

[293] V Vega, T Böhnert, S Martens, M Waleczek, J M Montero-Moreno, D Görlitz, V M Prida, and K Nielsch. Tuning the magnetic anisotropy of Co-Ni nanowires: comparison between single nanowires and nanowire arrays in hard-anodic aluminum oxide membranes. *Nanotechnology* , 23(46):465709, 2012.

[294] Rosa M. Corona, Ali C. Basaran, Juan Escrig, and Dora Altbir. Unusual behavior of the magnetization reversal in soft/hard multisegmented nanowires. *J. Magn. Magn. Mater.* , 438:168–172, 2017.

[295] Bong Gun Kim, Seung Jae Yoon, In Tak Jeon, Ki Ha Kim, Jun Hua Wu, and Young Keun Kim. Dimensional dependence of magnetic properties in arrays of CoFe/Au barcode nanowire. *IEEE Trans. Magn.* , 48(11):3929–3932, 2012.

[296] Rafal E. Dunin-Borkowski, Takeshi Kasama, Alexander Wei, Steven L. Tripp, Martin J. Hÿtch, Etienne Snoeck, Richard J. Harrison, and Andrew Putnis. Off-axis electron holography of magnetic nanowires and chains, rings, and planar arrays of magnetic nanoparticles. *Microsc. Res. Tech.*, 64(5-6):390–402, 2004.

[297] Y. Aharonov and D. Bohm. Significance of electromagnetic potentials in the quantum theory. *Phys. Rev.*, 115(3):485–491, 1959.

[298] E. H. Frei, S. Shtrikman, and D. Treves. Critical size and nucleation field of ideal ferromagnetic particles. *Phys. Rev.* , 106:446, 1957.

[299] H. Zeng, M. Zheng, R. Skomski, D. J. Sellmyer, Y. Liu, L. Menon, and S. Bandyopadhyay. Magnetic properties of self-assembled Co nanowires of varying length and diameter. *J. Appl. Phys.* , 87(9):4718, 2000.

[300] A. S. Arrott, B. Heinrich, T. L. Templeton, and A. Aharoni. Micromagnetics of curling configurations in magnetically soft cylinders. *J. Appl. Phys.* , 50:2387, 1979.

[301] R. Nakajima, J. Stöhr, and Y. U. Idzerda. Electron-yield saturation effects in l-edge x-ray magnetic circular dichroism spectra of fe, co, and ni. *Phys. Rev. B* , 59(9):6421, 1999.

[302] J. A. Seyforth. *Realisation of a Digitally Scanned Laser Light Sheet Fluorescence Microscope (DSLM) with determination of System Resolution*. PhD thesis, King's College London, 2016.

[303] W Rave, K Ramstöck, and A Hubert. Corners and nucleation in micromagnetics. *J. Magn. Magn. Mater.*, 183(3):329–333, 1998.

[304] O. Fruchart, B. Kevorkian, and J. C. Toussaint. Micromagnetic model of noncollective magnetization reversal in ultrathin magnetic dots with in-plane uniaxial anisotropy. *Phys. Rev. B*, 63(17):174418, 2001.

[305] J. Z. Sun. Spin-current interaction with a monodomain magnetic body: A model study. *Phys. Rev. B*, 62(1):570–578, 2000.

[306] D. Bedau, H. Liu, J.-J. Bouzaglou, A. D. Kent, J. Z. Sun, J. A. Katine, E. E. Fullerton, and S. Mangin. Ultrafast spin-transfer switching in spin valve nanopillars with perpendicular anisotropy. *Appl. Phys. Lett.*, 96(2):022514, 2010.

[307] M. Wyss, A. Mehlin, B. Gross, A. Buchter, A. Farhan, M. Buzzi, A. Kleibert, G. Tütüncüoglu, F. Heimbach, A. Fontcuberta i Morral, D. Grundler, and M. Poggio. Imaging magnetic vortex configurations in ferromagnetic nanotubes. *Phys. Rev. B* , 96:024423, 2017.

[308] M Staňo, S Jamet, J C Toussaint, S Bochmann, J Bachmann, A Masseboeuf, C Gatel, and O Fruchart. Probing domain walls in cylindrical magnetic nanowires with electron holography. *J. Phys.: Conf. Ser.*, 903:012055, 2017.

[309] L. Skoric, C. Donnelly, C. Abert, A. Hierro-Rodriguez, D. Suess, and A. Fernández-Pacheco. Micromagnetic modeling of magnetic domain walls in curved cylindrical nanotubes and nanowires. *Appl. Phys. Lett.*, 118(24):242403, 2021.

[310] U. Ebels, A. Radulescu, Y. Henry, L. Piraux, and K. Ounadjela. Spin accumulation and domain wall magnetoresistance in 35 nm Co wires. *Phys. Rev. Lett.* , 84(5):983–986, 2000.

[311] H. B. Braun. Nucleation in ferromagnetic nanowires —- magnetostatics and topology. *J. Appl. Phys.* , 85(8):6172–6174, 1999.

[312] P. Landeros, S. Allende, J. Escrig, E. Salcedo, D. Altbir, and E. E. Vogel. Reversal modes in magnetic nanotubes. *Appl. Phys. Lett.* , 90:102501, 2007.

[313] N. A. Usov, A. P. Chen, A. Zhukov, and J. GonzÀlez. Nucleation field of a soft magnetic nanotube with uniaxial anisotropy. *J. Appl. Phys.* , 104:083902, 2008.

[314] W. Wernsdorfer, B. Doudin, D. Mailly, K. Hasselbach, A. Benoit, J. Meier, J. Ph. Ansermet, and B. Barbara. Nucleation of magnetization reversal in individual nanosized nickel wires. *Phys. Rev. Lett.*, 77(9):1873–1876, 1996.

[315] M. Méndez, V. Vega, S. González, R. Caballero-Flores, J. García, and V. Prida. Effect of sharp diameter geometrical modulation on the magnetization reversal of bi-segmented FeNi nanowires. *Nanomaterials*, 8(8):595, 2018.

[316] E. M. Palmero, M. Méndez, S. González, C. Bran, V. Vega, M. Vázquez, and V. M. Prida. Stepwise magnetization reversal of geometrically tuned in diameter ni and FeCo bi-segmented nanowire arrays. *Nano Res.*, 12(7):1547–1553, 2019.

[317] J. A. Fernandez-Roldan and O. Chubykalo-Fesenko. Dynamics of chiral domain walls under applied current in cylindrical magnetic nanowires. *APL Materials*, 10(11):111101, 2022.

[318] A. de Riz. *Modélisation de la dynamique de parois de domaines dans des nanofils à section circulaire*. PhD thesis, Université Grenoble Alpes, 2021.

[319] H. Fangohr, D. S. Chernyshenko, M. Franchin, T. Fischbacher, and G. Meier. Joule heating in nanowires. *Phys. Rev. B*, 84(5):054437, 2011.

[320] C.-Y. You, I. M. Sung, and B.-K. Joe. Analytic expression for the temperature of the current-heated nanowire for the current-induced domain wall motion. *Appl. Phys. Lett.*, 89(22):222513, 2006.

[321] R. Guedas, V. Raposo, and J. L. Prieto. Micro and nanostrips in spintronics: How to keep them cool. *J. Appl. Phys.*, 130(19):191101, 2021.

[322] Y Rheem, B-Y Yoo, B K Koo, W P Beyermann, and N V Myung. Synthesis and magnetotransport studies of single nickel-rich NiFe nanowire. *J. Phys. D: Appl. Phys.*, 40(23):7267–7272, 2007.

[323] Y Rheem, B-Y Yoo, W P Beyermann, and N V Myung. Electro- and magneto-transport properties of a single CoNi nanowire. *Nanotechnology*, 18(12):125204, 2007.